

**Monitoring and modelling surface moisture in
north-east Jordan using ERS SAR data**

Thesis submitted for the degree of

Doctor of Philosophy

at the University of Leicester

by

Kevin James Tansey B.Sc. (Sheffield)

Department of Geography

University of Leicester

June 1999

UMI Number: U115817

All rights reserved

INFORMATION TO ALL USERS

The quality of this reproduction is dependent upon the quality of the copy submitted.

In the unlikely event that the author did not send a complete manuscript and there are missing pages, these will be noted. Also, if material had to be removed, a note will indicate the deletion.



UMI U115817

Published by ProQuest LLC 2013. Copyright in the Dissertation held by the Author.
Microform Edition © ProQuest LLC.

All rights reserved. This work is protected against
unauthorized copying under Title 17, United States Code.



ProQuest LLC
789 East Eisenhower Parkway
P.O. Box 1346
Ann Arbor, MI 48106-1346

Monitoring and modelling surface moisture in north-east Jordan using ERS SAR data

Kevin James Tansey

Abstract

The monitoring and modelling of soil moisture is important both for hydrological and geomorphological studies. In semi-arid and arid regions the measurement and monitoring of soil moisture conditions is made more difficult because of unpredictable rainfall, the nature of desert soils and sediments, accessibility and the costs of financing projects. Remotely sensed data offers good temporal and high spatial coverage at a reasonably low cost. To assess the usefulness of a remote sensing approach to soil moisture monitoring in desert regions, a time series of ERS-1 and ERS-2 SAR images were acquired between March 1995 and April 1998 of the north-eastern desert of Jordan. Previous research has demonstrated the sensitivity to soil moisture and surface roughness of the backscatter coefficient of the ERS SAR system. The following objectives were addressed: (1) To assess and exploit the ability of the ERS SAR instrument to monitor geomorphological and hydrological changes in the desert environment. (2) To calibrate theoretical microwave scattering models using field reference data (soil moisture, surface roughness, soil texture, climatic parameters and vegetation) and assess their application to desert environments. (3) To simulate the dependence of the backscatter coefficient on soil moisture fluctuations and surface roughness changes with the aim of improving the understanding of microwave interactions with desert surfaces. (4) To investigate the potential for extraction of quantitative soil moisture estimates from ERS SAR data.

Analysis of multitemporal backscatter coefficients, expressed in decibels (dB), for some desert surfaces show fluctuations of up to 6 dB during or after periods of rainfall. Basalt boulder or stone surfaces show very stable backscatter properties regardless of soil moisture conditions. This is because the roughness parameter dominates the scattering mechanism. Detailed analysis of surface roughness measurements and calculations are presented. To understand the scattering processes, the physical optics (PO), geometric optics (GO), small perturbation (SP) and integral equation models (IEM) were calibrated using field data. The results show the limitations of using the PO, GO and SP models in this natural environment, caused by the restrictive model validation domains. The calibration of the IEM yielded much better results, correlation coefficients greater than 0.8 were achieved between predicted and observed backscatter coefficients. Retrieval of soil moisture estimates with the IEM yielded a confidence level of 80%.

ERS SAR has demonstrated an ability to detect changes in the surface properties of desert surfaces. However, to improve model accuracy, detailed information on surface roughness properties, or a second image band of data is necessary. Future research should focus on interferometry and multi-parameter systems (e.g. ENVISAT) to improve dryland soil moisture estimates.

Table of Contents

Abstract	i
Table of contents	ii
List of figures and tables	vii
Acronyms	xxiv
Acknowledgements	xxv
Chapter 1. Introduction	1
1.1. The Jordan Badia Research and Development Programme	2
1.1.1. <i>Climatic characteristics</i>	4
1.1.2. <i>Geology and topography</i>	5
1.1.3. <i>Geomorphology</i>	6
1.1.4. <i>Flora and fauna</i>	10
1.1.5. <i>Soils</i>	10
1.1.6. <i>Water resources and requirements</i>	11
1.1.7. <i>Social and environmental aspects</i>	13
1.2. Soil moisture	14
1.2.1. <i>Methods of soil moisture measurement</i>	15
1.3. Soil moisture characteristics of the Badia surfaces	19
1.3.1. <i>Basalt and desert stone pavement surfaces</i>	20
1.3.2. <i>Playa (qa'a) surfaces</i>	22
1.3.3. <i>Marab and wadi surfaces</i>	26
1.4. Remote sensing of soil moisture	27
1.4.1. <i>Remote sensing methods: thermal infra-red</i>	27
1.4.2. <i>Remote sensing methods: passive microwaves</i>	28
1.4.3. <i>Remote sensing methods: active microwaves</i>	29
1.5. Research objectives	32
1.6. Thesis structure	32
Chapter 2. Microwave remote sensing of soil moisture	34
2.1. Principles of active microwave remote sensing	34
2.1.1. <i>The radar equation and other system parameters</i>	38
2.1.2. <i>Energy-target interactions: surface and volume scattering</i> ...	41

2.1.3. <i>Microwave backscatter dependence on dielectric properties</i>	44
2.1.4. <i>Microwave backscatter dependence on roughness properties</i>	49
2.2. Technical specification and characteristics of the ERS SAR	50
2.3. Data structure and acquisition periods	52
2.3.1 <i>SAR image geometric effects</i>	53
2.3.1.1. Foreshortening	53
2.3.1.2. Layover	54
2.3.1.3. Shadow	54
2.3.2. <i>SAR image speckle effects</i>	55
2.3.3. <i>Data coverage and acquisition</i>	57
2.4. Image geometric correction	60
2.5. Derivation of the backscatter coefficient	61
2.5.1. <i>Calibration methods and assumptions</i>	61
2.5.2. <i>Calculating the backscatter coefficient</i>	64
2.5.2.1. Simplified equation	64
2.5.2.2. Comprehensive equation	65
2.5.2.3. Applications of corrections to ERS SAR PRI products	65
2.6. Modelling the backscatter coefficient	67
2.6.1. <i>A brief review of microwave modelling</i>	69
2.6.2. <i>Model derivations, assumptions and ranges of validity</i>	71
2.6.2.1. Kirchoff and small perturbation models of surface scattering	72
2.6.2.2. The integral equation model (IEM) of surface scattering	75
2.6.3. Assumptions made concerning the nature of desert surfaces	77
2.6.3.1. Modelling the non-soil surface	78
2.6.3.2. The influence of dryland vegetation	78
Chapter 3. Multitemporal SAR image interpretation	80
3.1. Introduction	80
3.2. Multitemporal backscatter variation of desert surfaces	83
3.2.1. <i>Basalt and desert stone surfaces</i>	86
3.2.1.1. Basalt surfaces	86
3.2.1.2. Stone pavement (hammada) surfaces	92
3.2.2. <i>Playa (qa'a) surfaces</i>	94
3.2.3. <i>Vegetated marab surfaces</i>	102

3.2.4. <i>Implications of surface differentiation and temporal backscatter</i>	106
3.3. Comparison of ERS-1 and ERS-2 SAR data	107
3.4. Conclusions	110

Chapter 4. Field data and methodology

4.1. Introduction	111
4.2. Site selection and description	111
4.2.1. <i>General site criteria</i>	112
4.2.2. <i>Specific site overview</i>	113
4.2.3. <i>Sampling strategy</i>	120
4.3. Soil moisture	121
4.3.1. <i>Instrument</i>	121
4.3.2. <i>Sampling methods</i>	122
4.3.3. <i>Calibration</i>	123
4.3.4. <i>Data verification</i>	124
4.4. Surface roughness	125
4.4.1. <i>Definitions</i>	125
4.4.2. <i>RMS height</i>	126
4.4.3. <i>Correlation length</i>	127
4.4.4. <i>Autocorrelation function</i>	128
4.4.5. <i>The profilometer</i>	129
4.4.6. <i>Roughness profile length</i>	130
4.4.7. <i>Photograph analysis</i>	130
4.4.8. <i>Problems and alternative methods</i>	132
4.5. Soil texture	133
4.5.1. <i>Particle size analysis</i>	133
4.5.2. <i>Bulk density</i>	137
4.6. Specific basalt site analysis	138
4.6.1. <i>Percentage cover</i>	139
4.6.2. <i>Average stone dimensions</i>	139
4.7. Climate data	140
4.7.1. <i>Introduction</i>	140
4.7.2. <i>Precipitation</i>	141

4.7.2.1. Long-term rainfall patterns	141
4.7.2.2. Short-term rainfall patterns	144
4.7.2.3. The utility of the rainfall data	147
4.7.3. <i>Temperature</i>	148
4.7.3.1. Air temperature	148
4.7.3.2. Soil temperature	150
4.7.4. <i>Wind speed and direction</i>	150
4.7.4.1. Wind speed	151
4.7.4.2. Wind direction	152
4.7.5. <i>Evaporation</i>	154
4.8. Vegetation sampling and analysis	156
4.8.1. <i>Sampling methods</i>	157
4.8.2. <i>Vegetation analysis results</i>	158
4.9. Summary of field data and methodology	158
 Chapter 5. Roughness properties: theory, measurement and analysis	161
5.1. Introduction	162
5.2. Literature review: surface roughness and SAR	162
5.2.1. <i>Random data</i>	163
5.2.2. <i>Case studies</i>	163
5.2.3. <i>Higher levels of data analysis</i>	166
5.3. Data description and analysis	168
5.3.1. <i>Data collection methods</i>	168
5.3.2. <i>Roughness profiles: analysis and results</i>	169
5.3.2.1. RMS height	170
5.3.2.2. Probability distribution functions of surface heights	171
5.3.2.3. Correlation length	172
5.3.2.4. The influence of transect length on the correlation length	176
5.3.2.5. The influence of slope angle on the RMS height and correlation length	178
5.3.2.6. Comparison of the autocorrelation function with theoretical models	180
5.3.3. <i>Annual fluctuations in surface roughness properties</i>	182
5.4. Conclusions	185

Chapter 6. Deriving soil moisture estimates with theoretical models	187
6.1. Introduction	187
6.2. Backscatter sensitivity to surface parameters	190
6.2.1. <i>Sensitivity to soil moisture</i>	191
6.2.2. <i>Sensitivity to surface roughness</i>	194
6.2.3. <i>Sensitivity analysis – main land cover types</i>	198
6.3. Model calibration	200
6.3.1. <i>SP, PO and GO model calibration</i>	202
6.3.2. <i>IEM calibration</i>	206
6.3.3. <i>Optimal calibration results</i>	209
6.3.4. <i>Model calibration: conclusions</i>	210
6.4. Model inversion: results and limitations	211
6.4.1. <i>Soil moisture retrieval: Qa'a Qattafi</i>	212
6.4.2. <i>Soil moisture retrieval: Qa'a al Wassad</i>	215
6.4.3. <i>Soil moisture retrieval: Qa'a al Buqayawiyya</i>	216
6.4.4. <i>Soil moisture retrieval: Marab Suwaiid</i>	219
6.4.5. <i>Soil moisture retrieval: Marab Wutaydat</i>	222
6.4.6. <i>Soil moisture retrieval: Chert hammada</i>	224
6.4.7. <i>Soil moisture retrieval: Limestone hammada</i>	226
6.4.8. <i>Soil moisture retrieval: Fahda Vesicular basalt</i>	229
6.5. Model validation	232
6.6. Conclusions	240
 Chapter 7. Conclusions	 244
7.1. Objectives	244
7.2. Multitemporal image analysis	245
7.3. Parameterisation of roughness	247
7.4. Theoretical modelling	248
7.5. Application of results: Jordan Badia Research and Development Programme	253
7.6. Recommendations for future research and ENVISAT	254
7.6.1. ENVISAT	255
 Chapter 8. Bibliography	 259

List of Figures

Chapter 1:

Figure 1.1. (p. 3): Location of the Badia Research and Development Programme area.

Figure 1.2. (p. 4): Precipitation distribution in Jordan.

Figure 1.3. (p. 6): The geological divisions within the eastern Badia of Jordan (after Burdon 1959).

Figure 1.4. (p. 12): Cross-section between Azraq in the south-west and Ruwayshid in the north-east showing the major aquifers of the project area.

Figure 1.5. (p. 21): Four hypotheses of desert pavement surface evolution (after Higgitt and Allison 1998).

Figure 1.6. (p. 23): Hydrological classification, idealised morphology, and groundwater-surface water interaction of evaporative basins (after Bowler 1986).

Figure 1.7. (p. 24): Diagrammatic representation of the possible exchange pathways for water and salts in a playa (*qa'a*) system (after Torgersen *et al.* 1986).

Figure 1.8. (p. 30): The European Space Agency (ESA) first European Remote Sensing (ERS-1) Satellite.

Chapter 2:

Figure 2.1. (p. 35): The microwave bands as elements of wavelength and frequency (Trevett 1986).

Figure 2.2. (p. 37): Example of the synthetic aperture radar (SAR) approach, in a spaceborne application (Ulaby *et al.* 1981).

Figure 2.3. (p. 38): SAR imaging geometry (Trevett 1986).

Figure 2.4. (p. 42): Examples of (a) surface scattering and (b) volume scattering processes (Ulaby *et al.* 1982).

Figure 2.5. (p. 43): Penetration depth expressed given as a function of volumetric soil moisture (g cm^{-3}) of a loamy soil at three frequencies (Ulaby *et al.* 1982). As the frequency of the microwave increases the penetration depth decreases. Interpolation at ≈ 5.3 GHz, the wavelength of the ERS SAR system, between 4 GHz and 10 GHz indicates the penetration depth is approximately 3 cm at a volumetric soil moisture of 0.1, decreasing to less than 1 cm at a volumetric soil moisture of 0.4. At very low moisture levels the penetration depth increases significantly.

Figure 2.6. (p. 45): The complex dielectric constant, comprising real (ϵ'_{soil}) and imaginary (ϵ''_{soil}) parts, shown as a function of volumetric moisture content at four frequencies (after Ulaby *et al.* 1986).

Figure 2.7. (p. 46): The complex dielectric constant, comprising real (ϵ') and imaginary (ϵ'') parts, shown as a function of volumetric moisture content for three soil types at 5 GHz. Also shown are the approximate transition volumetric soil moisture values (W_t) discussed in the text (after Wang and Schmugge 1980).

Figure 2.8. (p. 47): Measured dielectric constants for five soil types as a function of volumetric soil moisture at 5 GHz (Hallikainen *et al.* 1985).

Figure 2.9. (p. 49): Fresnel reflectivity at normal incidence (an expression of the backscatter coefficient), in dB, described as a function of soil moisture for two soil types at 5 GHz (after Ulaby *et al.* 1986).

Figure 2.10. (p. 50): The dependence of the backscatter coefficient on RMS height and incidence angle at two microwave frequencies; 4.25 GHz and 7.25 GHz (Ulaby *et al.* 1978).

Figure 2.11. (p. 53): The distortion known as foreshortening caused by high relief (after Trevett 1986).

Figure 2.12. (p. 54): Radar layover distortion in areas of extreme relief (after Trevett 1986).

Figure 2.13. (p. 55): Radar shadow (after Trevett 1986).

Figure 2.14. (p. 59): ERS SAR scene coverage of the Jordan Badia Research and Development Programme area. The ascending scenes are shown as solid lines, the one descending scene is shown as a dashed line. ERS SAR track and frame numbers are shown for each image. Refer to Table 2.3 for further information.

Figure 2.15. (p. 63): The 95%, 90% and 50% radiometric confidence intervals versus ENL for ESA products. The ENL range from 3 (PRI product) to 370. The two horizontal dashed lines represent the ± 1 dB interval (after Laur *et al.* 1998).

Figure 2.16. (p. 71): Validity ranges for the integral equation model (tick points that have been confirmed by experiment), first-order small perturbation model (FPM) and Kirchoff model (KM) plotted in the standard deviation of surface height (Sigma) - correlation length (L) feature space, k is the wavenumber (Fung *et al.* 1992).

Chapter 3:

Figure 3.1. (p. 84): Location of the study sites analysed in Chapter 3. Each site is displayed as a colour representing the four main land cover units: basalt, *hammada*, *qa'a* and *marab*.

Figure 3.2. (p. 85): ERS-1 SAR PRI full scene of the northern section of the Programme area. The image was acquired on the 7th March 1996 and covers 100 by 100 km. The corner co-ordinates of the image are: 36.9157 °E, 31.786 °N (bottom-left); 37.9497 °E, 31.9695 °N (bottom-right); 37.7300 °E, 32.8739 °N (top-right); 36.6845 °E, 32.6902 °N (top-left). The solid line indicates the approximate position of the border with Syria (the northern border of the project area).

Figure 3.3. (p. 86): Monthly rainfall totals for Safawi, Azraq, Menara and *Marab Salma* precipitation stations. Please note boundaries of data collection listed in the text.

Figure 3.4. (p. 87): Multitemporal backscatter variation for three basalt formations located within the eastern Badia of Jordan (a) and associated error (1 standard error of estimation) bar (b). The temporal scale is expressed as a Julian Day, corresponding to the day of the year. The backscatter coefficients are calculated using the comprehensive equation given in Section 2.5. ERS-2 SAR measurements commenced in 1997 (day 87).

Figure 3.5. (p. 90): The relationships between the backscatter coefficient and (a) maximum height of rocks (h_{max}); and (b) the standard deviation of surface height (s) obtained empirically for arid land surfaces (Derooin *et al.* 1997).

Figure 3.6. (p. 91): ERS-1 SAR intensity image (dB) of the north-central region of the study area. The image was acquired on the 23 March 1995. It demonstrates the ability of SAR to qualitatively distinguish between basalt flows, mainly due to the large-scale morphological features (*qa'a*). The image covers approximately 35 by 16 km. The approximate image corner co-ordinates are; 37.007° E, 32.323° N, top-left; 37.022° E, 32.203° N, bottom-left; 37.398° E, 32.245° N, bottom-right; 37.357° E, 32.384° N, top-right. The Safawi to Ruwayshid road is clearly seen in the bottom of the image.

Figure 3.7. (p. 93): The temporal profiles of backscatter of the desert stone pavements (*hammadas*). Three *hammada* are shown, along with the temporal profile of the Abed Olivine basalt for comparison. Backscatter coefficients have been derived using the comprehensive equation.

Figure 3.8. (p. 94): ERS-1 SAR image sub-scene of the central region of the study area. The image was acquired on the 6 July 1995 and is displayed as an intensity image. It demonstrates the ability of SAR to qualitatively distinguish between rough basalt surfaces and less rough desert pavements (*hammada*). The image covers approximately 19 by 12 km. The approximate image corner co-ordinates are; 37.232° E, 32.002° N, top-left; 37.446° E, 31.868° N, bottom-right; north is up.

Figure 3.9. (p. 96): The temporal backscatter profiles of *Qa'a Qattafi* and *Qa'a al Abd*. The two surfaces have a different backscatter signature caused by different surface roughness properties.

Figure 3.10. (p. 99): ERS-1 SAR image sequence of *Qa'a al Abd* situated in the eastern Badia of Jordan. The images have been converted to an estimate of the backscatter coefficient. The area covers approximately 7.3 by 6.9 km, the scene is located at; 37.193° E, 32.515° N, top-left; 37.274° E, 32.438° N, bottom-right, north is up. Refer to the text for a description of the annotated points (A1 ... A6) shown in the images. Rainfall data to aid the interpretation are presented in Figure 3.3.

Figure 3.11. (p. 100): Multitemporal colour composite of *Qa'a al Abd*. The following date/colour combinations, 7 March 1996 (red), 6 July 1995 (green) and 11 April 1996 (blue) show the ability of ERS SAR to detect temporal fluctuations in the backscatter coefficient. Refer to the text for a description of the feature at point A7.

Figure 3.12. (p. 102): Multitemporal colour composite of *Qa'a Qattafi*, showing relative stable backscatter properties in the centre of the *qa'a* compared to the stony and vegetated surrounding areas. The images displayed are 7 March 1996 (red), 19 October 1995 (green) and 11 April 1996 (blue). Observations B-E are explained in the text. The image covers approximately 4.9 by 4 km, the corner co-ordinates are; 37.427° E, 31.872° N top-left; 37.482° E, 31.828° N bottom-left; north is up.

Figure 3.13. (p. 103): The temporal profiles of three *marab* surfaces, *Qa'a (marab) al Buqayawiyya*, *Shubayka* and *Wutaydat*. *Marab* sites showed the greatest variation in seasonal backscatter, believed to be caused by the increase of soil moisture and storage of the available moisture in the upper layers of the soil.

Figure 3.14. (p. 104): Multitemporal colour composite of *Qa'a al Buqayawiyya* and surrounding terrain, displayed using 7 March 1996 (red), 6 July 1995 (green) and 11 April 1996 (blue) images. For a description of points F, G and H, refer to the text. The image covers approximately 9.6 by 14 km, the corner co-ordinates are; 37.084° E, 32.140° N, top-left; 37.181° E, 31.985° N, bottom-right; north is up.

Figure 3.15. (p. 106): Multitemporal colour composite of *Marab Shubayka* and surrounding terrain using 7 March 1996 (red), 6 July 1995 (green) and 11 April 1996 (blue) images. The backscatter coefficient estimates on the 7 March 1996 acquisition clearly dominates the scene. The image covers approximately 7.5 by 5.3 km, the corner co-ordinates are; 37.184° E, 32.422° N, top-left; 37.268° E, 32.364° N, bottom-right; north is up. Descriptions of sites I, J and K are given in the text.

Chapter 4:

Figure 4.1. (p. 115): Location of the permanent monitoring sites (PMS).

Figure 4.2. (p. 120): Schematic diagram showing the general field methodology undertaken at each site. Data on the soil moisture, texture and roughness were collected and also data related to the vegetation if significant amounts were present.

Figure 4.3. (p. 121): The dielectric ThetaProbe measuring the volumetric soil moisture in *Qa'a ash Shubayka*.

Figure 4.4. (p. 128): Measured autocorrelation functions derived from field data shown against approximate Gaussian and exponential functions.

Figure 4.5. (p. 129): 48 cm (96 samples) profilometer used for measuring surface height values set up to record on a basalt surface (upper) and a *qa'a* surface (lower).

Figure 4.6. (p. 131): Example profiles recorded for a *qa'a* (black line) and a basalt (dashed line) surface. Both surfaces have a mean height of zero cm.

Figure 4.7. (p. 134): Location of the sites where soil texture analysis was undertaken in the BRDP study area.

Figure 4.8. (p. 137): Generalised soil particle distribution percentages for the four main surface types, (a) *qa'a* surface, (b) basalt surface, (c) *hammada* surface and (d) *marab* surface.

Figure 4.9. (p. 142): Locations of the automatic weather stations in the study area (Menara station is outside the study area).

Figure 4.10. (p. 144): Mean monthly precipitation values for the five long-term monitoring stations located within the study area for the period 1980 to 1990.

Figure 4.11. (p. 146): Rainfall values recorded at permanent (Umm El Quttein, Deir al-Kahf, Safawi and Azraq) and temporary (Menara and *Marab Salma*) weather stations in the eastern Badia of Jordan (1994/95 to 1996/97). Please refer to the text for the dates that these stations were used.

Figure 4.12. (p. 147): The temporal distribution and the magnitude of rainfall events recorded at the *Marab Salma* raingauge over a time period of 1 hour.

Figure 4.13. (p. 149): Mean daily air and soil temperatures recorded at the *Marab Salma* station for the period December 1995 to October 1996 (excluding April 1996).

Figure 4.14. (p. 149): Mean daily air temperatures recorded at the Menara AWS for the period August 1994 to August 1996 (excluding January 1995), (Kirk 1997).

Figure 4.15. (p. 151): Mean diurnal wind speeds at the *Marab Salma* station for the months of January, March, July and October 1996; (note: only 29 days for March and 27 days for October, caused by battery failure).

Figure 4.16. (p. 153): Diurnal wind direction variation for the months of January, March, July and October 1996 recorded at the *Marab Salma* station. The black line represents the mean wind direction for that hour.

Figure 4.17. (p. 154): Diurnal wind direction variation recorded between the period August 1994 and August 1996 at the Menara AWS (Kirk 1997).

Figure 4.18. (p. 156): Total daily evaporation rates calculated at the Menara station using an approximation of the Penman Equation. These are plotted against rainfall (bold line) for the period 7th August to the 20th October 1994 (from Kirk 1997).

Chapter 5:

Figure 5.1. (p. 165): The procedure for calculating the roughness parameters outlined in a hydrological study in the Abruzzo region of Italy (Chiarantini *et al.* 1995).

Figure 5.2. (p. 167): (a) Power spectra of dated basalt lava flows, showing surface roughness evolution with age, and (b) linear fits showing the slope and offset values to the power spectra (Farr, 1992).

Figure 5.3. (p. 170): The surface height profile for *Marab Shubayka* derived in the spring 1997 field campaign. The peaks and troughs correspond to hummocks and cracks on the *marab* surface.

Figure 5.4. (p. 172): Probability density functions of surface heights for *Marab Shubayka*. These are displayed for the full transect of 2.88 m (a); (b), (c) and (d) show the P.D.F. of the three ≈ 1 m transects.

Figure 5.5. (p. 174): Autocorrelation relationships derived using the two estimates (simple and Pearson) of autocorrelation for two sites, *Marab Shubayka* and *Marab Wassad*. The estimates of the correlation length for the sites shown above are: *Shubayka*, 12 and 11.9 cm, and *Wassad*, 19 and 21.6 cm for the simple (Equation 5.2) and Pearson (Equation 5.4) estimates respectively.

Figure 5.6. (p. 177): The influence of transect length on the autocorrelation coefficient is shown for the three ≈ 1 m profiles that comprise the full profile length (shown as a solid black line) for *Marab Shubayka*.

Figure 5.7. (p. 179): The influence of surface slope on the RMS height (top) and the correlation function (lower) for a *hammadra* site. The values of the parameters estimated are listed in the text.

Figure 5.8. (p. 181): Theoretical functions plotted against the measured autocorrelation function at the full profile length, *Marab Shubayka*. The best fit model is Gaussian, l is 11.9 cm.

Figure 5.9. (p. 182): Measured ≈ 1 m correlation functions (1,2,3) shown against theoretical functions, *Marab Shubayka*.

Chapter 6:

Figure 6.1. (p. 191): Sensitivity of the dielectric constant to soil moisture for two soil types. The clay soil comprises 45% clay and 10% sand sized particles, the sand soil comprises 60% sand and 5% clay particles in this example. For a given soil moisture above 0.03 (by volume) a sand soil has a greater dielectric constant.

Figure 6.2. (p. 192): Sensitivity of the backscatter coefficient to soil moisture for a specified soil type. The IEM simulation assumes a constant silt particle size content of 30%.

Figure 6.3. (p. 193): Sensitivity of the backscatter coefficient to soil moisture accounting for the variation in incidence angles across an ERS SAR image. The simulation displayed is for a 1° increment in incidence angles between 20° and 26° .

Figure 6.4. (p. 195): Sensitivity of the backscatter coefficient to RMS height for a specified correlation length (l). The autocorrelation function used in this simulation is Gaussian.

Figure 6.5. (p. 195): Sensitivity of the backscatter coefficient to RMS height for a specified correlation length (l). The autocorrelation function used in this simulation is exponential.

Figure 6.6. (p. 197): Sensitivity of the backscatter coefficient to RMS height accounting for the variation in incidence angle across an ERS SAR image. The simulation displayed is for 1° increments for incidence angles between 20° and 26° . This variation is accounted for in the image pre-processing stages of the analysis.

Figure 6.7. (p. 199): Sensitivity of the backscatter coefficient to soil moisture for the four main land cover types.

Figure 6.8. (p. 200): Sensitivity of the backscatter coefficient to RMS height for the four main land cover types.

Figure 6.9. (p. 202): Illustration of the validation criteria of the SP, PO, GO models and IEM used in this study. Field data, excluding basalt sites, are plotted in a roughness feature space comprising correlation length (l) against RMS height (σ), k is the wavenumber and ≈ 1.11 at 5.3 GHz. In this example, ≈ 1 m profiles have been used to calculate the roughness parameters and the simple method adopted for calculating the correlation length. Those sites that lie within the validation domains of the SP, PO and GO models (dashed polygons) are displayed as hollow circles, those that fit the criteria of only the IEM (solid polygon) are displayed as solid circles.

Figure 6.10. (p. 205): Kirchoff and small perturbation model calibration results for the ten scenarios listed in Table 6.1. Observed backscatter coefficients are derived from ERS SAR PRI data. Predicted backscatter coefficients have been calculated from the SP, PO and GO models using field data that have satisfied all of the validation criteria. The calibration coefficients between observed and predicted measurements are shown.

Figure 6.11. (p. 208): IEM calibration results for the ten scenarios listed in Table 6.2. Observed backscatter coefficients are derived from ERS SAR PRI data. Predicted backscatter coefficients have been calculated from the IEM using field data that have satisfied the validation criteria. The correlation coefficients between observed and predicted values are shown.

Figure 6.12. (p. 210): IEM calibration results for the selected optimal parameterisation with two correlation length methods.

Figure 6.13. (p. 213): Soil moisture - backscatter coefficient curves generated for *Qa'a Qattafi* using the calibrated IEM. The input parameters are; ERS-1 data, RMS height = 0.16 cm, correlation length = 4.5 cm, autocorrelation function = Gaussian, incidence angle = 23° ; ERS-2 data, RMS height = 0.23 cm, correlation length = 4.5 cm, autocorrelation function = Gaussian, incidence angle = 23° .

Figure 6.14. (p. 214): Estimated soil moisture values for *Qa'a Qattafi*, over the winter of 1995, calculated from backscatter coefficients derived from ERS-1 SAR data. Actual estimates of soil moisture from in-situ measurements (taken at the same time as the satellite acquisition) are shown for comparison. Rainfall data from the Safawi station are also presented.

Figure 6.15. (p. 215): Soil moisture - backscatter coefficient relationship curves generated for *Qa'a al Wassad* using the calibrated IEM. The input parameters are; ERS-2 data, RMS height = 0.17 cm, correlation length = 5.9 cm, autocorrelation function = exponential, incidence angle = 22° .

Figure 6.16. (p. 217): Soil moisture - backscatter coefficient curve generated for *Qa'a al Buqayawiyya*. The input parameters are; ERS-1 data, RMS height = 0.76 cm, correlation length = 25 cm, autocorrelation function = exponential, incidence angle = 21.2° .

Figure 6.17. (p. 218): Estimated soil moisture values for *Qa'a al Buqayawiyya*, over the winter of 1995, calculated from backscatter coefficients derived from ERS-1 SAR data. Actual estimates of soil moisture from in-situ measurements (taken at the same time as the satellite acquisition) are shown for comparison. Rainfall data from the Safawi station are also presented. The last estimation on May 16th 1996 shows good agreement with the measured value of soil moisture.

Figure 6.18. (p. 220): Soil moisture - backscatter coefficient curves generated for *Marab Suwaiid*. The input parameters are; ERS-1 data, RMS height = 0.2 cm, correlation length = 3.2 cm, autocorrelation function = exponential, incidence angle = 23.7° . ERS-2 data, RMS height = 1.38 cm, correlation length = 13.9 cm, autocorrelation function = Gaussian, incidence angle = 23.7° .

Figure 6.19. (p. 221): Estimated soil moisture values for *Marab Suwaiid*, over the winter of 1995, calculated from backscatter coefficients derived from ERS-1 SAR data. Actual estimates of soil moisture from in-situ measurements (taken at the same time as the satellite acquisition) are shown for comparison. Rainfall data from the Safawi station are also presented.

Figure 6.20. (p. 222): Soil moisture - backscatter coefficient curves generated for *Marab Wutaydat*. The input parameters are; ERS-1 data, RMS height = 0.87 cm, correlation length = 7 cm, autocorrelation function = Gaussian, incidence angle = 25° .

Figure 6.21. (p. 224): Estimated soil moisture values for *Marab Wutaydat*, over the winter of 1995, calculated from backscatter coefficients derived from ERS-1 SAR data. Actual estimates of soil moisture from in-situ measurements taken at the same time as the satellite acquisition are shown for comparison.

Figure 6.22. (p. 225): Soil moisture - backscatter coefficient curve generated for the chert *hammad*. The input parameters are; ERS-1 data, RMS height = 0.7 cm, correlation length = 5.5 cm, autocorrelation function = exponential, incidence angle = 21° .

Figure 6.23. (p. 226): Estimated soil moisture values for the chert *hammad* surface, over the winter of 1995, calculated from backscatter coefficients derived from ERS-1 SAR data. Actual estimates of soil moisture from in-situ measurements (taken at the same time as the satellite acquisition) are shown for comparison. Rainfall data from the Safawi station are also presented.

Figure 6.24. (p. 227): Soil moisture - backscatter coefficient curve generated for the limestone *hammada*. The input parameters are; ERS-1 data, RMS height = 0.66 cm, correlation length = 5.5 cm, autocorrelation function = Gaussian, incidence angle = 19.8°.

Figure 6.25. (p. 228): Estimated soil moisture values for limestone *hammada*, over the winter of 1995, calculated from backscatter coefficients derived from ERS-1 SAR data. Actual estimates of soil moisture from in-situ measurements (taken at the same time as the satellite acquisition) are shown for comparison. Rainfall data from the Azraq station are also presented.

Figure 6.26. (p. 230): Soil moisture - backscatter coefficient curve generated for the Fahda Vesicular basalt. The input parameters are; ERS-1 data, RMS height = 2.3 cm, correlation length = 7.2 cm, autocorrelation function = Gaussian, incidence angle = 21.9°.

Figure 6.27. (p. 231): Estimated soil moisture values for Fahda Vesicular basalt, over the winter of 1995, calculated from backscatter coefficients derived from ERS-1 SAR data. Actual estimates of soil moisture from in-situ measurements (taken at the same time as the satellite acquisition) are shown for comparison. Rainfall data from the Safawi station are also presented.

Figure 6.28. (p. 233): Estimates of soil moisture from ERS-2 SAR data compared against soil moisture estimates derived in-situ in 1998. Apart from the outlying over prediction of soil moisture at *Qa'a al Wassad*, the inversion model slightly under estimates the value of soil moisture estimated in the field. The line $x = y$ is shown.

Figure 6.29. (p. 236): Location of *Qa'a al Buqayawiyya* (shown in red) in the north-eastern Jordan Badia.

Figure 6.30. (p. 237): Soil moisture distribution maps of *Qa'a al Buqayawiyya*, derived from ERS-1 and ERS-2 SAR imagery. The images covers 9 by 8 km, north is to the top.

Chapter 7:

Figure 7.1. (p. 257): Dependence of the backscatter coefficient to changes in soil moisture ($\text{m}^3 \text{ water m}^{-3} \text{ soil}$) expressed as a function of polarisation and roughness. The RMS height of the *hammada* surface is 0.7 cm, and the $qa' a$, 0.22 cm.

Figure 7.2. (p. 258): Dependence of the backscatter coefficient to changes in soil moisture ($\text{m}^3 \text{ water m}^{-3} \text{ soil}$). The simulation indicates that a surface (e.g. *Marab Salma*) with a RMS height of 1.16 cm does not display different scattering intensities at VV and HH. At a lower RMS height (0.72 cm), the differences in backscatter are greater, a measurable indication of the absolute roughness of the surface.

List of Tables

Chapter 1:

Table 1.1. (p. 7): Basalt flow age, location and surface characteristics (after Ibrahim 1993).

Table 1.2. (p. 17): A summary of in-situ methods available to determine soil moisture, and specific advantages and disadvantages of their application.

Chapter 2:

Table 2.1. (p. 51): Technical specification of the ERS-1 SAR instrument (ESA 1992).

Table 2.2. (p. 52): ERS SAR PRI product characteristics (ESA 1993).

Table 2.3. (p. 58): Information related to the ERS SAR images used in this study; acquisition date, coverage and orbit details.

Chapter 3:

Table 3.1. (p. 109): Backscatter coefficients (in dB) of different surfaces calculated from ERS SAR tandem images. These have been derived using the two methods presented by Laur *et al.* (1996). The data indicate that a small reduction in the backscatter coefficient occurred for the majority of the sites shown (apart from Qa'a Qattafi). This data show that the relative radiometric correlation between the two instruments is acceptable at this particular time of image acquisition.

Chapter 4:

Table 4.1. (p.112): Dates of field campaigns and associated ERS SAR image acquisitions.

Table 4.2. (p. 114): Location and general characteristics of study sites located within the eastern Badia of Jordan.

Table 4.3. (p. 116-119): Field descriptions of the permanent monitoring sites (PMS), *Qa'a Qattafi*, chert gravel *hammada*, *Qa'a al Buqayawiyya*, limestone *hammada*, Fahda Vesicular basalt, *Marab Suwaiid*, *Marab Wutaydat* and *Qa'a al Wassad*.

Table 4.4. (p. 125): Results of the data verification experiments of comparing volumetric moisture readings from the ThetaProbe and more standard laboratory methods.

Table 4.5. (p. 136): Soil analysis results of particle size and bulk density measurements.

Table 4.6. (p. 139): Stone characteristics measured at the three basalt sites included in the study.

Table 4.7. (p. 141): Rainfall stations within the Azraq Basin. Adapted from Water Authority of Jordan (1998).

Table 4.8. (p. 157): Percentage vegetation cover measured at the marab sites.

Table 4.9. (p. 159): Dominant species, lifeform and palatability of vegetation found within the eastern Badia of Jordan.

Chapter 5:

Table 5.1. (p. 171): Data summary of the roughness parameters for (a) *Marab Shubayka* and *Marab Wutaydat*. Refer to the text for an explanation of the terms listed.

Table 5.2. (p. 175): Comparison of the two methods for calculating the correlation length.

Table 5.3. (p. 183): Calculated RMS heights for three field campaigns.

Chapter 6:

Table 6.1. (p. 203): Summary of the results of the calibration of the SP, PO and GO models using field data acquired during three field seasons. The models have been tested using 10 scenarios of different estimates of the correlation length, profile length and the calculation of the observed backscatter coefficient.

Table 6.2. (p. 206): Summary of the results of the calibration of the IEM using field data acquired during three field seasons. The models have been tested using 10 scenarios of different estimates of the correlation length, profile length and the calculation of the observed backscatter coefficient.

Table 6.3. (p. 233): Model validation results, developed for the retrieval of volumetric soil moisture information from 1998 ERS-2 SAR imagery.

Acronyms

<i>Acronym</i>	<i>Explanation</i>
DEM	Digital Elevation Model
GPS	Global (satellite) Positioning System
GCP	Ground Control Point
ESA	European Space Agency
SAR	Synthetic Aperture Radar
ERS	European Remote Sensing satellite
RMS	Root Mean Square
PRI	Precision Image
NERC	Natural Environment Research Council
GIS	Geographical Information System
BRDP	Badia Research and Development Programme
PDF	Probability Density Function
JERS	Japanese Earth Remote Sensing satellite
RADARSAT	Canadian Radar Satellite
IEM	Integral Equation Model
PO model	Physical Optics model
SPM	Small Perturbation Model
GO model	Geometrical Optics model
ENVISAT	Environmental Satellite (ESA's future mission)
ASAR	Advanced Synthetic Aperture Radar
HH	Horizontal transmit – Horizontal receive polarisation
VV	Vertical transmit – Vertical receive polarisation
MIMICS	Michigan Microwave Canopy Scattering model

Acknowledgements

I would like to acknowledge the following people. Marianne Edwards; colleague, friend and fellow field worker and George Mackay who also helped in the field. This research was undertaken as part of the RGS-IBG/HCST Badia Research and Development Project and I would like to take this opportunity to thank the Jordanian Director, Dr. Mohammed Shahbaz, for his logistical support in Jordan. I also acknowledge the support of the field staff in Safawi. I acknowledge the support of the University of Jordan for allowing us use their laboratories to analyse soil samples, in particular Dr. Anwar Battikhi and the soil technicians. Thanks to all at CORD in Durham for logistical assistance (Dr. Roderic Dutton and Alistair Kirk) and the crowd who live out in Jordan (Darius, Alan and Karen). I also thank my supervisors (Andrew Millington and Kevin White) for all the advice I received; for assistance in the laboratory and field; and for constructive criticism of my methods and ideas. Hopefully we can all work together again. I also thank my postgraduate and staff colleagues in the Department of Geography for making my PhD. such a learned and interesting experience. Thanks also to Rob Coles, Rob Witcher and Louise Morgan for being great friends. Finally, I would like to thank Rachel for being there and giving me the enthusiasm to write up this research.

The data were acquired through ESA Grant (A02.UK.125) to Andrew Millington and Kevin White (University of Reading). Kevin Tansey was funded under Natural Environmental Research Council Award (GT4/95/154/D).

1. Introduction

Monitoring soil moisture dynamics, both in space and time, is important for understanding soil-vegetation-atmosphere interactions. It is especially important in dryland environments as soil moisture, a critical parameter, is crucial in the effective utilisation of the soils and vegetation in these arid and semi-arid regions. Population growth in many dryland nations, combined with changes in land tenure systems, has forced settlers onto areas previously used only for seasonal grazing (Dutton 1998). These are increasingly being converted to rain-fed cultivation and permanent grazing, both of which are marginal economic activities. Such areas are vulnerable to climatic fluctuations and any developments in them need to be carefully sited with respect to water availability and carefully monitored. This study focuses on a dryland region in Jordan, a country which has seen one of the highest natural population increases in the world (Maani *et al.* 1998).

Section 1.1 describes the location of the study region and briefly introduces the history of the Jordan Badia Research and Development Programme (BRDP). The nature of the dryland surfaces that characterise this region are also introduced. Section 1.2 outlines some of the methods of soil moisture measurement and discusses the advantages and disadvantages of different methods. Furthermore, this section introduces the concept of remote sensing for soil moisture studies, discussed in greater detail in Section 1.4 and Chapter 2. Section 1.3 describes some of the issues concerning the soil moisture characteristics of the main desert surfaces that are found in the study region, with a specific interest in some of the geomorphological processes that may occur over the time frame of the research. The remote sensing of soil moisture is described briefly in Section 1.4. Research objectives are stated in Section 1.5. An outline of the thesis structure is given in Section 1.6.

1.1 The Jordan Badia Research and Development Programme

Jordan, a country with a population at present of approximately 4 million people, has a predicted population growth factor that could see the population double in 17 years (Findlay and Maani 1998). Population growth has been predicted to occur outside the main urban regions, in economically and ecologically marginal areas, which will put pressure on the natural resources in these areas. Where people in arid lands are truly dependent on their environment for their livelihood, they tend to treat it with great respect (Dutton 1998). This situation exists in the dryland regions of Jordan. Improvements in technology lead to a greater demand for dryland resources and a requirement for new products and services. Furthermore, a desire for an improvement in lifestyle that cannot be fully supported by the natural environment has emerged from the community. This growth of natural resource demand may ultimately lead to social instability being created. In the physical environment, consequences of instability may be the mis-management of land resources, over-exploitation of the vegetation or the pollution or salinisation of the water resource.

The Jordan Badia Research and Development Programme (BRDP) was established in 1991 to try and improve understanding of the desert environment in Jordan. The word 'Badia' means arid land. The Badia of Jordan comprise over four-fifths of the total land area. In the combined words of HRH Crown Prince El Hassan bin Talal and HRH The Duke of Kent (Patrons of the project), *"The wonderful world of the desert is revealed in all its glories and challenges in the Jordanian Badia. With its dunes and pavements, Bedouin and cultivators, its wadis and oases, oryxes and gazelles, it stretches from the Fertile Crescent into the heart of the Arabian peninsula"*. The Jordan Badia Research and Development Programme focuses on a region of Badia landscape in north-east Jordan. The project is currently approaching the stage where research becomes development. An initial aim of the Programme was to develop a better understanding of the natural resource base and the traditional and evolving uses of these resources in order to protect these resources and to ensure their long-term sustainability for future local populations (Dutton 1998). Research focused on specific themes including livestock, climate, earth science, plant taxonomy, biodiversity, development

anthropology, water resources, demography and education and health studies. A field study centre was established in Safawi, located on the highway interchange between Ruwayshid, Mafraq and Azraq. The second phase framework, comprising data collection, analysis and interpretation is about to be completed (1996-1998).

The project area covers 11,210 km² of the north-eastern Badia of Jordan (Figure 1.1) and is bounded by Syria to the north and Saudi Arabia to the south. To the west, the boundary follows the edges of the Azraq Basin; the eastern boundary comprises the western boundary of the Hammad Basin Project, centred at Ruwayshid. A description of the physical resources in the study area are given by Al-Homoud *et al.* (1996) and Allison *et al.* (1998) and are summarised in the following sub-sections.

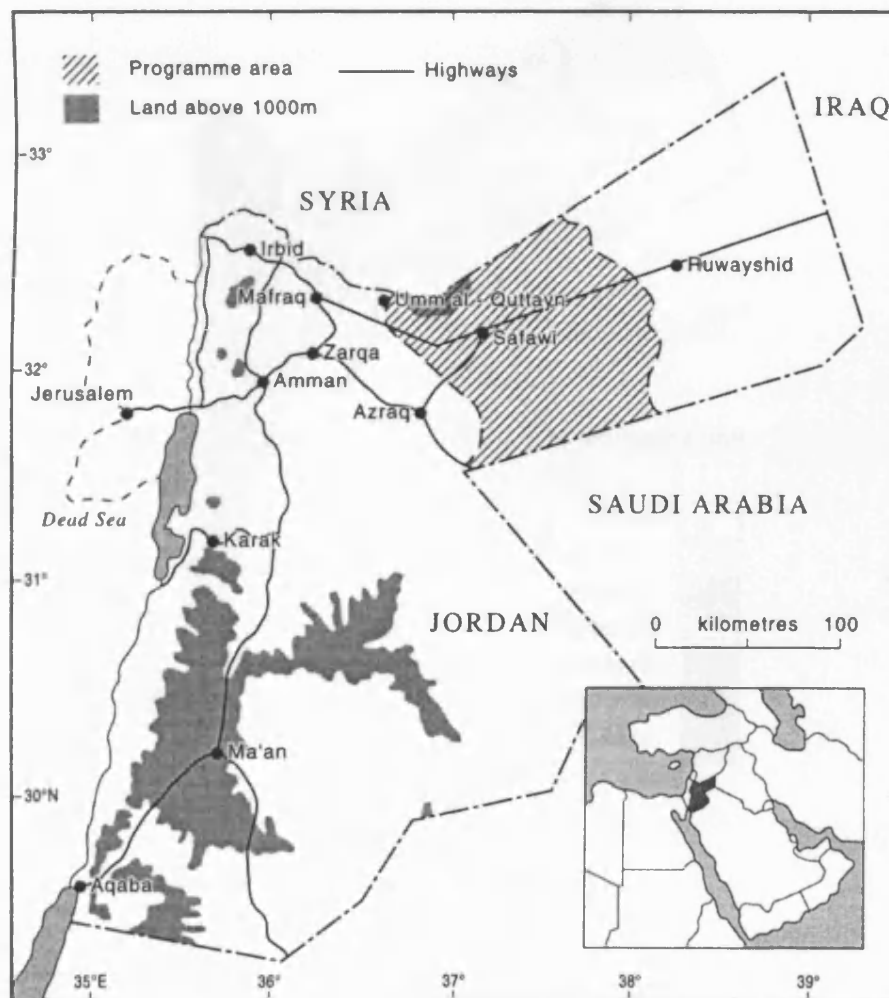


Figure 1.1. Location of the Badia Research and Development Programme area.

1.1.1 Climatic characteristics

The study area lies within an arid climatic zone (50-200 mm/a). Rainfall is infrequent, sporadic and unpredictable. The region is also exposed to large annual and diurnal temperature ranges, especially in the spring and autumn months. The study region is recognised as being in the transition zone between the wetter environment of the Jordan Valley and the dry, desert interior. The region experiences high evaporation rates, estimated to be in the region of 1,500 to 2,000 mm per annum, equivalent precipitation depth. The average precipitation distribution for Jordan is shown in Figure 1.2.

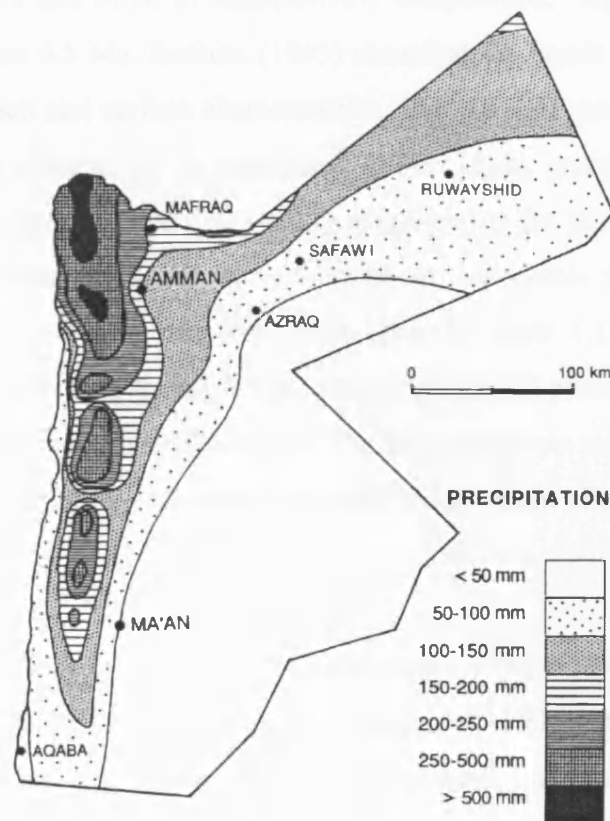


Figure 1.2. Precipitation distribution in Jordan.

In the north-west of the study area rainfall exceeds 150 mm, on average, due to higher relief and its westerly location. This value declines further south and east, reaching average precipitation amounts totalling 50 to 100 mm at Safawi, to less than 50 mm in the southern regions, close to the Saudi Arabian border.

1.1.2 Geology and topography

A comprehensive investigation into the geology of Jordan was undertaken by Bender (1974). Although the majority of Jordan is covered by sedimentary rocks, Tertiary-Quaternary continental basalt flows cover most of the study area (Figure 1.3). These comprise lava flows and tuffs, of alkali-olivine composition, ranging in age between 13.7 Ma to less than 0.5 Ma. Ibrahim (1993) classified the basalt outcrops in terms of their age, distribution and surface characteristics. The volcanic extrusion, known as the Harrat ash-Shaam super-group is comprised of five main groups; Bishriyya, Asfar, Safawi, Wisad and Rimah. Four flows within these groups are found in the Programme area, the Abed, Salaman, Madhala and Bishriyya (to which the Fahda Vesicular formation belongs), three are important, described in Table 1.1. All of these flows impose significant influence on large-scale geomorphological processes, such as erosion and deposition. To the south of the region, Tertiary sediments are present, overlain in places by Quaternary pelitic sediments, i.e. mudflats or recent alluvial deposits of sand and gravel.

The geology has a major influence on the topography of the study area. The difference in altitude, between the north-west of the study area (1,150 m) and the southern boundary (c. 400 m), is approximately 750 m. At Safawi, the mean altitude, above sea level, is approximately 700 m. The topography is best described as gentle to undulating hills with extensive flat regions. This is disrupted in localised sites by volcanic tuffs (mainly in the north of the project area) and sedimentary depressions (such as those found near to the Saudi Arabian border) to the south.

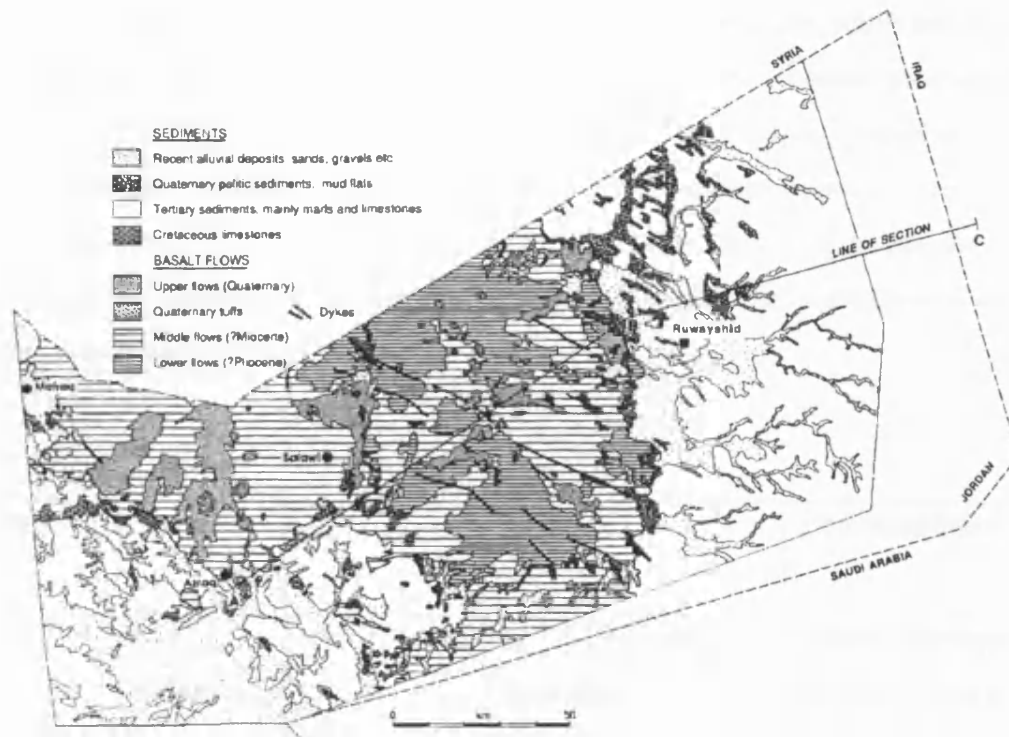


Figure 1.3. The geological divisions within the eastern Badia of Jordan (after Burdon 1959).

1.1.3 Geomorphology

Among the most fascinating aspects of deserts is their geomorphological diversity (Oberlander, 1994). The Badia of Jordan can be used as supporting evidence for this statement. On a large scale, differences in landforms and the processes that act on these forms occur as a result of differences in climatic and geologic setting. The lack of vegetation cover is of considerable importance for geomorphological processes and the development of landforms. Aeolian erosion is a major geomorphological agent. The role of moisture is also important in terms of geomorphological activity, especially during high energy flood events. The geomorphological characteristics of the study area are now presented, followed by a discussion on the similarity of these desert surfaces with those in other arid zones. Present, within the Programme area, are well developed catchment systems, drainage divides and channel features (wadis). On the basalt surfaces, the development of a drainage system is dependent upon the age, physical and

mineral characteristics of the basalt flows. For older flows, the landscape is more weathered and therefore the basalt boulders are more rounded, channel networks have developed and rill networks are present. More recent flows display irregular network patterns that are often disconnected and contain silt-filled depressions. A summary of the age, location and surface characteristics of the basalt flows found within the BRDP area are given in Table 1.1. Channel development within the sedimentary rocks is mostly well-established with obvious, incised wadis present.

Group	Formation	Age	Location	Characteristics
Safawi	Abed Olivine	8.45 - 9.3 Ma	Widespread and dominant around Al Azraq and Al Safawi and in Wadi el Abed.	Hummocky large boulders, light to dark brown weathering colour.
Asfar	Madhala Olivine	2.33 - 3.4 Ma	Three separate upland areas; Jebel Druze, Tllul el Ashaqif, and near to Saudi Arabian border.	Smooth ground surface, stones 5-30 cm in diameter, dark brown to black in colour. A lime crust may be present.
Bishriyya	Fahda Vesicular	< 2 Ma	Several outcrops occur; W of Jebel Aritayn, and 9 km E of Safawi are the main locations.	Young, fresh, blocky aa. Rubbly, vesicular surface. Purplish-black colour.

Table 1.1. Basalt flow age, location and surface characteristics (after Ibrahim 1993).

Greater than half of the total surface area is covered by basaltic boulders of varying size and shape. The fields of basalt rock are distinguished from each other by the age of flow, amount of stone cover, angularity and the size of the stones. Towards the west of the region, lichens cover the boulders, reflecting increasing moisture availability. A full description of the boulder characteristics measured at the basalt sites studied is given in Section 4.6. An extensive region to the south of Safawi has been described as a stone pavement, comprising deposits of gravel and stone sized chert and limestone clasts. A more detailed description of the properties of these surfaces, locally referred to as *hammada*, can be found in Section 1.3.

Two important geomorphological features that are found within the project area are *qa'a* and *marab*. *Qa'a* are flat, sometimes extensive, deposits of fine-grained sediment. They have similar characteristics to playa deposits, in that there is a flow of sediment and water into the *qa'a* system, but no obvious outflow. The *qa'a* found in the BRDP area are not saline, compared with those found in Tunisia (Archer 1995) and so can be classified as mud pans. The *qa'a* also vary in size and shape. Many small, and often interconnected, *qa'a* (of the order of tens of metres across) have developed in the youngest basalt flow, situated to the immediate north of Safawi. Larger *qa'a* (>1 kilometre square in area) can also be found within the eastern Badia. A detailed description of the moisture properties of *qa'a* surfaces is given in Section 1.3.

Marab are systems that are similar in many respects to *qa'a*, but they have a well-defined input flux and output drainage, normally in the form of a wadi channel. The *marab* in the project area can be quite extensive and support both seasonal and ephemeral vegetation growth. The surface sediments are normally coarser than for a *qa'a* surface. A number of *marab* have been developed within the project area to implement rain-fed cultivation, often close to water harvesting projects that have been set-up by the study. These regions support the growth of barley and other fodder crops that supplement the natural vegetation. Locations where desert cultivation practices are employed are *Qa'a ash Shubayka* and parts of *Qa'a al Buqayawiyya*, which are referred to in this study. Cultivation has been undertaken in the region towards Mafraq (west of the BRDP area) for over 50 years. The growth in cultivation practices and permanent

fields has expanded further east towards Safawi over time. Therefore, the region is increasingly becoming more dependent on rain-fed and irrigated agriculture.

For the purposes of this study, the desert surfaces that are considered to characterise the eastern Badia of Jordan are divided into four main types. These are basalt regoliths, *hammada*, *qa'a* and *marab*. Each surface plays an important role in the issues surrounding the availability of soil moisture and vegetation.

On a wider scale, these surfaces are represented in other desert regions. Thomas (1992) summarises data on the proportion of different landscape environments for five regions (southwest United States, Sahara, Libya, Arabia and Australia). The data shows that *qa'a* (playa) surfaces comprise, on average 1% of the surface area of these deserts. The percentage of land area occupied for dry watercourses is also 1% in the Sahara, Libya and Arabia, this figure rising to 3.6% in the southwestern United States. Desert flats (*hammada*) and low-angled bedrock surfaces occupy between 10 and 20% of the landscape in these desert regions. The proportion of recent volcanic deposits is reported to be less than 3% (Sahara), with no volcanic deposits in Australia and 2% in Arabia. These values bear some similarities between the proportion of land covers in the study area and with other desert regions. These similarities are in the proportion of dry watercourses and *qa'a* (playa) surfaces. However, there are greater proportions of volcanic deposits (> 50%) and desert flats (40%) compared to other extensive arid areas. Sand surfaces, which are well represented in the Saharan, Libyan, Arabian and Australian desert regions (> 20%) are not well represented in the study area, apart from a small area in the southeastern corner of the study area, occupying < 5% of the study area.

The potential for expanding this study outside the realms of the Jordan Badia is high, due to the fact that surfaces that characterise the Badia can be found in other dryland regions. This potential will increase if data on climatic and geomorphological properties of the desert environment are already available.

1.1.4 Flora and fauna

The species diversity of the Jordan Badia is very great, with over 322 species of flora so far having been recorded in 46 vascular plant families (Cope and El-Easawi 1998). Most plant growth is restricted to *marab* and wadi surfaces, where an influx and concentration of water occurs. A sparse cover of vegetation growth also occurs on the basalt surfaces, and in localised depressions on *hammada* surfaces. The main species growing both on the limestone and basalt surfaces are *Artemesia herba-alba*, *Artriplex halmus*, *Siedlitzia rosmarinifolia*, *Chenopodiaceae* and ephemeral grasses. The desert also supports both small, burrowing mammals and larger mammals. Over 100 species of bird have also been identified and recorded in the region. A detailed account of the vegetation found at the study sites is given in Chapter 4.

1.1.5 Soils

During the early 1990's, a major soil survey (The Soils of Jordan) was conducted for the whole of Jordan. Sites within the study area were included in levels I and II of the project. Data from the National Soil Map and Land Use Project (The Soils of Jordan 1993, 1994) have been utilised for this study, the relevant details of which can be found in Section 4.5.

The first taxonomic distinction of the soils of Jordan is concerned with the soil temperature regime. For the majority of the study area, the soils lie in a thermic temperature regime, which is defined as an average annual temperature between 15 and 22°C. In the south-west and south-east of the project area the soils are classified as being within a hyperthermic temperature regime, defined as an average annual temperature which is greater than 22°C. The second distinction is concerned with the soil moisture regime. The majority of the project area, apart from the far north-west, is classified as having an aridic moisture regime. The north-west lies within the transition zone between xeric and aridic regimes. Three distinct soil groups are present in the project area, mainly associated with the geologic parent material. The first group are soils situated on

the east Jordan limestone plateau. The soils are classified as Entisols and Aridisols of variable depth and parent material composition. In depressions, bedrock merges into sequences of gravel fan and gravel terraces; mudflats (*qa'a*) also occur. The second group are associated with the north Jordan basalt plateau. Different series occur in response to variations in topography and weathering. The development of the soil is related to the age of the basalt flow. Well-developed xerochrepts, sometimes with gypsic or calcitic horizons, occur on older basalt flows, weak structured xerothents occur on weakly developed basalt flows. The third group is associated with the north-east Jordan basalt plateau. A wide range of soils exist in this area, dependent on weathering factors of the basalt. These include gypsiorthids, camborthids and calciorthids on the older surfaces and torriothents and lithic soils on the younger surfaces (The Soils of Jordan 1993, 1994).

The difference between soils and sediments in dryland environments is important to distinguish. Soils are different to sediments by the presence of an organic layer (rare in arid regions), aggregated and structured horizons having characteristic chemical properties (helping to classify the soil type). In the study area, the *hammada* surfaces comprise mainly of unconsolidated sediments covered by a crust of coarser-grained sediments and stones. For the other land surfaces under study, evidence indicates that soil development has occurred.

1.1.6 Water resources and requirements

The water demand for Jordan has been predicted to reach 2,105 million m³ by the year 2020 (Allison *et al.* 1998). If the present trend of usage continues, potable water supplies will decrease from present values, of approximately 200 m³ per capita per year, to less than 100 m³ by the year 2020 (Jaber *et al.* 1997). If steps are not taken in the short-term then future supplies may be restricted. The main drainage basin covering the project area is in Azraq surface water basin. Runoff occurs usually every year in response to precipitation events that exceed infiltration capacity and/or saturation values of the soil. The distribution of groundwater in Jordan is fairly well understood from the

work by Blake (1928, 1930) and later by Bender (1968). Groundwater in the study area occurs in three complexes (Parker 1971), (Figure 1.4).

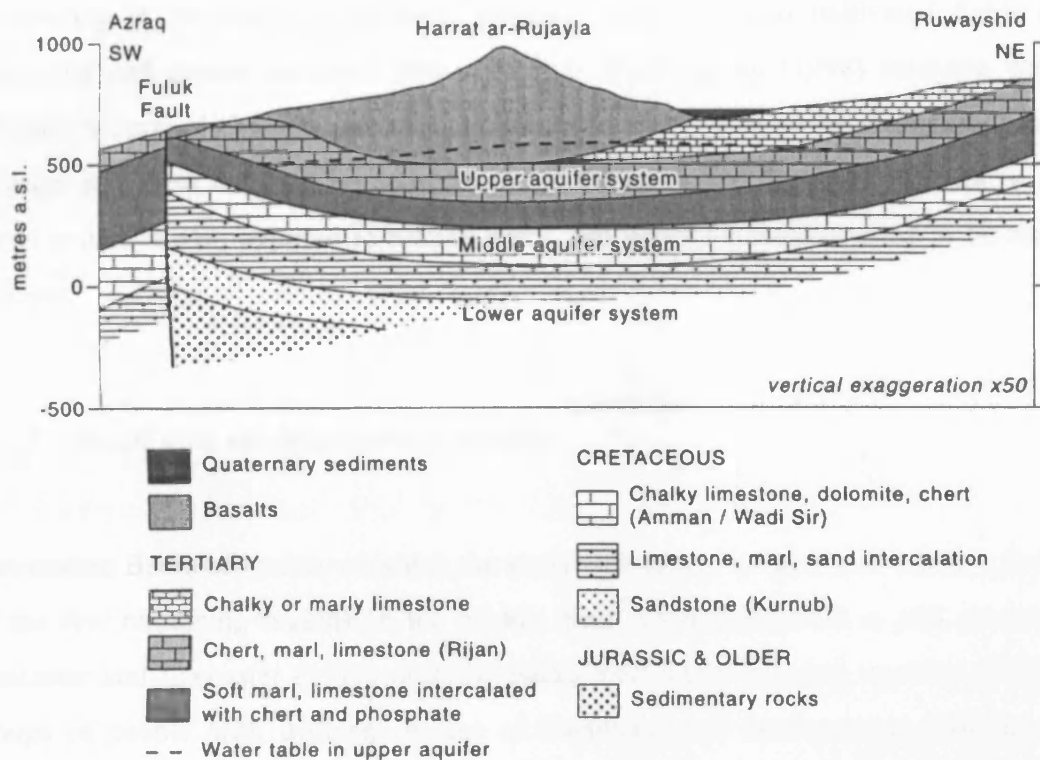


Figure 1.4. Cross-section between Azraq in the south-west and Ruwayshid in the north-east showing the major aquifers of the project area.

The upper aquifer comprises Quaternary basalts and the underlying Rijam cherty limestone. The middle aquifer comprises Cretaceous limestones of the Amman-Wadi Sir and Hummar aquifers located at a depth between 300 and 1,000 m. These aquifers are characterised by variable productivity and water quality. The lower aquifer comprises Cretaceous and older sandstones at depths between 1.3 and 3.4 km. The exploitation of the groundwater resource for industrial and public use has been well documented, as have the geochemistry and recharge rates of the aquifers (Dotteridge 1998; Drury 1998; Haaland 1998; Noble 1998). The main conclusion from this research is the great depth that has to be drilled to reach the water table.

The demand for water in the eastern Badia of Jordan comes mainly from the people living in the town of Safawi and the villages in the north-west of the study area. The demand has increased over recent years because of changes in land-tenure, farmers who were previously nomadic being forced to become settled, partially as a result of overgrazing in the Badia. In addition irrigated plantations and cultivated fields are expanding and create increased water demand. Waddingham (1998) studying water demand in Umm al-Quttayn, one of the larger villages, concluded that the management of water resources needs to be co-ordinated at the catchment level. Investment in the mains system is also required to reduce leaks, and irrigation systems need to be water efficient.

1.1.7 Social and environmental aspects

The eastern Badia of Jordan, of which the study area covers a significant amount, is one of the few remaining regions in the Middle East where nomadism is still practised. Lancaster and Lancaster (1997) describe Badia landscapes as being used by different groups of people with different means of livelihood and management strategies, at different times of the year and during different years. In the Badia, mobility between areas is essential, especially in the winter and spring months in response to available vegetation and water supplies. Lancaster and Lancaster (1997) suggest that the users of the Badia see their environment as a series of islands and corridors of grazing and water, areas of shelter and warmth for the winter and cooler uplands for the summer. This system, which has been in place for seven to eight thousand years (Briant 1982; Lancaster and Lancaster 1991) has started to change since the First World War (Campbell and Roe 1998). The changes have been mainly caused by a combination of three factors:

(i) Changes in herding practices; including a restriction of grazing areas caused by increased cultivation, border crossings, changes from camel to sheep livestock and greater demand for meat and dairy products from the urban centres and since 1996 a withdrawal of feed subsidies by the Jordanian government.

(ii) Increases in population. This increase places high demands on land productivity and natural resources.

(iii) Users of the Badia see their current environment as both stable and resilient over time, but they appreciate the unpredictable and arid climate (Lancaster and Lancaster 1997). An alternative hypothesis may suggest that farmers believe conditions are becoming more arid and are resorting to permanent cultivation in less arid regions.

1.2 Soil moisture

In this section some of the concepts and sources of soil moisture in arid regions are presented. The different techniques and measuring devices that are available to measure soil moisture are discussed. Also, the advantages and disadvantage of using different approaches in dryland environments are presented. Soil moisture is a critical parameter governing environmental issues in the eastern Badia. Soil moisture has a key role to play in surface water availability, runoff potential and the growth of vegetation. The vegetation depends on soil type and available soil moisture.

Sources of soil moisture in desert areas include rainfall, a high water table, frost, snow and dewfall (Agnew and Anderson 1988). The rainfall is mainly convective and highly localised, (as is described in Chapter 6), which can lead to sudden increases in soil moisture occurring over a small area, which may be difficult to monitor on the ground. In Jordan, frost and snow are rare, but not unheard of, even in the Badia. In addition, research has been undertaken by Clive Agnew in Jordan (personal communication) on the amount of dewfall under certain atmospheric conditions. Given these climatic conditions and the possibly highly localised occurrence of increased soil moisture, a measurement technique is required that can view large areas but provides enough detail (spatial resolution) to monitor variations in soil moisture over the order of metres to tens of metres. The pathways and movement of moisture within the profile after rainfall are upwards through evaporation, drainage in sub-soil layers, sub-surface lateral flow into ephemeral river channels and overland flow. If the infiltration capacity is exceeded by

an intense rainfall event then surface flow of water can occur. The drainage and water retention capacity of a soil depends on its physical properties. For example, a coarse textured surface soil allows rapid penetration and infiltration of water, but will also dry out quickly. A fine textured soil, with smaller pore sizes, allows storage of moisture under higher soil water tensions than for a coarse textured soil. Evaporation will still occur in a fine textured soil but at a slower rate. The distribution of different soil types will have an important influence on the infiltration and evaporation of soil moisture. Herbel and Gile (1973) measured soil moisture suction in southern New Mexico over a ten year period. The authors concluded that the most favourable conditions for plants, were landscapes that were level or almost level, had a thin coarse textured surface horizon to permit maximum infiltration of moisture, and a fine textured subsoil to prevent excessive deep drainage.

1.2.1 Methods of soil moisture measurement

Schmugge *et al.* (1980) state that there are three general approaches to measuring soil moisture: *in-situ* or point measurements, soil water models and remote sensing methods. The majority of studies involving the measurement of soil moisture use *in-situ* methods. *In-situ* methods include gravimetric and volumetric moisture determination (sample collected of known volume), neutron scattering, electromagnetic (capacitance probe), tensiometric (measures the capillary tension) and hygrometric (humidity) techniques. The theory, advantages and disadvantages of using in-situ methods are summarised in Table 1.2. A disadvantage of *in-situ* measurements is that single measurements do not account for spatial variations in soil moisture. Multiple measurements may establish any spatial variability but these measurements are difficult and costly to implement on a large scale in difficult terrain. Furthermore the nature of desert soils make them prone to surface disturbance that is both damaging and irreparable (this is especially a problem when using tensiometers, neutron scattering and capacitance probe techniques). In the Badia, soils are often capped by a tough, protective layer, especially the *qa'a* and *hammada* surfaces. Insertion of the measuring device is problematic, more so in very dry soils, due to loss of cohesion between the probe and the surrounding soil.

The advantages of making *in-situ* measurements are that they are often more accurate than other methods, such as water balance models (when care is taken during installation), the majority of methods enable the data to be recorded and logged at regular intervals and subsoil moisture contents can be measured by placing, for example, capacitance probes at different depths within the profile. Furthermore, using tensiometers at different depths, allows the direction of water movement in the soil profile to be determined.

In addition, *in-situ* measurements in desert environments are also difficult to obtain due to the general inaccessibility of many areas. This is particularly true in the Badia, which has few roads, and the basalt boulder fields prevent access. A final problem is the limited usefulness of point data compared to spatial data. In desert environments, soil moisture may vary significantly over small spatial scales, as indicated by the patchiness of vegetation and localised precipitation events. Point measurements may not be able to quantify this small-scale variation with sufficient accuracy.

The use of soil water models to determine the moisture content utilises the conservation of mass balance of water in a soil column. At any one time the soil moisture of a soil column can be calculated using the relationship between precipitation, surface runoff, subsurface outflow, evaporation, transpiration, capillary rise, percolation and the antecedent soil moisture content. Models have been developed mainly for agricultural applications. Saxton *et al.* (1974) for example, simulated soil-plant-atmosphere-water interactions using physics-based and semi-empirical approaches. Hydrologists have also developed models to estimate soil moisture. Hillel (1977) describes several physically-based models under bare soil conditions. An advantage of using soil water models is that they can provide timely soil moisture information without the necessity of field visits. A disadvantage is the errors involved in making estimations (Schmugge *et al.* 1980). These errors may be further exaggerated in desert regions, where accurate and timely data about the parameters that influence soil moisture, such as precipitation and evaporation, may be limited.

METHOD	THEORY	ADVANTAGES	DISADVANTAGES	REFERENCES
Gravimetric	Oven-drying to a constant weight. Vol. water content requires bulk density.	Samples easily obtained with an auger, inexpensive, estimate easily calculated.	Obtaining representative sample is difficult, sample contamination caused by destruction of the site.	Brakensiek <i>et al.</i> (1979), Black (1965).
Neutron scattering	Measures the thermal or slow neutron density. Emits a neutron field from a radioactive source.	Moisture measured in any state, data logged, measure any depth profile, quick response to changing conditions.	Inadequate depth resolution, value depends on chemical and physical properties of soil, health risk, cannot measure surface moisture.	Visvalingham and Tandy (1972), Rawls and Asmussen (1973).
Electromagnetic	Moisture dependence on the dielectric properties of the soil medium. Resistor or capacitor device.	With calibration, can yield absolute values of moisture, placed at any depth, control of volume of soil medium tested, high precision.	Minimise disturbance, long-term calibration may be unreliable, cost of logging and telemetry devices is high.	Wang <i>et al.</i> (1978), Nadler and Lapid (1996), Zegelin <i>et al.</i> (1989).
Tensiometric	Measures the capillary tension, or energy with which the water is held by the soil.	Easy to design and construct, cheap, system response is rapid, system can make measurements in saturated or unsaturated states.	Knowledge of soil properties required, easily broken, results can only be accurately obtained in the 0 to 800 cm water tension range.	Anderson and Burt (1977), Richards (1949)
Hygrometric	Exploits the relationship between moisture content in a porous material (soil) and the relative humidity.	Simple apparatus required and low cost.	Deterioration of the sensing element through interaction with the soil, special calibration of each material required.	Phene <i>et al.</i> (1971, 1973).

Table 1.2. A summary of in-situ methods available to determine soil moisture, and specific advantages and disadvantages of their application.

The remote sensing of soil moisture depends upon the measurement of electromagnetic energy that has either been reflected or emitted from the Earth's surface (Schmugge *et al.* 1980). Remote sensing can yield information about the spatial distribution of soil moisture and therefore can be used as input to distributed models that account for soil moisture in two dimensions. Water is unique in that it is near the extremes in its thermal and dielectric properties, these properties are discussed in greater detail in Chapter 2. Remote sensing techniques makes use of this property of water by using sensors that are sensitive to variations in temperature (thermal infra-red) and dielectric properties (microwaves). Further details on the measurement of soil moisture using remote sensing techniques are presented in Section 1.4.

The users of the Badia are very much aware of the requirements of winter rainfall. For good grazing, rainfall is needed during November and December and once again in February and March (Lancaster and Lancaster 1997). Usually four or five steady downpours, lasting up to a week, are required, to regenerate the perennials and also to bring about the growth of ephemeral plants considered essential for good milk production. Observations made in the spring months of 1996, 1997 and 1998 indicated that widespread grass growth occurred only in 1997. The winter of 1995 recorded less than average rainfall for the eastern Badia region.

Accurate mapping of areas of soil moisture accumulation or regions of active soil moisture dynamics is an aim of this research. Soil moisture can be related to rainfall and other parameters, which together determine the availability of water to support plant growth. Thomas and Squires (1991) propose a land capability assessment on the basis of soil moisture availability, ultimately to derive estimates of potential productivity. Information about the distribution of soil moisture will be useful to research scientists from different disciplines and will also be useful for the users of the Badia because of the increased accuracy and availability of the information.

1.3 Soil moisture characteristics of the Badia surfaces

Arid environments have been classified under a number of different schemes. Heathcote (1983), in reviewing published literature concerning drylands, found definitions that continuously referred to these environments as being 'inhospitable', 'barren', 'unvegetated' and 'devoid of water'. Other scientific definitions, based on physical criteria include: Climatic parameters based on plant growth (Köppen 1931); drainage patterns (de Martonne and Aufrère 1927); erosion processes (Penck 1894); and vegetation types (Shantz 1956). All of these classifications involve a consideration of the moisture availability, which is normally expressed as a relationship between precipitation and evaporation. Dryland environments can be categorised as hyper-arid, arid and semi-arid, based on the precipitation record and the seasonal precipitation regime (Meigs 1953), whose classification is based on Thornthwaite's moisture index and includes an evaporation term. The classification by Meigs (1953) estimated that 36.3% of the total global land area is arid. This amount comprises 15.8% semi-arid lands, 16.3% arid lands and 4.3% hyper-arid lands. Other estimates (see Heathcote 1983) do not vary greatly from this classification.

The general shortage of soil moisture has a major impact on plant growth in these regions. The amount of vegetation present in drylands affects not only wind-driven processes but also water-driven processes. Therefore, the distribution and type of vegetation has considerable influence on the nature of geomorphological processes and hence the development of landforms (Thomas 1988). The spatial variability of the geology, topography and climatic variations in the eastern Badia of Jordan has also contributed to the development of different landscapes.

Rainfall occurs more often than may be supposed in deserts, the number of rainy days are sometimes comparable with more humid areas (Goudie 1992). Moisture is also available in the form of dew although little data are available to quantify the contribution of dew to the total precipitation values in arid environments. Effective management of these sources of moisture is therefore an important issue in dryland regions to maximise its use.

Moisture is available in a variety of forms that may promote weathering and erosion processes. The role of moisture in landscape development can be recognised in many desert landforms. The evolution of desert crusts (calcrete, gypcrete or silcrete) are, more often than not, the products of specific hydrological or pedological processes, characteristic of arid and semi-arid environments (Watson 1992). Other landforms, found within the study area that are the products of geomorphological processes in which moisture has played a significant role, are playas (*qa'a*), ephemeral river channels (wadis) and their associated outflow spreads (*marab*) and desert pavements (*hammada*). The role of moisture and moisture availability on their development over a long time scale and over the time scale of the study are discussed in more detail in Section 1.3.1.

1.3.1 Basalt and desert stone pavement surfaces

Stone surfaces are characteristic of many desert areas but their origin remains a matter of contention (Dixon 1994). The term desert pavement usually refers to a uniform mantle of stones, of one or two stone thickness and of small axial dimension, which overlie finer material ranging from several centimetres to metres thick (Cooke 1970; Wells *et al.* 1985; McFadden *et al.* 1984, 1987). The local term *hammada* encompasses the desert pavements found in the central and southern parts of the project area. Basalt pavements, considered here as a separate desert surface, are located in the north and east of the area. Stone pavement surfaces are remarkably flat and smooth. They can be found in central Sahara (Peel 1960), eastern Sahara, Australia, western United States and in north-western China. A review of the morphology, genesis and gravel source of stone pavements is presented by Dixon (1994).

Stone pavement sediments are understood to be remnants of old alluvial deposits that have been preserved by Quaternary aridity (Breed *et al.* 1992). The process of sediment sorting, deflation and water movement in the evolution of desert pavements is illustrated in Figure 1.5. Four such evolutionary models have been proposed.

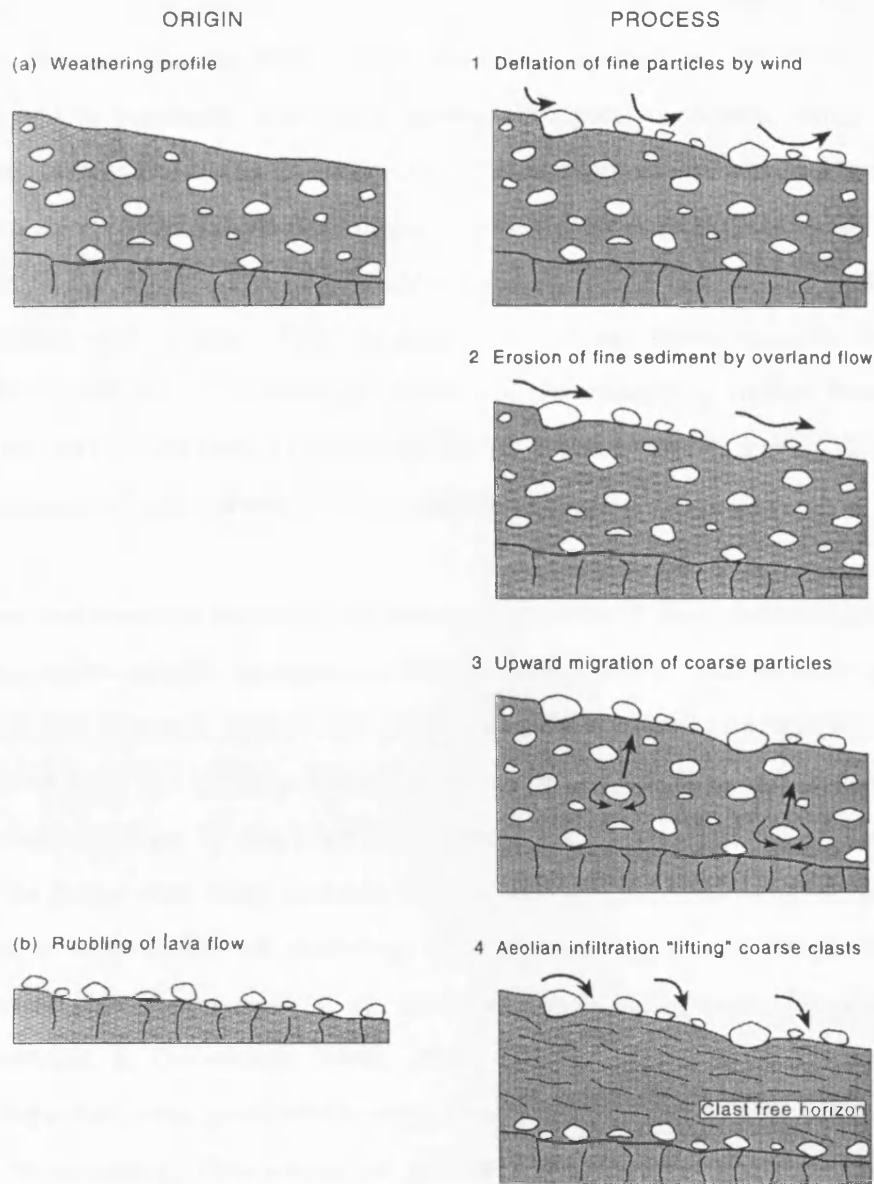


Figure 1.5. Four hypotheses of desert pavement surface evolution (after Higgitt and Allison 1998).

In the original state, the stone clasts are mixed throughout the sediment. Hypotheses 1, 2 and 3 provide explanations for mechanisms which lead to clasts being exhumed from the finer sediment. The finer sediment may be removed by wind or runoff, or alternatively the coarse particles may migrate towards the surface during freeze-thaw or wetting-drying cycles. Hypothesis 4 suggests that the original substrate is clast free, and deposition of finer sediment over time increases the thickness of the sediment layer

raising the elevation of the desert pavement (McFadden *et al.* 1987). The accretion hypothesis replaces the deflation hypothesis as a mechanism for stone pavement formation and is consistent with other geomorphological processes acting on stone pavements, such as the uniform application of fine sediment by winds blowing over large areas. Research into the morphological properties of basaltic lava fields has been undertaken in the Mojave Desert of California (Farr 1992) and in the Jordan basalt plateau (Higgit and Allison 1998; Ibrahim 1993). From these research findings it appears that basalt surfaces provide protection for the underlying surface from aeolian deflation and also encourages deposition of fine aeolian sediment as a result of boundary layer disturbance of desert winds (Figure 1.5, hypothesis 4).

The surface soil moisture retention and storage properties of these surfaces are difficult to ascertain. After rainfall, evaporation from the stone surface will be very quick and penetration of the ground surface will only occur after a certain amount of rainfall has thoroughly wetted the surface. Observations made in the field indicate that after significant precipitation the finer sediment beneath and in-between boulders retain soil moisture for longer than other surfaces. This is most likely due to reduced evaporation caused by a combination of sheltering from the wind and less direct insolation. Vegetation is almost non-existent, the exception is in topographic depressions and channel systems. In the eastern Badia, growth in the basalt regions is a little more abundant especially after good winter rains, ephemeral grasses thriving in the relatively sheltered environment. This source of natural vegetation is very important for the grazing livestock as often basalt fields need to be crossed to reach new grazing areas.

1.3.2 Playa (qa'a) surfaces

The origins of playas have been ascribed to many different sources. These range from simple desiccation of depressions filled under seasonal rainfall or wetter palaeoclimates to tectonic activity or aeolian deflation (Shaw and Thomas 1992). A hydrological classification, linking morphology, groundwater-surface water interactions and evaporite sequence is illustrated in Figure 1.6.

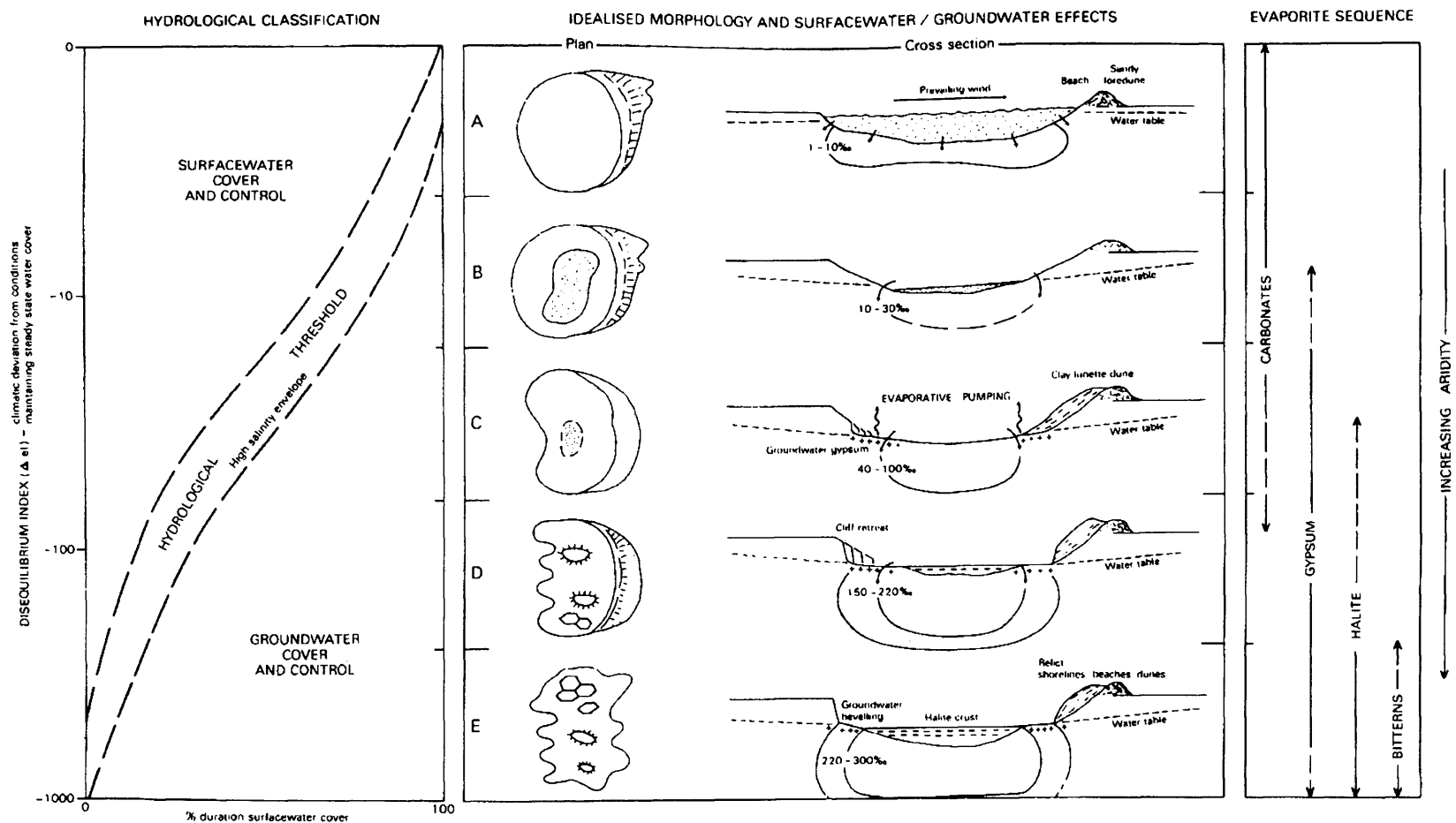


Figure 1.6. Hydrological classification, idealised morphology, and groundwater-surface water interaction of evaporative basins (after Bowler 1986).

Playas are highly variable in size and shape, hydrology, morphology and pedology, reflecting the complex interactions between the local setting and evolutionary paths. Playas are generally classified as depositional environments (Bryant 1993). Dominant sediment types are fine grained and brought in by either surface flows and precipitated solutes. The main ions are derived from both surface water and ground water sources and comprise SiO_2 , Ca^{2+} , Mg^{2+} , K^+ , Na^+ , Cl^- , HCO_3^- , CO_3^- and SO_4^{2-} (Shaw and Thomas 1992).

Playas are generally found in regional or local topographic lows. They lack any surface outflows, usually have flat surfaces, demonstrate a hydrological budget where evaporation exceeds inputs of moisture and are normally devoid of vegetation. The latter criteria is not always satisfied, vegetation may exist in specific locations and associations. In the eastern Badia, playa lakes do not occupy a large proportion of the area, relative to other land cover types. The pathway of water and salt exchange of playa surfaces is illustrated in Figure 1.7.

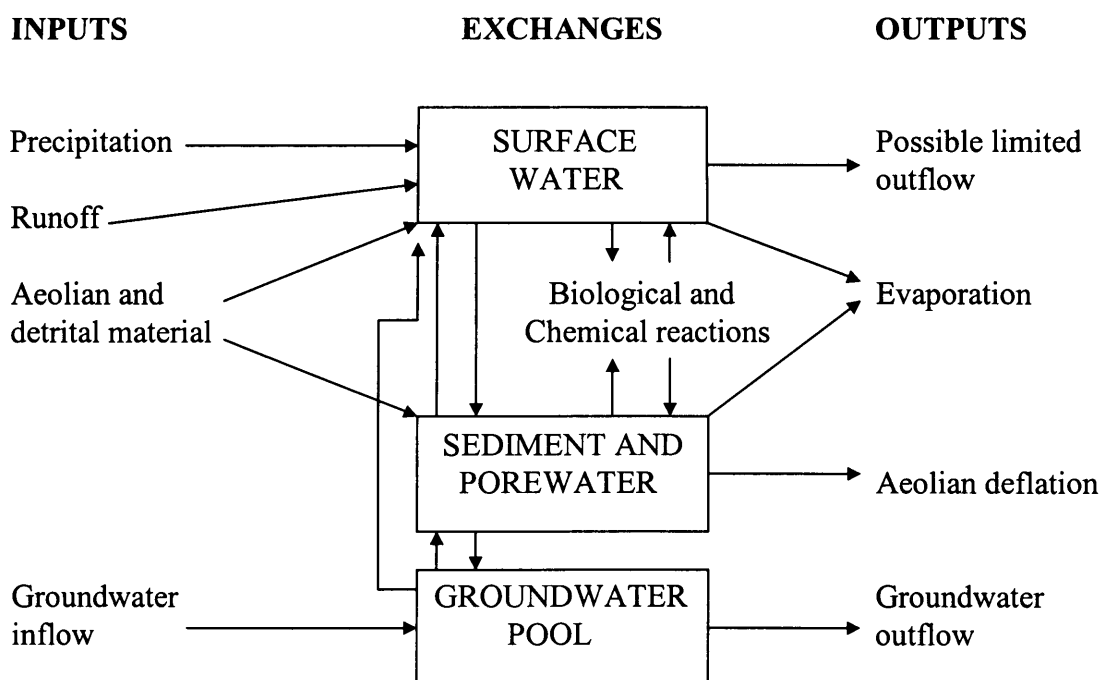


Figure 1.7. Diagrammatic representation of the possible exchange pathways for water and salts in a playa (qa'a) system (after Torgersen et al. 1986).

Three stores of water are evident; at the surface, in the sediments and deeper into the ground. All of the exchanges have implications for the magnitude and frequency of the processes that act upon the surface (Figure 1.7). Playas are sometimes saline, due to an accumulation and subsequent evaporation of waters high in salts. The presence or absence of salt minerals in a playa environment can have a significant influence on the type of surface desiccation and fracture. However, due to a combination of hydrological and climatic factors, the *qa'a* surfaces of the eastern Badia of Jordan are generally low in salt content. Therefore the depositional classification that can be assigned to them would be a clay-floored basin with low groundwater input. They often display pronounced desiccation features due to the high smectite clay content. These are known as gilgai or patterned ground, produced as a result of heave between cracks, heave above cracks, contraction over cracks and heave due to loading (Knight 1980). Surface polygonal cracking is also present, ranging in size from centimetres through to tens of metres in scale (Cooke and Warren 1973). These features are primarily the result of desiccation of crusts that are rich in swelling clays.

Observations made of *qa'a* surfaces located within the study area indicate that surface water is the dominant control of *qa'a* processes. The depositional environment can be described as less arid (Figure 1.6) due to the lack of saline evaporites at the surface and relatively regular inundation by surface flows. As mentioned previously (Section 1.1.3) the *qa'a* vary in size. Furthermore, the surface morphology between *qa'a* is highly variable. Polygonal cracking is present to some extent on all of the *qa'a* observed, but the scale, size and degree of cracking is variable and is dependent upon local environmental factors. During each field visit it was deemed important to note the surface characteristics and register any temporal variation in surface morphology. Some of the surface features of *qa'a* are the most ephemeral of geomorphological phenomena, lasting no longer than the interval between the rainfall events (Shaw and Thomas 1992).

The knowledge that might be gained about *qa'a* surfaces from this study include the monitoring of surface processes and fluctuations. Furthermore rainfall events that cause flooding of these *qa'a* surfaces can be identified. The geomorphological response to wetting and drying cycles may also be monitored.

1.3.3 *Marab and wadi surfaces*

Ephemeral channel systems found in dryland environments are different to their perennial counterparts. A major difference is the generation of the flood wave. Ephemeral rivers do not usually have a characteristic hydrograph as different parts of the catchment may be contributing to the flood at any one time, responding to the cellular convective nature of rainfall events in desert regions. The amount of water that is lost through transmission into the surface sediments is greater than in perennial systems. Transmission depends on the porosity, depth of the channel fill layer and the hydraulic conductivity of the least permeable layer. During flood events ephemeral rivers can move vast quantities of sediment. Sediment is readily available to be transported, both from the channel sides and the stream bed. Ephemeral stream deposits appear to have three attributes (Reid and Frostick 1992). The first is thin beds of sands and pebbly sands between 0.1 and 0.3 m thick, this thickness depending on the depth of scouring. The second is the presence of horizontal lamination of sediments. The third is the presence of mud drapes and mud intraclasts, in the region of 0.1 m thickness, thought to be laid down by stagnant flood water in the final stages of flow.

The wadi systems that drain the eastern Badia are extensive. The main channel system, the Wadi Rajil, drains from north of the border in Syria (from the Jebel al Arab) into the Azraq Basin and on to the border with Saudi Arabia. Furthermore, the drainage plane is incised with smaller wadis which feed into the Wadi Rajil. *Marab* surfaces develop where there is a lessening of the slope angle and the wadi channel is allowed to spread laterally over the flood plain. They are characterised by shallow surface slopes and vegetated by perennial shrubs and ephemeral grasses. Their surface sediments are mainly dominated by silt and sand-sized particles, and are therefore more coarser grained than *qa'a* surfaces. The soil moisture characteristics of *marabs* are very important as they provide significant moisture reserves for the vegetation communities that are found on them. After winter storms, wadi and *marab* regions often flood. However, the water quickly drains away either down channels or into sediments. The presence or absence of vegetation gives an approximate indication of the water holding capacity of wadi and marab sediments.

1.4 Remote sensing of soil moisture

Two types of electromagnetic radiation can be utilised to extract information about soil moisture; thermal infra-red ($10.5 < \lambda < 12.5\mu\text{m}$) and microwaves ($0.1 < \lambda < 100\text{cm}$). Microwave radiation is more commonly used than thermal infra-red radiation. In microwave applications, two approaches are considered, active and passive methods. A justification for the approach that is taken in this project is presented. Three approaches to the remote sensing of soil moisture have been developed: thermal infra-red, passive microwaves and active microwaves.

1.4.1 Remote sensing methods: thermal infra-red

The factors that influence the diurnal variation in soil surface temperature are internal factors (e.g. thermal conductivity and heat capacity) and external factors (e.g. solar radiation, relative humidity and wind). Increases in soil moisture lead to an increase in the values of the internal factors and, hence, any changes in soil moisture should be measurable in the thermal infra-red wavelengths ($10.5 < \lambda < 12.5\mu\text{m}$). An important limiting factor is surface evaporation, which reduces the net energy input at the Earth's surface. Idso *et al.* (1975a, 1975b) showed that maximum diurnal temperatures ranges were significantly different before and after irrigation. Their results also showed that the amplitude of the diurnal range, plotted as a function of soil moisture, yielded good relationships at soil depths between 0 to 4 cm.

The lack of a suitable airborne or spaceborne sensor with a high (30 m) spatial resolution and providing an extensive areal coverage (100 km^2) prevents this technique from being further exploited. Soil moisture variation in desert regions can be extremely variable and therefore a fine spatial resolution is an important sensor characteristic. In addition, an absence of accurate and timely meteorological data for regions where this method could be used (e.g. dryland regions), make this approach disadvantageous. Cloud cover is also a problem, even in a desert environment (Edwards 1999). Cloud can

frequently be observed on images acquired of the eastern Badia of Jordan by optical and thermal sensors (TM and ATSR-2).

1.4.2 Remote sensing methods: passive microwaves

The dielectric properties of a soil medium are strongly influenced by its water content. This relationship is discussed in greater detail in Chapter 2. In simple terms, the amount of water influences the propagation of the electromagnetic wave within the soil medium. A microwave radiometer measures the intensity of emission from a soil surface, therefore the measuring system is passive. The emission of radiation from a soil is proportional to the product of the surface temperature and the surface emissivity referred to as the brightness temperature (T_B). Due to the fact that at microwave wavelengths > 5 cm the atmospheric transmission is almost 99% (Engman and Chauhan 1995) the expression for the brightness temperature is given as (Schmugge 1990):

$$T_B = (1-r) T_{\text{soil}} = eT_{\text{soil}} \quad (1.1)$$

where, r is the smooth surface reflectivity, T_{soil} is the thermometric temperature of the soil and $e = (1-r)$ is the emissivity of the soil surface and is dependent on the dielectric properties and surface roughness of a bare soil.

Various experiments have been conducted to assess the sensitivity to soil moisture of the brightness temperature (Njoku and Entekhabi 1996; Pampaloni and Paloscia 1986; Jackson and Le Vine 1996; Owe *et al.* 1992; John 1992). The main advantages of using a passive microwave system are; the relatively small number of parameters that influence the brightness temperature (Equation 1.1); cloud free operation for airborne and spaceborne systems (discussed in the following section); and the ability of the microwave emission to penetrate vegetation (this depends on the wavelength of the microwaves and the density of the vegetation biomass). A major disadvantage of using a space-borne passive radiometer is the poor spatial resolutions obtainable (5 to 10 km at best). This would be totally unsuited for the spatial scale of the application investigated in this study. At this pixel size, interference in the resolution cells of emissions from

different sources, such as from urban regions, introduces errors when assuming homogeneity, known as the mixed pixel effect.

1.4.3 Remote sensing methods: active microwaves

Active microwave remote sensing of soil moisture is based on the same principles as passive systems, namely the differences in the electromagnetic dielectric properties between dry and wet soils. An electromagnetic signal is produced at a power source, propagated through space to the target, and is reflected off the surface at an off-nadir angle. The sensor then receives the returned signal. The phase and amplitude of the return signal is recorded. From this information a received/transmitted power ratio (or backscatter coefficient) is calculated. Different surfaces have characteristic backscatter coefficients at different wavelengths caused by the interaction of the radiation with scatterers of different sizes. In addition, the amount of soil moisture influences the return signal by affecting the amplitude of the backscatter coefficient. The amount of change is related to the dielectric properties of the soil. Reviews of the status of microwave soil moisture measurements using remote sensing techniques are given by Engman and Chauhan (1995) and Schmugge (1983). Comprehensive details of the theory and application of this method for soil moisture determination are presented in Chapter 2.

An active microwave approach is the method adopted in this study for the following reasons.

- The availability of radar imaging systems and imagery is extensive and an opportunity to obtain data under a European Space Agency (ESA) investigation scheme from the European Environmental Remote Sensing (ERS) Synthetic Aperture Radar (SAR) (Figure 1.8) was exploited (project AO2.UK.125)

- There is an extensive literature available on the method based on field and laboratory studies from the 1970's to the present day.

- The spatial resolution of the imaging systems (a spatial resolution of less than 30 metres) was good enough to be able to map and monitor soil moisture estimates in desert regions to an appropriate spatial scale that enables change in landcover type to be established and accounted for.

- The ability of the microwave system to operate regardless of cloud cover and atmospheric conditions due to almost perfect (99%) atmospheric transmission at the wavelength of the radar system. An active system generates its own energy, therefore, the image acquisitions were also independent of solar illumination.



Figure 1.8. The European Space Agency (ESA) first European Remote Sensing (ERS-1) Satellite.

The disadvantages of using an active microwave system are the system noise, referred to as ‘speckle’, that is caused by interference of the radar signal (Chapter 2). Speckle is inherent in any imagery of this type. A limited swath width, the influence of vegetation

on the scattering process and calibration of the signal are also disadvantages of using this approach. The temporal resolution of space-borne systems is generally not good for monitoring such a dynamic variable as soil moisture. The system used had a repeat overpass cycle of 35 days. However, some sites were covered twice in this period lying in the overlap between satellite tracks.

The first spaceborne active radar system was on board the Seasat satellite flown in 1978 by the National Aeronautics and Space Administration (NASA). Although in orbit for slightly over 3 months the instrument clearly demonstrated the potential of using SAR systems for geological, land and sea surface surfaces. A review of Seasat imagery is given by Ford *et al.* (1980). The Seasat SAR was succeeded by Shuttle Imaging Radars (SIR-A, B and C) which incorporated multi-incidence angles and variations in other system parameters. These satellites were followed by Cosmos 1870 and ALMAZ-1 (USSR) launched in 1987 and 1991 respectively. The launch of the ERS-1 satellite (Figure 1.9) in July 1991 provided the first opportunity for scientists to obtain global and multitemporal radar imagery for significant parts of the Earth's surface. This satellite was quickly followed by a Japanese SAR system (JERS-1) operating at a longer wavelength and more recently the Canadian RADARSAT. Future SAR missions planned include the ENVISAT (ESA) and LightSAR (USA) platforms expected to be operational in the year 2000.

Schmugge *et al.* (1980) states that an optimal soil moisture monitoring experiment must utilise all three approaches and not to rely on just one. *In-situ* measurements must be used for calibration and validation of soil moisture models and models developed from remote sensing applications. Ultimately, the approach adopted must reflect the aims and objectives of the research and what method, or combination of methods, best answer these aims.

1.5 Research objectives

The research described in this thesis is concerned with the application of microwave remote sensing to the study of soil moisture monitoring and measurement in a dryland environment. Specifically, the project has the following objectives:

(1) To assess and exploit the ability of the ERS SAR instrument to monitor geomorphological and hydrological changes in the environment of the north-eastern Badia (desert) of Jordan.

(2) To calibrate theoretical microwave scattering models using field reference data (including soil moisture, surface roughness, soil type and vegetation) and assess their application to desert environments.

(3) To simulate the dependence of the backscatter coefficient on soil moisture fluctuations and surface roughness changes with the aim of improving the understanding of microwave interactions with desert surfaces.

(4) To investigate the potential for extraction of quantitative soil moisture estimates from ERS SAR data.

These four research objectives were investigated in north-east Jordan as part of the Jordan Badia Research and Development Programme (BRDP).

1.6 Thesis structure

Chapter 2 describes the theory behind microwave remote sensing of land surfaces. Commencing with background information on the development of this technique, the chapter describes the technical specification and characteristics of the ERS SAR instrument that is utilised in this study. Following on, Section 2.3 describes the image structure and the data acquisition periods. The next section outlines the method of

calculating the backscatter coefficient. The microwave scattering models that are utilised in this study are then introduced (Section 2.6).

Chapter 3 focuses on the information that can be extracted from a sequence of ERS SAR images acquired for the study area. Using multitemporal analysis, an indication of the potential for monitoring environmental variables is illustrated. The interpretations expressed at this stage are qualitative.

Chapter 4 describes the field sampling strategy adopted for the calibration of the scattering models presented in Chapter 2. Sites selected for monitoring are described. The methodology and instrumentation employed to collect *in-situ* measurements of soil moisture, surface roughness, soil type and vegetation are presented. Climatic data obtained from automatic weather stations installed in the area are analysed.

Chapter 5 discusses the various methods of measuring and determining the roughness of a natural surface. Although the model input parameters are fixed, different algorithms are available to determine the roughness parameters which have a significant influence on the overall model performance.

Chapter 6 presents the model calibration results for estimating soil moisture. Simulation of various soil moisture conditions are displayed in an attempt to gain further understanding of the hydrological and geomorphological processes that are influencing the microwave scattering. Site specific inversion algorithms are developed to relate changes in the backscatter coefficient to soil moisture. A time series of soil moisture maps are presented for some test sites. The models are validated using field data from image acquisitions obtained in the spring of 1998.

Chapter 7 summarises the results obtained from previous chapters and relates these to the objectives set out in the previous section. The application of the results to desert regions in general are discussed, though particular attention is paid to the interests of the Jordan BRDP. The final section suggests topics for future research with particular reference made to ENVISAT, the next generation ESA satellite.

2. Microwave Remote Sensing of Soil Moisture

This chapter introduces general concepts of microwave remote sensing and explains the theories and approaches to the remote sensing of soil moisture. Section 2.1 defines the main concepts referred to throughout the study and looks at the dependence of the microwave signal to surface parameters including soil moisture. Section 2.2 describes the technical specification and characteristics of the satellite sensor (ERS SAR) used in this study. Section 2.3 looks at the data structure and the periods of data acquisition over the study region. To be able to locate study sites within the image, the data have to be corrected to a geographical co-ordinate system, Section 2.4 covers image analysis and Section 2.5 describes how information is extracted from images. Finally, Section 2.6 discusses modelling approaches used in this study in an attempt to understand the interactions that are occurring between the incident energy and the Earth's surface.

2.1 Principles of active microwave remote sensing

Active microwave instruments generate their own energy. This energy is in the form of an electromagnetic wave that propagates through the atmosphere at the speed of light and interacts with the ground surface. The frequency of the microwave can vary from very low values such as 3 MHz (wavelength, $\lambda = 100$ m) which can travel long distances to very high frequency radars of 35 GHz or more ($\lambda = 1$ mm) that have selected wavelengths dependent on atmospheric absorption. The microwave spectrum has been classified into different bands that have been assigned names. These are shown in Figure 2.1 and reference is made to these letters throughout this study. The major attraction of radar systems are their ability to produce high resolution images of large areas from space irrespective of solar illumination and cloud cover. This is due to the fact that, at wavelengths of the order of cms (of which C-band, X-band and L-band are most popular), the atmospheric transmission is almost 100%.

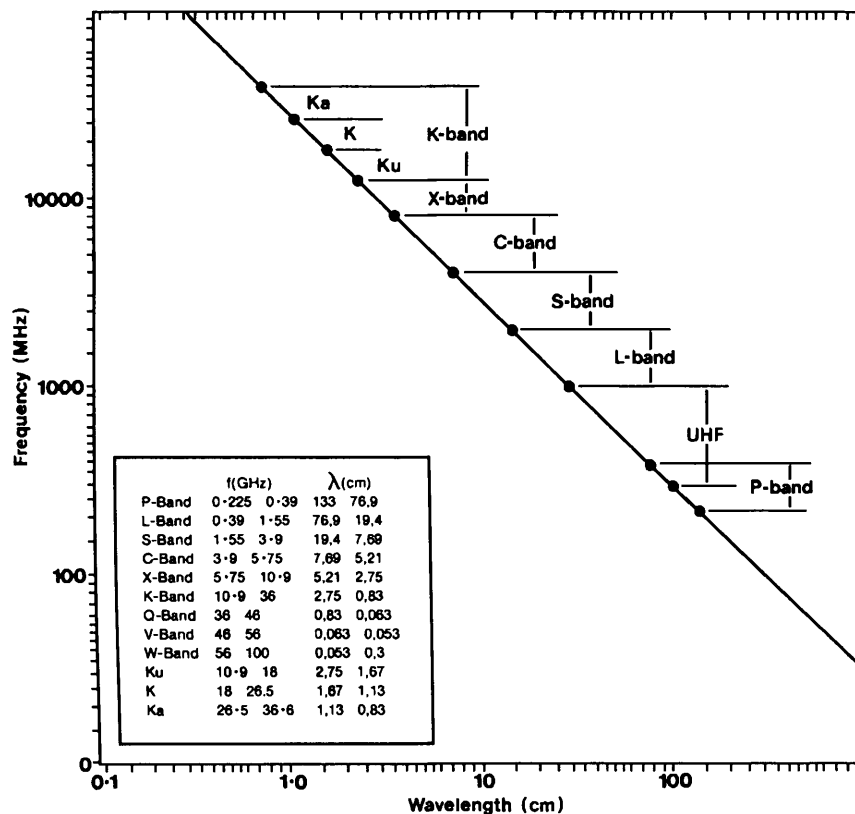


Figure 2.1. The microwave bands as elements of wavelength and frequency (Trevett 1986).

The most commonly used radar instruments are side-looking airborne radars (SLAR) where the antenna points to the side of the platform that is in motion. SLARs transmit a radar signal and receive the signal after it has returned from the target surface, noting any change in intensity and phase, the latter indicating the range position of the scatterer. SLARs are grouped into two systems. First, real aperture systems, whose resolution is dependent on the width of beam produced at the antenna (so ultimately dependent on antenna size). Secondly, synthetic aperture radar systems (SAR) that depend upon signal processing techniques that account for a smaller beam width and uses the Doppler frequency shift to increase the resolution of the image in the azimuth direction.

The Doppler shift is a measure of the change in signal frequency as the surface scatterer enters the beam of energy until the scatterer leaves the irradiated area. For a single scatterer, on each pulse of the radar the two-way propagation to and from the antenna causes the phase (ϕ) to change by:

$$\phi_l = 2 \frac{2\pi}{\lambda} s_l \quad [\text{radians}] \quad (2.1)$$

where, s_l is the distance between the radar and the scatterer when the l th pulse is emitted.

The Doppler frequency is directly related to the speed of the platform and is given by:

$$f_D = -\frac{2u_R}{\lambda} \quad (2.2)$$

where, u_R is the speed in the R-direction. The use of Doppler synthesis enables high resolution imagery to be acquired without the need for a large antenna.

The multitude of pulse returns contains the unique phase history of that scattering element. The phase histories of the scattering elements are resolved in the processing of the imagery. Another advantage of a SAR system over a real aperture system is that the resolution in the along track (azimuth) direction is independent of range (Ulaby *et al.* 1981, Kingsley and Quegan 1992). For a SAR system an increased spatial resolution can be gained using a shorter antenna, the complete opposite to a real aperture system. The advantage of a synthetic aperture approach over a real aperture approach is illustrated in Figure 2.2. Resolution in the along track direction (r_a), for a SAR, can theoretically be as small as:

$$r_a = l/2 \quad (2.3)$$

where, l is the length of the antenna in the along track direction.

For a real aperture system the resultant along track resolution is:

$$r_a = \beta_h R \quad (2.4)$$

where, β_h is the beamwidth $\approx \lambda/l$ (radians) and R is the slant range, the distance from radar to target.

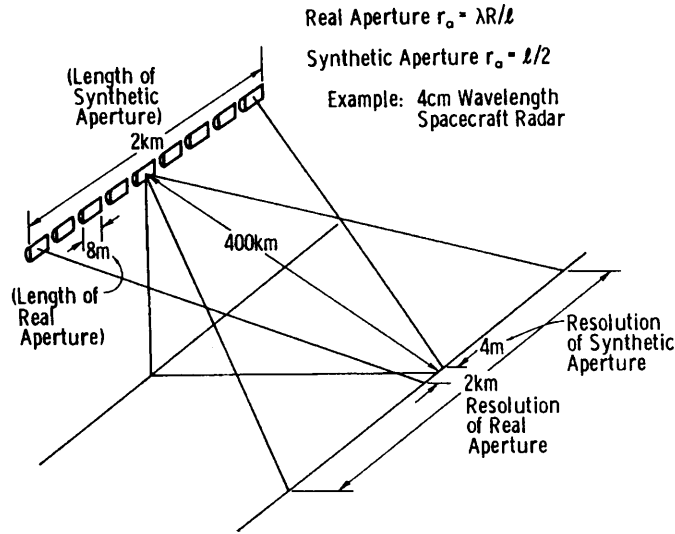


Figure 2.2. Example of the synthetic aperture radar (SAR) approach, in a spaceborne application (Ulaby et al. 1981).

The across track resolution (range) of the image is dependent on the pulse duration and the angle of incidence angle given by:

$$r_p = \frac{c}{2B \sin \theta} \quad (2.5)$$

where, B is the frequency modulated chirp pulse of bandwidth B , c is the velocity of light and θ is the incidence angle. The imaging geometry of a SAR system is shown in Figure 2.3.

2.1.1 The radar equation and other system parameters

The SAR system transmits pulses of energy that interact with the target surface, the level of this interaction is dependent on the wavelength and on the energy required within the medium to cause molecular excitement. The pulse of energy is normally polarised as a horizontal or a vertical waveform. On contact with the target, the form breaks up, the returning signal being received possibly being both vertically and/or horizontally polarised. This enables multi-polarisation observations to be made. The abbreviation VV therefore refers to a system that transmits and receives the vertical component of the energy wave. Other possible combinations are HH, HV and VH. The ERS SAR sensor used in this study has a VV polarisation specification.

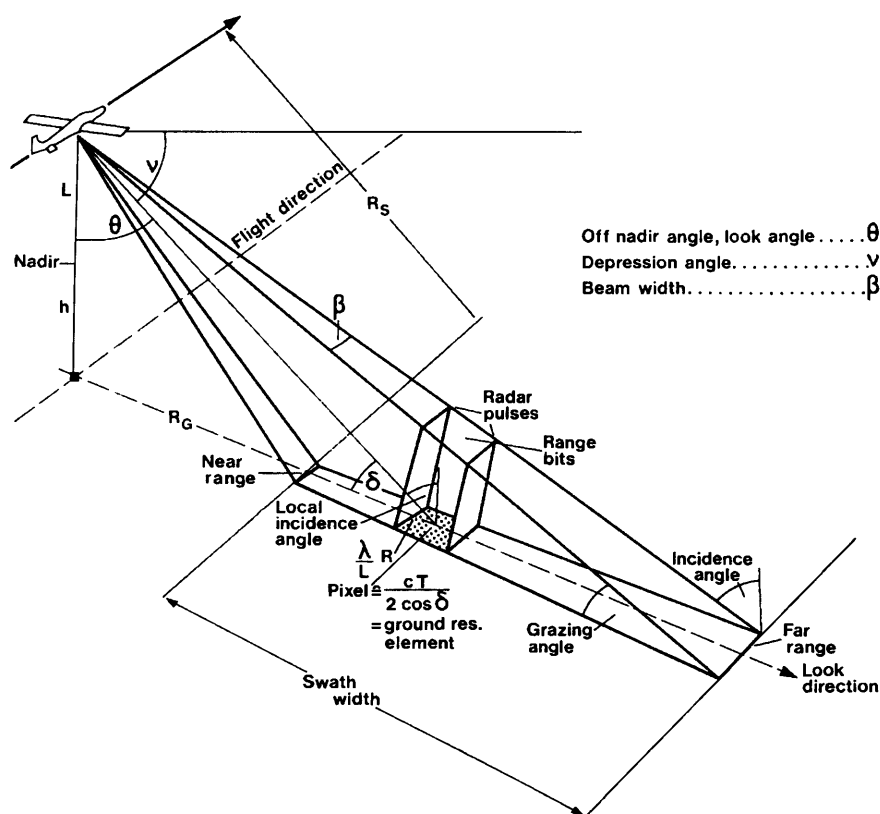


Figure 2.3. SAR imaging geometry (Trevett 1986).

The ability of a radar system to detect a target is expressed in terms of the radar equation. The power received at the antenna is a function of the energy transmitted by the radar and the power received at the target. The amplitude is also dependent on the ability of the target to re-radiate the energy (referred to as the radar cross-section or RCS), gain factors of the receiving antenna and any system loss factors (Kingston and Quegan 1992). The power received (P_r) by the antenna from the target is given as:

$$P_r = \frac{P_t G_t G_r \sigma \lambda^2 L_s}{(4\pi)^3 R^4} \quad (2.6)$$

where,

P_r is the mean power received by the antenna,

P_t is the mean power transmitted by the antenna,

G_r and G_t are the gain factors for the receiving and transmitting antennas respectively,

σ is, in this case, the radar cross-section (RCS),

L_s is the system loss factor, and

R is the distance to the target.

The RCS determines the variation in intensity of the radar image because of the radar's ability to detect the apparent area of the target or surface under study. The RCS depends initially on the wavelength, polarisation and also the angle of incidence (Champion 1996). This dependency accounts for the fact that some surfaces are detectable on SAR images at some wavelengths but invisible at other wavelengths (Blom 1988). The following general conditions apply (Kingston and Quegan 1992):

- For target sizes $\gg \lambda$, the RCS is roughly the same size as the real area of the target (normal to incidence), known as the optical region.
- For target sizes $\approx \lambda$, the RCS varies greatly with changes in wavelength.
- For target sizes $\ll \lambda$, the $\text{RCS} \propto \lambda^{-4}$, known as the Rayleigh region.

In Earth surface applications, the size of the target area can be approximated to a roughness measure of the surface. The Rayleigh criterion stipulates that a surface will be radiometrically 'flat' if:

$$\sigma < \frac{\lambda}{8 \cos \theta} \quad (2.7)$$

where, σ is the standard deviation of surface height (defined in Section 4.4), and θ is the incidence angle. At the wavelength of the SAR system used in this study, the Rayleigh criterion shows that a surface will be radiometrically flat if $\sigma < 0.76$ cm.

As the incidence angle becomes smaller (tending towards nadir) the radar energy field is coherent and can only give an indication of the surface slopes in the target area. As incidence angles approach 90° much of the energy is specularly reflected away from the receiver and information content within images is generally poor. As incidence angles tend away from nadir the scattering at the surface becomes dependent on system and surface parameters. It is the dependence of the RCS to these system and surface parameters that enable the monitoring of important environmental variables such as soil moisture to be achieved.

The RCS of various targets forms the basis for theoretical modelling studies. Assumptions are made which are related to the properties of soil surfaces and vegetation. For example, trees are modelled as cylinders and plates of material with known RCS. Similarly, soil surfaces are modelled, in simple terms, as planes of homogeneous mediums with a constant RCS. The RCS is, therefore, directly related to the backscatter coefficient of a resolution cell. Estimates of the backscatter coefficients for soil, rock and vegetation are given in Ulaby and Elachi (1990).

2.1.2 Energy-target interactions: surface and volume scattering

When incident microwave radiation strikes the interface between two media with different dielectric properties the wave form is changed. The complex dielectric constant of a medium is given as a measure of the propagation characteristics of an electromagnetic wave in the medium. It therefore affects the emissive and reflective properties at the surface. The complex dielectric constant, ϵ , is given as:

$$\epsilon = \epsilon' - j\epsilon'' \quad (j = \sqrt{-1}) \quad (2.8)$$

where, ϵ' is the permittivity of the material, the real component defining the velocity and wavelength of the refracted wave in the material; and ϵ'' is the dielectric loss factor, the imaginary component expressing energy lost through absorption of the wave in the medium. Further information of experimental work carried out into the dielectric properties of natural materials is given by Ulaby *et al.* (1986).

The incident energy is effectively absorbed or scattered. Two types of scattering can occur which are dependent on system parameters, surface roughness and surface dielectric properties. These are known as surface scattering and volume scattering. Also of importance is the ability of the microwaves to penetrate the surface layers. If the lower medium is homogeneous then a portion of the transmitted wave proceeds into the surface medium, the rest being scattered at the surface. This could therefore be treated as a surface scattering problem. However, if the lower medium is inhomogeneous (comprising materials with mixtures of dielectric components, such as a vegetative layer) then the transmitted wave may be scattered in all directions and may re-bounce back over the boundary surface (Ulaby *et al.* 1982). Scattering within the lower medium is referred to as volume scattering. Figure 2.4 illustrates both surface and volume scattering processes.

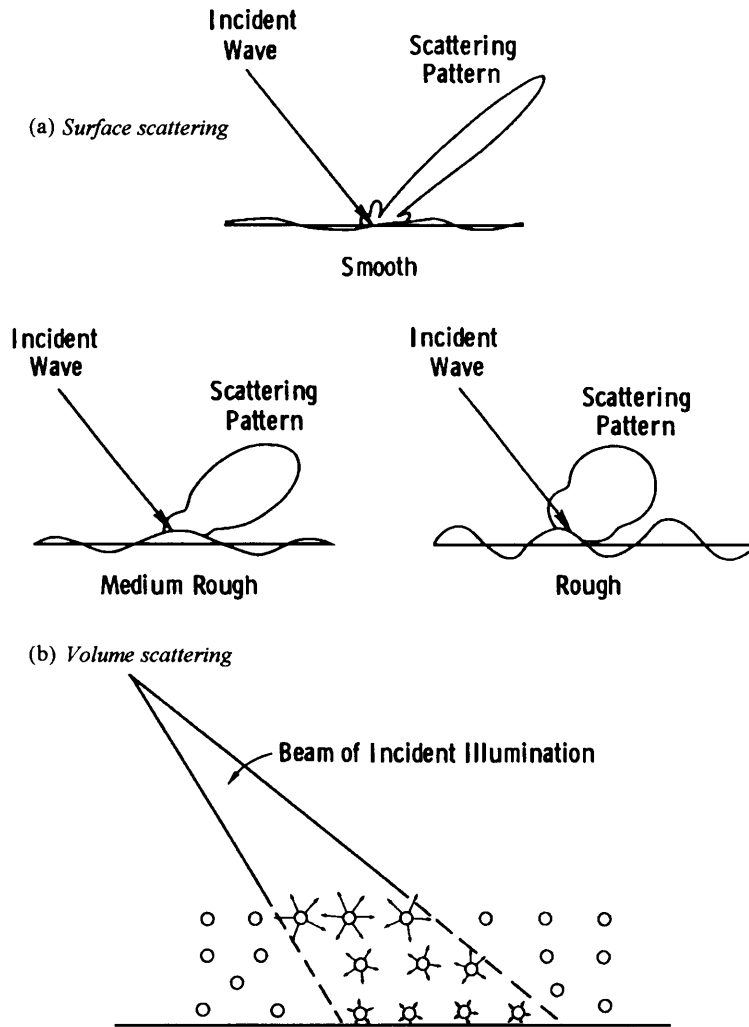


Figure 2.4. Examples of (a) surface scattering and (b) volume scattering processes (Ulaby *et al.* 1982).

The depth to which volume scattering occurs, known as the penetration depth, is a function of frequency and moisture content (Figure 2.5). It is usually assumed that, for a wet soil, the penetration depth is small enough to ensure that any inhomogeneities in the soil layer cause negligible amounts of volume scattering. In Figure 2.5 the penetration depth between 4 and 10 GHz is ≤ 5 cm, for soil moisture contents $>0.05 \text{ m}^3 \text{ water m}^{-3} \text{ soil}$ (or g cm^{-3}). The frequency of the radar system used in this study is 5.3 GHz (Section 2.2) indicating that surface scattering is likely to be the dominant scattering process for the soil surfaces under consideration. Also, due to the complex nature of volume scattering (Ulaby *et al.* 1982, Chapter 13), deriving a suitable model and collecting the field data for calibration purposes is beyond the scope of this study.

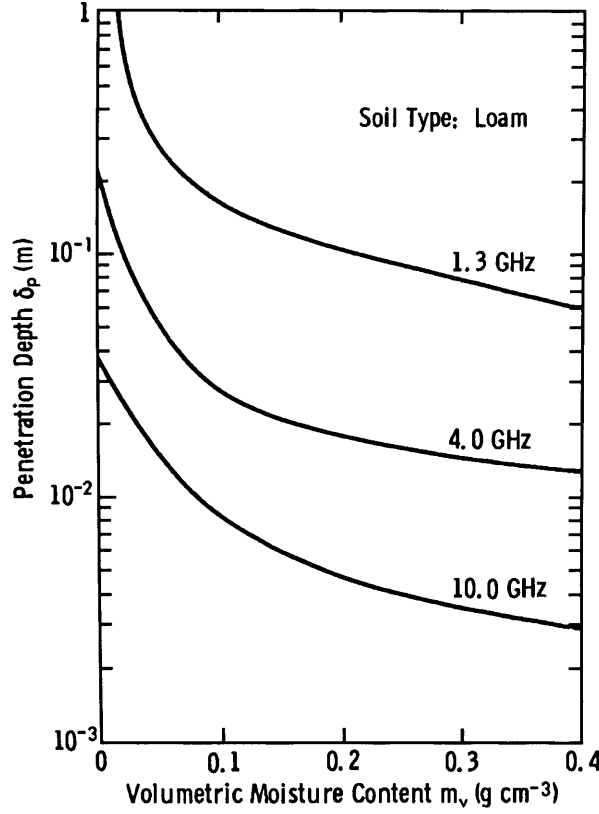


Figure 2.5. Penetration depth expressed given as a function of volumetric soil moisture (g cm^{-3}) of a loamy soil at three frequencies (Ulaby *et al.* 1982). As the frequency of the microwave increases the penetration depth decreases. Interpolation at ≈ 5.3 GHz, the wavelength of the ERS SAR system, between 4 GHz and 10 GHz indicates the penetration depth is approximately 3 cm at a volumetric soil moisture of 0.1, decreasing to less than 1 cm at a volumetric soil moisture of 0.4. At very low moisture levels the penetration depth increases significantly.

The backscatter coefficient of a non-periodic random surface can be expressed as the product of two functions (Ulaby *et al.* 1986):

$$\sigma^\circ(\theta) = f_r(\epsilon_s, \theta) \cdot f_s(\rho(\xi), \theta) \quad (2.9)$$

where, $f_r(\epsilon_s, \theta)$, the dielectric function, accounts for the dependence of the backscatter coefficient on the relative dielectric constant of the surface ϵ_s , and $f_s(\rho(\xi), \theta)$, the roughness function, accounts for the dependence of the backscatter coefficient on surface roughness $\rho(\xi)$.

The first series of papers discussing the dependence of the backscatter coefficient on these functions and function parameters were published at the end of the 1970's and addressed bare soil, vegetation covered soil and soil moisture situations (Ulaby *et al.* 1978, 1979, Dobson and Ulaby 1981).

2.1.3 Microwave backscatter dependence on dielectric properties

The theoretical basis for measuring soil moisture using microwave remote sensing is based on the large contrast between the dielectric properties of liquid water and dry soil (Engman and Chauhan 1995). At L-band wavelengths, the dielectric constant for water is approximately 80 compared to a value between 3 and 5 for dry soil. Very wet soils can have a dielectric constant of around 20. Values are similar at C-band wavelengths. As volumetric soil moisture increases both components of the complex dielectric constant, real and imaginary, increase (Figure 2.6).

This rate of increase is frequency dependent. As frequency increases in the microwave spectrum, the sensitivity to increasing soil moisture decreases for the real component and increases for the imaginary component. These relationships are illustrated in Figure 2.6 for a loamy soil. At 6 GHz, (the frequency approximating that which is used in this study) the sensitivity of the real component (ϵ'_{soil}) is significant and the sensitivity of the imaginary component (ϵ''_{soil}), a measure of losses, is reduced compared to the other frequencies shown. C-band radar should, therefore, be more appropriate than other frequencies for measuring soil moisture.

Two distinct features can be identified in the relationship between the soil dielectric constant and the amount of water in the soil. Firstly, as soil moisture values (which are initially at zero) increase, the dielectric constant increases slowly. After a transition value of soil moisture (W_t), the dielectric constant increases sharply with increasing soil moisture. The second feature is that the transition soil moisture content is dependent on the soil texture; it is lower for sandy soils and greater for clay soils (Wang and Schmugge 1980).

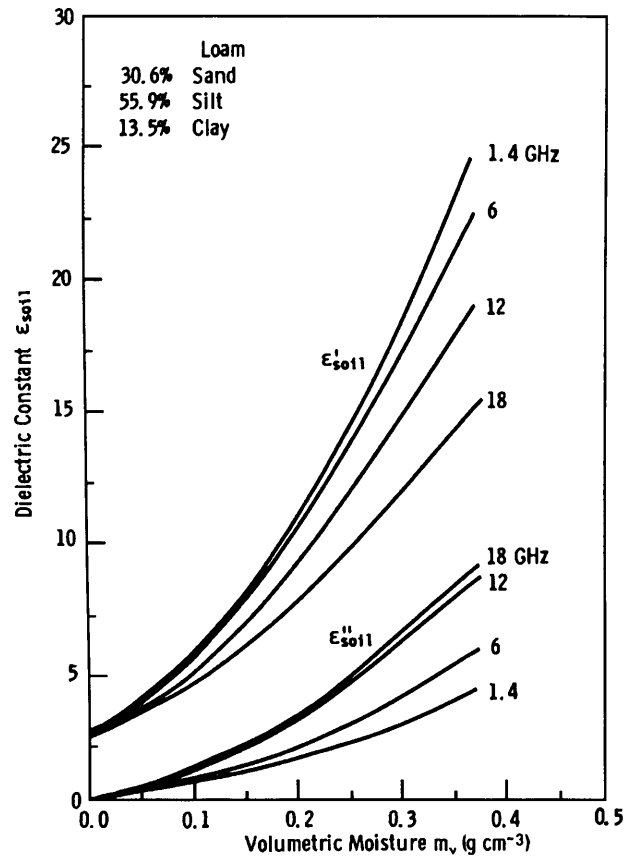


Figure 2.6. The complex dielectric constant, comprising real (ϵ'_{soil}) and imaginary (ϵ''_{soil}) parts, shown as a function of volumetric moisture content at four frequencies (after Ulaby et al. 1986).

One explanation of this occurrence is that, at moisture levels less than the transition soil moisture content, water is tightly bound to the soil particles by matric and osmotic forces (bound water). It is difficult for these water molecules to polarise. As soil moisture increases, water is able to move more freely around the soil particles and this free water will have a dominant effect on the dielectric constant. Hence, the greater the amount of free water in the soil medium, the greater the dielectric constant. For a given volumetric soil moisture, a sandy soil has a greater amount of free water compared to a clay soil. This is due to a smaller amount of particle surface area being available in a sandy soil which will, therefore, exhibit a greater dielectric constant. A fuller explanation of the dependence of soil-water parameters on the soil texture is given by

Schmugge (1980). The dependence of the dielectric constant to soil texture and an estimate of the transition soil moisture content (W_t) are shown in Figure 2.7. In this diagram, best-fit lines are fitted to values derived experiments.

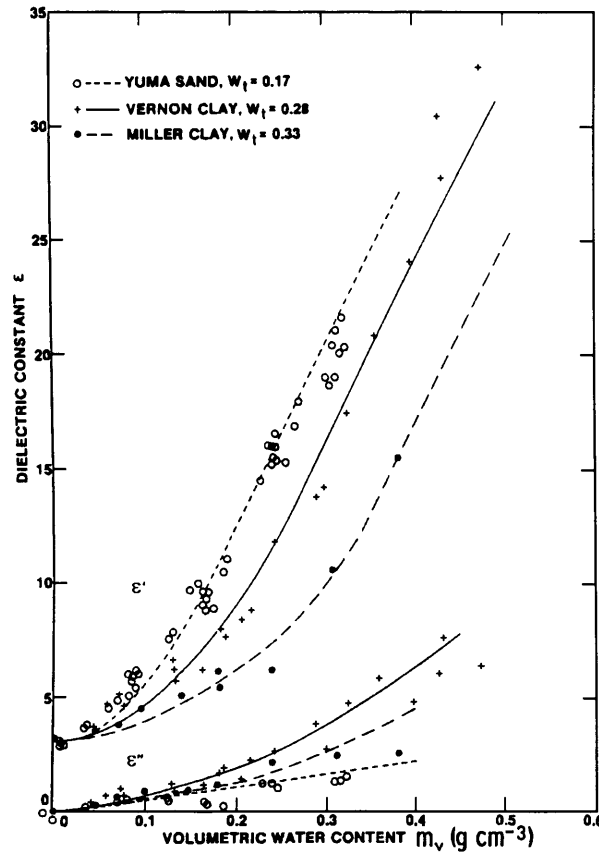


Figure 2.7. The complex dielectric constant, comprising real (ϵ') and imaginary (ϵ'') parts, shown as a function of volumetric moisture content for three soil types at 5 GHz. Also shown are the approximate transition volumetric soil moisture values (W_t) discussed in the text (after Wang and Schmugge 1980).

The relationships between soil moisture, texture and the dielectric constant has been empirically derived through mixture modelling of various soil types and dielectric measurements. Wang and Schmugge (1980) presented a mixture model with porosity, volumetric water content and dielectric constants of air, water, rock, ice and absorbed water. Hallikainen *et al.* (1985) and Dobson *et al.* (1985) noted that previous investigations into the determination of these relationships had reported differences in

terms of the absolute level of the dielectric constant for similar soils and in terms of the dependence of the dielectric constant on soil texture. None of the existing techniques allowed mixture modelling of the soil-water medium using soil physical parameters. They aimed to establish an accurate empirical model that accounted for several frequencies between 1 and 18 GHz and several soil types based on soil physical parameters. Concentrating at the frequency approximating that of the system used in this study (5.3 GHz), the results of their experiments are illustrated in Figure 2.8.

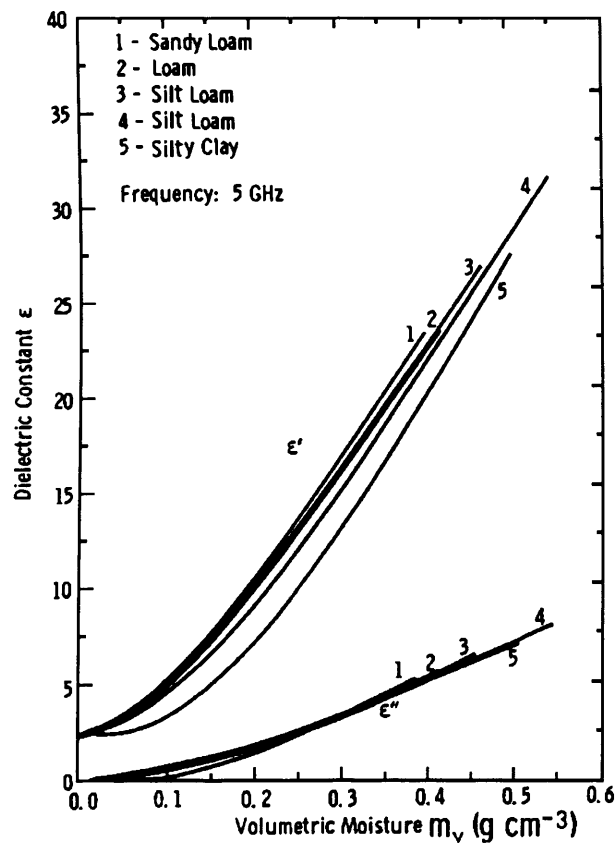


Figure 2.8. Measured dielectric constants for five soil types as a function of volumetric soil moisture at 5 GHz (Hallikainen et al. 1985).

This shows that the measured dielectric constant (ϵ) for five soil types is a function of volumetric moisture content at 5 GHz. An interesting point to note is the similarity of the imaginary component of the dielectric component and the approximate similarity of the real component at this specific frequency.

Polynomial expressions were constructed for selected frequencies for both the real and imaginary components, the general expression is given as:

$$\epsilon = (a_0 + a_1S + a_2C) + (b_0 + b_1S + b_2C)m_v + (c_0 + c_1S + c_2C)m_v^2 \quad (2.10)$$

where, S and C are the sand and clay components of the soil (percent by weight) respectively, m_v is the volumetric soil moisture and $a_0 \dots c_2$ are constants. The constants can be found in the article by Hallikainen *et al.* (1985) for each class of frequency. The constants used in this study were calculated for a 6 GHz frequency (even though Figure 2.8 shows data for a 5 GHz SAR only 6 GHz model parameters were tabulated) as this most closely approximated the frequency of the ERS SAR system.

The relationship between dielectric constant and the backscatter coefficient is approximately linear up to a volumetric soil moisture of 0.35. When the reflectivity is expressed in decibels (dB), in a log form, the relationship takes the form shown in Figure 2.9 (overleaf). The Fresnel reflectivity is a measure of the amount of signal return and is expressed at an incidence angle normal to the surface. The relationships still hold for incidence angles up to 20° , due to the small angular variation in the Fresnel reflectivity (Le Toan 1982) and therefore is comparable with the incidence angle of the SAR system used in this study (see Section 2.2). The two curves represent soils of different texture, one a sandy loam and the other a silty clay. The dependence of soil type decreases with increasing frequency.

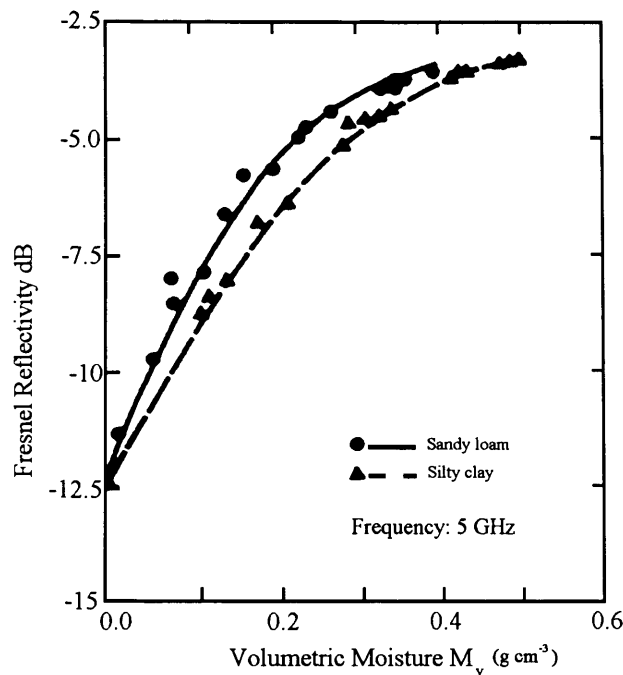


Figure 2.9. *Fresnel reflectivity at normal incidence (an expression of the backscatter coefficient), in dB, described as a function of soil moisture for two soil types at 5 GHz (after Ulaby et al. 1986).*

2.1.4 Microwave backscatter dependence on roughness properties

The roughness of a surface influences the type of radar scattering. Even though Le Toan (1982) showed that the variations in intensity to changes in soil moisture are not influenced by surface roughness, the magnitude of the backscatter coefficient is determined by roughness properties. A complete and accurate description of the roughness of a surface is difficult to obtain. Therefore, in practice the roughness of a surface is expressed as a variation in the surface heights and a description of the relationships between surface heights in the horizontal direction. A full definition and discussion of these roughness parameters are given in Section 4.4. For a range of frequencies between 1 and 10 GHz, the backscatter coefficient increases with increasing surface roughness for incidence angles greater than 10° . These relationships are shown in Figure 2.10 at frequencies of 4.25 and 7.25 GHz. The relationships become less strong as the frequency increases. Although expressed for HH polarisation, the results

are not significantly different for a VV polarising radar system. Figure 2.10 shows that, for maximum soil moisture monitoring capability, the incidence angle of a SAR system should be between 10 and 20° at C-band wavelengths.

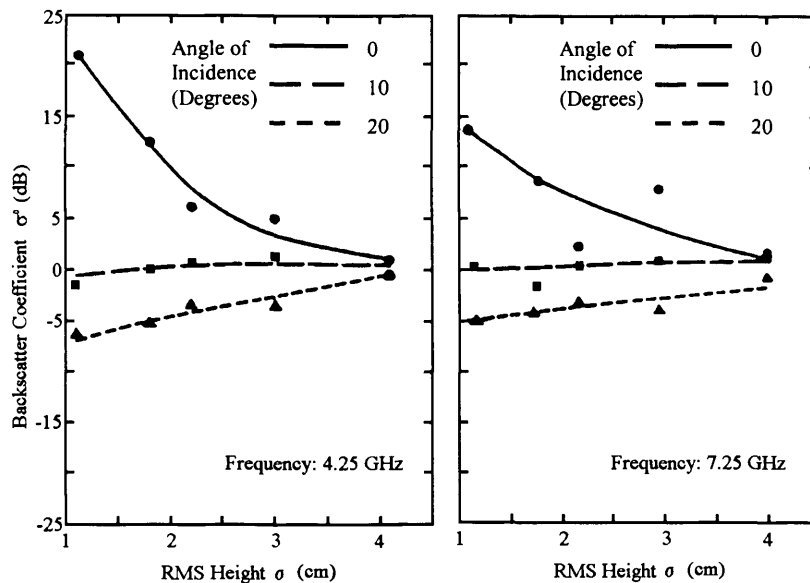


Figure 2.10. The dependence of the backscatter coefficient on RMS height and incidence angle at two microwave frequencies; 4.25 GHz and 7.25 GHz (Ulaby *et al.* 1978).

2.2 Technical specification and characteristics of the ERS SAR

The synthetic aperture radar (SAR) on board the European Environmental Remote Sensing (ERS) series of satellites is used in this study. The ERS SAR operates at a fixed wavelength (C-band), fixed mean incidence angle (23°) and VV polarisation. The chosen specification incorporated knowledge gained from previous spaceborne SAR missions such as SEASAT, SIR-A and SIR-B, all of which operated at longer wavelengths (L-band) and at HH polarisation. These previous missions provided the first real opportunity to realise the full potential of a spaceborne SAR instrument for estimating soil moisture (Wang *et al.* 1986, Dobson and Ulaby 1986). Following work by Ulaby *et al.* (1978) the optimal specification of a SAR system for maximum soil

moisture sensitivity was a C-band system operating at an incidence angle between 10 and 20°. The European Space Agency selected the characteristics of the ERS SAR (Table 2.1) to maximise surface scattering as opposed to volume scattering (due to the shorter wavelength), to be more sensitive to small scale surface roughness and to have an increased sensitivity to soil moisture. ERS-1 was launched in 1991 with its successor ERS-2, launched in May 1995. The SAR instruments on board have outlived their expected life cycle and have shown to be radiometrically stable while operational (Laur *et al.* 1993).

ERS SAR Satellite Specification	
Incidence angle - near range	$\approx 20.1^\circ$
Incidence angle - mid range	$\approx 23^\circ$
Incidence angle - far range	$\approx 25.9^\circ$
Frequency	5.3 GHz (C-band)
Bandwidth	15.55 ± 0.1 MHz
Polarisation	Vertical transmit, vertical receive (VV)
Antennae size	10 m by 1 m
Spatial resolution - azimuth	≤ 30 m
- range	≤ 26.3 m
Temporal resolution (during this phase)	35 days
Radiometric resolution	≤ 2.5 dB at $s^\circ = -18$ dB
Dynamic range	≥ 21 dB
Radiometric stability	≤ 0.95 dB
Maximum operation time	10 minutes per orbit
Swath width	102.5 km (telemetered) 82.5 km (full performance)
Swath stand-off	250 km to right of satellite track
Localisation accuracy	azimuth ≤ 1 km; range ≤ 0.9 km

Table 2.1. Technical specification of the ERS-1 SAR instrument (ESA 1992).

2.3 Data structure and acquisition periods

ERS SAR imagery was collected and archived at the Italian Processing and Archiving Facility (I-PAF) under a data exploitation agreement with ESA (Project AO2.UK.125). ERS SAR precision image (PRI) data was used as this was most applicable for remote sensing applications involving soil moisture estimation. PRI imagery is generated from raw SAR data using algorithms that have been developed by ESA to account for the effects of the SAR antenna pattern and range spreading loss. PRI data are also multi-look reducing the effects of speckle, by taking the average of three independent looks of each pixel. The 16 bit data can also be converted to a backscatter coefficient (σ^0) for geophysical modelling, which is essential to this particular study. The imagery has not been geo-coded, this was carried out separately. Nor has it been corrected for the influence of the terrain in the scene (layover and foreshortening), these corrections are discussed in the next section. The specification of PRI data is given in Table 2.2.

ERS SAR Precision (PRI) Data	
Pixel size	Eastings – 12.5 m Northings - 12.5 m
Scene area	range - 100 km azimuth – 102.5 km
Scene size	range – 8000 pixels per line azimuth – at least 8200 lines
Pixel depth (data type)	unsigned 16 bit
Product location accuracy	range - 100 m azimuth – 200 m
Total product volume	≈ 131 Mbytes
Annotation in image	lat./long. of scene centre and four corners
Projection	ground range
Number of looks	3

Table 2.2. ERS SAR PRI product characteristics (ESA 1993).

2.3.1 SAR image geometric effects

The effects of geometric distortions are caused by the surface being non-uniform or sloping. PRI data are projected into ground range co-ordinates (i.e. the distance from the satellite's nadir point on the Earth's surface to the specified target) as opposed to slant range co-ordinates (i.e. the distance from the satellite to the target). The ground range projection is sensitive to the local incidence angle and is therefore dependent on the slope conditions at the target. The slant range is measured by determining the time that it takes the pulse of radar energy to reach the target and return to the satellite and is invariably more accurate. The terrain characteristics at the target will therefore have an influence on the characteristics of the returned radar signal. These influences produce effects such as foreshortening, layover and shadow. They are discussed in the context of their influence in this study.

2.3.1.1 Foreshortening

In areas of high relief, for all slopes facing the satellite, the projected image distance between the foot of the slope and the slope summit will appear shorter than the actual distance (Figure 2.11).

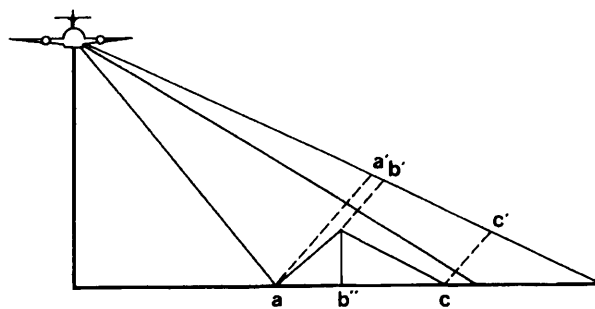


Figure 2.11. The distortion known as foreshortening caused by high relief (after Trevett 1986).

This distortion is shown in Figure 2.11 where the actual distance $a-b''$ is greater than the projected image distance $a-b'$. The radar returns on the slopes facing the satellite are more perpendicular to the signal and are compressed into a smaller radar cross section than those facing away. The effects of foreshortening are increased at near range.

2.3.1.2 Layover

In areas of exaggerated relief, or when the incidence angle is particularly great, the foreshortening causes the summit of the slope to be detected before the foot of the slope. In Figure 2.12 the actual projection point should be b'' . However, the radar return of point b is b' , ahead of a' . In the study region the surface terrain is mainly flat to undulating and any localised regions of high relief, such as incised wadi channels and volcanic cones, have been avoided. High backscatter return can be observed in some of these regions on those slopes facing the satellite and can therefore be delineated. Such areas are not considered in this study.

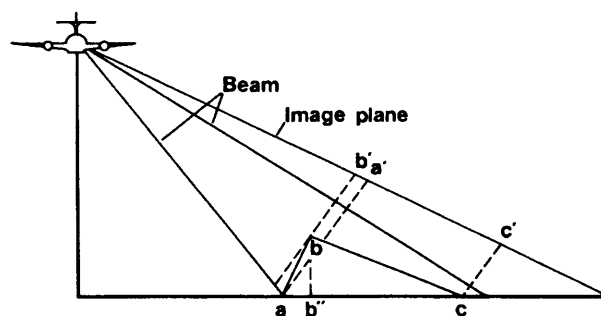


Figure 2.12. Radar layover distortion in areas of extreme relief (after Trevett 1986).

2.3.1.3 Shadow

Regions of shadow occur in imagery when relief is high or the incidence angle is large. They comprise regions in the lee slopes of hills and contain no data. Figure 2.13 shows how shadow in radar imagery is formed. The radar energy striking target b , is projected

as point b' , beyond which the next point on the ground surface that the radar energy strikes is point d . In between these points the radar has not targeted any of the ground surface and therefore in the space b' to d' on the image plane no data has been recorded. In this study the effects of shadow are observed only locally, on the lee slopes of volcanic cones that are present in the study region. These areas have not been considered.

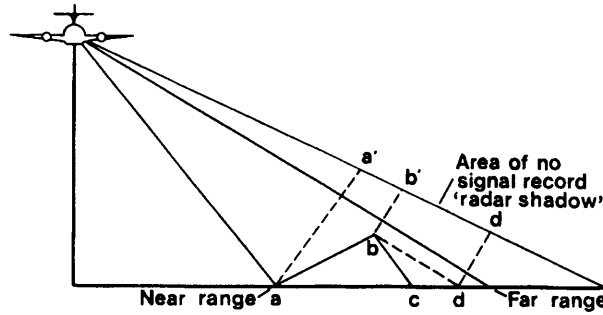


Figure 2.13. Radar shadow (after Trevett 1986).

2.3.2 SAR image speckle effects

Scattering elements on the Earth's surface generate a backscattered wave whose amplitude and phase has been changed by the nature of the scatterer (Quegan 1995). The actual measurement made by the SAR system is a weighted average of the vertically polarised wave component contributed by all the scatterers within the resolution cell. Speckle causes backscatter measurements made over a uniformly distributed target to have an intensity, I , whose probability density function, $\rho(I)$, is a negative exponential described as:

$$\rho(I) = \frac{1}{\sigma} e^{-I/\sigma} \quad (2.11)$$

where, $\sigma \geq 0$ and is proportional to the average radar cross-section (RCS) of the target.

During the integration of all these scattering elements comprising different amplitudes and phases, constructive and destructive interference occurs causing speckle, an interference phenomena, to occur. Speckle is often thought of as being unwanted noise within an image scene and manifests itself on a per-pixel basis, even when the surface under consideration is homogeneous. However, interferometric SAR research (InSAR) uses speckle noise as a real electromagnetic interaction phenomena (phase). InSAR uses data collected at different times (repeat pass) to correlate the speckle between channels to derive phase difference images. Applications of InSAR techniques have included digital elevation model generation from space (Zebkar and Goldstein 1986); geotectonics, in particular the elevation of seismic displacements (Massonnet *et al.* 1993); the retrieval of vegetation parameters (Wegmuller and Werner 1997) and more recently to characterise arid land surfaces (Wegmuller *et al.* 1998).

At the pixel level and for small scale geophysical modelling, speckle reduces the information content of the image and, in an attempt to solve this, algorithms have been designed to suppress the influence of speckle. If the interest is in single images of distributed targets then one way to reduce speckle is using a multi-look process. ERS SAR PRI data effectively forms three intensity sub-images, each using one third of the available Doppler bandwidth, which are averaged to form the PRI image. Many algorithms alter the original pixel values (DN) so speckle reduction has not been applied in this study as original pixel DN values were required. Backscatter coefficients were derived for the average of a number of pixels in accordance with the recommendations of Laur *et al.* (1996). These techniques are discussed in Section 2.5. Hence, apart from multi-look averaging undertaken at the I-PAF, no specific speckle reduction algorithms have been applied to the imagery. Archer (1995) applied several speckle reducing algorithms, to an ERS SAR image, including mean, median, Lee adaptive (1980), Kuan *et al.* (1985) and Frost *et al.* (1981) filters, with no significant enhancement of the image observed. The remaining component that comprises a radar image is referred to as the image texture. Texture is the spatial variability in the scattering properties of the scene illuminated by the radar (Posner 1993).

2.3.3 Data coverage and acquisition

SAR data were acquired from the ERS satellite in the 35 day repeat overpass mode. Due to the location of the receiving stations, all but one of the scenes acquired were from ascending passes. The time of the overpass was approximately 10 p.m. local time. Figure 2.14 shows the ERS SAR coverage of the study area. In the proposal presented to ESA, two scenes that covered the study area were to be collected every month over a period of 24 months, effectively totalling a maximum of 48 scenes. However, to fully encompass the whole of the study area 6 scenes were needed. It was decided at an early stage that the two centre scenes were most important for monitoring the surface changes for the majority of the study area and that it was essential to acquire as many of the two centre scenes as possible on a 35 day repeat overpass basis. In addition, when field work were being undertaken, the scenes adjacent to the centre scenes were acquired to maximise the amount of image data that was acquired. Unfortunately, the schedule was altered by the European Space Agency because of sensor conflicts, missing data and faulty telemetry. In some cases, satellite data were not acquired when field work was undertaken (27 April 1996 and 17 April 1998) which limited the usefulness of the field data. Table 2.3 lists the dates and locations of the ERS SAR PRI images used in this study.

The first scenes were acquired in March 1995, before the first field visit. These scenes were acquired because local reports indicated that the winter rainfall was greater than average providing an opportunity to investigate an image obtained under wet conditions. Areas of localised flooding surrounded by regions of high backscatter indicating high soil moisture levels can be observed. Good temporal coverage was acquired over the winter and spring of 1995/96 which covered two field visits (see Table 4.1). ERS-1 was replaced by ERS-2 during the winter of 1996 but, due to sensor conflicts, no further images were obtained until March 1997. This coincided with the third field visit. After this period I had to negotiate with ESA for an extension of the number of images that I could receive. The argument was based on the cross calibration of the ERS-1 and ERS-2 SAR sensors discussed in Section 3.3. The project was granted an extension and obtained images during the spring of 1998, coinciding with the final field visit. I also

acquired two images from November 1995. These were collected when the ERS sensors were in tandem mode, i.e. ERS-2 collecting data 24 hours after ERS-1 had collected data. One descending overpass was collected the day after the failed 27 April 1996 overpass, this coverage shown in Figure 2.14 (dashed line).

Satellite	Date	Orbit-Track	Frames	Ref. No. (Figure 2.14)
ERS-1	23-March-95	19283-257	639/621	3 and 4
	6-July-95	20786-257	639	3
	19-Oct-95	22289-257	639/621	3 and 4
	23-Nov-95	22790-257	639/621	3 and 4
ERS-2	24-Nov-95	03117-257	639/621	3 and 4
ERS-1	9-Dec-95	23019-486	639/621	5 and 6
	12-Dec-95	23062-028	639/621	1 and 2
	28-Dec-95	23291-257	639/621	3 and 4
	1-Feb-96	23792-257	639/621	3 and 4
	7-March-96	24293-257	639/621	3 and 4
	11-April-96	24794-257	639/621	3 and 4
	28-April-96	25030-493	2961	7 (descending)
	30-April-96	25066-028	639/621	1 and 2
	16-May-96	25295-257	639/621	3 and 4
ERS-2	9-March-97	09859-486	639/621	5 and 6
	28-March-97	10131-257	639/621	3 and 4
	13-April-97	10360-486	639/621	5 and 6
	6-Feb-98	14640-257	639/621	3 and 4
	29-March-98	15370-486	639/621	5 and 6

Table 2.3. Information related to the ERS SAR images used in this study; acquisition date, coverage and orbit details.

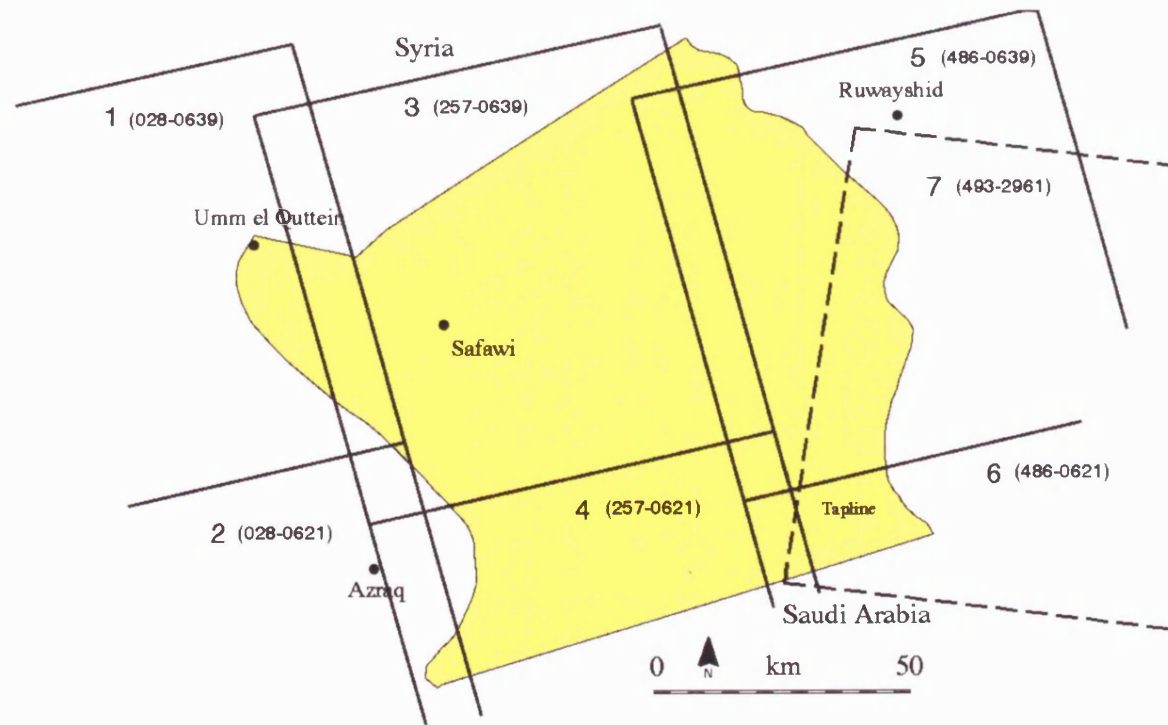


Figure 2.14. ERS SAR scene coverage of the Jordan Badia Research and Development Programme area. The ascending scenes are shown as solid lines, the one descending scene is shown as a dashed line. ERS SAR track and frame numbers are shown for each image. Refer to Table 2.3 for further information.

2.4 Image geometric correction

To be able to locate study sites within the SAR image it is necessary to rectify the image to an ellipsoid that represents the Earth's surface. This can be achieved through a variety of methods; e.g. using a geographic map, a digital elevation model or using the network of orbiting satellites to fix points that can be located, with accuracy, both in the field and on the imagery. The latter method, utilising the global positioning system (GPS) of orbiting satellites to collect ground control points (GCPs), was adopted in this study. The first stage of the rectification process involved visual analysis of the images to identify suitable GCPs. SAR is very good at distinguishing between rough and smooth surfaces and was therefore able to detect the edges and junctions of roads, small piles of basalt boulders surrounded by smooth mud pans (*qa'a*) and headlands of basalt protruding into these abundant mud pans. In addition, corners of cultivated fields were also used. The points were located in the field and their geographic location derived using a hand-held Garmin 45 GPS, set-up to display the latitude and longitude (degrees) of the GCP. The GPS was also used to record the location of the study sites. In most cases, three separate recordings were made at each GCP and the average calculated. Recordings were made after the GPS display remained constant for several seconds. The GPS was calibrated to the WGS84 ellipsoid, a global datum that approximates the Earth's surface. In total 33 GCPs were collected, although it was found that 13 of these could not be located in the image with accuracy. For the best results, GCPs should be collected at random locations over the image. Unfortunately the pattern of GCP collection followed the main roads in the region and for large parts of the study area, no GCPs were obtained due to the region's low accessibility. The full size images were also reduced to fit the programme area, this increased the accuracy of the correction process given the GCPs available.

The next stage was to identify the GCPs within the SAR scene. The pixel location could then be assigned a geographic location and the whole image transformed to latitude-longitude co-ordinates. The processing was undertaken using IMAGINE software developed by ERDAS. It was assumed that once one image was accurately geo-rectified, then this image could be used to correct the other images. In all cases, at least six points

were used as this was the minimum requirement to undertake a second-order polynomial transformation. In all cases nearest neighbour re-sampling was used, as this method maintains the original pixel values. This was achieved with an RMS error of transformation of <1 pixel. To test the accuracy of the transformation some of the original GCPs that were not used in calculating the transformation were located in the imagery and their geographic co-ordinates compared to the co-ordinates calculated with the GPS. The accuracy of the transformation was also tested using the location of study sites and knowledge of their location and surroundings. No major errors in geo-rectification were observed.

The final stage involved correction of similar scenes by relating GCP points from the corrected image. This enabled scenes to be overlain and sites to be located in all of the available images. In regions where GCPs are infrequent, the image to image transformation calculations will not be as accurate as in regions where GCPs were more frequent. It is therefore important to have GCPs reasonably near to the study sites and this was achieved in nearly all cases.

2.5 Derivation of the backscatter coefficient

ERS SAR PRI data generated by ESA can be calibrated to a backscatter coefficient (σ^0) to aid geophysical modelling of the scattering properties of the Earth's surface. The properties of the backscatter coefficient were discussed earlier in this chapter (Section 2.1). This section discusses how backscatter estimates are calculated from PRI data and how this information can be used to interpret characteristics of land surfaces.

2.5.1 Calibration methods and assumptions

The PRI image is a standard product from ESA and has the following characteristics (Laur *et al.* 1996):

- The pixel value in the image is proportional to the square root of the intensity.

- The intensity value is proportional to the radar brightness β° .
- The radar brightness β° , is proportional to the backscattering coefficient σ° , divided by the sine of the pixel incidence angle.
- The image is corrected for the in-flight elevation antenna gain.
- The image is compensated for the range spreading loss.

It is possible, therefore, to derive a simple equation to calculate the backscatter coefficient. However, ESA have identified various sources of radiometric and stability errors and have proposed an alternative comprehensive equation to calculate the backscatter. These sources of error have been attributed to on-board instrumentation and processing at the PAFs. In this study, estimates of the backscatter coefficient were calculated using both the simple method and a version of the comprehensive equation. The derivation procedure assumes the following:

- Flat terrain. The incidence angle is dependent only of the ellipsoid and varies from 19.5° at the near range pixel to approximately 26.5° at the far range.
- Any change in incidence angle across a distributed target is neglected.
- To reduce statistical uncertainties in the imagery caused by speckle (Section 2.2) the backscatter coefficient is calculated using intensity averaging.

The third assumption accounts for the speckle effects by increasing the equivalent number of looks (ENL). Speckle (Section 2.3.2) is defined here as the inverse of the normalised variance of the signal intensity in the image of a homogenous target (Bally and Fellah 1995). The radiometric resolution of an image is defined in terms of the radiometric confidence intervals, or how well an individual pixel intensity represents the

true intensity given the effects of speckle. The backscatter coefficient expressed in a linear form is given as:

$$\sigma^{\circ} = \frac{1}{N} \sum A_{ij}^2 \quad (2.12)$$

where, A_{ij} is the amplitude corresponding to the pixel location (i, j) in the image, and N is the number of pixels within the area of interest (AOI).

To determine N , consideration must be given to the size and homogeneity of the target and to the likely radiometric confidence intervals required. Figure 2.15 shows radiometric confidence intervals as a function of the equivalent number of looks as ENL is ranging from 3 to 370. This shows that, in the case of PRI products (3 look) the 90% radiometric confidence interval bounds are ± 4.5 dB.

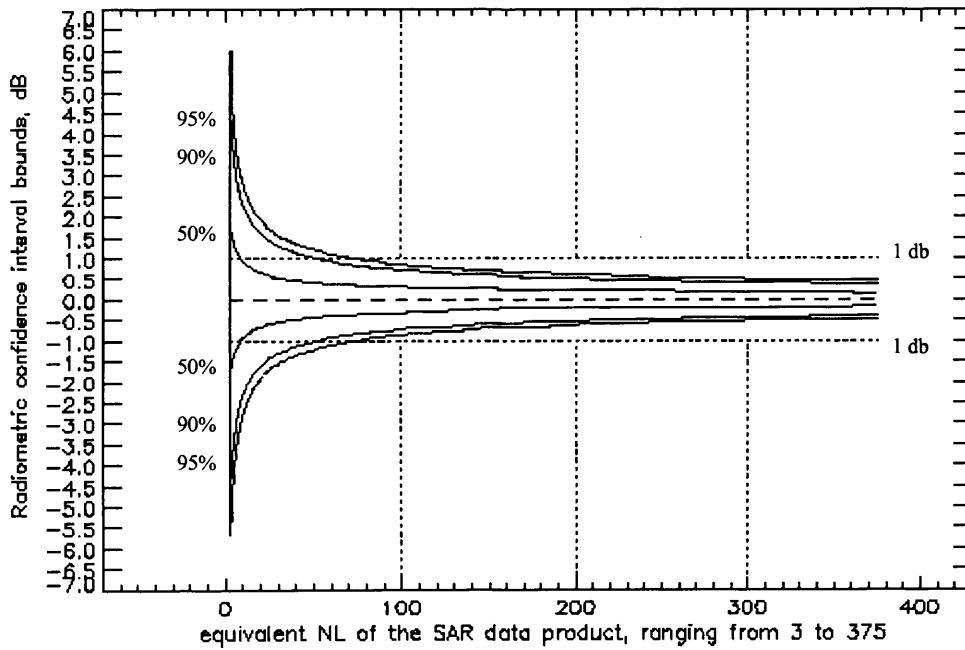


Figure 2.15. The 95%, 90% and 50% radiometric confidence intervals versus ENL for ESA products. The ENL range from 3 (PRI product) to 370. The two horizontal dashed lines represent the ± 1 dB interval (after Laur et al. 1998).

In an example cited by Laur *et al.* (1996) a value of N of 240 (pixels) yields 90% confidence interval bands of ± 0.5 dB (shown as the second curve from the bottom in Figure 2.15). In consultation with other researchers and after reviewing literature (e.g. Archer 1995), it was decided that an AOI of 25 by 20 pixels would be used. This would yield a large ENL value (500) and increase the confidence limits to yield backscatter estimates within 0.5 dB ($> 99\%$ confidence); n.b. these confidence limits are actually off the limits of the diagram shown in Figure 2.15. It was also a primary criteria of the site selection process that the sites could be assumed to be approximately homogeneous over an area of 500 by 500 m (Section 4.2).

2.5.2 Calculating the backscatter coefficient

The backscatter coefficient (σ°) is usually expressed in decibels (dB) taking the form of a logarithmic relationship:

$$\sigma^\circ_{(dB)} = 10 \cdot \log_{10} \sigma^\circ \quad (2.13)$$

For Equations 2.14 and 2.15 the backscatter coefficient is expressed in its linear form.

2.5.2.1 Simplified equation

Taking into account the assumptions outlined above, and not allowing for radiometric and stability fluctuations, the backscatter coefficient is calculated as follows:

$$\sigma^\circ = \left[\frac{1}{N} \cdot \sum_{i,j=1}^{i,j=N} DN_{ij}^2 \right] \cdot \frac{1}{K} \cdot \frac{\sin \alpha}{\sin \alpha_{ref}} \quad (2.14)$$

where,

K is the calibration constant, specific to the type of data product and the processing centre ($K = 686379$ for ERS-1 and 944000 for ERS-2 SAR),

DN_{ij} is the digital number corresponding to pixel located at co-ordinates (i, j),
 α is the average incidence angle within the distributed target and,
 α_{ref} is the reference incidence angle, i.e. 23 degrees at mid-range.

2.5.2.2 Comprehensive equation

The full equation to calculate the backscatter coefficient from PRI products using the comprehensive method that accounts for radiometric and stability errors is given as:

$$\sigma^{\circ} = \left[\frac{1}{N} \cdot \sum_{i,j=1}^{i,j=N} DN_{ij}^2 \right] \cdot \frac{1}{K} \cdot \frac{\sin \alpha}{\sin \alpha_{ref}} \cdot C \cdot \frac{\text{ProductReplicaPower}}{\text{ReferenceReplicaPower}} \cdot \text{Powerloss} \quad (2.15)$$

where,

C is the factor that accounts for updating the gain due to the elevation antenna pattern,

$\frac{\text{ProductReplicaPower}}{\text{ReferenceReplicaPower}}$ is the replica pulse power variations correction factor and,

Powerloss is the analogue to digital converter (ADC) power loss.

For the source of these values refer to Laur *et al.* (1996).

2.5.2.3 Application of corrections to ERS SAR PRI products

Within each of the AOIs in the image product for which backscatter coefficients were derived, the incidence angle of the radar energy did not change enough to influence the scattering pattern thereby satisfying assumption (ii) of the derivation process (Section 2.5.1). The location of the AOIs in the range direction and the local incidence angle were required to satisfy the parameter $\sin \alpha / \sin \alpha_{ref}$ in Equations 2.14 and 2.15. The relative incidence angle of any pixel in the image product can be calculated based on information related to the processed scene centre latitude, the near range incident angle and the zero Doppler range time of the first range pixel (Laur *et al.* 1996). These data are obtained from the product header files. The ellipsoid model used is the Goddard Earth Model 6 (GEM6) and does not account for local surface slopes. The model

parameters were entered into a spreadsheet to calculate estimates of incidence angle, look angle and both simple and comprehensive estimates of the backscatter coefficient for all AOIs used.

The value of the parameter C, for products generated at the I-PAF after the 16th July 1995 is 1. This is because the improved antenna pattern algorithm had already been applied. Although three images were acquired before this date, they are not directly related to fieldwork periods, for which it is essential to derive the most accurate estimates of backscatter.

The product replica power is the power of the replica pulse used to generate the imagery. The reference power is the replica pulse power of the reference image. To perform automatic internal calibration successfully, the replica pulse power should be directly proportional to the transmitter's pulse power (Laur *et al.* 1996). This is not so (Smith *et al.* 1994), and therefore the replica pulse power variations introduced by the SAR processor need to be removed. Product replica power values are located in the image header products; reference replica power values of ERS-1 and ERS-2 are 205229 and 156000 respectively.

The power loss factor is related to saturation occurring when the input signal to the analogue to digital converter is high. Power gain may also occur when the input signal level is low. The general recommendation given by ESA for ERS-1 SAR products is that if the backscattering coefficient, using the simple equation over a large distributed target, is greater than -7 dB, then the correction should be applied. A large distributed target, is defined as an area covering 1200 (range) by 400 (azimuth) pixels (this usually applies to rough seas or a large town). In this study, only basalt areas are capable of producing backscatter estimates that exceed -7 dB. However, backscatter coefficient measurements calculated for three basalt areas (from a July 1995 image) indicate that these surfaces do not have average backscatter coefficients that exceed the critical value. For a Fahda Vesicular basalt (32.3275° N, 37.1649° E) the average backscatter is -7.81 dB, for a Madhala Olivine basalt (32.1513° N, 36.9854° E) the average backscatter value is -8.63 dB, and for an Adeb Olivine basalt (32.4157° N, 37.3750° E) the average backscatter value is -7.03 dB. ERS-2 SAR ADC powerloss is much reduced due to

improvements in the system. Correction only needs to be applied for large distributed targets with an average backscatter coefficient > -2 dB for ERS-2 SAR data. This does not occur over any of the sites in the Jordan Badia programme area. Therefore the value of power loss used in this study is 1 for both ERS-1 and 2 SAR products.

The comprehensive method therefore takes into account the fluctuations in the product replica power only. The geometrical data and relevant header information were entered into the calibration spreadsheet with corresponding values of the average intensity I to calculate both simple and comprehensive estimates of the backscatter coefficient.

2.6 Modelling the backscatter coefficient

Geophysical modelling of the backscatter coefficient attempts to simplify the complex interactions that occur between electromagnetic energy and the Earth's surface. This has been achieved with laboratory experiments that have defined the parameters that influence the backscatter coefficient, discussed in Section 2.1, utilising mathematical and physical principles. The objectives of theoretical modelling can be summarised as (Fung 1994):

- To assist data interpretation by providing a relation for the measured quantity as a function of the electromagnetic, geometric and target parameters, based on the physics of the problem.
- To study the sensitivity of the measured quantity to various parameters of interest.
- To provide a tool for interpolating and interpreting data.
- To provide simulated data in simulation studies or training of neural networks for classification and inversion procedures.
- To assist in the design of experiments through model prediction.

Richards *et al.* (1987) suggested that radar backscatter modelling can be viewed from three different positions. The first is based on an analytical framework in which models are derived upon electromagnetic theory and well known physical expressions. However, it must be made clear what assumptions are made about this theoretical approach when geometrical surfaces represent the actual physical structure. The second approach consists of regressing preconceived mathematical expressions to backscatter data. A problem with this empirical approach is that it does not explain specific surface medium-energy interactions merely that the two parameters may have something in common. The third approach would be to consider the system under study to be represented by a completely unrelated system but which behaves in a similar manner. This approach has been used to model backscattering from crops by adopting a cloud model (Attema and Ulaby 1978). These models are sometimes referred to as conceptual.

The selection of a theoretical model rather than a regression model in this study was done to firstly, test how well theoretical models could be calibrated in this desert environment. Second, due to the logistics of the data collection campaign and the limitations on the numbers of people in the field an empirical model would have been ineffective. Empirical models are available, such as the one developed by Oh *et al.* (1992), based on a limited data set and reducing the numbers of parameters of interest to the standard deviation of surface height, wave number and the relative dielectric constant. Another empirical model (Deroin *et al.* 1997) interprets relationships between backscatter and arid land surface roughness. Empirical models often utilise multi-polarisation or -frequency data that are not available in this study. An example of such a model, with a particular focus on measuring soil moisture, is presented by Dubois *et al.* (1995).

As outlined in Section 2.1.2 the incident radar energy is either scattered at the surface or within the upper surface volume. Accounting for the general availability of scattering models and the complex nature of volume scattering, the models used in this study account for surface scattering only. In this study, we accept that volume scattering is an important process, especially in areas of low soil moisture (Le Toan *et al.* 1994), but

only the processes of surface scattering and the modelling of such phenomena are examined here.

2.6.1 A brief review of microwave modelling

The earliest models of scattering were based on surfaces comprising many point scatterers, often spherical in nature. For example, Clapp (1946) analysed how the backscatter coefficient was influenced by the incidence angle for such a surface. Other approaches used facets. This involved approximating the surface through a number of small planar facets, each of them tangential to the actual surface. This idea was developed further with the introduction of curved facets.

Among the many surface scattering theories, the Kirchoff or Physical Optics formulation is one of the most widely used (Beckmann and Spizzichino 1963). The basic assumption of the Kirchoff method is that, at any point on the surface, the total radar field can be computed as if the incident wave is impinging upon an infinite plane tangent to the point (Ulaby *et al.* 1982). The Kirchoff method is applicable to surfaces whose average horizontal dimension is large compared with the incident wavelength and has gentle undulations. Two types of approximation were considered. Firstly, for surfaces with large standard deviations of surface height, a stationary phase approximation (meaning that scattering can only occur along directions for which there are specular points on the surface) was used (Wu and Fung 1972). A geometrical optics (GO) solution is used in this case. Secondly, for surfaces with small slopes and a small to medium standard deviation of surface height, a scalar approximation is used. In this case, a physical optics (PO) or small perturbation (SP) solution is considered. The two approximations are used in this study as they give a simplified appreciation of the scattering processes that are occurring. The limitations of the Kirchoff method are highlighted by specific regions of validity based on the roughness of the surface compared to the wavelength of the incident radar energy.

These validity conditions and model derivations are discussed in the following subsection, but it should be noted here that there were large gaps where surfaces with

certain roughness parameters did not conform to the validation criteria of the Kirchhoff scattering model. It was the occurrence of these gaps, where the scattering processes could not be resolved, that prompted the search for a more complex scattering model.

The integral equation model (IEM) was developed by Fung *et al.* (1992) and is also described by Fung (1994). The model is expected to be applicable to a wide range of roughness scales. This is achieved by computing terms for both single and multiple scattering elements. When surface roughness is large but the surface slope is small, only the single scattering term corresponding to the standard Kirchhoff model is significant. If the surface slope is large then multiple scattering becomes important and needs to be accounted for. Because the model is an integrative iteration of the Kirchhoff method, reduction to single scattering terms yield components of the Kirchhoff method: first-order solutions of the geometric optics (GO), small perturbation (SP) and second-order perturbation model for slightly rough surfaces. The validation ranges in terms of surface roughness are significantly increased. Figure 2.16 shows the validity conditions of the IEM, compared to the first-order small perturbation model (SPM) and Kirchhoff approximations.

In Chapter 6, there are detailed examples showing where these models have been utilised in land surface, remote sensing applications. It is the purpose of this section to explain the background to the models, derive them mathematically and to discuss their regions of validity.

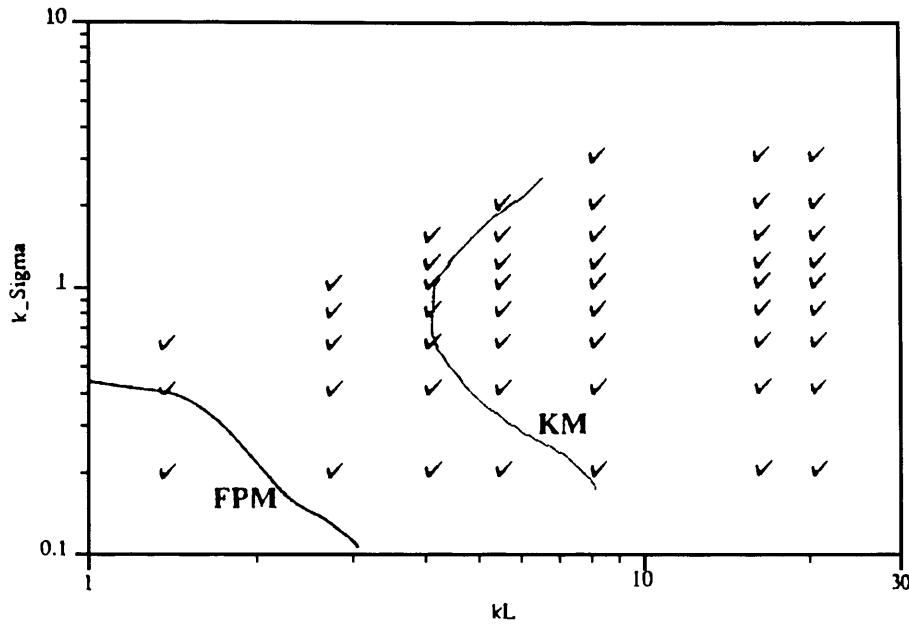


Figure 2.16. Validity ranges for the integral equation model (tick points that have been confirmed by experiment), first-order small perturbation model (FPM) and Kirchhoff model (KM) plotted in the standard deviation of surface height (Σ) - correlation length (L) feature space, k is the wavenumber (Fung et al. 1992).

2.6.2 Model derivations, assumptions and ranges of validity

The models described here estimate the backscatter coefficient of a random, distributed target. They are a function of sensor characteristics (polarisation, incidence angle, wavelength) and surface characteristics (roughness, dielectric properties). Each of the models make generalisations about the interactions that occur at the Earth's surface and the nature of the scattering as outlined in previous sections. In some cases further assumptions were made. The models can be divided into two sub-groups. The first contains the classical Kirchhoff (comprising the geometrical optics GO, and physical optics PO) and small perturbation (SP) models. The second contains the integral equation model.

2.6.2.1 Kirchhoff and small perturbation models of surface scattering

The selection of the Kirchhoff approach adopted (either a stationary phase or a scalar approximation) depends on the relative roughness of the target surface. The Kirchhoff approach is only valid for like-polarised predictions as it is a first order solution. The physical optics solution is applicable to surfaces with gentle undulations, and whose non-coherent backscattering coefficient is given by:

$$\sigma_{ppn}^{\circ}(\theta) = 2k^2 \cos^2 \theta \Gamma_p(\theta) \exp[-(2k\sigma \cos \theta)^2] \cdot \sum_{n=1}^{\infty} [(4k^2 \sigma^2 \cos^2 \theta)^n / n!] \cdot \int_0^{\infty} \rho^n(\xi) J_0(2k\xi \sin \theta) \xi d\xi \quad (2.16)$$

where, σ_{ppn}° is the non-coherent like-polarised backscattering coefficient,

θ is the incidence angle, σ is the standard deviation of surface height,

k is the wavenumber $= 2\pi/\lambda$ (λ is the wavelength),

$\rho^n(\xi)$ is the autocorrelation function for the incoherent scattering component n ,

$J_0(\)$ is the zeroth-order Bessel function of the first kind, and

$$\Gamma_p(\theta) = \text{Fresnel reflectivity} = |R_{pp}(\theta)|^2 \quad (2.17)$$

As the coherent backscattering term is only important at near nadir incident angles then the total backscattering coefficient approximates Equation 2.16.

For rougher surfaces whose backscattering coefficient remains almost independent of the incidence angle at angles near nadir, the geometrical optics solution of the Kirchhoff method under the stationary phase approximation is more suitable. It is stated in Ulaby *et al.* (1986), that, as the standard deviation of surface height usually is such that $k\sigma$ is of the order of unity, then the coherent term is once again not important.

Hence, the total backscattering coefficient approximates the non-coherent term and is given by:

$$\sigma_{ppn}^{\circ}(\theta) = \frac{\Gamma(0) \exp(-\tan^2 \theta / 2m^2)}{2m^2 \cos^4 \theta} \quad (2.18)$$

where, m is the RMS slope (calculated by dividing the standard deviation of surface height by the correlation length). The value m is also dependent on the autocorrelation function. $\Gamma(0)$ is the Fresnel reflectivity at normal incidences.

The validity conditions of these Kirchoff approximations are determined by the assumption that plane-boundary reflection occurs at every point on the surface (Ulaby *et al.* 1982). The surface horizontal scale roughness (l) must be larger than the wavelength. Furthermore, the vertical scale of surface roughness must be small enough that the average radius of curvature is larger than the wavelength. These restrictions can be summarised as:

$$\begin{aligned} kl &> 6 \\ l^2 &> 2.76\sigma\lambda \end{aligned} \quad (2.19)$$

Additional conditions are imposed for the geometrical optics approximation to be valid (Equation 2.20) and for the physical optics model to be more accurate (Equation 2.21):

$$(2k\sigma \cos \theta)^2 > 10 \quad (2.20)$$

$$m < 0.25 \quad (2.21)$$

For conditions where $kl < 6$ and the surface roughness is very slight, the small perturbation model introduced in the previous section may be used. The expression for the non-coherent backscatter coefficient is given by:

$$\sigma_{ppn}^{\circ}(\theta) = 8k^4 \sigma^2 \cos^4 \theta |\alpha_{pp}(\theta)|^2 W(2k \sin \theta) \quad (2.22)$$

where,

$$\alpha_v(\theta) = (\varepsilon_s - 1) \frac{\sin^2 \theta - \varepsilon_s (1 + \sin^2 \theta)}{[\varepsilon_s \cos \theta + (\varepsilon_s - \sin^2 \theta)^{1/2}]^2} \quad (2.23)$$

and, p is the polarisation and equals vertical or horizontal,

ε_s is the permittivity of the surface,

$W(\)$ is the normalised roughness spectrum, i.e. the Bessel transform of the correlation function $\rho(\xi)$, evaluated at the surface wave number of $2k \sin \theta$.

For a Gaussian correlation function (which is assumed for the Kirchhoff and perturbation models), given by $\rho(\xi) = \exp(-\xi^2 / l^2)$, the normalised roughness spectrum is given by:

$$W(2k \sin \theta) = \frac{1}{2} l^2 \exp[-(kl \sin \theta)^2] \quad (2.24)$$

The validity conditions for the small perturbation method are given where the standard deviation of surface height is very much less than the wavelength ($\leq 5\%$) and the average surface slope is less than or equal to the surface standard deviation multiplied by the wavenumber.

Mathematically this is expressed as:

$$\begin{aligned} k\sigma &< 0.3 \\ m &< 0.3 \end{aligned} \quad (2.25)$$

In Section 6.3 the validity ranges are plotted with corresponding points of surface roughness that have been estimated from field measurements. The reasons why these models are, in most cases, invalid for natural desert surfaces are discussed.

The models were adapted from the Michigan microwave canopy scattering (MIMICS) model (Ulaby *et al.* 1990, McDonald and Ulaby 1993). Individual components of the scattering model, if not required (e.g. branches, trunks and leaves), were flagged to zero and removed from the scattering simulation. The code was written in Fortran 77 programming language and was compiled on the University of Leicester UNIX system; processing time was very quick. The inputs to the model are the soil standard deviation of surface height (cm), soil correlation length (cm), volumetric soil moisture (m^3 water m^{-3} soil) and soil type. The two latter parameters are expressed as a relative dielectric constant through the empirical relationships derived by Hallikainen *et al.* (1985) given in Equation 2.10. The model is independent of soil temperature.

2.6.2.2 The integral equation model (IEM) of surface scattering

The complex version of the IEM presented by Fung *et al.* (1992) and Fung (1994) accounts for a wide range of surface roughness and radar frequencies. For this purpose, an approximate solution is used (Altese *et al.* 1996). The limitation on this approximation is that the standard deviation of the surface height times the wavenumber must be less than three ($k\sigma < 3$). Two further assumptions are made. Firstly, that only the real part of complex dielectric component is used; Sreenivas *et al.* (1995) state that this is a reasonable approach. Secondly, that the autocorrelation function is assumed isotropic and is explained by either a Gaussian or an exponential function (Section 5.3.2.6) (Su and Troch 1996). The model is written in C programming language and was compiled on the University of Leicester UNIX system, processing time was again very quick. The specified dielectric constant of the surface was calculated using the empirical equations given by Hallikainen *et al.* (1985) (Equation 2.10).

The backscatter coefficient, for any polarisation combination is given by Altese *et al.* (1996):

$$\sigma_{pq}^{\circ} = \frac{k^2}{2} \exp(-2k_z^2 \sigma^2) \sum_{n=1}^{\infty} \sigma^{2n} |I_{pq}^n|^2 \frac{W^n(-2k_x, 0)}{n!} \quad (2.26)$$

where,

$$I_{pq}^n = (2k_z)^n f_{pq} \exp(-\sigma^2 k_z^2) + k_z^n [F_{pq}(-k_x, 0) + F_{pq}(k_x, 0)] / 2$$

p, q = vertical (v) or horizontal (h) polarisation,

$$f_{vv} = 2R_{\perp} / \cos \theta$$

$$f_{hh} = -(2R_{\perp} / \cos \theta)$$

$$F_{vv}(-k_x, 0) + F_{vv}(k_x, 0) = \frac{2 \sin^2 \theta (1 + R_{\perp})^2}{\cos \theta} \cdot \left[\left(1 - \frac{1}{\varepsilon}\right) + \frac{\mu \varepsilon - \sin^2 \theta - \varepsilon \cos^2 \theta}{\varepsilon^2 \cos^2 \theta} \right]$$

$$F_{hh}(-k_x, 0) + F_{hh}(k_x, 0) = \frac{2 \sin^2 \theta (1 + R_{\perp})^2}{\cos \theta} \cdot \left[\left(1 - \frac{1}{\mu}\right) + \frac{\mu \varepsilon - \sin^2 \theta - \mu \cos^2 \theta}{\mu^2 \cos^2 \theta} \right]$$

R_{\perp}, R_{\parallel} = Fresnel reflection coefficients, for vertical and horizontal polarisations, respectively at θ angle of incidence in the low frequency region or slightly rough surfaces,

$$R_{\perp} = \frac{\varepsilon \cos \theta - \sqrt{\varepsilon - \sin^2 \theta}}{\varepsilon \cos \theta + \sqrt{\varepsilon - \sin^2 \theta}}$$

$$R_{\parallel} = \frac{\cos \theta - \sqrt{\varepsilon - \sin^2 \theta}}{\cos \theta + \sqrt{\varepsilon - \sin^2 \theta}}$$

(2.27)

and at normal incidence in the high frequency (frequency > 4.2 GHz) region,

$$R_{\perp, \parallel}(0) = \frac{1 - \sqrt{\varepsilon}}{1 + \sqrt{\varepsilon}}; \quad (2.28)$$

where, ε = dielectric constant,

μ = magnetic permeability,

$k_z = k \cos \theta$,

$k_x = k \sin \theta$,

θ = incidence angle,

$W^{(n)}(u, v)$ = roughness spectrum of the surface related to the n th power of the surface correlation function $\rho(\xi, \zeta)$ by the Fourier transform given by:

$$W^{(2n)}(u, v) = \frac{1}{2\pi} \int_{-\infty}^{+\infty} \rho^n(\xi, \zeta) \exp(-ju\xi - jv\zeta) d\xi d\zeta \quad (2.29)$$

In Section 6.3 the validity ranges are also plotted with corresponding points of surface roughness that have been derived from data collected in the field. Comparison with the validation criteria of the Kirchhoff and small perturbation methods shows that the scope for using the integral equation model is much greater.

2.6.3 Assumptions made concerning the nature of desert surfaces

The models described above predict the radar backscatter response from soil surfaces where surface scattering is the dominant scattering process, as opposed to volume scattering processes (Section 1.3.1). With reference to the desert surfaces mentioned in Section 1.3, two further issues are of concern.

- (i) Using the models described above, can the scattering pattern be modelled over all non-soil covered surfaces, such as the basalt and desert pavement surfaces that occupy large parts of the region?
- (ii) Is the vegetation at the regional and local scales dense enough to influence the backscatter signal in deserts?

2.6.3.1 Modelling the non-soil surfaces

Two of the main land cover units, the basalt flows and desert pavements, cannot be accurately classified as soil surfaces. In common with all such stone surfaces, some soil was exposed (as much as 60% of the ground surface, Section 4.6) but it was usually overlain by stones, rocks or boulders that increased the surface roughness significantly. Ideally these surfaces would be modelled as a two-component dielectric surface, comprising a rough, randomly distributed layer of rocks that have dielectric properties which are approximately constant and could be estimated from Ulaby *et al.* (1990a) with an occasional gap revealing a smooth, soil dielectric with known characteristics. Unfortunately, no such model was available, although an approach to the problem of simulating the scattering from an inhomogeneous surface is given by Sarabandi *et al.* (1996), the calculations involved are beyond the scope of this study. Therefore it was assumed that the basalt surfaces were comprised of randomly distributed, sometimes isolated clumps of soil medium that were surrounded by a flat region of the same soil medium. The assumption was also used for the stone pavement (*hammada*), the clumps and overall surface roughness being smaller.

2.6.3.2 The influence of dryland vegetation

Section 4.8 gives vegetation cover estimates for the selected study sites in the eastern Badia of Jordan. In brief, percentage cover in any of the vegetated study sites did not exceed 10%. Vegetation decreases the sensitivity of the backscatter coefficient to soil moisture, due to increased scattering and attenuation of the signal. Dobson *et al.* (1992) stated that the presence of a sparse vegetation layer would have little influence on the backscatter coefficient, attenuating the backscatter by less than 0.2 dB, with the soil moisture and roughness parameters still having the dominant influence on the backscatter signal. Mo *et al.* (1984) found that the scattering component from vegetation covered soils only becomes dominant at incidence angles $> 30^\circ$, i.e. greater than that for the ERS SAR system. Other studies in drylands (e.g. Ridley *et al.* 1996) have considered

scattering from the vegetation component using a cloud model of randomly oriented disks and cylinders (Chuah and Kung 1994). The combination of model availability and complexity with the reported low vegetation covers estimated, has led to the effects of vegetation to be assumed negligible and therefore, vegetation was not considered in this study. It is acknowledged that volume scattering may be an important mechanism in dryland regions and further work, beyond this study, needs to clarify the scattering responses of dryland vegetation.

3. Multitemporal SAR Image Interpretation

Observations made of the temporal behaviour of the backscatter coefficient from ERS SAR data are interpreted in this chapter. These interpretations are based on information related to soil moisture, surface types and lithologies. They enable changes in surface topography (roughness, of the order of cm's), that occur during the year and between years, and soil moisture and standing water to be monitored. Section 3.1 introduces the methods used, discusses what surface parameters may be distinguishable from the imagery, and also examines the geomorphological processes that are responsible for changes in surface topography. Section 3.2 looks at the specific land surface units that characterise the eastern Badia of Jordan, where SAR has been able to identify features related to dryland environmental processes and how these are interpreted. Intensity images, both single band and multitemporal colour composites, are presented. The importance of monitoring these surfaces lies in the implications these surfaces have for the possible extraction of soil moisture information based on these observations. The data indicate a poor correlation between the backscatter coefficients derived from the ERS-1 and the ERS-2 SAR instruments. Section 3.3 discusses the differences between these data and presents a solution to overcome the problem.

3.1 Introduction

In the previous chapter, the potential of using a fixed-polarisation and a fixed-wavelength system for modelling is limited due to the number of parameters influencing the backscatter coefficient. As other radar data were not available for use within this project, multitemporal data analysis of ERS SAR was conducted to try and understand the causes of any fluctuations in the backscatter signal. Certain assumptions were made concerning the nature of the SAR system and processing factors. It was important that as many of the parameters that influence the backscatter coefficient (described in Chapter 2) were kept constant. These parameters include the local incidence angle at each site, SAR orbit geometry, and image processing and calibration.

In Chapter 1, it was shown that remote sensing methods could be utilised for a wide range of applications in dryland regions. Geomorphological processes in dryland regions occur over a range of spatial and temporal scales (Millington *et al.* 1995) and it is important to establish which processes are occurring over the temporal resolution of satellite data collection. For example, Archer (1995) distinguished seasonal and episodic changes in multitemporal ERS SAR imagery of a salt playa in Tunisia. Seasonal changes were caused by the development of salt crusts in response to fluctuations in rainfall, soil moisture and evaporation. Episodic changes are caused by the formation of ephemeral lakes, the movement of water through ephemeral channels, and the development of temporary surface crusts. Similar seasonal and episodic processes may be applicable to the drylands studied in Jordan.

The aim of multitemporal backscatter coefficient analysis is often to relate empirically changes in the backscatter coefficient with changes in the parameter of interest on the ground surface. Cihlar *et al.* (1992) established estimates of the relative mean backscatter values and the annual backscatter range for a range of different surfaces. The data was obtained by C-band SAR over a test site in Ottawa. When these estimates are plotted against each other the different land covers were distinguished. Surfaces that appeared relatively radiometrically stable were lake bodies, urban areas and water courses. Surfaces with moderate stability were coniferous and deciduous forests, and hay fields. Corn fields and marshes displayed high annual variations in backscatter values. Multitemporal change detection techniques with SAR are hindered by the speckle phenomena. However, by increasing the equivalent number of looks, either by averaging or a speckle reduction algorithm, the influences of speckle on the backscatter coefficient is reduced. Other change detection techniques are discussed by Rignot and van Zyl (1993). Through multitemporal methods it is possible to assign a temporal profile (or signature) to different land covers, which can help to interpret, and even classify, single polarisation and frequency radar images. Examples of backscatter signatures of commonly found crops are given by Borgeaud *et al.* (1994). The temporal signatures of dryland surfaces situated in the eastern Badia region of Jordan are discussed in the following section.

Processes that may induce a change in the surface topographic properties also need to be considered. These processes range over a time scale from thousands of years, such as rock weathering, to days and weeks, for example the growth of salt crystals in a saline pan. It is the processes that are likely to influence surface roughness over a time scale of weeks to a few years that this study is most interested in. Surface cracking is one such process that has been observed in the Jordan Badia. The cracks are formed by the desiccation and subsequent cracking of soils and crusts rich in swelling clays, such as montmorillonite. These variations are associated with both diurnal and seasonal changes in temperature and moisture. Extensive cracking and thrusting of surface soils and sediments are associated with the influx of salt-rich ground water (Dixon, 1994).

The action of strong winds on exposed desert surfaces which have weathered material available to be entrained and transported will result in topographic surface changes. The amount of erosion, removal and deposition of sediment by the wind depends on the texture of the surface, vegetation cover, degree of cohesion and crusting and the nature of air flow across the surface (Lancaster and Nickling, 1994). The trapping of moving grains of sand by vegetation leads to hummocks being formed (known as *nebkhas*) around the base of the vegetation increasing the roughness of the surface. Subsequently, during high wind energy events this sand is removed. In the Jordan Badia, only a small region in the south-east is covered by a blanket of sand. The sand layer reaches up to 5 cm in depth and provides protection, against evaporation, to the finer layer below. Vegetation is present, in relative terms (< 10% cover), and hummocks of sand (< 5 cm tall at the highest point) form around the base of the plants. With such diverse land cover types in the Jordan Badia, monitoring the effects of wind-induced surface roughness change is difficult. No studies have been conducted into wind erosion in the study area. Another processes that may induce surface change is erosion by surface water during flood events. This process can lead to a flattening of the surface by the action of flowing water and rill and gullies where flows are concentrated. Human modification of the natural landscape can also lead to changes in topographic roughness. Any kind of development needs to be monitored, especially agriculture which can lead to very significant changes of surface roughness over short time scales, e.g. ploughing.

3.2 Multitemporal backscatter variation of desert surfaces

The desert surfaces of the Jordan Badia provide a range of land cover types. These different types of land cover are very interesting as, in geomorphic terms, they may indicate various stages of landscape evolution and indicate different levels of susceptibility to environmental change. They can be divided into four major land surface units: basalt lava flows, desert stone pavement (*hammada*), *marab* and *qa'a*. Sections 1.1 and 1.3 give detailed explanations of the geomorphological characteristics of these surfaces. The sites referred to in the following section can be located on Figure 3.1. It is important to derive temporal profiles for each of these land surfaces and interpret the profiles in terms of geomorphological or hydrological change. Furthermore, from these temporal profiles, it is possible to gain a first indication of the likelihood of retrieving information on soil moisture from ERS SAR data. A full ERS SAR PRI amplitude scene of the northern section of the Programme area is shown in Figure 3.2. The image was acquired on the 7th March 1996 and shows the town of Safawi and locations of important land surface types. The image covers 100 by 100 km.

To aid our interpretation of the temporal variation in the backscatter coefficients, precipitation data collected at four locations in the study area are displayed in Figure 3.3. Monthly precipitation totals were obtained from two permanent weather stations located at Safawi (F0002-H5 evaporation station) and Azraq (F0009 evaporation station). This information was obtained from the Water Authority of Jordan (see Section 4.7). Further precipitation data from weather stations in the north of the study area located at Menara (32.20° N, 36.75° E, from October 1994 to August 1996) and north of *Marab Salma* (32.44° N and 37.27° E, from December 1995 to October 1996). Further analysis of the precipitation and other climate data is presented in Section 4.7. Reference is made to Figure 3.3 in the following sections. It is interesting to observe that records show the winters of 1994 and 1996 were wetter on average, eventually producing extensive grass growth. This is reflected in the distribution of the rainfall at the Safawi and Azraq stations. The winter of 1995 shows very little rainfall recorded, except at the higher, wetter Menara site.

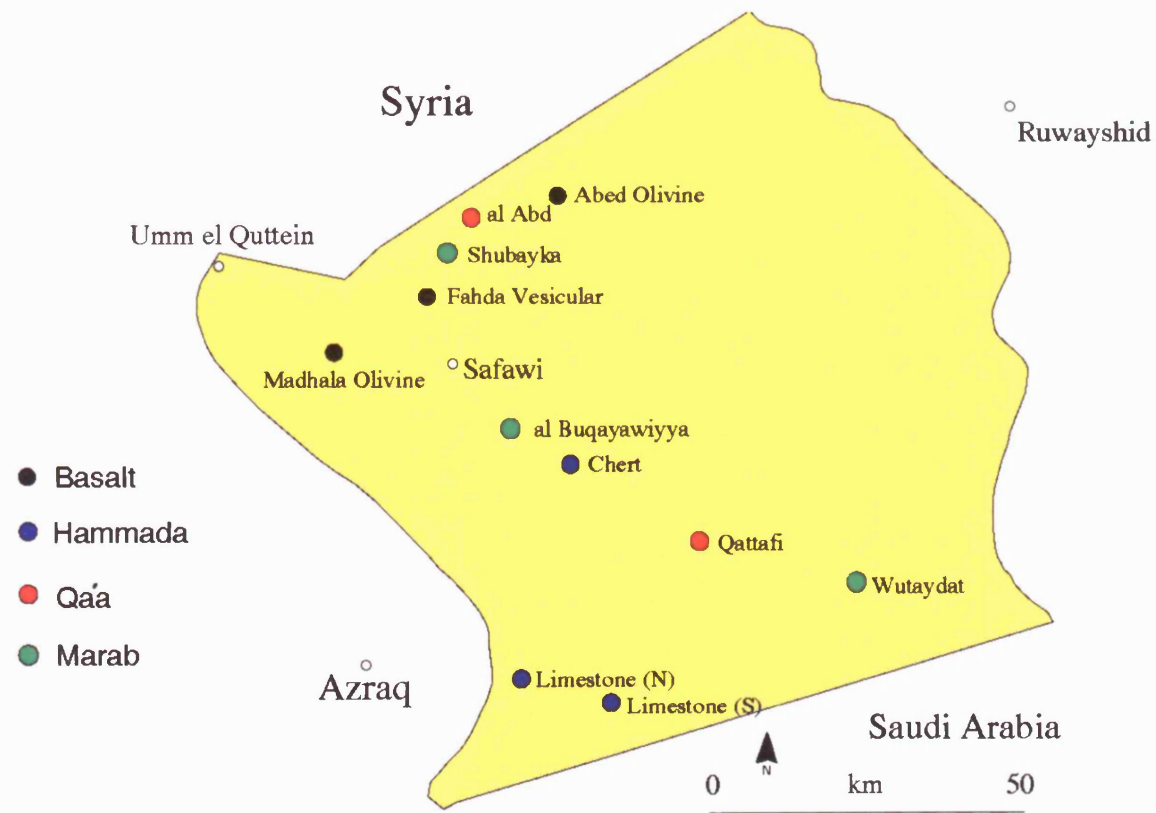
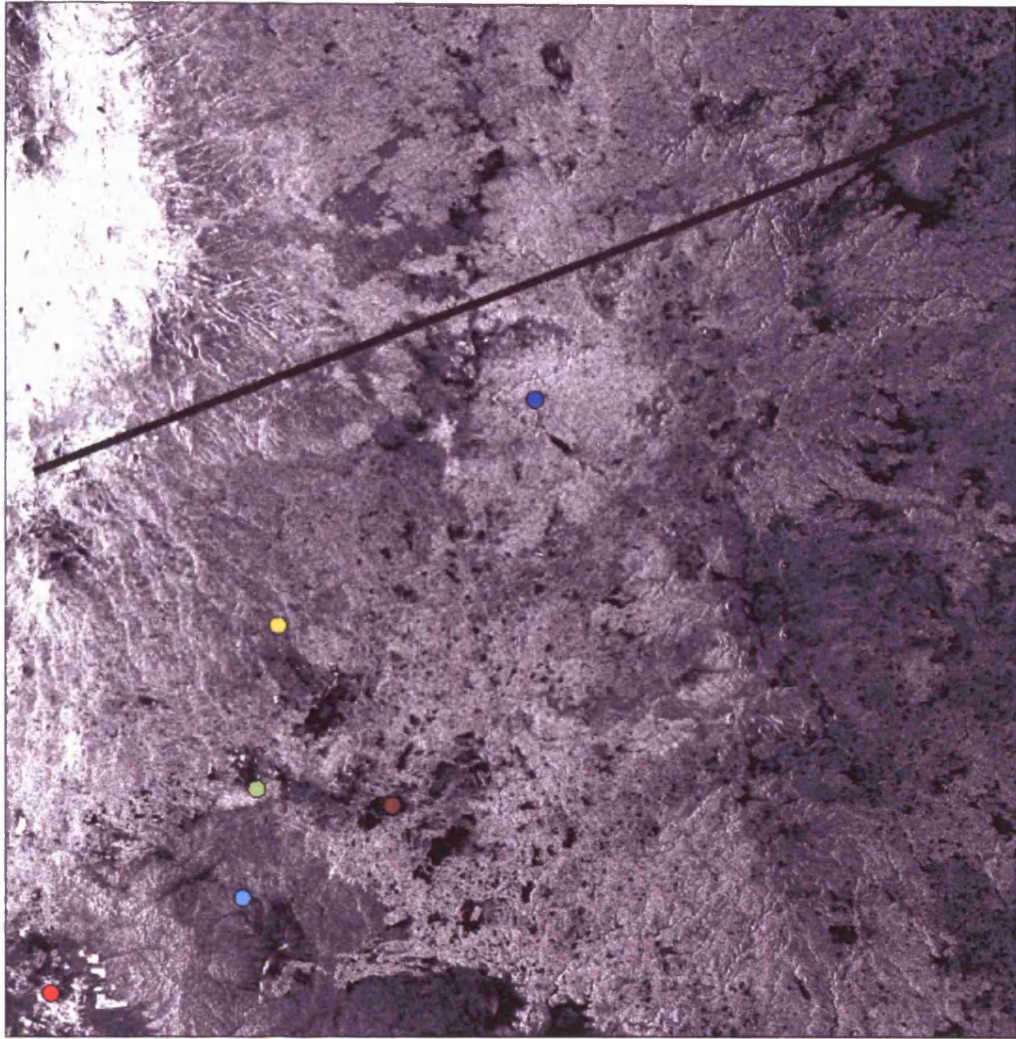


Figure 3.1. Location of the study sites analysed in Chapter 3. Each site is displayed as a colour representing the four main land cover units: basalt, hammada, qa'a and marab.



Key to figure:

- | | |
|--------------------------------|------------------|
| ● Fields to the north of Azraq | ● Safawi town |
| ● Qa'a surface | ● Basalt surface |
| ● Qa'a al Buqayawiyya (Marab) | |
| ● Chert <i>hammada</i> surface | |



Figure 3.2. ERS-1 SAR PRI full scene of the northern section of the Programme area. The image was acquired on the 7th March 1996 and covers 100 by 100 km. The corner co-ordinates of the image are: 36.9157 °E, 31.786 °N (bottom-left); 37.9497 °E, 31.9695 °N (bottom-right); 37.7300 °E, 32.8739 °N (top-right); 36.6845 °E, 32.6902 °N (top-left). The solid line indicates the approximate position of the border with Syria (the northern border of the project area).

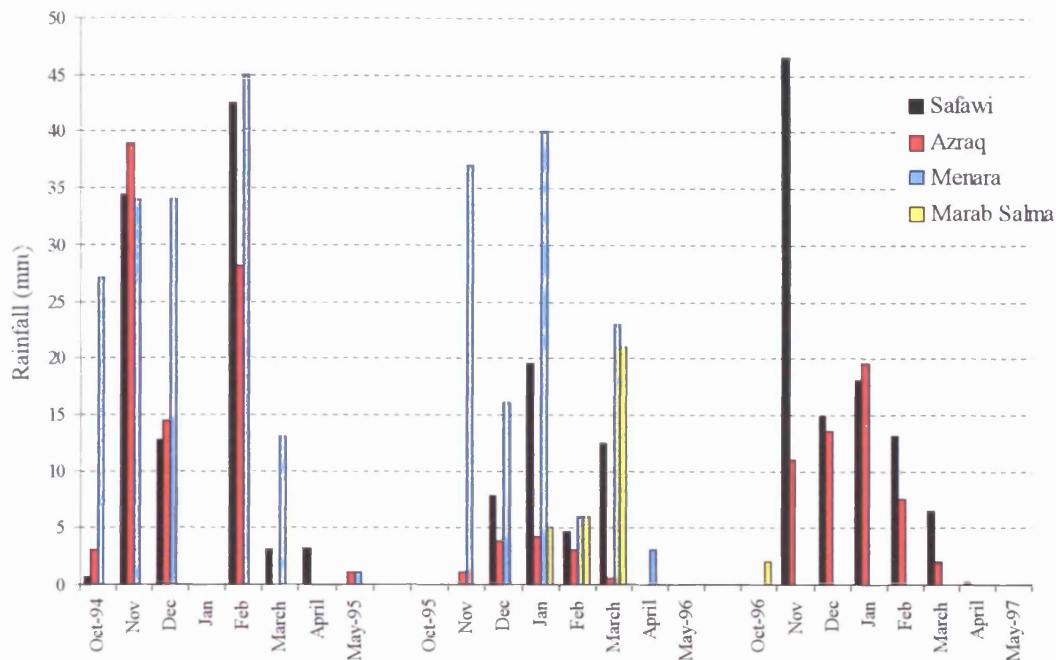


Figure 3.3. Monthly rainfall totals for Safawi, Azraq, Menara and Marab Salma precipitation stations. Please note boundaries of data collection listed in the text.

3.2.1 Basalt and desert stone surfaces

3.2.1.1 Basalt surfaces

Greater than half of the study region is covered with a regolith of stones of varying size and lithology. Because of the dependency of the backscatter coefficient on surface roughness and dielectric properties, regions of relatively recent volcanic activity can be distinguished. The basaltic lava flows can be distinguished (i) between each other; and (ii) from desert stone pavement, as the latter comprise smaller, more angular fragments of basalt or chert. The distinction between lava flows is caused by a number of factors including different ages of basalt, variations in the exposure time weathering regimes and basalt mineralogy. The temporal profiles of three basalt flows are shown in Figure 3.4a. In Figure 3.4b error bars (± 1 standard error of estimation) are displayed for the same data.

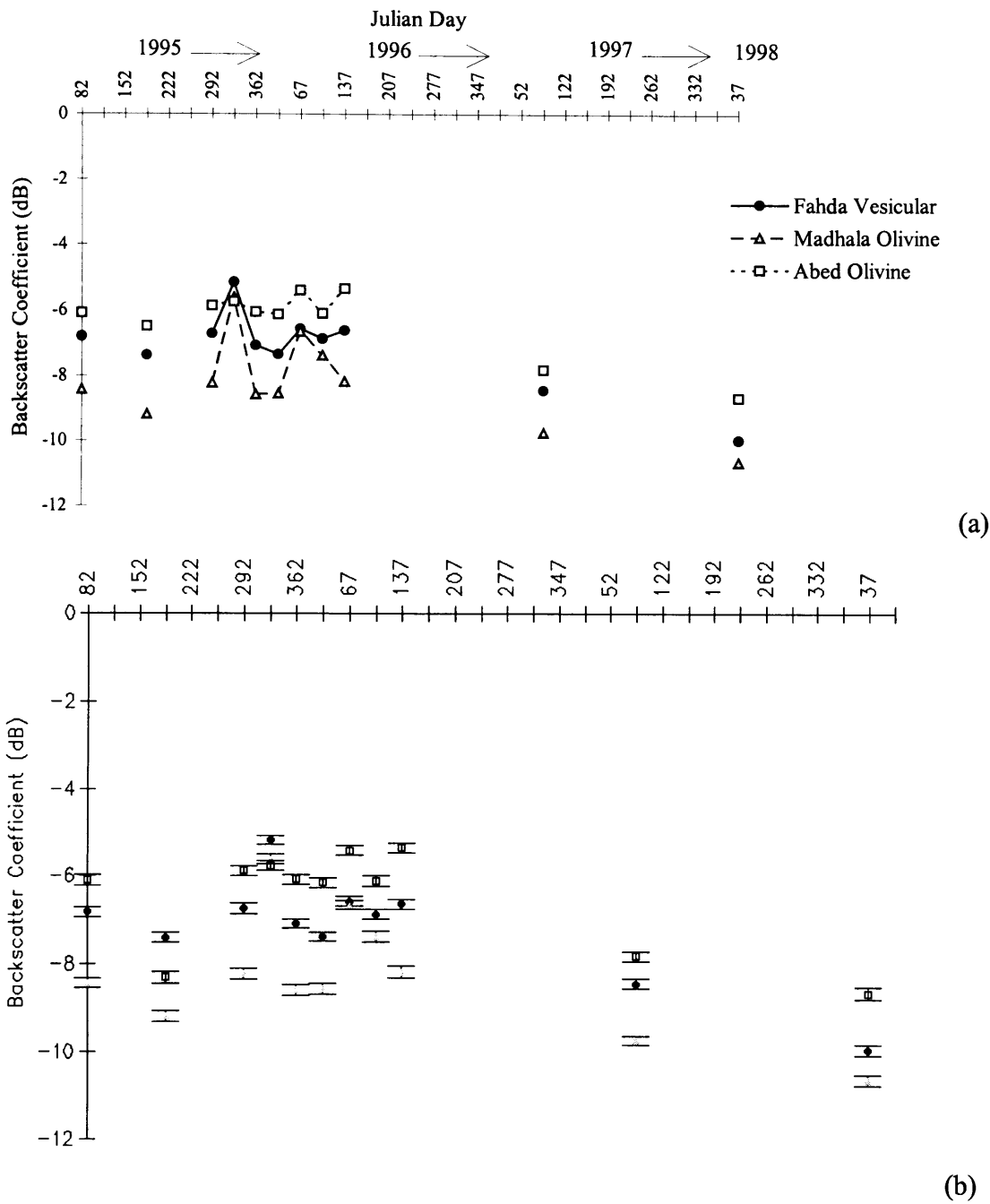


Figure 3.4. Multitemporal backscatter variation for three basalt formations located within the eastern Badia of Jordan (a) and associated error (1 standard error of estimation) bar (b). The temporal scale is expressed as a Julian Day, corresponding to the day of the year. The backscatter coefficients are calculated using the comprehensive equation given in Section 2.5. ERS-2 SAR measurements commenced in 1997 (day 87).

The Fahda Vesicular formation, the youngest flow (0.1 - 1.45 Ma.) is characterised by a rough, angular surface with little exposure of the underlying soil surface. The surface has a very rugged appearance (Ibrahim 1993). The Madhala Olivine Basalt formation, part of the Asfar group (2 - 3.5 Ma.) covers considerable areas in the north-west of the study region. This basalt is characterised by smaller stones, compared to other basalt flows, covering over 60% of the ground surface (Tansey *et al.* 1996). The Safawi Group, which dominates the region, contains the Abed Olivine Phyric formation, which is characterised by lighter colours, relatively low ground coverage of stones (approximately 50%) which are smooth and rounded. Detailed descriptions of these stone surfaces are given in Higgitt and Allison (1998) and Sections 4.1 and 4.6. The standard errors of estimation are of the order of ± 0.2 dB, due to the number of pixels that are used to derive the backscatter coefficient (500 pixels). The error interval for the estimate of the backscatter coefficient are similar to estimates for other desert surfaces studied in this project. Therefore, error bars are not displayed for temporal profiles of the remaining desert surfaces.

Close examination of Figure 3.4a indicates that these surfaces are relatively stable at microwave wavelengths. This makes sense when the time scale of observations and the time scale of the processes acting upon these surfaces are taken into account. It is very unlikely that significant changes in surface roughness would occur over these surfaces during the three years of radar observations. A rainfall event recorded at the Menara and Azraq stations, and also observed at *Qa'a al Buqayawiyya* (10 km south of Safawi), on the 23 November 1995 (Julian Day 327 in 1995) that must have deposited water onto the stone surfaces seems to have a small effect on the backscatter coefficient. A similar event occurred on the 7 March 1996 (Julian day 67) resulted in a similar response. This small increase, compared to other surfaces (as will be shown later in this chapter) may be due to any water deposited onto the boulders and surrounding soil either quickly draining off into the soil below or evaporating. On the basis of these findings a basalt surface, would make a good calibration surface for future microwave remote sensing missions. The second point to note is the distinction between formations. The mean and standard deviations of backscatter coefficients (derived from ERS-1 SAR data) for the three formations are; Fahda Vesicular, -6.74 and 0.66; Madhala Olivine, -7.86 and 1.12; Abed Olivine, -5.92 and 0.37. The estimates of the standard deviations are small when

compared to the errors in deriving the backscatter coefficient caused by system noise. This shows that the basalt formation possibly could be distinguished in terms of their backscatter signatures. The reasons why basalt surfaces can be distinguished appears to be mainly due to the roughness of the surface (Tansey *et al.* 1996). Derooin *et al.* (1997) established empirical relationships between the backscatter coefficient and maximum boulder height and standard deviation of surface height. These relationships are shown in Figure 3.5. They show that both parameters have a significant influence on the backscatter coefficient. Field measurements show that the average stone size of the Abed Olivine formation (refer to Table 4.6 for details) is significantly greater than for the other two formations and therefore would, according to Figure 3.5, yield a greater backscatter. The distinction between the Fahda Vesicular and Abed Olivine formations, essentially having the same average stone size properties, can possibly be attributed to differences in the stone coverage on the ground and stone angularity. The Fahda Vesicular formation has higher values for both of these parameters and therefore is likely to have a greater surface scattering component and, consequently, an increased backscatter return.

Furthermore, the magnitudes of the peak responses in backscatter are possibly dependent on the location and magnitude of the rainfall event. It appears that the more westerly the formation is located the greater the response of the backscatter coefficient to a rainfall event (Tansey *et al.* 1996). This is related to a rainfall gradient that exists both from west to east and north to south in the study area. In this example, the Madhala Olivine formation is located furthest west and the Abed Olivine formation located furthest east.

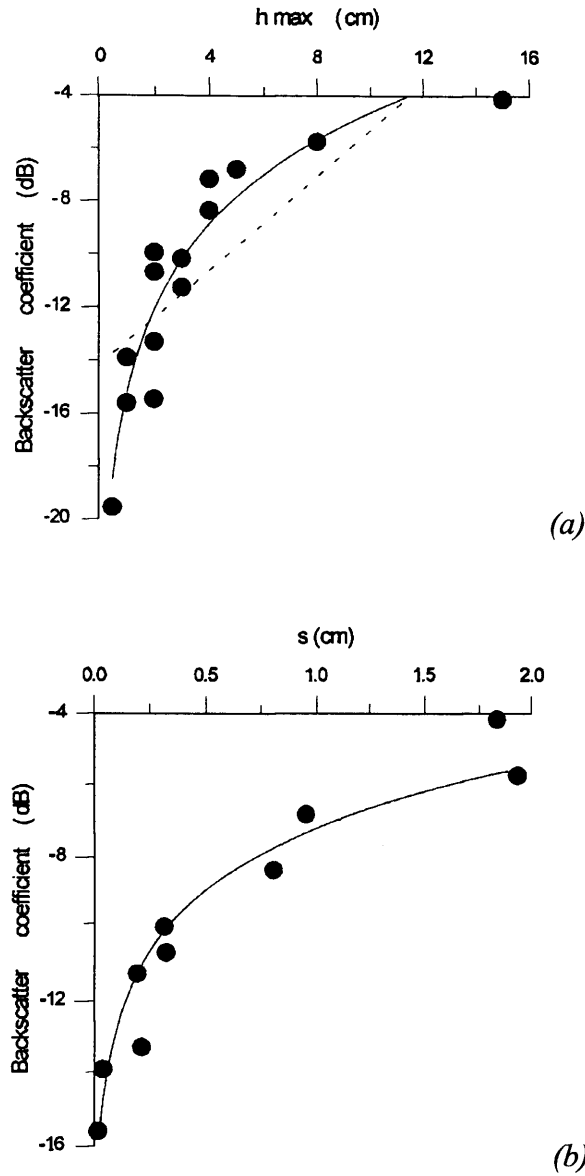


Figure 3.5. The relationships between the backscatter coefficient and (a) maximum height of rocks (h_{max}); and (b) the standard deviation of surface height (s) obtained empirically for arid land surfaces (Deroin et al. 1997).

A further interesting observation is the reduction in the estimate of the backscatter coefficient calculated from the ERS-2 SAR instrument compared to estimates from ERS-1 SAR. The values do not correspond well with the stability of measurements obtained from the ERS-1 SAR instrument. There are several reasons for this phenomenon which are discussed in more detail in the Section 3.3.

The ability of SAR to differentiate basalt flows of different ages is shown in Figure 3.6. Displayed is a subset of an image for the north-central part of the study area, acquired on the 23 March 1995. The basalt surfaces, which are strong scatterers, appear as white to light-grey regions on a grey-scale image (Figure 3.6). The boundaries of the basalt flows have been overlaid on the image. However, it is not just the small scale of roughness properties that enable basalt surfaces to be distinguished, but also the larger scale surface form and morphology and the landscape development within the basalt regolith (e.g. the presence or absence of small clay *qa'a* basins).

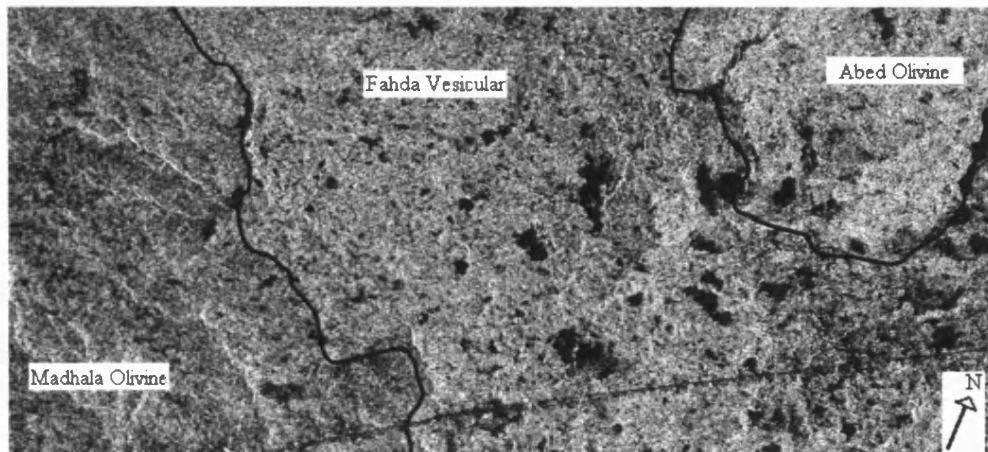


Figure 3.6. ERS-1 SAR intensity image (dB) of the north-central region of the study area. The image was acquired on the 23 March 1995. It demonstrates the ability of SAR to qualitatively distinguish between basalt flows, mainly due to the large-scale morphological features (qa'a). The image covers approximately 35 by 16 km. The approximate image corner co-ordinates are; 37.007° E, 32.323° N, top-left; 37.022° E, 32.203° N, bottom-left; 37.398° E, 32.245° N, bottom-right; 37.357° E, 32.384° N, top-right. The Safawi to Ruwayshid road is clearly seen in the bottom of the image.

Data on the physical properties of the basalt surfaces is provided in Table 1.1. The multitemporal characteristics of a basalt surface are shown in Figure 3.14. When displayed as a multitemporal false colour composite the basalt surfaces appear as bright, light-grey areas. This is caused by large amplitude coefficients and stable temporal characteristics.

3.2.1.2 Stone pavement (*hammada*) surfaces

The temporal signatures of desert stone pavements (*hammada*), which cover most of the southern part of the study area, are different from those of the basalt surfaces. In an ERS SAR intensity image they are displayed in mid-grey tones, indicating a reduction in the intensity of the return signal, compared to light grey tones for basalt surfaces. This is almost entirely due to the scattering interaction with less rough surfaces (desert stone pavements usually have a standard deviation of surface height < 1 cm, see Chapter 4). Three *hammada* sites were studied (Figure 3.1); the first is located south of Safawi (32.0031° N, 37.1210° E) lying on stone fragments of basalt and chert; the second and third are situated on limestone *hammadas*, east of Azraq (northern site (N), 31.7104° N, 36.9731° E and the southern site (S), 31.6412° N, 37.1638° E). The temporal profiles of these three stone pavement surfaces are shown in Figure 3.7. They are compared to the temporal profile of the Abed Olivine basalt surface.

The profiles of the *hammadas* show a reduction in the average backscatter coefficient compared to that of the Abed Olivine basalt surface. The temporal profiles of two of the *hammada* surfaces, the northern limestone site and the chert *hammada* display greater seasonal fluctuations in their backscatter responses than for the basalt surface and the southern limestone *hammada*. The observation of a stable temporal profile at the southern *hammada* site may be caused by a reduction in the amount of rainfall received at the southern boundary of the study area. Over a five year period, 1992/93 to 1996/97 the average rainfall at the Safawi and Azraq recording stations were 68.7 and 43.4 mm respectively (Water Authority of Jordan, 1998). As the backscatter coefficient is sensitive to surface moisture, the more arid the climate, the more stable the temporal profile would be. To support this theory, obvious peaks in the temporal signatures (1995 day 327 and 1996 day 67) are noted at the dates of known rainfall events (November 1995 and March 1996) discussed in the case of the basalt surfaces (Figure 3.3). The fluctuations are shown in this study to be caused by soil moisture changes (assuming radiometric calibration stability) because these surfaces are very stable with regard to changes in surface roughness.

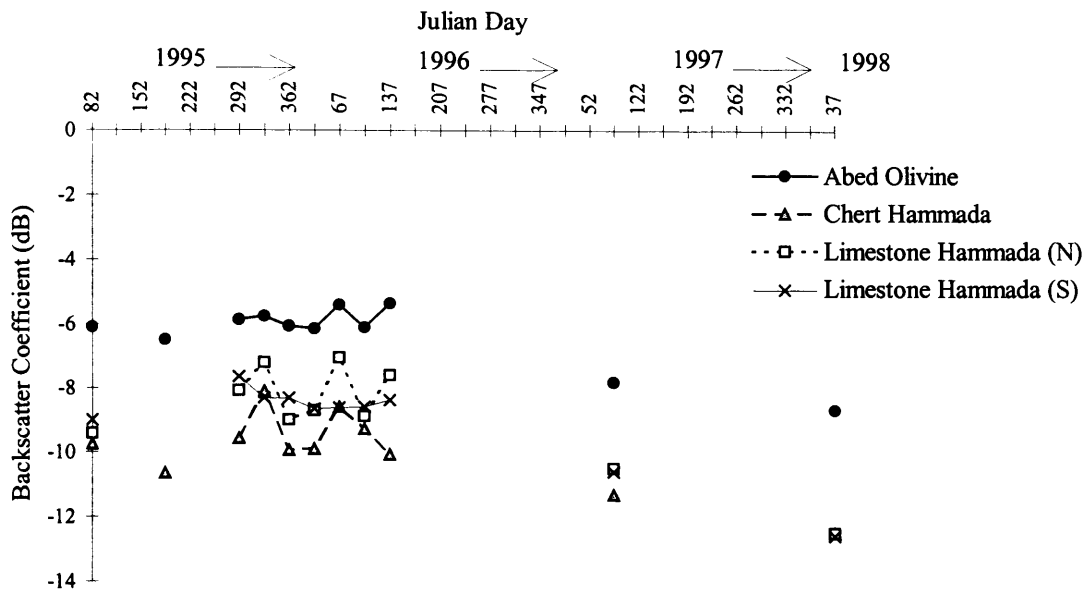


Figure 3.7. The temporal profiles of backscatter of the desert stone pavements (hammadas). Three hammada are shown, along with the temporal profile of the Abed Olivine basalt for comparison. Backscatter coefficients have been derived using the comprehensive equation.

The processes that lead to the development of these remarkably flat, smooth desert pavements have been investigated thoroughly by Cooke (1970) and McFadden *et al.* (1984, 1987) and have been discussed in Section 1.3.1. Due to the sharp precipitation gradient between the semi-arid north and central part of the study area and the very arid southern reaches, it is possible that rainfall events and high soil moisture levels recorded at sites in the north which are detected by SAR, do not fall and are not recorded in the south (Figure 3.3, Safawi and Azraq stations). This highlights the potential of SAR to map the limits of local precipitation events that have occurred prior to the overpass date.

The distinction between *hammada* and basalt surfaces can easily be made using a single intensity image. Figure 3.8 is an image sub-scene, which clearly shows the basalt boundary with a chert *hammada*. The basalt displays strong scattering properties, the *hammada* to the south displaying more moderate scattering. The darker areas within the image are small mudflats (*qa'a*) that are radiometrically smoother than their surroundings and hence have lower backscatter coefficients. A multitemporal image

(refer to Figure 3.14) displays *hammada* surfaces in subtle colours reflecting moderate fluctuations in the backscatter coefficient.

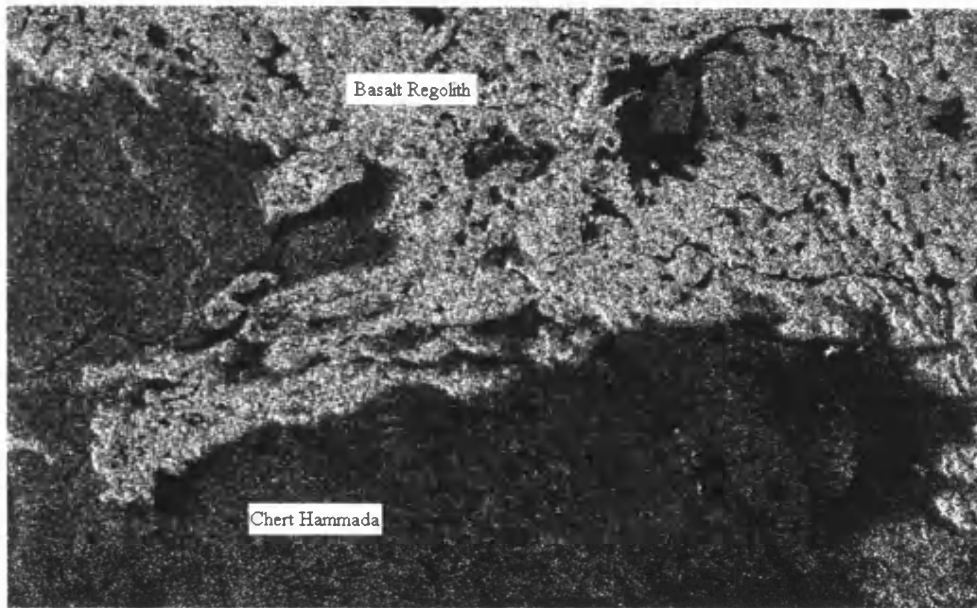


Figure 3.8. ERS-1 SAR image sub-scene of the central region of the study area. The image was acquired on the 6 July 1995 and is displayed as an intensity image. It demonstrates the ability of SAR to qualitatively distinguish between rough basalt surfaces and less rough desert pavements (hammada). The image covers approximately 19 by 12 km. The approximate image corner co-ordinates are; 37.232° E, 32.002° N, top-left; 37.446° E, 31.868° N, bottom-right; north is up.

3.2.2 Playa (qa'a) surfaces

Playa surfaces, also referred to as mud-pans or by the local name, *qa'a*, are extremely flat surfaces that are devoid of vegetation (Section 1.3.2). They are important in desert hydrological and geomorphological systems as they are stores of water and sediment. The sediments are characterised by high proportions (> 50%) of clay-size minerals that form a hard, compact surface layer. This impedes infiltration and, during periods of rainfall where the intensity of precipitation exceeds the infiltration rate, these surfaces become flooded. More importantly, *qa'a* also become flooded because they comprise

the low points in the regional drainage network. The texture of the sediments and the very low surface roughness signifies that the intensity of the backscattering component of the incident wave is small. However, as was noted in Figure 3.5, the backscatter coefficient is highly dependent on the surface roughness at RMS height values < 0.5 cm. Therefore, very small changes in surface roughness of the *qa'a* surfaces could yield large differences in the backscatter coefficient. The implications of these relationships have a significant bearing on the possibility of retrieving soil moisture information from these surfaces (Tansey and Millington, in press). The dependence of the backscatter coefficient to surface roughness changes may be too great to detect variations in the dielectric properties of the surface, even if roughness change in the order of millimetres occurred.

The temporal profiles of *qa'a* are characterised by a low average backscatter coefficient, normally less than -15 dB. Observations indicate that the average annual variations in the backscatter coefficient are different for the *qa'a* surfaces monitored in this study (Figure 3.9). The amount of variation in the backscatter coefficient is thought to be dependent on several factors, including the geographic location, surface sediment properties, seasonal roughness change characteristics, position within the hydrological system and the probability of flooding. The geographic location of the *qa'a* is also important when considering precipitation events as *qa'a* in the north and west will receive more precipitation (Chapter 1 and Figure 3.3). The clay mineralogy, comprising mainly the smectite group of clays formed as a result of basalt weathering, controls surface swelling and shrinking caused by repeated wetting and drying. These processes ultimately affect the surface roughness. Desiccation cracking, that often form natural polygons that range in size and scale, from centimetres to metres, are features that are relatively abundant on *qa'a* surfaces in the study region. Seasonal changes have been recorded in these. During wetter periods the clay minerals expand and desiccation cracking is almost absent. During dry periods significant cracking of the surface has been seen in response to mineral contractions.

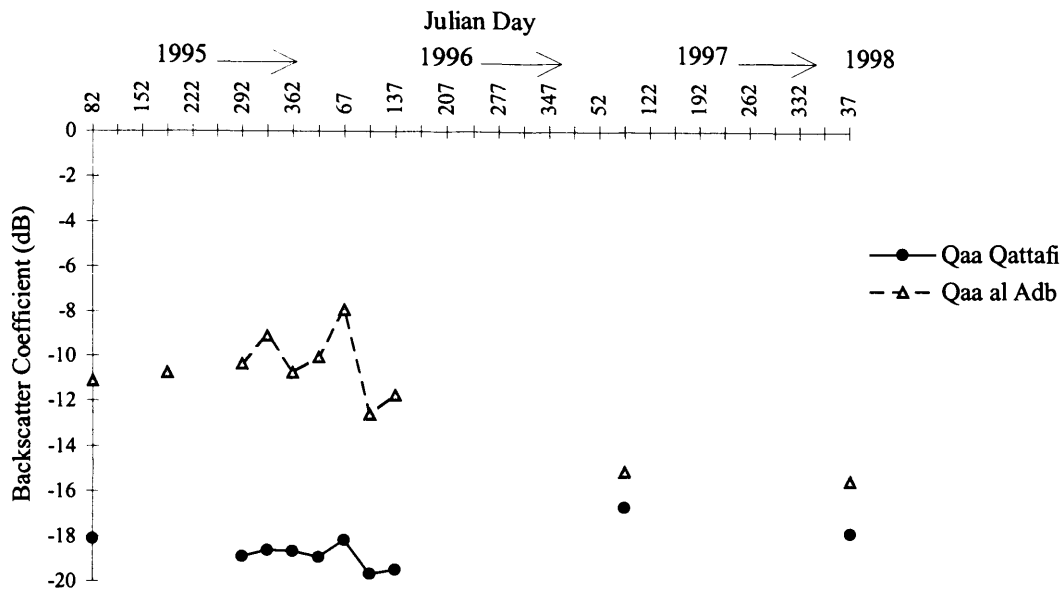


Figure 3.9. The temporal backscatter profiles of Qa'a Qattafi and Qa'a al Abd. The two surfaces have a different backscatter signature caused by different surface roughness properties.

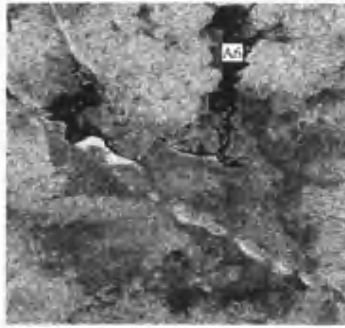
The *qa'a* in the Badia area are unaffected by excessive salinity. The amount of soluble salts in soils increase as rainfall decreases, these exceptions being wadi soils which have additional leaching. Leaching occurs when there is excessive flow of water down the profile, if flow is impeded at depth then concentrations can occur. When this concentration is found at the surface, possibly as a result of very low rainfall, then salt crystal growth can occur. In the study areas covered by level II of the National Soil Map and Land Use Project (The Soils of Jordan 1993, 1994) most of the soils have undergone sufficient leaching. For those soils lying within xeric moisture regimes, their calculated salinity value, expressed as an exchangeable sodium percentage (ESP) are 0.9% (topsoil) and 3.3% (subsoil). Soils of transitional moisture regimes have ESP values of 3.0% (topsoil) and 7.3% (subsoil) and aridic soils exhibit values of 16.4% (topsoil) and 17.1% (subsoil). Generally, soils derived from basalt have lower ESP values than the equivalent soils derived from limestone. The dielectric constant of soil water is dependent on the salinity content and hence this would influence the backscatter coefficient if salts were present in great amounts. The backscatter is also influenced by the presence of salts on these surfaces, and crystal growth and decay can have significant effects on the surface roughness (Archer 1995; Wadge *et al.* 1994;

Millington *et al.* 1995). The *qa'a* used as test sites in this study have not been observed to exhibit symptoms associated with salt crystal growth and excess salinity. The *qa'a* in the Badia region can be distinguished as dry mudflats on the basis of an abundance of desiccation features over intrasediment evaporites (Smoot and Lowenstein 1991).

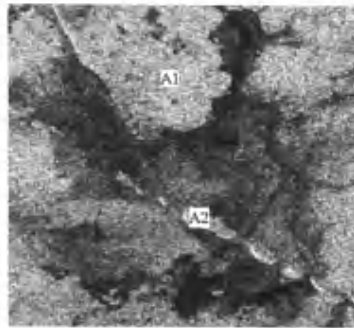
The variations in surface roughness and soil moisture are reflected in the magnitude of the backscatter coefficient derived. The temporal profile of two *qa'a* (located in Figure 3.1) are displayed in Figure 3.9. Both *qa'a* are devoid of vegetation but have very different surface roughness properties. *Qa'a Qattafi*, which is situated in the central part of the study region, lacks any major surface desiccation features. This observation was consistent during all field visits (November 1995, spring 1996, 1997 and 1998). The backscatter coefficient values of *Qa'a Qattafi* are very low (-16 to -20 dB) and do not fluctuate by any significant amount. The small increases in the backscatter coefficient during the spring months of 1997 may reflect increases in soil moisture as rainfall in the central parts of the Badia region were higher than average (Figure 3.3).

Qa'a al Abd, which is located in the north of the study region near the Syrian border (Figure 3.1), displays significant and pronounced surface cracking during dry periods. The spatial distribution and physical size of the desiccation cracking is not constant between seasons and consecutive years. This observation is a reflection of the variable distribution of soil moisture for a given precipitation event and also the variation in morphological response of the surface to different precipitation amounts. Furthermore, *Qa'a al Abd* was inundated after two periods of prolonged rainfall, in the springs of 1995 and 1998 which would cause clay surface expansion and a decrease in surface roughness after the surface water has evaporated. The average backscatter coefficient of *Qa'a al Abd* almost approximates to that of a *hammada* surface (Figure 3.7), making any attempt to differentiate *qa'a* and *hammada* using multitemporal SAR potentially erroneous. The sharp reduction in the backscatter coefficient estimated from ERS-2 SAR data, is thought to be due to cross-calibration differences observed between ERS-1 and ERS-2 SAR backscatter data acquired for the study area.

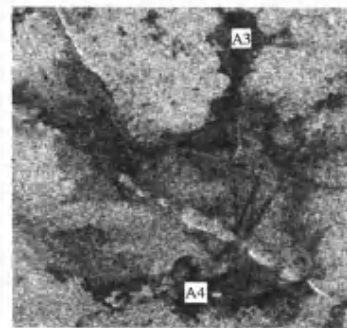
The temporal fluctuations in the backscatter properties of *Qa'a al Abd* are illustrated in Figure 3.10. A sequence of images were acquired, which start in March 1995 and continue to May 1996. *Qa'a al Abd* is almost totally surrounded by basalt. The basalt is characterised by high backscatter values and is displayed as bright, light grey regions in the backscatter coefficient image (Figure 3.10, A1). The areas of basalt display a constant intensity throughout the temporal sequence. The *qa'a* surfaces are depicted as dark grey or black regions. A line of volcanic cones (A2) can be clearly seen extending in a diagonal from the bottom right to the middle left of the image. A number of interesting observations can be made. Many parts of the *qa'a* do not appear to fluctuate a great deal, unless experiencing extreme conditions; e.g. areas include the northern protrusion (A3) and the area south of the volcanic cones (A4). However, the north-western protrusion (A5) does show seasonal fluctuation, which may be caused by a combination of fluctuating soil moisture and/or surface roughness changes. The image acquired on the 23 March 1995 shows that sections of the *qa'a* were flooded (A6), these areas characterised by low values of backscatter caused by the specular nature of microwave scattering at the boundary of a water surface. Rainfall records from Safawi show that 42.4 mm of rain fell in February 1995. Although values were lower in March 1995, (3.0 mm), these measurements are only approximations to the true depths of rainfall that would have occurred in the higher, wetter northern regions of the study area into Syria. The flooded areas are surrounded by pixels with high backscatter values. These are most likely areas with high soil moisture that are almost saturated. In Chapter 2, it was shown that increases in soil moisture, through influencing the soil dielectric properties, increases the backscatter coefficient of the surface. This increase is detectable using a C-band SAR system. The response of the *qa'a* surface to non-flooding rainfall events (Figure 3.3 for Safawi, Menara and *Marab Salma* sites) prior to the image acquisition can be seen in Figure 3.10g, acquired on the 7 March 1996. The majority of the *qa'a* surface is indistinguishable from the surrounding basalt surface apart from a small area towards the south of the *qa'a*.



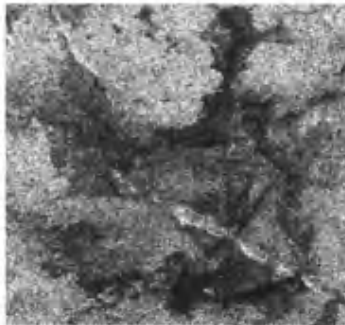
(a) 23 March 1995



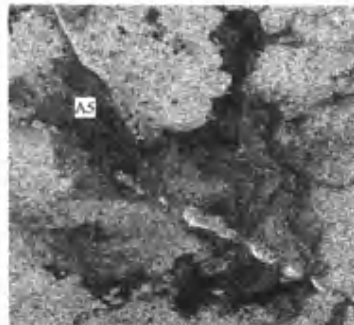
(b) 6 July 1995



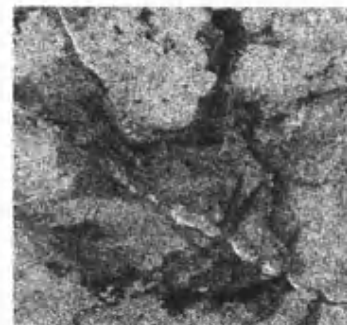
(c) 19 October 1995



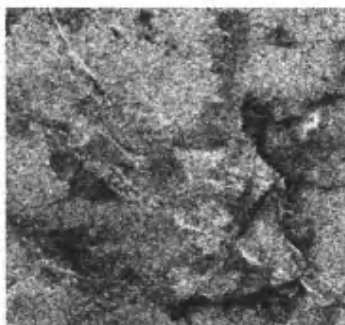
(d) 23 November 1995



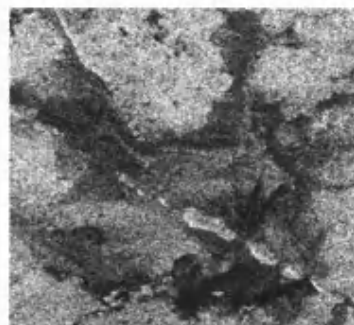
(e) 28 December 1995



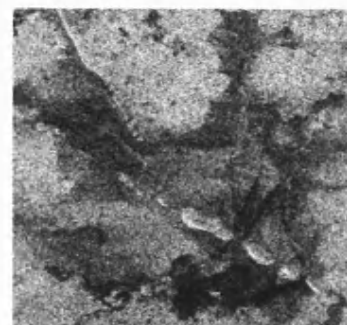
(f) 2 February 1996



(g) 7 March 1996



(h) 11 April 1996



(i) 16 May 1996

Figure 3.10. ERS-1 SAR image sequence of Qa'a al Abd situated in the eastern Badia of Jordan. The images have been converted to an estimate of the backscatter coefficient. The area covers approximately 7.3 by 6.9 km, the scene is located at; 37.193° E, 32.515° N, top-left; 37.274° E, 32.438° N, bottom-right, north is up. Refer to the text for a description of the annotated points (A1 ... A6) shown in the images. Rainfall data to aid the interpretation are presented in Figure 3.3.

The image acquired at the next overpass (11 April 1996) shows that conditions on the *qa'a* have returned to conditions that enable the *qa'a* surface to be distinguished from surrounding land surface covers. SAR, in this example, provides a useful tool in mapping the size and extent of standing water as this presents a huge hazard for the movement of vehicles.

If the images acquired on the 7 March 1996, 6 July 1995 and 11 April 1996 are displayed as a false colour composite (red, green, blue) of actual backscatter values then patterns of surface changes are observed (Figure 3.11).

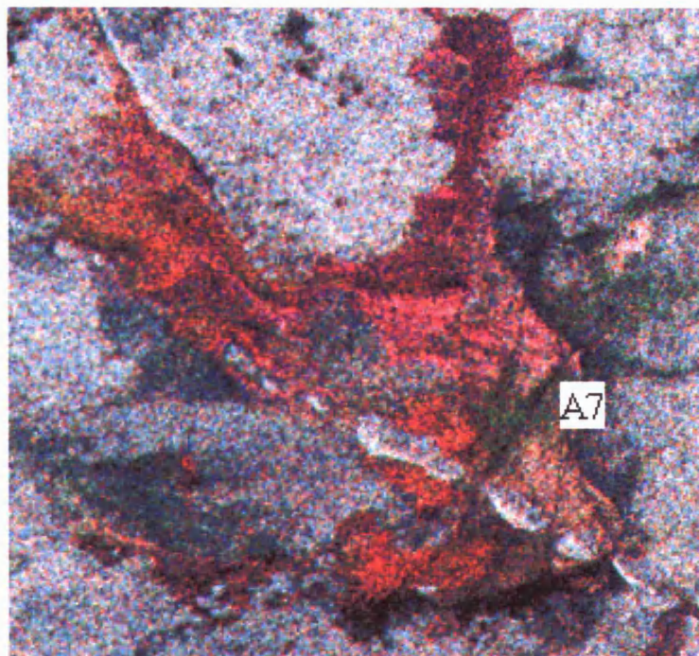


Figure 3.11. Multitemporal colour composite of Qa'a al Abd. The following date/colour combinations, 7 March 1996 (red), 6 July 1995 (green) and 11 April 1996 (blue) show the ability of ERS SAR to detect temporal fluctuations in the backscatter coefficient. Refer to the text for a description of the feature at point A7.

The dominant backscatter signal comes from data acquired on the 7 March 1996. This coincides with an increase of soil moisture across the *qa'a*, caused by significant amounts of rainfall in this month (Figure 3.3). Purple hues in northern sections of the *qa'a* may indicate that levels of soil moisture were still high on 11 April 1996. Rainfall

and temperature data presented in Figure 3.3 and Section 4.7 show that by the first week in April 1996, air and soil temperatures did not increase significantly and that a large precipitation event occurred during the month of March. As expected the backscatter signal acquired on the 6 July 1995 overpass is far less than the other two image acquisitions. By July, temperatures will have risen, resulting in high evaporation rates and no surface water left. Hence, backscatter decreases. However, there is one section of the *qa'a* (A7) where the backscatter, on the 6 July 1995, was greater than on the other two dates. This observation may be caused by an increase in surface roughness caused by surface cracking in dry conditions.

A multitemporal colour composite of *Qa'a Qattafi* (Figure 3.12) shows radiometric stability for all of the three scenes in the centre of the *qa'a* (Figure 3.12, area B). The band combinations for this image are 7 March 1996 (red), 19 October 1995 (green) and 11 April 1996 (blue). Water and sediment are carried into this *qa'a* from the north-east through a vegetated *marab* which is displayed in red and green hues (C). Sediment is trapped between the distinctive lines of vegetation that grow on pronounced (of the order of 10s of cm's) hummocks of sandy material. These are clearly distinguishable on the image (D). Part of the *qa'a* appears to have a fluctuating backscatter signal (E). This is an area at the lower end of the *qa'a* where pathways of water through the *qa'a* will congregate, thereby yielding temporal variations in the backscatter coefficient. This is also an area of gravel and stone accumulation on the surface of the *qa'a*, thereby increasing surface roughness. The reddish hues may be due to increased soil moisture caused after rainfall events at the beginning of March 1996 (Figure 3.3). The surrounding basalt stone and gravel fields also display slightly red hues. No speckle reduction filter has been applied to the data.

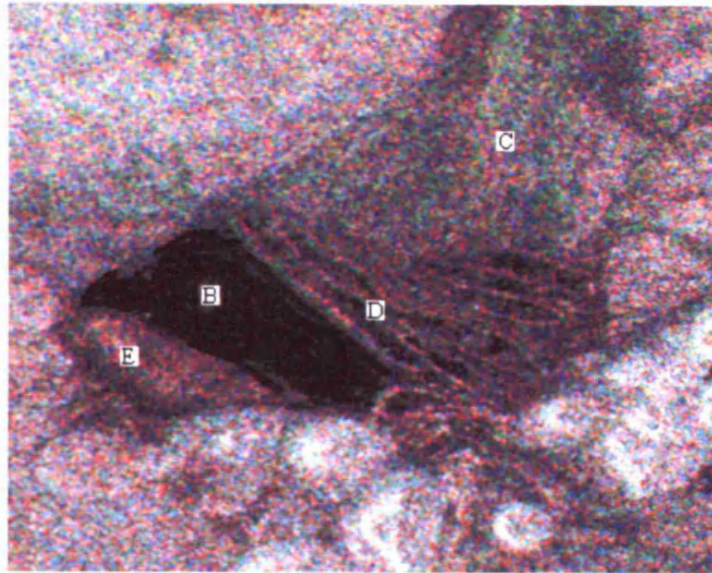


Figure 3.12. Multitemporal colour composite of Qa'a Qattafi, showing relative stable backscatter properties in the centre of the qa'a compared to the stony and vegetated surrounding areas. The images displayed are 7 March 1996 (red), 19 October 1995 (green) and 11 April 1996 (blue). Observations B-E are explained in the text. The image covers approximately 4.9 by 4 km, the corner co-ordinates are; 37.427° E, 31.872° N top-left; 37.482° E, 31.828° N bottom-left; north is up.

3.2.3 Vegetated marab surfaces

The temporal profiles of the vegetated surfaces (*marab*) in the eastern Badia are markedly different from other surfaces because of the observed temporal variation in the backscatter coefficient. The temporal profiles also vary a great deal from site to site. These site to site differences are due to differences in their geographic location, surface roughness and textures of the surface sediments of different *marabs*. The presence of vegetation, even at low percentages (<10%) indicates that soil moisture conditions at certain times of the year are sufficient enough to support plant growth. Therefore, differences in soil moisture levels will also lead to changes in backscatter from season to season. Although most of the land surfaces within the study region can support some species of vegetation it is within the ephemeral wadi channels and *marab* where growth

is most abundant. A description of the soil moisture properties of *marab* surfaces is given in Section 1.3. The temporal profiles of three *marab* are shown in Figure 3.13.

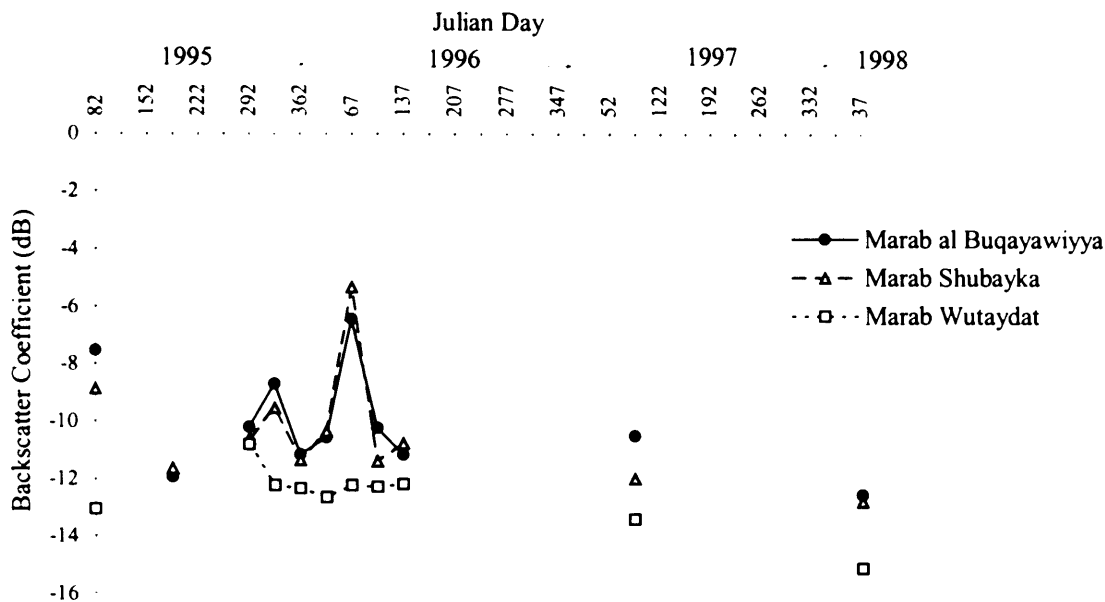


Figure 3.13. The temporal profiles of three *marab* surfaces, *Qa'a* (*marab*) al *Buqayawiyya*, *Shubayka* and *Wutaydat*. *Marab* sites showed the greatest variation in seasonal backscatter, believed to be caused by the increase of soil moisture and storage of the available moisture in the upper layers of the soil.

Qa'a al Buqayawiyya (although known as a *qa'a* it is in fact vegetated) is a silt-clay *marab* south of *Safawi* (Figure 3.1). A detailed description of this *marab* can be found in Section 4.2. Parts of the *marab* have been cultivated, however the temporal profile shown is for a naturally vegetated area. The variation in seasonal backscatter is quite pronounced, the backscatter increasing significantly during the winter months. Much the same is true for *Marab Shubayka*, a vegetated expanse of land to the south of *Qa'a al Abd* (Figure 3.1). Variations in the order of 6 dB are seen between wet and dry seasons at both of these sites. *Marab Wutaydat* is located in a more arid region (Figure 3.1). The surface sediment contains > 80% sand. The temporal profile records a lower fluctuation in the backscatter coefficient than those observed for the other two *marab*. Furthermore, the two peaks estimated of the backscatter coefficient for the November 1995 and

March 1996 images are absent reflecting the localised precipitation in the region. The peaks in the backscatter coefficient can be related to the occurrence of precipitation prior to image acquisition (Figure 3.3).

A multitemporal colour image showing the seasonal fluctuation in the backscatter coefficient of *Qa'a al Buqayawiyya* is displayed in Figure 3.14 using similar band combinations to the other multitemporal scenes (7 March 1996 (red), 6 July 1995 (green) and 11 April 1996 (blue)).

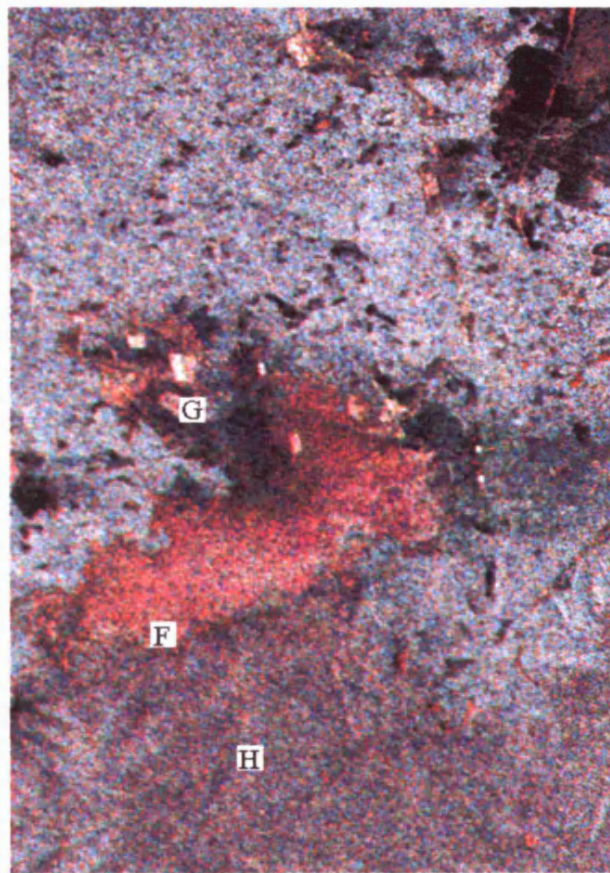


Figure 3.14. Multitemporal colour composite of Qa'a al Buqayawiyya and surrounding terrain, displayed using 7 March 1996 (red), 6 July 1995 (green) and 11 April 1996 (blue) images. For a description of points F, G and H, refer to the text. The image covers approximately 9.6 by 14 km, the corner co-ordinates are; 37.084° E, 32.140° N, top-left; 37.181° E, 31.985° N, bottom-right; north is up.

The strong increase in the backscatter coefficient for the March 1996 overpass becomes obvious with the full extent of the vegetated region being highlighted (F). The increase in the backscatter coefficient at the time of this acquisition is due to an increase in surface soil moisture across many parts of the *marab*. Large quantities of rainfall were recorded at locations throughout the study area at the beginning of this month (Figure 3.3). A strong backscatter signal is received from the small agricultural fields that have been ploughed (G). This is because of greater surface roughness properties of these surfaces (RMS height > 3 cm). A smaller response to the rainfall occurring at this time is observed on the *hammada* plains to the south of the *marab* (H). This observation is in agreement with the small peak recorded for the chert *hammada* and the northern limestone *hammada* sites for the March 1996 acquisition (Figure 3.7). The basalt regolith, making up the majority of the northern half of Figure 3.14 is displayed as light grey tones reflecting the stable nature of the temporal backscatter coefficient profile for these surfaces (Figure 3.4).

A similar multitemporal image of *Marab Shubayka* is shown in Figure 3.15 using the same band combinations as in Figure 3.14. Once again the backscatter coefficient derived from the 7 March 1996 image, after a rainfall event (Figure 3.3 and field observations), dominates the image (I). Again, it is interesting to note that the surrounding basalt land units do not react to rainfall events in the same way as the *marab* surfaces (J). The areas displayed in black tones in Figure 3.15 are characterised as flat, *qa'a* surfaces, displaying low values of backscatter coefficient for each of the three images (K). These examples show that multitemporal SAR is useful in defining areas in which surface parameters are fluctuating and areas where they are not. If this change was caused by soil moisture increasing in the wet season, then it is important to quantify this change to predict the growth of, or 'greening-up', of vegetation.

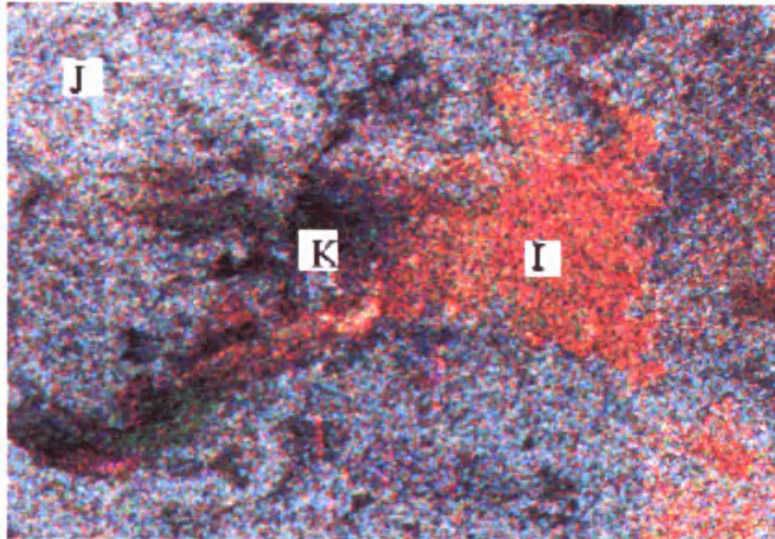


Figure 3.15. Multitemporal colour composite of Marab Shubayka and surrounding terrain using 7 March 1996 (red), 6 July 1995 (green) and 11 April 1996 (blue) images. The backscatter coefficient estimates on the 7 March 1996 acquisition clearly dominates the scene. The image covers approximately 7.5 by 5.3 km, the corner co-ordinates are; 37.184° E, 32.422° N, top-left; 37.268° E, 32.364° N, bottom-right; north is up. Descriptions of sites I, J and K are given in the text.

3.2.4 Implications of surface differentiation and temporal backscatter monitoring for soil moisture modelling

Previously in Section 3.2, it has been shown that ERS SAR is able to detect fluctuations in the backscatter coefficient of relatively undisturbed desert surfaces that are not attributable to errors introduced in the image acquisition and signal processing stages. Of the four main land surface types studied, the basalt surfaces (which comprise $> 50\%$ of the study area) display very stable radiometric properties. This is probably due to the dominance of the surface roughness parameter over all other elements contributing to the backscatter. This observation may make the retrieval of soil moisture information from the fine textured 'soil' between basalt boulders difficult. Some variation is observed in the temporal signature of *hammada* surfaces; this may be linked to the occurrence of rainfall and the distribution of surface soil moisture. Both the basalt and *hammada* surfaces are important resources for vegetation for the reason that they

provide much of the food stuffs for the flocks of sheep and goats as they move between one vegetated region and another. Today though, most farmers choose to transport their flock from grazing areas using vehicles (Campbell and Roe 1998).

Fluctuations in the temporal profiles of *qa'a* surfaces appear to be strongly influenced by textural characteristics of the sediments and the frequency of water inputs. Given the mesotopographic flatness of *qa'a* surfaces and the strong sensitivity of the backscatter coefficient at these values of surface roughness, the extraction of soil moisture information from microwave data of these surfaces is difficult. The errors involved in measuring microtopographic variations increase this difficulty beyond that which may be considered acceptable for soil moisture studies (errors of $\pm 0.1 \text{ m}^3 \text{ water m}^{-3} \text{ soil}$ can be made, at this scale of roughness). The land units that yield the greatest temporal variation in backscatter are the vegetated *marab* surfaces.

Overall, variations observed especially at northern *marab* sites are significant. However, it is through quantitative modelling of changes in surface parameters that influence the backscatter coefficient that will facilitate a greater understanding of the geomorphological and hydrological processes that are present in these desert regions.

3.3 Comparison of ERS-1 and ERS-2 SAR data

It has been noted in Section 3.2 that the differences between backscatter coefficients derived from ESA PRI data from ERS-1 and 2 can be large. Although the temporal coverage of the region has not been as complete for ERS-2 data as for ERS-1 data, if future investigations are to be made, within the context of the Badia research and development programme, then the differences between the two instruments need to be quantified as ERS-2 is now fully operational and ERS-1 is in stand-by mode.

The differences arise from the observed reduction in the backscatter coefficient calculated from the ERS-2 instrument. The ERS-2 SAR images were collected during the wet season, at the end of winters which had higher than average rainfall amounts. Backscatter estimates are more likely to be greater at this time than during dry winters.

This reduction is consistent for the majority of the sites studied (see Figures 3.4, 3.7, 3.9 and 3.13). The reductions are noted for all surfaces (except *Qa'a Qattafi*), including those that have very stable radiometric properties, e.g. basalt surfaces (Figure 3.4). Reasons for this observed difference might be due to the calibration constants that are used to calculate the backscatter coefficient. These may be erroneous. Furthermore, the two methods available to derive the backscatter coefficient (Laur *et al.* 1996) can yield different estimates of the backscatter coefficient (Section 2.5.2). This is especially true for the ERS-2 instrument. To illustrate this point, the simple estimate of the backscatter coefficient for a basalt site calculated from the 28 March 1997 image is -6.78 dB. The comprehensive equation, which accounts for the ratio between product replica power and the reference replica power (Section 2.5.2), gives a value of -7.82. This difference is even greater for the image acquired on the 6 February 1998. The values calculated were -6.98 dB and -8.68 dB respectively. In most cases, backscatter coefficients from ERS-2 SAR data, calculated using the simple equation, are more comparable to ERS-1 SAR data.

Table 3.1 shows estimates of the backscatter coefficient calculated using both methods for the tandem acquisition dates for a number of sites already discussed in this chapter. This phase of the ESA ERS mission was to provide coherence images (interferometry applications) of the same region with only 24 hours difference. One tandem pair was acquired, on the 23 (ERS-1) and 24 (ERS-2) November 1995 for the central part of the study region. The data shown in Table 3.1 do not indicate any cause for concern as the comprehensive estimates in both cases approximate to the simple estimates. However, large differences are calculated between ERS-1 SAR data and ERS-2 data for 1997 and 1998 data (see for example Figure 3.4). Therefore simple estimates of the backscatter coefficient were used, for ERS-2 SAR data, in the analysis phase of this study. These estimates of the backscatter coefficient were undoubtedly more comparable to ERS-1 SAR data than those derived using the comprehensive method. Further investigation of the cross-calibration problem is required.

Backscatter Estimation Method	Simple	Comprehensive	Simple	Comprehensive
Site Name	ERS-1 23 November 1995		ERS-2 24 November 1995	
Fahda vesicular basalt	-5.06	-5.17	-6.76	-7.08
Abed olivine basalt	-5.65	-5.75	-6.11	-6.43
Chert hammada	-7.99	-8.1	-9.21	-9.52
Limestone hammada	-8.03	-8.32	-8.89	-9.19
Qa'a al Abd	-9.01	-9.12	-9.73	-10.05
Qa'a Qattafi	-18.51	-18.63	-16.45	-16.75
Qa'a Buqayawiyya	-8.6	-8.71	-9.16	-9.48
Marab Shubayka	-9.46	-9.56	-9.72	-10.04

Table 3.1. Backscatter coefficients (in dB) of different surfaces calculated from ERS SAR tandem images. These have been derived using the two methods presented by Laur et al. (1996). The data indicate that a small reduction in the backscatter coefficient occurred for the majority of the sites shown (apart from Qa'a Qattafi). This data show that the relative radiometric correlation between the two instruments is acceptable at this particular time of image acquisition.

After submission of this thesis, it was acknowledged that revisions of the document 'Derivation of the Backscattering Coefficient Sigma-Nought in ESA ERS SAR PRI Products' made in 1997 and confirmed in June 1998 stated that the replica pulse power variations correction is not needed for ERS-2. Results shown in Chapter 6 assume that

this correction is not needed and therefore the assumption stated in the data analysis is scientifically supported by the ESA publication (Laur *et al.*, 1998).

3.4 Conclusions

- This chapter has demonstrated the ability of ERS SAR to detect temporal fluctuations in the backscatter signal from the main desert surfaces that characterise the eastern Badia of Jordan.

- Much of the land surface in the study region is covered by a regolith of basalt, chert or limestone. These surfaces are radiometrically stable at microwave wavelengths and have the potential to become ‘control’ surfaces to compare with more radiometrically active surfaces.

- The fluctuations in the backscatter coefficient between consecutive months, and between wet and dry seasons, is significantly greater than the fluctuation that might be due to system noise for some *marab* and *qa’a* surfaces. The variations in backscatter coefficient may be attributable to changes in surface roughness (e.g. on *qa’a*), or changes in soil moisture (e.g. on *marab*) or a combination of these processes.

- Analysis of the temporal signatures of desert surfaces has highlighted a potential problem in comparing backscatter coefficients between the ERS-1 and the ERS-2 SAR instruments. In nearly all cases a significant reduction in the backscatter occurs when estimates are derived from ERS-2 data. Without resorting to detailed analysis, the simple method of calculating the backscatter coefficient from ERS-2 data has been selected as this best represents the trend of previous observations. Further information on the calculation of the backscatter coefficient can be found in Section 2.5.

4. Field Data and Methodology

4.1 Introduction

To fully understand the interactions between microwave electromagnetic radiation and the desert surfaces, all of the main surface types were considered. The land surface types found in the eastern Badia of Jordan fall into four main surface units. Within each of these main units (*basalt*, *marab*, *qa'a* and *hammada*) sites were chosen that represented the major land unit but that were also unique in terms of their properties or surroundings. The field methodology was continuously modified and improved as a consequence of data analysis and interpretation. Data were collected on the surface soil moisture content, surface roughness, soil texture, vegetation cover and climatic data at the sites chosen. This chapter outlines the procedures for data collection and describes the preliminary analysis conducted on the parameters measured.

4.2 Site selection and description

Four field campaigns were carried out between October 1995 and September 1998. The dates are given in Table 4.1; also given in this table are the acquisition dates for the ERS SAR imagery. The first field visit during November and December 1995 served the following purposes. First, to select sites through a combination of studying imagery and visiting areas, second, to test methods of data collection given limited human resources and the requirement for the team to fulfill all their data collection targets and, third, to obtain ideas about selected physical processes occurring in the Jordan Badia. Future field campaigns were carried out after the winter rains, in March and April, to obtain measurements when soil moisture levels were at a maximum before conditions became too hot and dry reducing surface soil moisture levels to zero

Dates of field campaigns	ERS SAR image overpass dates
18-November-1995 to 18-December-1995	23-November-1995 (track 257) 09-December-1995 (track 486) 12-December-1995 (track 028)
27-March-1996 to 17-May-1996	11-April-1996 (track 257) 28-April-1996 (descending track 493) 30-April-1996 (track 486) 16-May-1996 (track 257)
26-March-1997 to 28-April-1997	28-March-1997 (track 257) 13-April-1997 (track 486)
25-March-1998 to 20-April-1998	29-March-1998 (track 486) 17-April-1998 (track 257- missing lines)

Table 4.1. Dates of field campaigns and associated ERS SAR image acquisitions.

4.2.1 General site criteria

To minimise the influence of other factors that would affect the backscatter return, sites were chosen based on a set of general criteria:

(i) There are no large significant surface slopes that would have to be accounted for with a digital elevation model (DEM). Areas with significant relief are easily distinguishable in the study region.

(ii) Each site was assumed homogenous over an area of at least 500 by 500 m to allow for possible errors in site location on the imagery. To expand on this further each site was located within a larger square that had approximately the same surface characteristics. For example, no one part of the area was ploughed, no major changes in surface slope angles or in surface roughness properties occurred that could not be observed and accounted for.

4.2.2 *Specific site overview*

During the four field campaigns many sites were visited, 26 of which were used in the final analysis. These sites are grouped into the four major land surface types, (Table 4.2). Selected sites that were relatively accessible and considered important after initial data analysis were ear-marked for further study. Of these sites, 8 became known as permanent monitoring sites (PMS). The PMS sites are listed in Table 4.3 along with their location (Figure 4.1) and description information and a photograph displaying the site characteristics. These areas were visited at times of satellite data acquisition for the majority of the field campaigns. The remaining sites, which are termed short-term validation sites, either have been identified later on during a field campaign or have been excluded from long term monitoring because of accessibility or a preference for a similar site elsewhere. The pattern of site development can be summarised as follows:

(i) Winter 1995 campaign: 18 sites were established but due to logistical problems with the equipment some data could not be used. This campaign yielded 16 sample points.

(ii) Spring 1996 campaign: 7 new sites were visited and 2 sites were excluded from further analysis. This campaign yielded 10 sample points.

(iii) Spring 1997 campaign: After a major review of data collection methods, 2 new sites were visited and 6 sites were excluded from further visits. This was done to undertake more detailed studies on the PMS sites. This campaign yielded 14 sample points.

(iv) Spring 1998 campaign: Field data collection strategies were now focused on the PMS and the validation of the relationships developed by the models for the PMS (Chapter 6). 19 sample points were acquired, of which 11 were used in the model validation.

Major land unit	Site name Permanent monitoring site	Geographic co-ordinates (N, E), WGS 84 datum	Years visited in the field	General field characteristics
Qa'a	Qattafi (PMS) al Abd at Ra'd al Wassad (PMS) al Wutaydat	31.8508 N, 37.4438 E 32.4653 N, 37.2555 E 32.4098 N, 37.3676 E 31.8992 N, 38.0018 E 31.8478 N, 37.7538 E	1995, 1996, 1997, 1998 1995, 1997, 1998 1997 1995, 1996, 1997, 1998 1996, 1997, 1998	<i>Qa'a</i> are very flat regions of alluvial in-fill of fine particles. As Infiltration rates are low, <i>qa'a</i> sometimes collect and store surface water. The surfaces are compact with desiccation features.
Basalt	Fahda Vesicular (PMS) Madhala Olivine Phyric Abed Olivine Phyric Madhala Olivine Phyric Harrat edh Dhirwa	32.3275 N, 37.1649 E 32.1513 N, 36.9854 E 32.4157 N, 37.3750 E 32.0775 N, 37.0557 E 31.6383 N, 37.4161 E	1995, 1996, 1997, 1998 1995, 1996 1995, 1996, 1997, 1998 1995, 1996 1996	As described in Chapter 1, basalt covers a large proportion of the region. The basalt is a surficial coverage of varying age reflecting the weathering regime over a soil of mostly medium to coarse sized particles.
Hammada	Chert gravel (PMS) Limestone gravel (PMS) Shahbat el Hazim Shumaysaniyyat Sandflat	32.0031 N, 37.1210 E 31.7104 N, 36.9731 E 31.6412 N, 37.1638 E 31.7620 N, 37.7667 E 31.7588 N, 37.6423 E	1996, 1997, 1998 1995, 1996 1996, 1998 1995, 1996 1996	The <i>hammada</i> refers to surfaces of coarse, angular fragments of rock be it basalt or limestone. Beneath this desert pavement is a soil of mainly sand sized particles. Vegetation is very sparse in these regions.
Marab	Feidat ed Dihikiya Hashad Wadi el Hazim Qattafi Salma al Wassad al Wutaydat (PMS) al Buqayawiyya (PMS) al Buqayawiyya (cultivated) ash Shubayka Suwaiid (PMS)	31.5620 N, 37.1483 E 32.4789 N, 37.2586 E 31.5967 N, 37.2475 E 31.8588 N, 37.4668 E 32.4370 N, 37.2684 E 31.8826 N, 37.9897 E 31.8272 N, 37.7554 E 32.0544 N, 37.1416 E 32.0759 N, 37.1130 E 32.3944 N, 37.2450 E 32.2789 N, 37.4580 E	1995, 1996, 1998 1995 1996 1995, 1997 1996, 1997, 1998 1995, 1996, 1997, 1998 1995, 1996, 1997, 1998 1995, 1996, 1997, 1998 1995 1997, 1998 1995, 1996, 1997, 1998	<i>Marab's</i> form the outwash plains of the ephemeral channel systems that dissect the region. Vegetation growth occurs naturally although some of the sites are utilised for the cultivation of barley. The soils are normally coarse silts and sands and are more structured than other soils in the region. The slopes in the <i>marab's</i> are shallow. The soils are increasingly heterogeneous in these areas.

Table 4.2. Location and general characteristics of study sites located within the eastern Badia of Jordan.

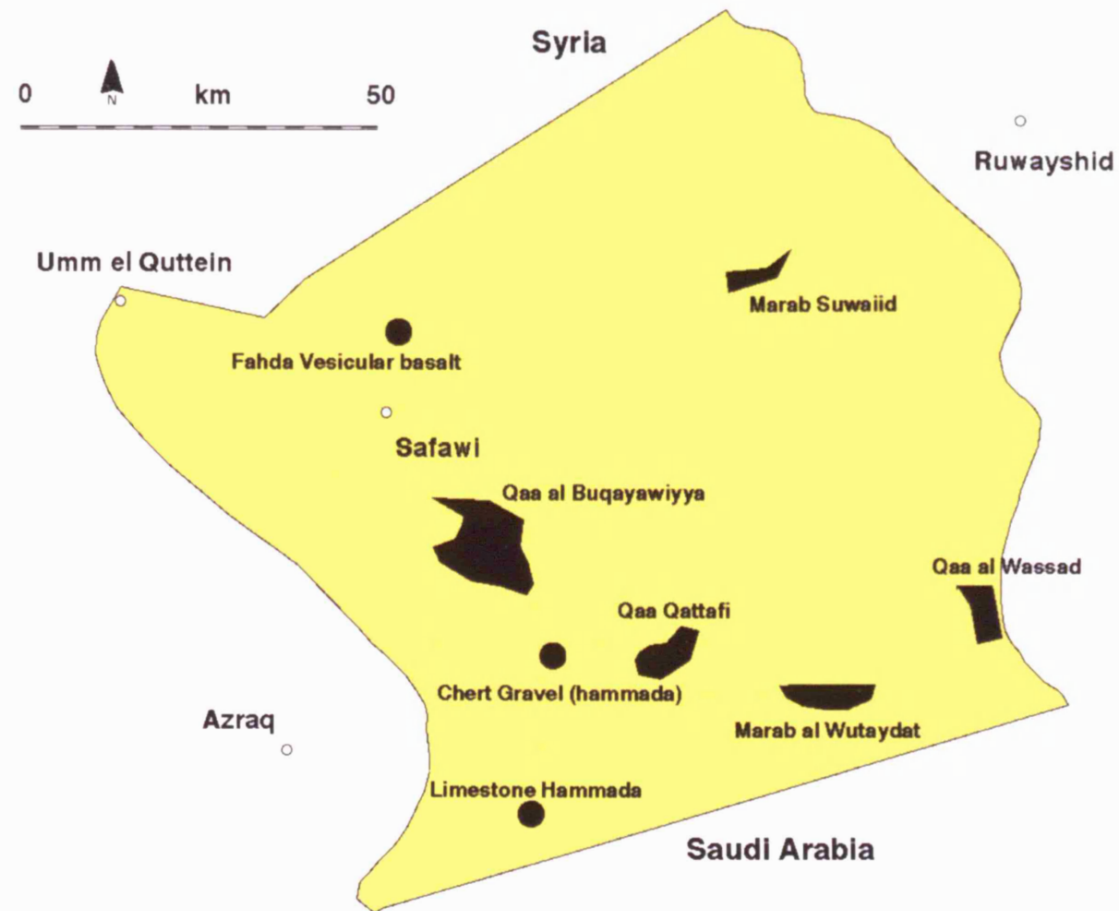


Figure 4.1. Location of the permanent monitoring sites (PMS).

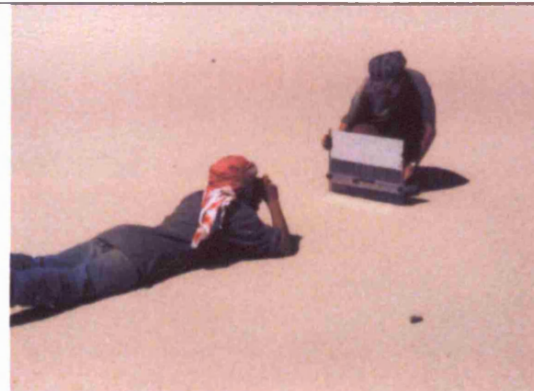

Site name and unit classification	Location N, E (degrees)	Site description and major features	Field Photograph
Qa'a Qattafi	31.8508 N, 37.4438 E	A very flat <i>qa'a</i> forming the sediment and water store for a <i>marab</i> to the north-west. The surface soil comprises nearly 65% silt content and is also high in clay content. The upper surface layers are heavy and compacted. The <i>qa'a</i> shows very little surface cracking and flaking in response to changes in the soil moisture status. In roughness terms the surface is flat with only small undulations, there is no significant surface slope.	
Chert gravel (hammada)	32.0031 N, 37.1210 E	The large, flat expanse of gravel fragments covering large parts of the central section of the study area. The site is characterised by chert fragments overlying a well structured soil surface. The fragments cover approximately 60% of the ground surface and are much smaller than those at the basalt sites. The <i>hammada</i> pavements are almost devoid of vegetation, which is restricted to localised depressions.	

Table 4.3. Field descriptions of the permanent monitoring sites (PMS), Qa'a Qattafi and the chert gravel hammada.

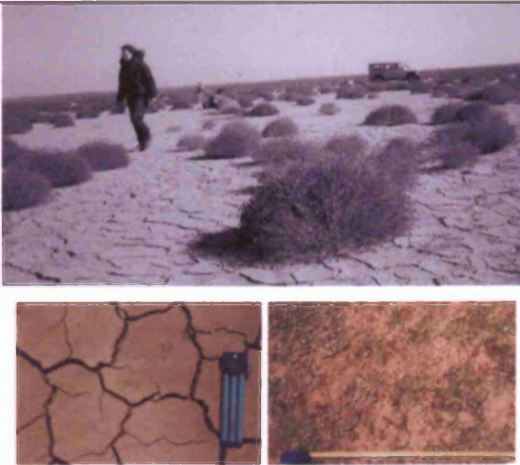

Qa'a al Buqayawiyya (marab)	32.0544 N, 37.1416 E	<p>Qa'a 'Wia is the most intensively studied site. The flat, massive expanse drains several wadi's south of Safawi. Vegetation is present through most times of the year in a senesced state greening up after winter rains. Grass growth can be significant. The surface soil is quite platy and cracking is visible in some parts. These cracks can be up to a few cm's wide. The texture of the soil is mainly silt but high quantities of clay particles are also present.</p>	
Limestone hammada	31.7104 N, 36.9731 E	<p>Located south at the Saudi Arabian border there is an extensive regolith of calcite fragments, lying on the compact, unstructured surface. The soil beneath is more compact and lies within the hyper-aridic soil temperature classification. the topography of the site studied is mainly flat although there are regions of undulating anticlines and synclines. Vegetation is almost totally absent on these <i>hammada</i> surfaces.</p>	

Table 4.3 (cont.). Field descriptions of the permanent monitoring sites (PMS), Qa'a al Buqayawiyya and the limestone hammada.

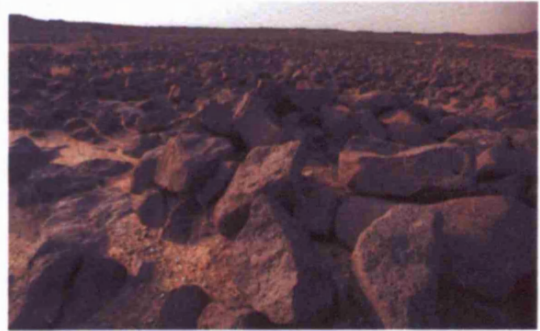

Fahda Vesicular basalt	32.3275 N, 37.1649 E	<p>The youngest basaltic regolith is still in the stages of being weathered and eroded. The boulders are not well developed, the average major axis length being 10.3 cm. Surface cover is approximately 84 % the underlying soil is quite loose and unconsolidated. The soil beneath comprises on average 31% sand and 55% silt content. In roughness terms the surface has a large standard deviation of surface height but also has smaller scale roughness properties due to the vesicular pock-marked nature of the boulders. Much of the eastern Badia is overlain by basalt boulders.</p>	
Marab Suwaiid	32.2789 N, 37.4580 E	<p>Marab Suwaiid is a intensively monitored and studied <i>marab</i> along the main road towards Ruwayshid. The <i>marab</i> is well vegetated and in response to experiments being undertaken was ploughed during the autumn of 1996. The changes in surface roughness have been accounted for. The soil is considered to be quite nutrient poor and contains high quantities of sand and silt sized particles.</p>	

Table 4.3 (cont.). Field descriptions of the permanent monitoring sites (PMS), Fahda Vesicular basalt and Marab Suwaiid.

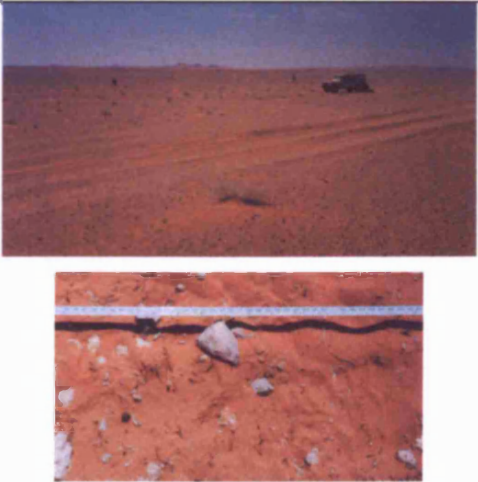
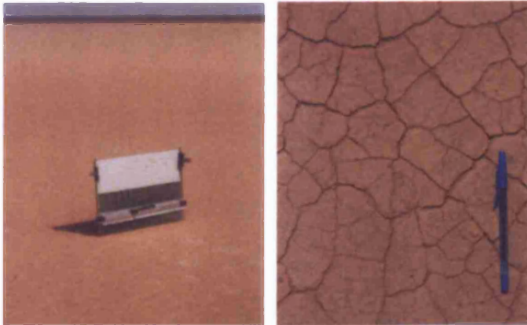
Marab Wutaydat	31.8272 N, 37.7554 E	<p>Marab Wutaydat is a large vegetated <i>marab</i> in the south-east of the region. It lies within an area that is overlain with a blanket of sand sized particles that come across from the sand seas in Saudi Arabia. This is reflected in the texture of the surface soil with nearly 75% being sand-size particles. The vegetation cover is low, the main species being shrubs and occasionally some ephemeral grass and flowers.</p>	
Qa'a al Wassad	31.8992 N, 38.0018 E	<p>Qa'a al Wassad is located in the far south-eastern corner of the study area. The area is characterised by a very flat, compact surface. Small-scale desiccation cracking is present, having a negligible influence on the surface roughness. There is no vegetation present on the <i>qa'a</i>, it is however present on the adjacent <i>marab</i> that has coarser sediments, hummocky roughness and provides suitable grazing and nesting for animals and birds.</p>	

Table 4.3 (cont.). Field descriptions of the permanent monitoring sites (PMS), Marab Wutaydat and Qa'a al Wassad.

4.2.3 Sampling strategy

An area of 30 by 30m was located within the larger square defined in the general criteria for site selection. This covered approximately 3 by 3 pixels within a SAR scene, each pixel having a size of approximately 12.5 by 12.5m on the ground. Within each 30 by 30m area information was collected on the surface soil moisture, surface roughness and texture and vegetation cover (Figure 4.2). Please see the individual sections for a complete description of the methodology used to acquire these data.

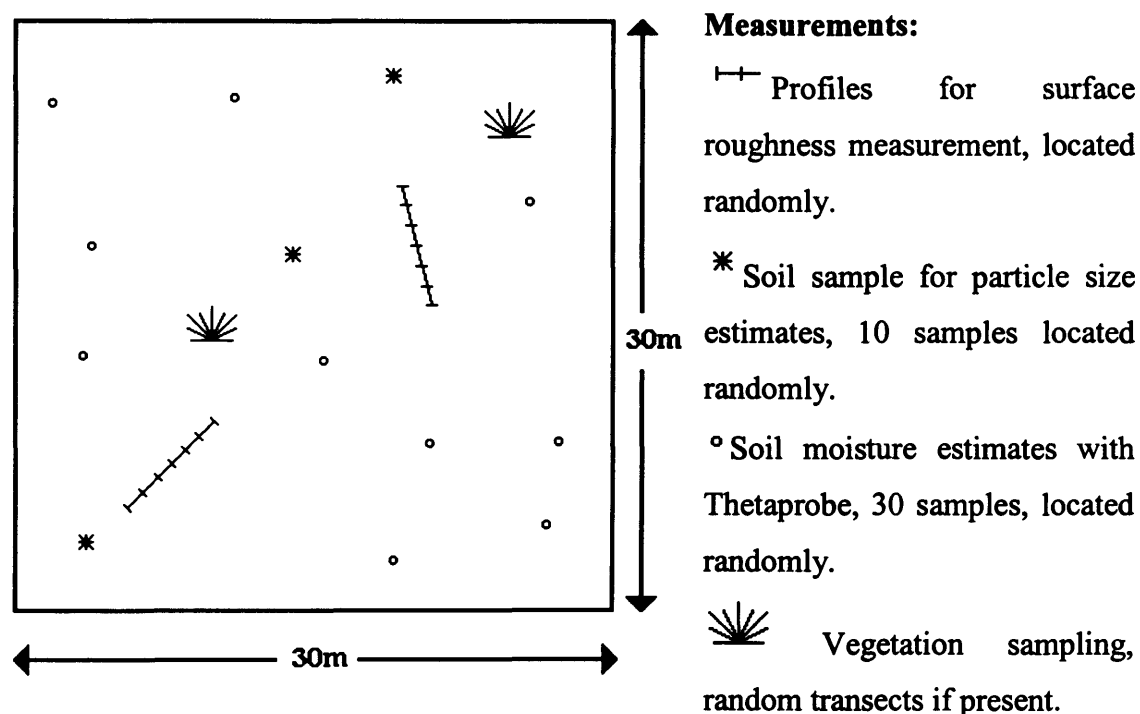


Figure 4.2. Schematic diagram showing the general field methodology undertaken at each site. Data on the soil moisture, texture and roughness were collected and also data related to the vegetation if significant amounts were present.

4.3 Soil moisture

4.3.1 Instrument

Data was collected on the surface soil moisture content using a ThetaProbe soil moisture sensor designed by Delta-T devices and the Macaulay Land Use Research Institute. The instrument derives a measure of the volumetric soil moisture, θ_v , measured in cm^3 water cm^{-3} soil, by responding to changes in the apparent dielectric constant. The instrument converts the signal into a direct current (dc) voltage shown to be almost proportional to the soil moisture content. The probe (Figure 4.3) comprises four sharpened prongs of 6 cm in length. An estimate is obtained for a 30 cm^3 column of soil within these prongs.



Figure 4.3. The dielectric ThetaProbe measuring the volumetric soil moisture in Qa'a ash Shubayka.

A comprehensive description of the operating principles of the probe are given by Gaskin and Miller (1996). The impedance of the emitted 100 MHz signal is influenced by two properties; the apparent dielectric constant and the ionic conductivity. The signal frequency minimises the effect of changes in the ionic conductivity to maximise the

sensitivity of the signal to changes in the dielectric constant. The reported absolute accuracy of the probe is given as between ± 0.02 and $\pm 0.05 \text{ cm}^3 \text{ water cm}^{-3} \text{ soil}$ depending on which calibration method is used. The output voltage readings (V) were recorded on a digital voltmeter.

4.3.2 Sampling methods

The first task was to check that the probe was operating normally and that the probes were clean, any small offset in voltage was noted before sampling began. The probe was then inserted into the soil, perpendicular to the soil surface. The voltage reading was allowed to stabilise and then this value was noted. Thirty estimates were taken at random locations within the 30 by 30m area to account for the spatial heterogeneity of soil moisture within the quadrat. The average of the recordings was then calculated and considered representative of the soil moisture content at that particular site. Due to the compactness of some of the desert surfaces, the upper layers had to be loosened using a trowel (this increased the amount of air in the sampled layer). This was thought necessary in some cases as, during the first field campaign, one of the outer prongs became detached from the instrument due to constantly driving it into compacted sediment. The instrument was kept in use as realistic readings were still being derived and correspondence from Delta-T Devices stated that the missing prong should not effect the reading too much. To check this, tests were carried out with the probe once it was returned to Leicester by taking readings in a soil with known moisture contents with the instrument having three prongs and then four prongs once it had been repaired. Approximately similar values were recorded. For the future safety of the instrument in taking measurements in compact soils it was required that the surface layers were loosened with a trowel and then compacted down again before a measurement was taken. In addition a metal instrument that resembled the probe was used to create four holes in the surface soil before insertion with the moisture probe.

4.3.3 Calibration

The stated relationship between the output voltage of the ThetaProbe and the volumetric soil moisture content is non-linear and dependent on the type of soil analysed. The calibration relationship chosen in this study is for the mineral soils. There is an absence of either organic or humus layers in all the soils observed in the Badia region. The relationship between the output voltage (V) and the square root of the dielectric constant ($\sqrt{\epsilon}$) can be expressed very accurately ($R^2 = 1.0$) by the 5th order polynomial (Whalley 1993):

$$\sqrt{\epsilon} = 1 + 6.19V - 9.72V^2 + 24.35V^3 - 30.84V^4 + 14.73V^5 \quad (4.1)$$

The simple relationship between $\sqrt{\epsilon}$ and θ_v can be expressed in the form:

$$\sqrt{\epsilon} = a_0 + a_1\theta_v \quad (4.2)$$

giving

$$\theta_v = \frac{[\sqrt{\epsilon} = 1 + 6.19V - 9.72V^2 + 24.35V^3 - 30.84V^4 + 14.73V^5] - a_0}{a_1} \quad (4.3)$$

The coefficients chosen for a_0 and a_1 are given as 1.6 and 8.4 respectively. These are derived from a large number of tests carried out on mineral soils. The value of θ_v was used as an input to the theoretical models when this parameter was specified. Otherwise, if the real component of the dielectric constant was specified as an input to the models used, the relationship given by Hallikainen *et al.* (1985) was used. This relationship utilises both soil moisture and textural information to give an estimate of the dielectric properties. The models are described in Section 2.6.

4.3.4 Data verification

For selected sites, gravimetric samples were collected to compare moisture measurements made by the ThetaProbe and laboratory methods. The standard procedure was to collect 10 samples in the region where measurements were taken with the ThetaProbe. A representative sample was collected using sections of plastic gutter piping 6 cm in length and approximately 4 cm in diameter. The initial weight of the sample was taken, oven dried at 105°C for over 24 hours, and then re-weighed. The average gravimetric moisture content, normally expressed as g water g⁻¹ soil (oven dried) or as a percentage, was then calculated using the following formula:

$$\text{gravimetric moisture} = \text{mass of water lost} / \text{mass of oven dried soil} \quad (4.4)$$

Conversion to an estimate of the volumetric moisture content is achieved with knowledge of the bulk density of the dry soil sample. Problems were encountered in keeping the structure of the soil constant during removal of the sample. This was caused by low values of soil moisture and the poor, unconsolidated structure of desert soils. Therefore, values of bulk density were derived from published work conducted under a National Soil Map and Land Use Project undertaken in parts of the region (The Soils of Jordan 1993, 1994). Their method involved a sharp edged cylinder being hammered into the ground, thus reducing compaction of the soil at the cylinder sides. Due to the low number of observation sites their survey only produced five locations that had corresponding gravimetric moisture and bulk density measurements. The formula that converts gravimetric moisture content to volumetric is given by:

$$\theta_v = \text{gravimetric water content} * \text{bulk density} \quad (4.5)$$

The results of this data verification exercise are shown in Table 4.4. The results show poor approximations of measurements made by the ThetaProbe compared with more time-consuming laboratory methods. There seems to be a general under-estimation of the volumetric moisture using laboratory methods. This could possibly be due to the loss of small amounts of moisture before samples were analysed in the laboratory caused by the lack of laboratory facilities at the field centre. Weighing of the samples

could only be done, in some cases, up to several days later in the laboratories of the University of Jordan. More estimates, particularly of bulk density, are required to fully test the validity of the readings. However, due to the problems in collecting this data, it was decided that the recording made by the ThetaProbe would be used and not measurements that relied on gravimetric and bulk density estimates.

Site name	Volumetric moisture estimate with ThetaProbe (cm ³ water cm ⁻³ soil)	Volumetric moisture estimate in the lab. (cm ³ water cm ⁻³ soil)
Qa'a ash Shubayka	0.08 (mean of 30 samples)	0.04 (mean of 10 samples)
Chert gravel (hammada)	0.12	0.03
Qa'a al Abd	0.11	0.04
Qa'a al Buqayawiyya (1)	0.12	0.08
Qa'a al Buqayawiyya (2)	0.11	0.09

Table 4.4. Results of the data verification experiments of comparing volumetric moisture readings from the ThetaProbe and more standard laboratory methods.

4.4 Surface roughness

4.4.1 Definitions

As outlined previously (Chapter 2) it is essential to quantify the roughness properties of a surface as this parameter can influence the backscatter signal to some degree. There are two statistical parameters that have been shown to be important in radar studies and which feature as inputs to the theoretical models used in the study. They are known as the standard deviation of surface height, also known as root mean square (RMS) height and abbreviated as σ ; and the correlation length l . Both are presented in units of centimetres. The method of measurement and derivation of each of these parameters are discussed below. This information is reflected in the specification of the equipment used

and the field methodology employed. Outlined below are the basic definitions of these parameters and the procedures that were adopted in the field. Various issues are raised on the usefulness of the roughness data, in particular the correlation length, in such studies. These were based on observations made during the data analysis phase of the research and are discussed in Chapter 5.

4.4.2 RMS height

The RMS height of a surface indicates to what degree discrete measurements of the height of a surface above an arbitrary plane varies. Obviously the greater the spread of height measurements, the greater the value of RMS height. For studies with radar, in particular radar at wavelengths of the order of centimetres (C band = 5.6 cm), the general rule of thumb is that the spacing interval, Δx , between measurements is such that $\Delta x < 0.1\lambda$ (Ulaby *et al.* 1982). Therefore, it has been established that the optimal sampling interval to derive discrete height measurements is approximately 0.5 cm. For the series z_i ; $i = 1, 2, \dots, n$ the RMS height for the discrete one-dimensional case is given by:

$$\sigma = \left[\frac{1}{N-1} \left(\sum_{i=1}^N (z_i)^2 - N(\bar{z})^2 \right) \right]^{\frac{1}{2}} \quad (4.6)$$

where,

$$\bar{z} = \frac{1}{N} \sum_{i=1}^N z_i$$

and N is the number of samples.

In all cases the number of discrete height measurements exceeded 58. The actual number taken was varied in two ways. Firstly, with respect to deriving the correlation coefficient value, and secondly, in an attempt to derive an optimised methodology of data collection with the aim of making the data collection process more efficient.

4.4.3 Correlation length

The relationship between the height above an arbitrary plane of one point located at point a and the height of another point a' distant from a can be statistically expressed in the form of an autocorrelation coefficient. The variation in the value of the autocorrelation coefficient as the distance between the two points increases is referred to as the autocorrelation function. On occasion this function can be mapped to a mathematical function such as the exponential or Gaussian (normal) distributions. The correlation length (l) is the displacement from the original point, a , when there exists no statistical relationship between the two points. The normalised autocorrelation function, $\rho(a')$ in the discrete case, is given by:

$$\rho(a') = \frac{\sum_{i=1}^{N+1-j} Z_i Z_{j+i-1}}{\sum_{i=1}^N Z_i^2} \quad (4.7)$$

for a spatial displacement $a' = (j-1)\Delta x$, where j is an integer ≥ 1 .

The surface correlation length, l is usually defined as the displacement a' for which $\rho(a')$ is equal to $1/e$:

$$\rho(a') = 1 / e \quad (4.8)$$

Consider, for example, two of the natural surfaces found in the study region, the basalt and $qa'a$ surfaces. The randomly distributed, non-uniform shape and size of the basalt should yield relatively short correlation lengths because of a quickly diminishing relationship between displacement from the origin and the surface height measurement. Alternatively on a $qa'a$ surface, which is characteristically very flat, with almost undetectable variations in surface height, even points with a large displacement from the origin will be highly correlated with the height measurement of the origin point. It also makes sense that a perfectly flat surface will have a correlation length of infinity as all

points that could be sampled will be of the same height and therefore fully correlated. In addition, an increase of surface slope, with respect to an horizontal reference surface, would lead to an increase in the correlation length. Therefore, measurements were taken in areas where surface slope was negligible.

4.4.4 Autocorrelation function

The autocorrelation function describes the relationship between how the correlation length behaves as the distance a , becomes larger. To satisfy the model criteria, explained in more detail in Section 2.6, the measured data should approximate either exponential or Gaussian distributions. Figure 4.4 shows two examples from sites that approximate exponential and Gaussian theoretical distributions. A number of sites analysed displayed autocorrelation functions that did not approximate to a theoretical distributions, in which case further analysis of these profiles were undertaken.

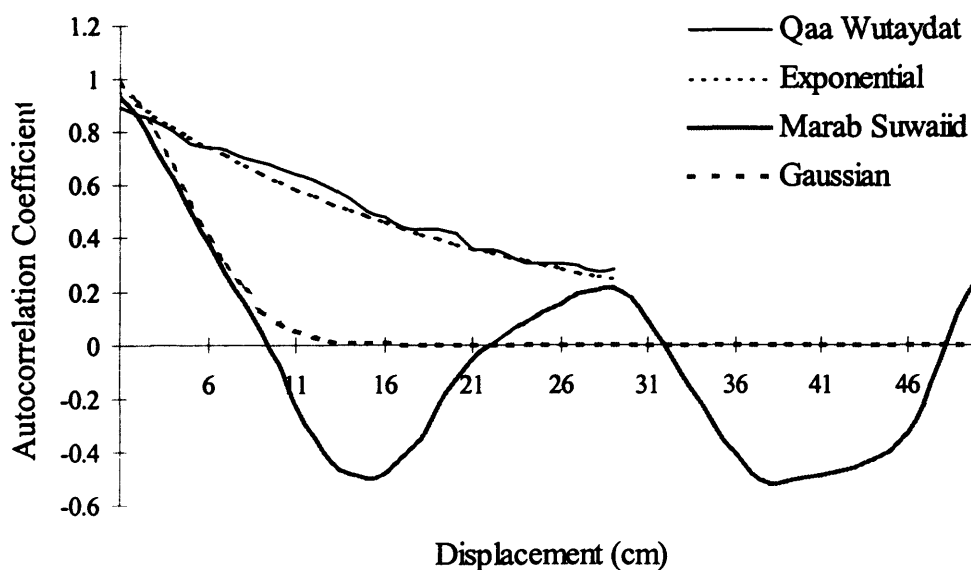


Figure 4.4. Measured autocorrelation functions derived from field data shown against approximate Gaussian and exponential functions.

4.4.5 The profilometer

The equipment used to derive both the RMS height and the correlation length was referred to as a pin profilometer. The device initially was constructed with 60 pins with a separation of 0.5 cm; a larger profilometer was constructed later which comprised 96 pins. The pins were attached to a frame with locking clips that could trap the pins against the frame. Also fixed to the frame was a spirit level to enable the frame to be on a horizontal plane. Behind the frame was attached a sheet of thin wood covered with graph paper, this providing a reference with which the pins would be shown against. The profilometer fully set is shown in Figure 4.5 for a basalt surface (upper) and a *qa'a* surface (lower).

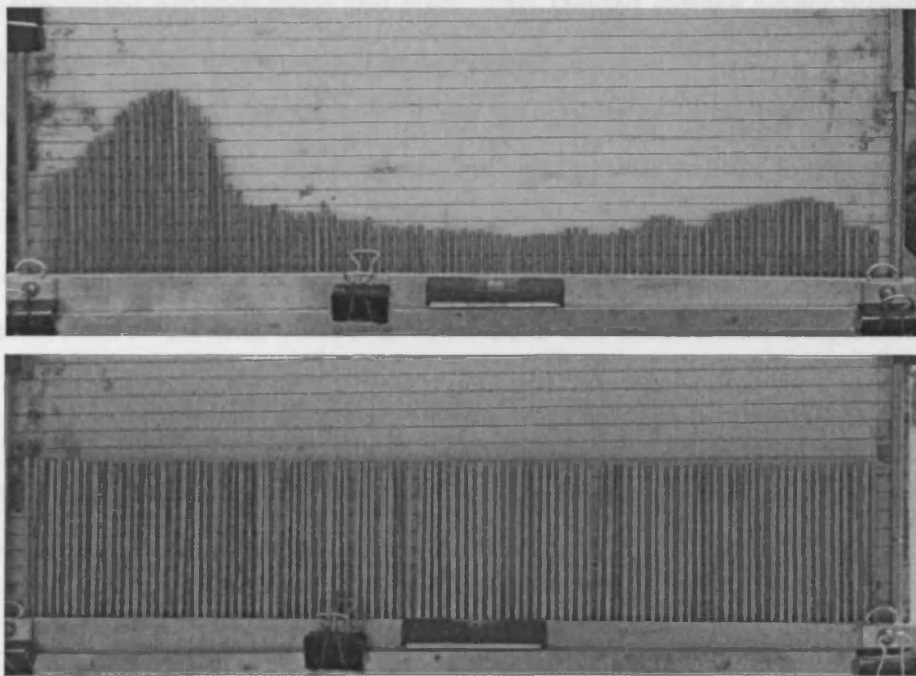


Figure 4.5. 48 cm (96 samples) profilometer used for measuring surface height values set up to record on a basalt surface (upper) and a *qa'a* surface (lower).

The procedure was first to reset the pins, to place the profilometer vertically on the surface and adjust the metal rods at the side so that the spirit level indicated that the frame was horizontal. The pins were then released and would assume the shape of the

surface below. When all of the pins were just touching the ground a photograph of the pins was taken against the background of graph paper.

4.4.6 Roughness profile length

It was intended that for each of the sites visited a surface roughness measurement would be obtained. The method and number of samples was also modified in light of further understanding gained after fieldwork. Ideally many profiles would be needed to fully describe the surface roughness properties, but the type of equipment and the human resources available deemed a reduced sampling methodology the only feasible option. At random locations within the 30 by 30 m quadrat consecutive profiles were collected. During the first two field visits, each profile was 30 cm long and the number of profiles at each site varied between three and eight. This yielded surface height measurements, at a resolution of 0.5 cm, over a length between 60 and 240 cm. Care was taken to ensure the start and finish points were in the same place and that the surface slope over the whole length of transect was minimal. Following modifications to a more structured and consistent methodology, and using a longer profilometer (48 cm) during the spring 1997 field visit, a transect length of 2.88 m, consisting of six individual profiles were collected at each of the sites visited. In some cases two transects were collected, making a total of 12 individual profiles per site. The analysis phase after this particular field visit was very time-consuming and it was thought that one three meter transect was adequate, this technique being used in the final field visit (spring 1998). Data were therefore available for calculating the roughness parameters from a range of transect lengths which, developed considerable interest in the author and is discussed in more detail in the next chapter.

4.4.7 Photograph analysis

The photographs were developed to A4. The photo was then digitised using ARC INFO software by choosing a horizontal level and digitising the top of the pins with reference to this plane. This was carried out until all of the pins were digitised. The relative heights of the pins were then converted to centimetres by transforming the edges of the

graph paper to units of length. For example, the length of the background of graph paper was 50 cm and the height 20 cm. This yielded the height of the pins (cm) for the whole transect. It should be noted that the absolute value of the heights are less important, than the statistics of their heights. The measurements were entered into a spreadsheet for further analysis. Profiles were stitched together by assuming that the first height measurement on profile 2 was the last height measurement of profile 1 and therefore these heights could be matched and the adjustments made for subsequent points on profile 2. Figure 4.6 shows two example profiles collected for a *qa'a* and a basalt surface. In both cases the values fluctuate around a mean of zero.

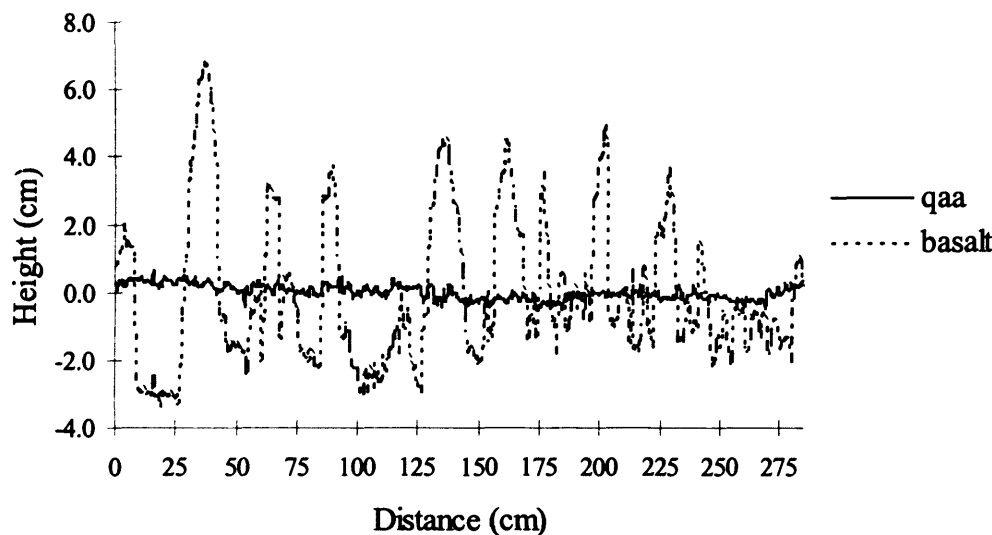


Figure 4.6. Example profiles recorded for a qa'a (black line) and a basalt (dashed line) surface. Both surfaces have a mean height of zero cm.

The profiles show the *qa'a* surfaces are characteristically very flat with only small fluctuations in height caused by cracks, small depressions and uplifts. Basalt surfaces are comparatively rough with large deviations in surface height being caused by stones and boulders lying on the surface. The underlying soil surface is reasonably flat. Care was taken to correctly record each point accurately. A review of the potential sources of error in deriving the roughness parameters, from a similar pin profilometer, is given by Archer (1995) who digitised profiles taken on a smooth, flat glass surface. Likely sources of error would come from small differences in the length of the pins and in the

digitising process. Archer (1995) approximated the error term to be ± 0.105 mm. Some points in each profile were checked to make sure the digitising and transformation procedures had been correctly implemented. Each profile took approximately fifteen minutes to process.

4.4.8 Problems and alternative methods

Using the pin profilometer method, there are numerous ways in which errors can be introduced into the analysis. Initially, the profile has to be horizontal and checks need to be made to ensure all the pins are touching the ground. The photograph should also be taken on the level. When digitising, it is important that the very tip of the pin is registered for every profile. However these errors can be minimised with proper due care and attention. Other methods of obtaining the surface roughness measurements required were investigated. The laser profilometer (Huang and Bradford 1990) is one such method. This instrument, originally developed to look at micro-relief in wind erosion studies, measures surface elevation data by storing the elevation data recorded by a laser beam returning from the surface of the soil. The resolution of the sampling can be controlled from a computer and typically would be 0.5 cm over a 1 by 1m grid, this would yield over 40, 000 readings per plot. Obviously such a high resolution of readings would not be required for this study, five transects of 1m at the sampling resolution of 0.5 cm would be ideal. However, the advantages for such a device are numerous; surface elevations and roughness statistics could be calculated directly using a simple computer program, human error would be negligible and other work could be undertaken, soil moisture sampling for example, while the laser profilometer was operating. Investigations into obtaining such an instrument led to correspondence being made with the United States Department of Agriculture, specifically to Ted Zobeck of the Agricultural Research Service (personal communication, 1996) who informed me that the only device in Europe was located in Belgium. There was no such equipment available in the UK. Attempts at locating one in the UK proved fruitless, no such device were owned by the equipment pools of the NERC and EPSRC. The cost of building such a device in-house was beyond the budget of the research funding. Therefore the pin profilometer was used throughout the duration of the study period and any potential sources of error minimised.

4.5 Soil texture

4.5.1 *Particle size analysis*

The texture of the soil influences the dielectric properties of the soil medium, described in Section 2.1.3 and therefore it is important that these properties are measured. The methodology uses two sources of data. First, primary data consisting of original samples being collected in the field and analysed in the laboratory. Secondly, secondary data collected by soil scientists for the National Soil Map and Land Use Project (The Soils of Jordan 1993, 1994) during the early 1990's. Parts of the project area were covered by reconnaissance and semi-detailed surveys by the project (levels I and II). The locations of the sites analysed for their textural properties are displayed in Figure 4.7.

Data on the particle size distribution of the soil at 16 sites were analysed in the laboratories of the Universities of Leicester and Jordan. At each site, within the 30 by 30m quadrat, 10 samples were collected from the upper 5 cm of the surface material. The mass of the sample was approximately 100 grams. The method for deriving the particle size distribution in terms of percentage sand, silt and clay uses a sedimentation technique followed by sieving. The particle size class distinction is one commonly used in the United Kingdom; sand-size particles are greater than 63 μm , clay-size particles are less than 2 μm and silt-size particles are in between these class boundaries. The sand fraction is separated using a 63 μm sieve, whereas the clay fraction is determined by particle settling times in distilled water of a constant temperature. The standard laboratory procedures followed are given in Rowell (1994).

The methods used here to determine the particle size distribution are suitable for most soils and sediments. Dry sieving can only be conducted if high proportions of sand are present. As most soils contain significant amounts of silt and clay pipette and hydrometer methods (based on sedimentation techniques) have to be used. However, prior to textural analysis, it is necessary to pretreat most soils. This involves two processes, the removal of organic matter and the disaggregation of the soil.

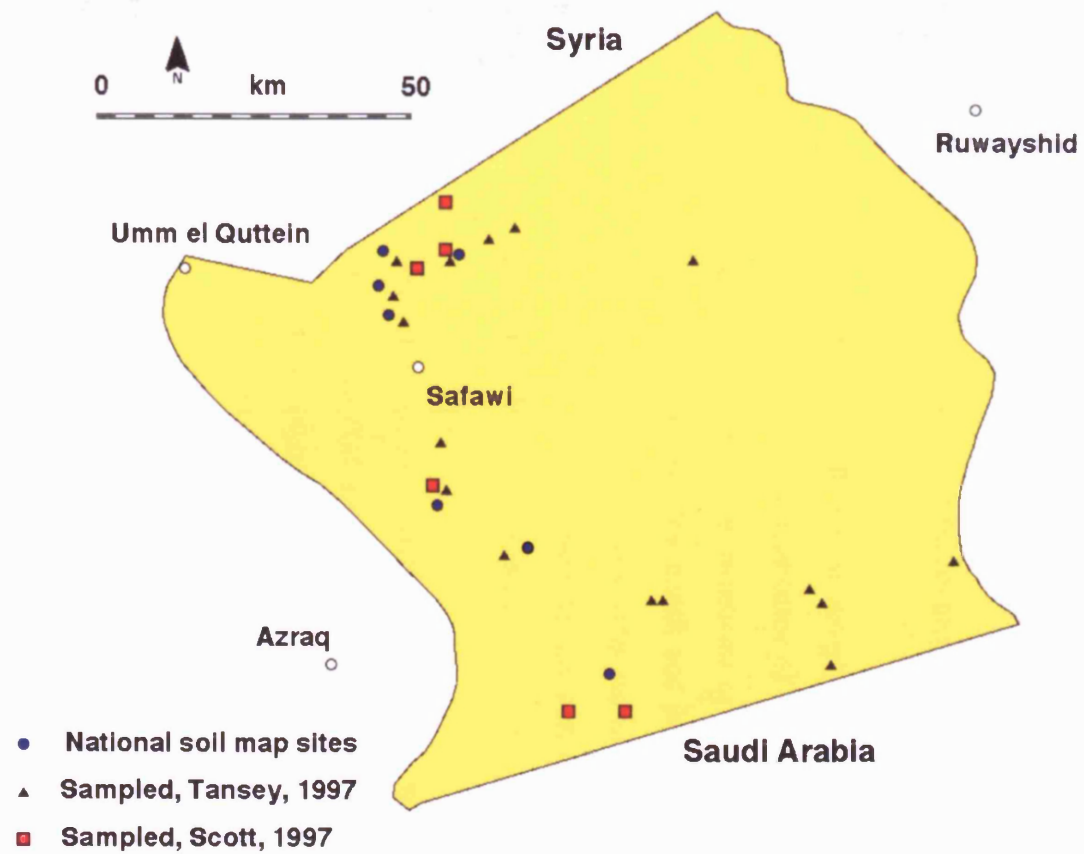


Figure 4.7. Location of the sites where soil texture analysis was undertaken in the BRDP study area.

The former step can sometimes be omitted, as is the case in this study, when organic matter levels are very low. The second step is essential, normally using the dispersant sodium hexametaphosphate. If this step is not carried out then the amounts of clay -size particles will be under-represented. The technique of sedimentation is based on theoretically derived settling times for particles of different sizes. These times, calculated using Stokes' Law assume that the particles are spherical, are of constant density and that the density of the settling liquid is constant. Obviously, the soil particles are not spherical, clay particles are often platy, and therefore at least some errors are expected in this procedure. The density of the settling liquid is kept constant using a water bath, set at a constant temperature of 20°C, and great care is taken not to disturb the samples after they have been thoroughly mixed.

The results of the particle size analysis for the samples collected are shown in Table 4.5. Figure 4.8 shows the particle size characteristics of the main land surface units. The *qa'a* surfaces are characterised by large quantities of clay and silt-size particles and small amounts of sand-size particles. The basalt and *hammada* surfaces show a high representation of sand and silt-size particles. The *marab* surfaces mainly have large proportions of silt-size particles but also show the greatest variation in particle size. The example cited in Figure 4.8 is for *Marab Salma*.

Data were also utilised from analysis conducted by Dawn Scott at the University of Durham for a number of sites that are used in this study. The samples were firstly treated to remove traces of organic material using hydrogen peroxide and then disaggregated using sodium hexametaphosphate. They were analysed using a Coulter LS 230 Lazer granulometer. The particle size classes are from the Wentworth grain size classification. Five samples were collected at each site of which six sites were useful for this study. The results from this analysis are shown in Table 4.5.

Land unit	Site	% Gravel	% Sand	% Silt	% Clay	Bulk density (g cm ⁻³)
Analysis by K. Tansey, in the labs. of Universities of Jordan and Leicester, 1997						
Qa'a	al Abd	N/A	2.3	67.6	30.1	N/A
	Qattafi	N/A	4.5	65	30.5	N/A
	Witadi	N/A	5.2	71	23.8	N/A
	al Ra'd	N/A	7.4	77.4	15.2	N/A
Basalt	Abed	N/A	35.6	59.8	4.6	N/A
	Fahda	N/A	31	54.9	14.1	N/A
Hammada	gravel	N/A	49	48.7	2.3	N/A
	sand	N/A	95.3	3.3	1.4	N/A
Marab	Shubayka	N/A	6	87.2	6.8	N/A
	Salma	N/A	14.8	71.9	13.3	N/A
	Suwaiid	N/A	41.5	43.9	14.6	N/A
	'Wia agri.	N/A	13.1	56.3	30.5	N/A
	Qattafi	N/A	25.7	51.7	22.5	N/A
	'Wia	N/A	1.6	81.3	17.1	N/A
	al Wassad	N/A	88.7	8.8	2.5	N/A
	Wutaydat	N/A	74.4	22.8	2.8	N/A
Analysis by D. Scott in the labs. of the University of Durham, 1997						
Basalt	near Abed	1.6	55.1	27.8	17.5	N/A
Hammada	Hazim	2	84.9	8.4	4.7	N/A
Marab	Dihikiya	0.2	32.2	29	38.6	N/A
	'Wia	1.6	36.1	30.2	32.1	N/A
	Hashad	2.6	63	19.3	15.1	N/A
	Salma	0	68.5	18.4	13.1	N/A
Analysis by scientists of the National Soil Map and Land Use Project, 1991						
Qa'a	al Abd	N/A	3.3	60	36.7	1.36
	nr. Fahda	N/A	4.5	62.1	33.4	N/A
Basalt	near Abed	N/A	47.2	36.1	16.7	N/A
Hammada	chert 1	N/A	1.5	52.4	46.1	1.58
	chert 2	N/A	48.6	37.2	14.2	1.58
Marab	'Wia	N/A	1.2	68.1	30.7	1.54
	Shubayka	N/A	1.5	44.0	51.5	1.35

Table 4.5. Soil analysis results of particle size and bulk density measurements.

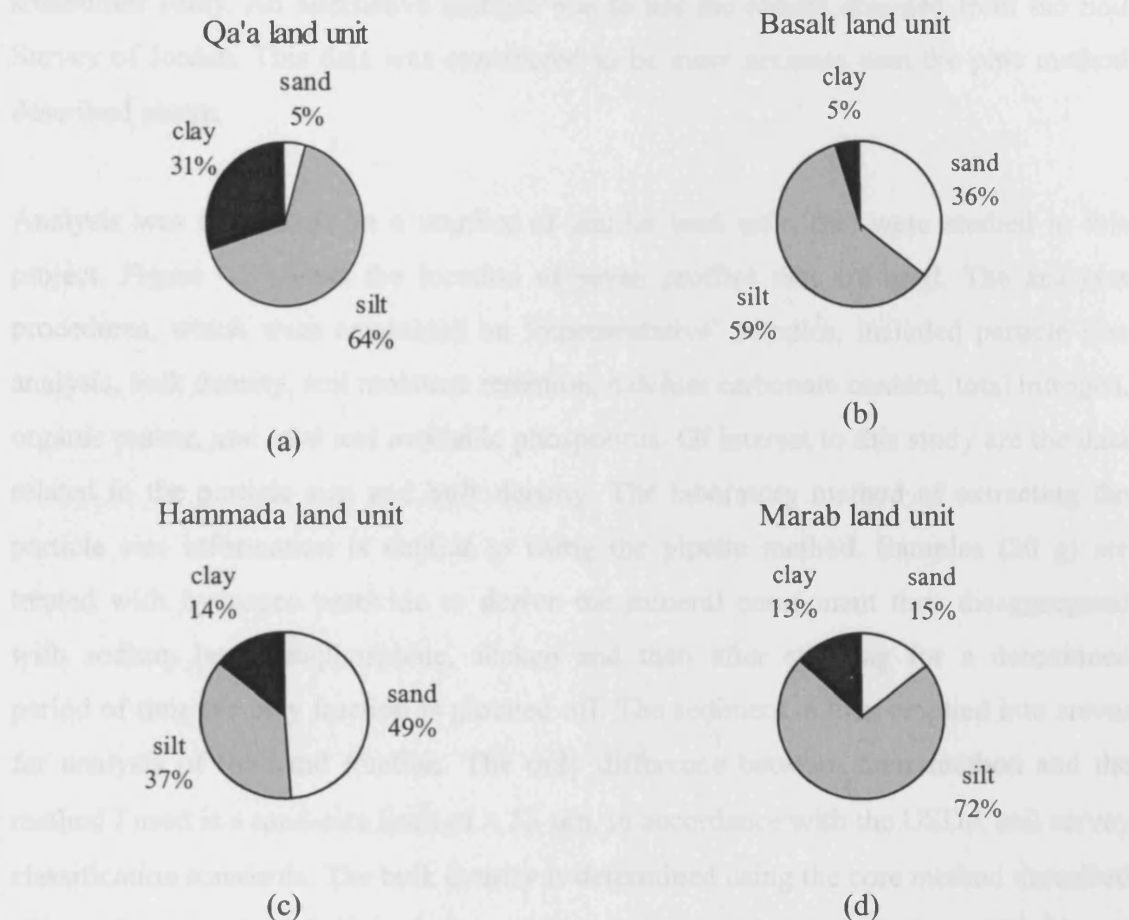


Figure 4.8. Generalised soil particle distribution percentages for the four main surface types, (a) qa'a surface, (b) basalt surface, (c) hammada surface and (d) marab surface.

4.5.2 Bulk density

The bulk density of a soil is a parameter that has to be determined if the volumetric moisture content is to be calculated by the gravimetric moisture content. For a detailed explanation of the method of extracting a soil sample and measuring bulk density the reader is referred to Rowell (1994, pp. 67-69). The most popular method is using a plate and cylinder that is driven into the soil. A similar method, using sections of thin drainpipe, was used in the field. However due to the dry, structureless nature of the soils, reliable intact samples could not be collected as they tended to break up. These

soils can be described as problem soils, consisting of large pores, cracks and are sometimes stony. An alternative method was to use the results obtained from the Soil Survey of Jordan. This data was considered to be more accurate than the pipe method described above.

Analysis was carried out in a number of similar land units that were studied in this project. Figure 4.7 shows the location of seven profiles that are used. The analyses procedures, which were conducted on 'representative' samples, included particle size analysis, bulk density, soil moisture retention, calcium carbonate content, total nitrogen, organic matter, and total and available phosphorus. Of interest to this study are the data related to the particle size and bulk density. The laboratory method of extracting the particle size information is similar to using the pipette method. Samples (20 g) are treated with hydrogen peroxide to derive the mineral component then disaggregated with sodium hexametaphosphate, shaken and then after standing for a determined period of time the clay fraction is pipetted off. The sediment is then emptied into sieves for analysis of the sand fraction. The only difference between their method and the method I used is a sand-size limit of $> 53 \mu\text{m}$, in accordance with the USDA soil survey classification standards. The bulk density is determined using the core method described above. Once in the laboratory the samples are oven dried overnight at 105°C and weighed. The bulk density is calculated by dividing the mass of the oven dried soil by the volume that it occupied in the core cylinder. The results from the analyses are also shown in Table 4.5.

4.6 Specific basalt site analysis

It was considered important to collect data relating to the distribution, size and cover of basalt rocks in the three basalt covered sites visited in the field. The aim of this exercise was to produce relationships between the satellite signal and the basalt rock properties. The following data were collected (Table 4.6) and are described in Tansey *et al.* (1996).

Parameter	Fahda Vesicular (B1)	Madhala Olivine (B2)	Abed Olivine (B3)
<i>Percentage Cover (5 X 30m transect):</i>			
Mean soil cover %	16.1	44.7	47.9
Mean rock cover %	83.9	55.3	52.1
<i>Stone Dimensions (3 X 2* 2m quadrat):</i>			
Average x, y, z axis	10.3, 7.6, 4.9 cm	10, 7.5, 4.8 cm	17, 12.5, 8.7 cm
s.d. x, y, z axis	5.6, 4, 2.8 cm	6.7, 5.3, 3.2 cm	9.3, 6.7, 5.4 cm
Total no. of stones	669	N/A	334
Stones / quadrat	223	155	111
Mean stone volume	715 cm ³	2245 cm ³	3539 cm ³

Table 4.6. Stone characteristics measured at the three basalt sites included in the study.

4.6.1 Percentage cover

Five 30m transects were taken at random angles from a point to measure the amount of soil cover recorded as a distance along the transect. This yielded an estimate of the percent of soil cover and hence percent rock cover at the surface. The results are shown in Table 4.6, the percentage cover varying for the different sites and related to the age of the basalt flows, described in Section 1.1.

4.6.2 Average stone dimensions

Three 2 by 2m quadrats were completely stripped of stone cover (stones being considered anything larger than 2 cm in any major axis). Each stone was measured in the directions of the three major axes, x, y and z. Once all the stones were measured, the

average and standard deviation of the dimensions and number of stones per quadrat were calculated. These are shown also in Table 4.6 for the Fahda Vesicular (B1) and Abed Olivine (B3), data were not collected for Madhala Olivine basalt flow (B2), but is shown instead from a basalt formation within the same Group (Asfar) as the B2 basalt.

4.7 Climate data

4.7.1 Introduction

Weather conditions prevalent over desert regions have a major influence on soil moisture levels. Therefore measuring climatic parameters is important in understanding their effects on the water content of soils. In Jordan, the majority of the information about the weather and climate are obtained from either the Water Authority of Jordan or the Department of Meteorology, measurements being recorded on a hourly or a daily basis (Table 4.7). These permanent recording stations are thinly scattered in the study area (Figure 4.9). To support the data already being collected, data from two temporary weather stations have been used. The first, owned by the University of Leicester, was set-up to the north of *Marab Salma*, adjacent to a large *qa'a* near to 32.44027° N and 37.27084° E (Figure 4.8). The station was operational at the following times; 15-December-1995 to 29-March-1996 recording values every minute and averaging over 20 minutes, 14-May-1996 to 28-October-1996 taking values every 5 minutes and averaging these over an hour. The second station, owned by NERC, was set-up at Lower Farm, Menara situated at approximately 32.2° N, 36°.75 E (actually outside of the study area) and was operation from between August 1994 and August 1996. The station at Menara obtained samples every 10 seconds downloading an output to the logger every hour. Unfortunately, during the summer of 1997 the AWS belonging to the University of Leicester (located at *Marab Salma*) was stolen, no recovery was ever made. Both stations were equipped to monitor the following parameters; incoming solar radiation, net radiation, temperature and humidity, wind direction and speed and rainfall. In addition the station situated near Marab Salma also monitored the soil temperature and soil heat flux. Data was output to a logger and downloaded to a PC.

Station name	Palestinian grid reference (N, E)	Altitude (m a.s.l.)	Date Established	Type of Raingauge ¹
Deir al Kahf	185° 325°	1025	1963	D
Umm El-Quttein	192°5 303°5	986	1947	D & R
H5 – As-Safawi	180° 348°5	715	1968	D & R
Azraq evap. station	141°5 320°	533	1962	D & R

¹ D: Manual daily, D & R: Automated daily and recorder.

Table 4.7. Rainfall stations within the Azraq Basin. Adapted from Water Authority of Jordan (1998).

The locations of these weather stations are classified into topographically affected (Deir al Kahf, Umm El-Quttein and Menara) or non-topographically affected (Safawi, Azraq and *Marab Salma*) stations. Figure 4.9 shows the approximate locations of these stations (apart from the Menara station which located west of Umm El-Quttein outside of the study region) and the precipitation record for the winter of 1995/96. Data from these stations are analysed in the following sections.

4.7.2 Precipitation

4.7.2.1 Long-term rainfall patterns

Rainfall is probably the most important influence on the distribution and amount of soil moisture. The nature of rainfall in semi-arid and arid regions is very different from that in temperate regions. Briefly summarised, it normally consists of events of high intensity, short duration with sporadic and inconsistent return periods. The climate of the eastern Jordan Badia is influenced by synoptic scale weather conditions in the winter caused by cyclones and low-pressure systems over the Mediterranean, and also by smaller-scale orographic effects caused by the Jebel Hauran in the north of the study area. The majority of the precipitation falls between the months of October and April.

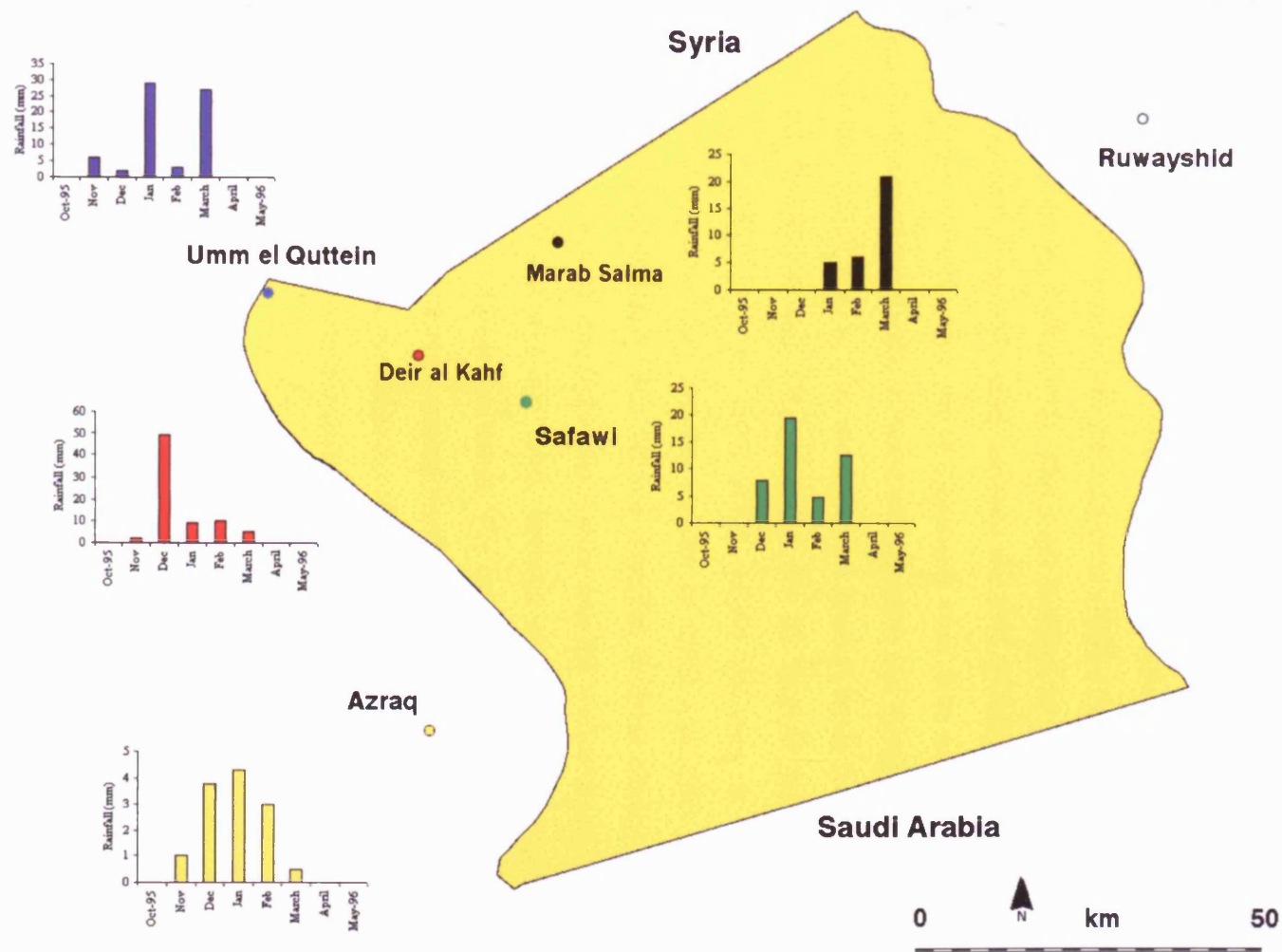


Figure 4.9. Locations of the automatic weather stations in the study area (Menara station is outside the study area).

However there are significant differences between when and where rainfall falls in the eastern Badia on a year to year basis.

Analysis of the long-term data available from the gauges owned by the Jordanian Water Authority, show large annual fluctuations of precipitation since measurements began, resulting in a large standard deviation of measurements at all sites. Also, that topographic effects, on the amount and distribution of precipitation, are significant and do not form any clear relationships with the rainfall recorded at sites without any topography. Therefore, cross-correlation of rainfall values estimated at these weather stations is difficult. A synthesis of the long-term (1963-1989) variation in rainfall in the study area is given by Kirk (1998). The main findings of Kirk's analysis are that the standard deviation in annual values account for 45% of the annual total. Furthermore, the topographic affected sites show a decrease with time in average annual rainfall values and the non-topographic affected sites (Safawi and Azraq) show more consistent, stable annual rainfall values. The mean annual rainfall totals for topographic affected sites, Umm El-Quttein and Deir al Kahf for all records are 169 and 136 mm respectively. During 1980 to 1989, mean values decrease to 137 and 110 mm respectively. Additional data for the winters of 1992 and 1993 further confirm a decrease in rainfall totals, 13 and 80 mm recorded in these winters at the Umm El-Quttein station. However, the following winter was the wettest since 1979 (the annual total at the Menara site was 204 mm). Rainfall at the non-topographically affected stations appears not to follow this trend. The inter-annual mean rainfall totals display significant fluctuation. The mean annual rainfall at the Safawi site for the period 1963 to 1989 being 76 mm, the same value for the Azraq site is 70 mm. These data seem to resemble a somewhat random distribution with no specific trends recognisable.

The pattern of rainfall distribution over the winter period (1980-1990) is shown in Figure 4.10. The maxim of rainfall at all stations with long-term records occurs in December. Umm El-Quttein has the highest rainfall at approximately 122 mm a year on average. Deir al Kahf, situated further east, receives an average of 113 mm of rainfall a year. At topographically affected sites most of the rainfall falls in December, significant amounts can fall through until March. The rainfall distribution for the non-topographically affected sites, Safawi and Azraq, bears little resemblance to the pattern of distribution at the stations in the higher north-west of the region. The Azraq station

also shows an average October rainfall value that is almost double for any other site and more rainfall falls during the month of April in the region of Safawi than at any other station. The Safawi and Azraq graphs show no distinct intra-seasonal trends and no particular maximas (Kirk 1998).

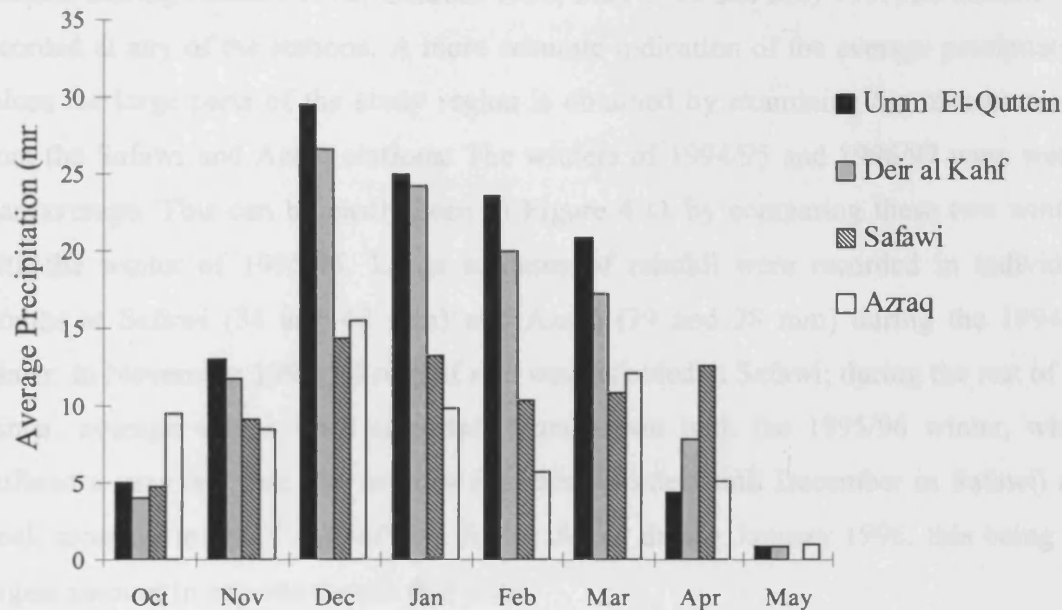


Figure 4.10. Mean monthly precipitation values for the five long-term monitoring stations located within the study area for the period 1980 to 1990.

4.7.2.2 Short-term rainfall patterns

In order to investigate the amount and distribution of soil moisture content it is required to obtain information related to the location, amount and duration of precipitation events. It is especially important in relating the occurrence of a precipitation event to the acquisition date of satellite imagery. Precipitation data from the winter 1994/95 to the winter of 1996/97 are presented from the four permanent weather stations described previously. In addition, data from the temporary weather stations at *Marab Salma* and *Menara* (Figure 4.11) are presented.

Rainfall at the three topographically affected sites (Umm El-Quttein, Deir al Kahf and Menara occurs during most of the winter months. During individual months up to 50 mm of rainfall was recorded at these stations, although no pattern of rainfall can be detected in the measurements (Figure 4.11). This is, of course, assuming that the monthly totals is a reflection of the number of rainfall events, for which there are no daily data available. The temporal distribution of rainfall events can best be described as random. During January 1995, October 1996, May 1996 and May 1997, no rainfall was recorded at any of the stations. A more accurate indication of the average precipitation values for large parts of the study region is obtained by examining the measurements from the Safawi and Azraq stations. The winters of 1994/95 and 1996/97 were wetter than average. This can be easily seen in Figure 4.11 by comparing these two winters with the winter of 1995/96. Large amounts of rainfall were recorded in individual months at Safawi (34 and 42 mm) and Azraq (39 and 28 mm) during the 1994/95 winter. In November 1996, 44 mm of rain was recorded at Safawi; during the rest of the winter, average values were recorded. Comparison with the 1995/96 winter, which suffered a very dry first few months (no rain recorded until December in Safawi) and small monthly totals (5 mm of rain fell in Azraq during January 1996, this being the largest amount in any one month that year).

Analysis of individual rainfall events at *Marab Salma* for two time periods (December 1995 - March 1996 and May 1996 - October 1996) is presented in Figure 4.12. 14 precipitation events were recorded resulting in a total of 30.5 mm. Seven events occurred during March were concentrated around two dates (not shown in Figure 4.12), the 6th and 25th. The highest intensity recorded was 6 mm h^{-1} (6 March 1996). The low amount of precipitation recorded during the winter of 1995/96 can be explained in two ways. First, as described previously, winter rainfall was lower than average. Second, the plastic raingauge used was constructed by Environmental Measurements and the type and size of tipping bucket used may have led to an underestimate being made. One reason is that 52% of rainfall events recorded at the Menara site were less than 0.5 mm in magnitude and the bucket size used at the Salma site was calibrated to tip every 0.5 mm of rainfall, possibly indicating that half of the rainfall events were not recorded at all (Kirk 1997). However, in tests conducted by Tansey (1994) it was shown that at low intensities the gauge tended to over-estimate the amount of rainfall by up to 2 %.

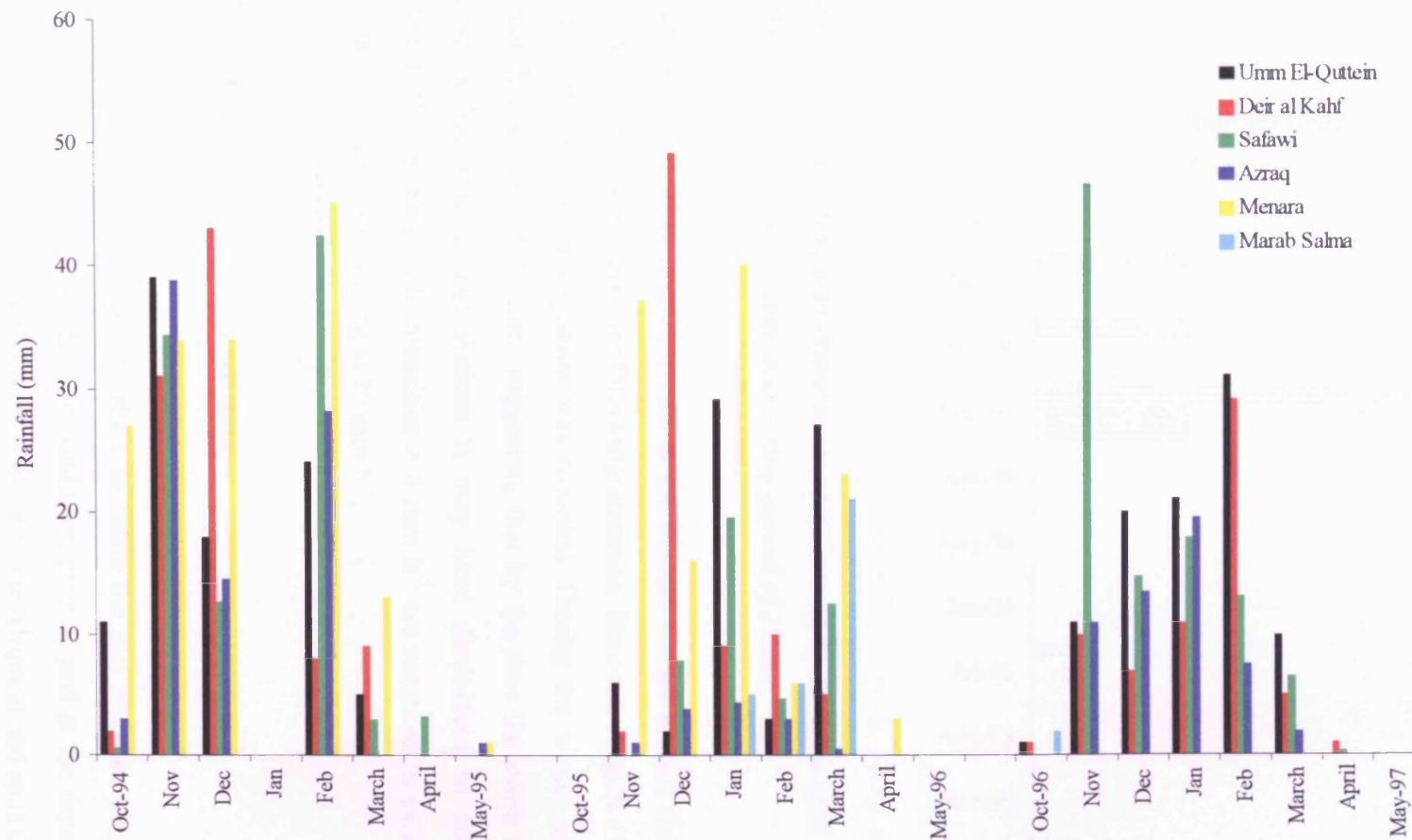


Figure 4.11. Rainfall values recorded at permanent (Umm El Quttein, Deir al-Kahf, Safawi and Azraq) and temporary (Menara and Marab Salma) weather stations in the eastern Badia of Jordan (1994/95 to 1996/97). Please refer to the text for the dates that these stations were used.

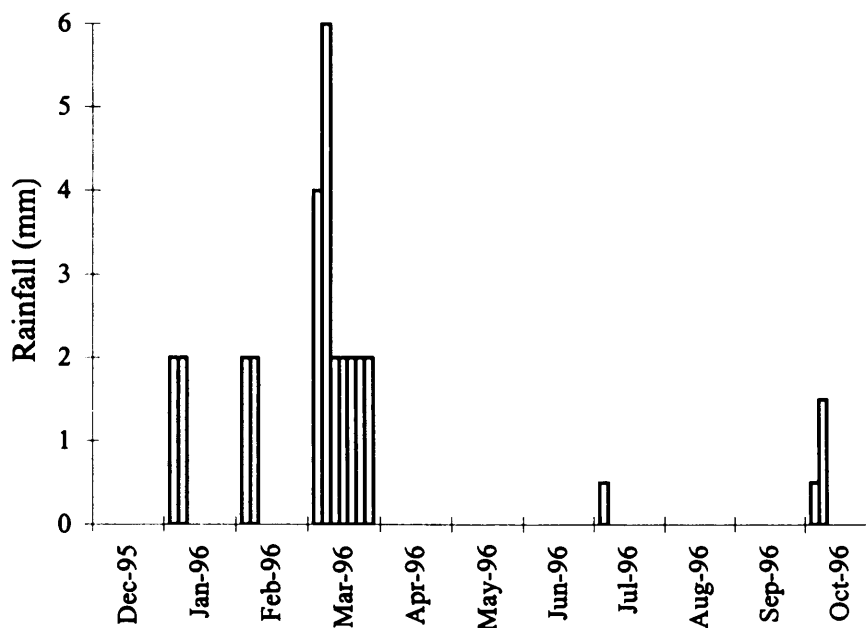


Figure 4.12. The temporal distribution and the magnitude of rainfall events recorded at the Marab Salma raingauge over a time period of 1 hour.

Analysis of individual rainfall events at the Menara station located farther to the west than *Marab Salma* yielded the following statistics. Between August 1994 and August 1996, 190 hours of precipitation was recorded. During the winter of 1995, 66% of rainfall hours were of 0.5 mm (suggesting that by the time the storm cell reached the *Marab Salma* and Safawi stations it may have diminished in size and become undetectable). Storms with intensities $> 4 \text{ mm h}^{-1}$ are recorded in small numbers, the maximum intensity registering at 20 mm h^{-1} .

4.7.2.3 The utility of the rainfall data

The rainfall data are used in this study to relate the soil moisture conditions that are measured in the field to the climatic conditions prior to and at the time of the satellite overpass. Therefore particular interest is given to the temporal and spatial distribution of rainfall from the period March 1995, when the first image was collected, through to the spring of 1998 when the last image was acquired. By correlating the occurrence of

precipitation events with the acquisition of satellite imagery it is possible to study the influence of increases in surface soil moisture on the response of the radar signal. Furthermore, studying these surfaces when there has been no rainfall is important to determine the scattering behaviour in dry conditions. It was shown in Chapter 3 that precipitation data is critical to the interpretation of SAR imagery.

4.7.3 Temperature

4.7.3.1 Air temperature

A brief introduction to the range of air temperatures experienced in the eastern Badia was given in Section 1.1. The variation in air temperature is marked but not extreme over diurnal and annual periods. Greater extremes of temperature exist the further east one progresses as the influence of Mediterranean climate diminishes. The air temperature at the *Marab Salma* station was measured at a height of 2 m above the ground and was recorded along with relative humidity. The mean daily temperature, shown in Figure 4.13, ranged between 34.8 °C in July and 4.6 °C in January. The air temperatures rarely ventured above 40 °C, occurring on 19 days and only descended below 0 °C on 11 nights, usually in the hours of darkness just before the sun came up. The highest and lowest recorded hourly temperature was 42.4 °C and -2.5 °C respectively.

The measurements fit well with observations taken at the Menara station shown in Figure 4.14. The mean daily temperatures are slightly lower as the station is situated further to the west and enjoys a more Mediterranean climate. The greatest diurnal variation in temperature occurs with the onset of hot, daytime winds blowing from the Saudi Arabian peninsula combined with cold clear nights. This occurs at the end of April and May each year. Least diurnal variation occurs in the winter months.

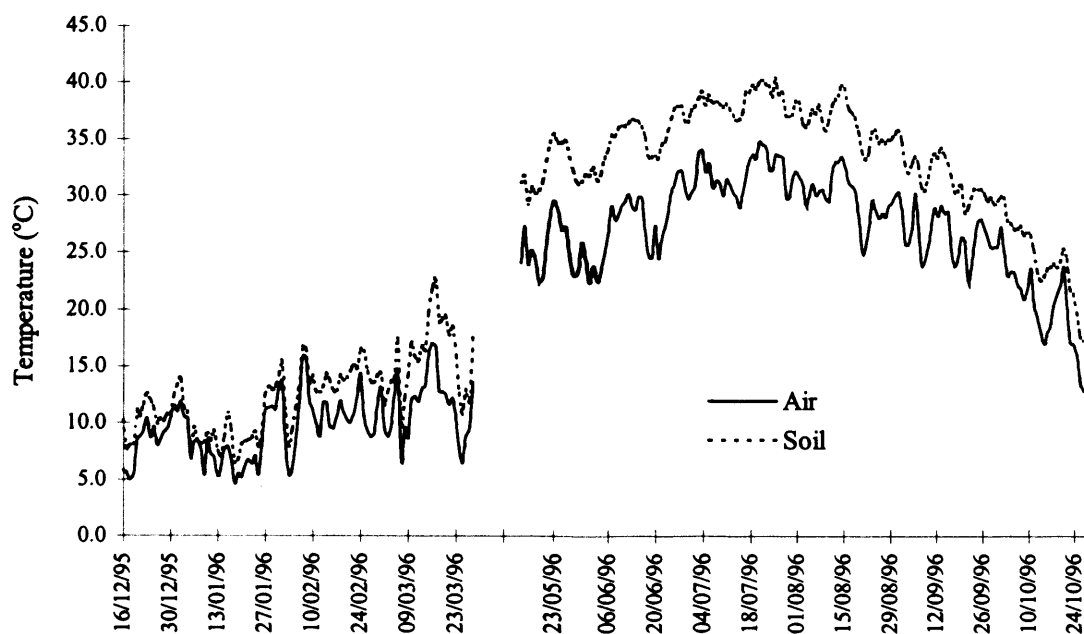


Figure 4.13. Mean daily air and soil temperatures recorded at the Marab Salma station for the period December 1995 to October 1996 (excluding April 1996).

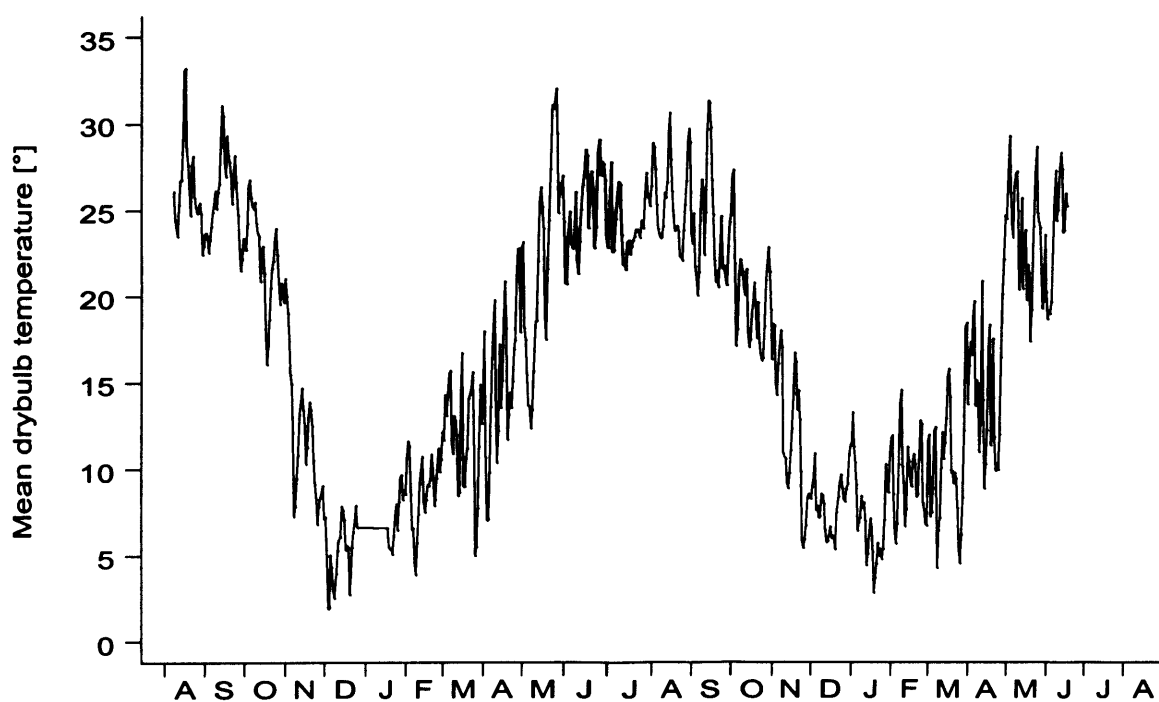


Figure 4.14. Mean daily air temperatures recorded at the Menara AWS for the period August 1994 to August 1996 (excluding January 1995), (Kirk 1997).

4.7.3.2 Soil temperature

At the *Marab Salma* station the average temperature of the soil between 2 cm and 6 cm was measured using thermocouples manufactured by Campbell Scientific Instruments. Measurements were taken at least every 20 minutes and averaged over an hour. The variation in soil temperature is shown as the dashed line in Figure 4.13. The soil temperature is almost always greater than the air temperature even in winter, the difference being greatest in the summer. The shape of the line resembles that of the air temperature although the fluctuations are not so massive and the small fluctuations, or noise, in the air temperature recordings have been smoothed out. To highlight these two points, the mean and standard deviation (s.d.) of daily temperatures ($^{\circ}\text{C}$) in January 1996, of the air, are 8.1 (mean) and 2.36 (s.d.), and of the soil, are 9.7 (mean) and 2.27 (s.d.). The same values for July 1996 are 32.0 (mean) and 1.66 (s.d.) for air temperatures and 38.5 (mean) and 1.09 (s.d.) for soil temperatures. Also it should be noted that the maximum variation in daily temperatures in both the air and soil occur in the late spring and at the end of the summer in October.

4.7.4 Wind speed and direction

Wind is an important control on the amount of evaporation that takes place in the Badia and this ultimately will affect the amount of soil moisture in the surface layers. It is therefore important to establish the predominant wind direction and the strength of the wind at particular times of the day and year. This information may help to explain some of the weather patterns observed over the Badia region. Hourly averages were obtained from the *Marab Salma* station. These directional data were compared to values obtained by the Menara station. The sampling resolution of the data limits the likelihood of detecting gusts that may be important in terms of erosion and transport of airborne material.

4.7.4.1 Wind speed

The diurnal variation in wind speed for four months covering the four seasons of 1996 are shown in Figure 4.15 for *Marab Salma*. These values have been derived by averaging the hourly recordings made during every day of the month.

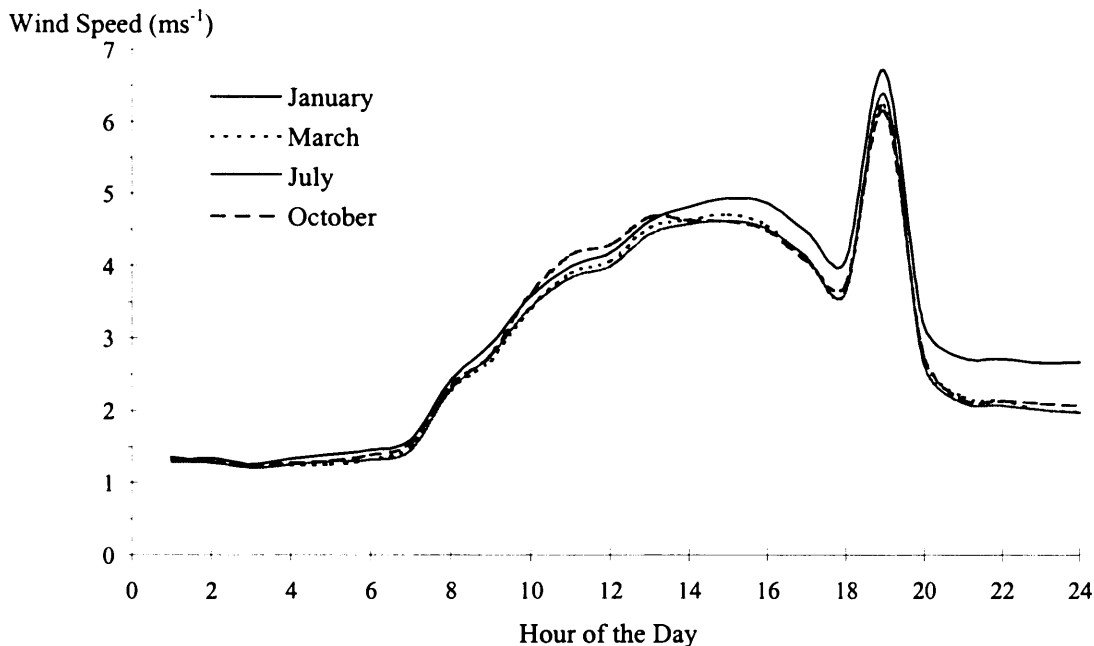


Figure 4.15. Mean diurnal wind speeds at the Marab Salma station for the months of January, March, July and October 1996; (note: only 29 days for March and 27 days for October, caused by battery failure).

The trends for each month are very similar indicating that average wind speeds during each month shown, and therefore season, do not vary significantly in magnitude. Wind speeds tend to increase around 7 a.m., from an average speed of slightly over 1 m s^{-1} , continuing to increase through midday to a peak at around 4 p.m. of 5 m s^{-1} . Over the next two hours there is a reduction in average speed to between 3.5 m s^{-1} and 4 m s^{-1} , then suddenly the winds pick up, accelerating sharply to reach a peak of over 6 m s^{-1} in all seasons around 7 p.m. The decline in wind speed during and after the sun has set is rapid, reaching a stable value almost always by 10 p.m. Another interesting observation is the sharp decline just past the midnight hour, especially in the winter, to a lower

stable average value stated previously of just over 1 m s^{-1} on average. Average wind speeds are slightly higher over the winter months.

4.7.4.2 Wind direction

Directional data may be useful in predicting what sort of wind vector and speed are common during precipitation events and to look at the variation in direction over the different seasons. Figure 4.16 shows the diurnal variation in wind direction for the months of January, March, July and October 1996, depicted as circles, from the *Marab Salma* station. The black line shows the mean of the values for each hour. There appears to be no major trends that can be clearly detected. In fact, there is a wide spread of directions recorded at all times of the year, the only noticeable gaps being winds from the north-west to the north-east during daylight hours. In January, the wind direction is random distributed, although some trends can be detected (Figure 4.16). The winds are southerly during the night (Figure 4.16) and, as shown in Figure 4.15, are on average weak. After sunrise there is a slight movement of the winds to a south-west (225°) direction which stabilises around 10 a.m. After sundown and maybe associated with the sharp increase in wind speed around 7 p.m. the wind shifts back towards a southerly direction stabilising at this direction for the rest of the night. After this time the spread of recordings is large indicating that there is no one dominant wind direction.

The situations for March and October are similar, in that the average direction shifts from a southerly through to a westerly direction during daylight hours. This is indicated by a high proportion of circles in the westerly quarter as the sun sets. After sun down the winds tend to shift back to the south. In October there are very few recordings from a north-westerly direction during the night. During the summer the fluctuation of the mean diurnal wind direction becomes more pronounced. The standard deviation of the hourly mean wind directions for July is 36.9° compared to 21.5° in January. However the trend in wind direction change during the day is still approximately the same, although the shift from south-easterly (just before midnight) to south-westerly (at around 7 p.m.) is constant; and is seemingly unaffected by sun-rise. The transition back to a mean south-easterly wind is quickly accomplished in about three hours between 7 and 10 p.m.

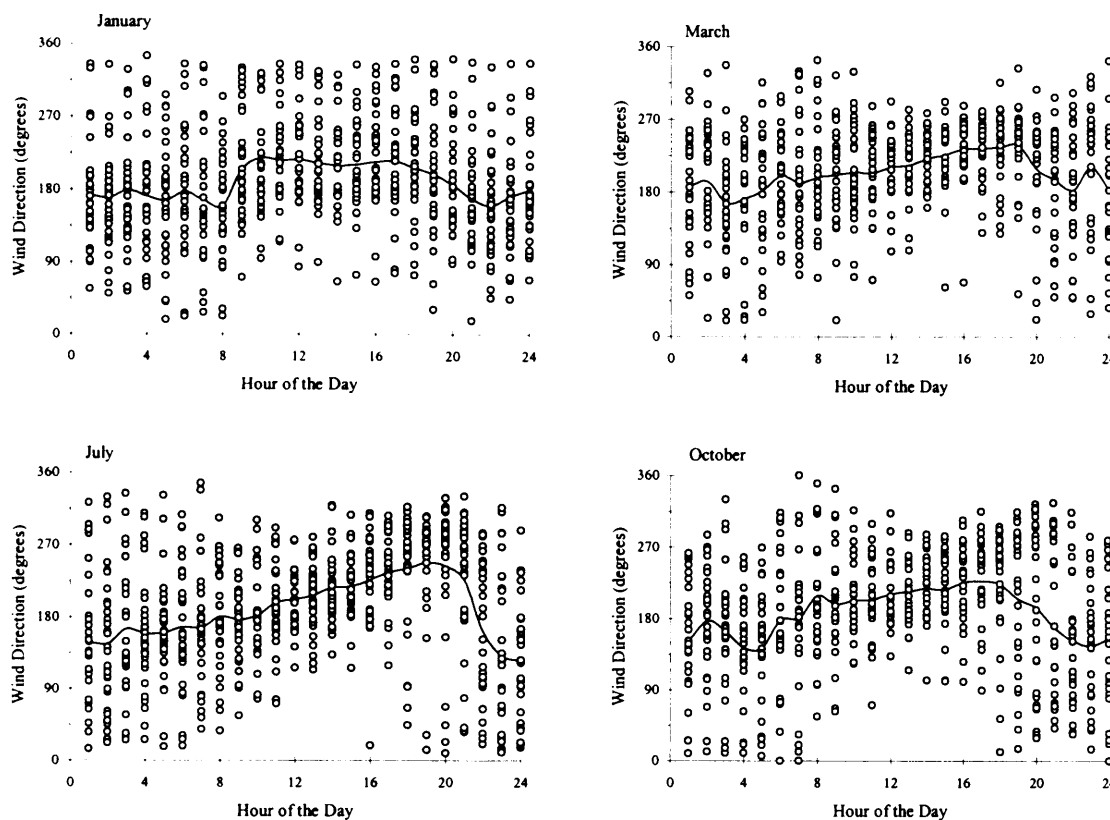


Figure 4.16. Diurnal wind direction variation for the months of January, March, July and October 1996 recorded at the Marab Salma station. The black line represents the mean wind direction for that hour.

If comparison is made to wind direction data collected at the Menara station (Figure 4.17), it can be seen that the situation is significantly different. During the winter months at Menara the wind direction is mainly from the south-east shifting through a southerly direction to the west. Once again conditions resemble each other in the months of April and October. During darkness the average wind direction is from the north and east. In daylight hours the winds shift to a more southerly and westerly direction. Winds in the early hours predominantly come from the north-east. During the day there seems to be three options; either to shift south completely through west and north until once again blowing from the north-east shift south like the previous example but after the sun sets reverse and resume the north-easterly direction, or remain constant from a northerly direction during the day. In summer the winds very rarely blow out of

the south, the only such occurrence recorded during the morning hours after sunrise. The winds are almost dominantly from the north-east at night shifting through north to the north-west during daylight hours. There are numerous explanations for the differences between the two stations, including their setting in relation to the local topography. The directional data are important in understanding the links between prevalent wind direction and precipitation events.

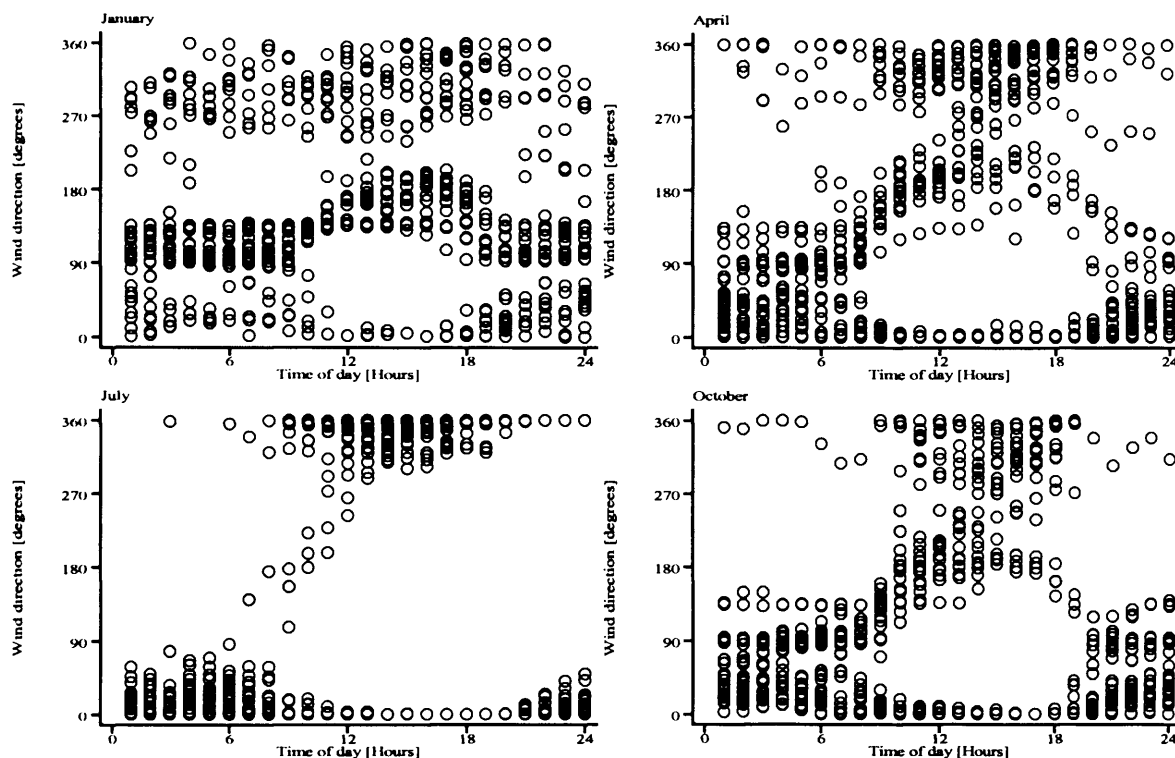


Figure 4.17. Diurnal wind direction variation recorded between the period August 1994 and August 1996 at the Menara AWS (Kirk 1997).

4.7.5 Evaporation

The rate of evaporation will have an important influence on the amount of moisture in the upper layers of the soil profile. Desert regions are characterised as having low rainfall and high rates of evaporation, caused by strong humidity gradients, high amounts in incoming solar radiation and persistent winds. These conditions prevail for

many months of the year in arid regions, during which time a negative water balance exists. The presence of a soil crust will reduce the capillary rise and evaporation demand due to the compaction and reduction in the number of micro and macro pores (Bresler and Kemper 1970, see Kirk 1997). During winter months, temperatures are low, incoming solar radiation is reduced and moisture vapour in the atmosphere is at a maximum. These parameters affect evaporation rates, to such an extent that there may be a positive soil moisture flux. Kirk (1997) measured a positive water balance at Menara occurring, for a few days, as early as October (sporadic 'end-of-summer' precipitation events). From data collected at the Menara AWS, Kirk (1997) calculated the evaporation rate (E) using a formula based on the Penman Equation, an approximation given in Equation 4.9 (Penman 1948). Input parameters were net radiation, wind speed and humidity:

$$E = \frac{\Delta}{\Delta + \gamma} (R_n) + \frac{\gamma}{\Delta + \gamma} \left(\frac{2.3uS}{\gamma} \right) \quad (4.9)$$

where,

Δ = gradient of saturation vapour pressure / temperature curve (hPa / °C)

γ = psychrometric constant (0.61 hPa / °C at 800m a.s.l.)

R_n = net solar radiation (W m⁻²)

u = wind speed (ms⁻¹)

S = saturation deficit (hPa)

Figure 4.18 shows the results of these calculations from the beginning of August 1994 through to near the end of October 1994. As expected, evaporation rates in the summer are high and, although the fluctuations on a daily basis can be significant there is a general pattern of decreasing values as autumn sets in. After and during rainfall events there is a reduction in the calculated evaporation rate and as the end of October is reached values are below 5 mm per day. Given the mean altitude of the Badia at ≈800m, the Penman Equation (using the psychrometric constant value) predicts a reduction in importance of the wind speed and humidity terms. The net radiation parameter becomes more important. As wind speeds at the weather station locations have been shown to be relatively constant, the humidity and radiation parameters become even more influential

on the amount of evaporation. Unfortunately, evaporation data were not available from the Safawi or Azraq sites even though evaporation pans are present at these locations.

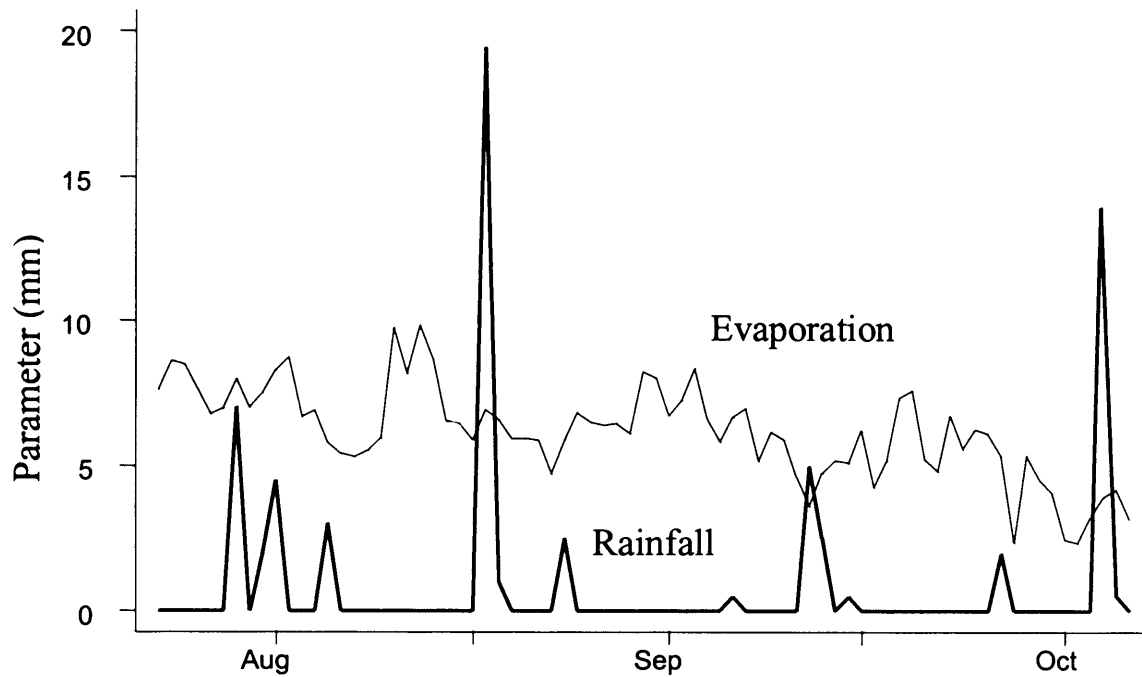


Figure 4.18. Total daily evaporation rates calculated at the Menara station using an approximation of the Penman Equation. These are plotted against rainfall (bold line) for the period 7th August to the 20th October 1994 (from Kirk 1997).

4.8 Vegetation sampling and analysis

Data were collected on the main vegetation species present in the *marab* monitoring sites. It is important to determine the percentage cover of the vegetation, the main species present, spatial distribution and greenness of these species. This is because the backscatter signal is influenced by the dielectric properties and shape distribution of the vegetation layer (Section 2.6.3). In desert regions, vegetation cover is low, but can significantly vary both spatially and temporally. Therefore, vegetation covers at different *marab* monitoring sites need to be determined as well as repeating the

measurements during consecutive field visits. Vegetation was sampled at the *marab* sites listed in Table 4.2 and the results are summarised in Table 4.8.

Site name	% Vegetation cover		
	Autumn 1995	Spring 1996	Autumn 1997
Marab Salma	10.7 ²	28	29
Qa'a Qattafi	3.7	8	7.9
Wadi el Hazim	N/A	22.4	15.6
Feidat ed Dihikiya	3	5.2	13.6
Marab al Wassad	6	3.8	5.6
Marab al Wutaydat	4.7	4	N/A
Qa'a al Buqayawiyya	8.2	6.2	15.1

² different area measured to the following two years

Table 4.8. Percentage vegetation cover measured at the *marab* sites.

4.8.1 Sampling methods

Three quadrats, 30 by 30 m square, were analysed at each *marab* location. Commencing at random coordinates and displaced at a randomly generated orientation, ten line transects of 20 m in length were measured in each 30 by 30 m area. The following parameters were recorded over the length of the transect; amount of bare ground, amount of vegetated ground, shrub length, width and height, species type and shrub greenness. In the instances where grasses were present, the amount of their cover was estimated as well. From these measurements, an average vegetation cover can be estimated for each quadrat. In addition, the main species characteristics and vegetation shapes were determined for further research into semi-arid vegetation modelling. By making measurements at three quadrats, any large-scale heterogeneity in the *marabs* could be accounted for. Each quadrat was fixed using a GPS to ensure that during consequent field visits, the same areas could be analysed. Field sites were visited during the autumn of 1995, the spring of 1996, and the autumn of 1997.

4.8.2 Vegetation analysis results

Table 4.8 describes the percentage vegetation cover measured in the field. *Marab Wutaydat* and *Marab Wassad* show very little change in percentage cover between field visits. These sites, located in the south-east of the region, are characterised by woody perennials and show very little evidence of ‘greening-up’ after winter rains. There is also little ephemeral grass growth. For *Feidat ed Dihikiya* and *Qa’a Qattafi*, an increase in vegetation cover was observed between the autumn of 1995 and the spring of 1996 suggesting a response to winter rains and increased moisture availability. At *Marab al Buqayawiyya* a large increase in vegetation cover was measured in the autumn of 1997 compared to previous field visits. A similar observation was calculated at *Marab Salma*. The winter of 1996 was wetter than average and the amount of vegetation has increased in response to this rainfall.

The dominant species, lifeforms and palatability of the vegetation found at the *marab* sites are listed in Table 4.9. Analysis of all transects measured in the eastern Badia region show that 64 % of the plants were classified as being spherical. The next dominant group were spiky in shape. Plants were classified spiky if they were present in low densities and had no distinct shape (Edwards 1999). 322 species, in 46 vascular groups, have been identified in the eastern Badia region (Cope and El-Easawi 1998).

4.9 Summary of field data and methodology

This chapter has outlined the methods of ground-based data collection. These data will aid interpretation of the microwave remote sensing imagery acquired from the ERS SAR series of satellites. The data were collected with consideration to the input requirements of the theoretical models that were to be calibrated in a desert environment. The following measurements were obtained:

Site name	Dominant species	Lifeform	Palatable
Marab Salma	<i>Archillea fragrantissima</i>	bush	Palatable
	<i>Artemisia herba-alba</i>	bush	palatable
Qa'a Qattafi	<i>Seidlitzia rosmarinus</i>	bush	palatable
	<i>Salsola vermiculata</i>	bush	palatable
Wadi el Hazim	<i>Atriplex halimus</i>	shrub	palatable
	<i>Hammada eigii</i>	bush	palatable
Feidat ed Dihikiya	<i>Archillea fragrantissima</i>	bush	palatable
	<i>Tamarix tetragyna</i>	shrub	palatable
Marab al Wassad	<i>Anabasis articulata</i>	bush	palatable
	<i>Zilla spinosa</i>	herb	unpalatable
Marab al Wutaydat	<i>Anabasis syriaca</i>	bush	palatable
Qa'a al Buqayawiyya	<i>Capparis ovata</i>	herb	unpalatable
	<i>Archillea fragrantissima</i>	bush	palatable

Table 4.9. Dominant species, lifeform and palatability of vegetation found within the eastern Badia of Jordan.

- Soil moisture measurements were taken using a dielectric probe that estimated with volumetric water content of the upper 6 cm of soil. These measurements were compared to the values obtained using gravimetric methods.

- Surface roughness measurements were taken using a pin profilometer. The equations for the extraction of the RMS height, correlation length and autocorrelation function were derived. Methods of data analysis and sources of error were also discussed.

- The methods of data collection concerning the nature of the soils and basalt regolith in the eastern Badia region were presented.

- Climatic data obtained from two temporary and five permanent automatic weather stations located in the project area are displayed. Climatic parameters discussed in this chapter are the precipitation, temperature, wind speed and direction, and evaporation.

- The field methodology for obtaining percentage vegetation cover at *marab* monitoring sites is presented.

5. Roughness Properties: Theory, Measurement and Analysis

5.1 Introduction

The roughness of a surface is described by Wesemael *et al.* (1996) as a dynamic property which, determines to a large extent, erosion and infiltration rates. Although this statement is very generalised, it clarifies the important role that surface roughness plays in geomorphological processes. Roughness is also an important parameter in hydrological and aeolian studies (McCarroll 1992, McCarroll and Nesje 1996). The roughness of the surface also influences the backscatter coefficient of electromagnetic radiation at radar wavelengths (Section 2.1.4). Oh *et al.* (1994) stated that the causes of backscatter variation in radar image scenes are, in order of importance, surface roughness, moisture content, correlation length, soil type and soil temperature. Therefore, it is very important to quantify roughness as accurately as possible.

To accurately quantify the roughness of a surface is difficult, as roughness is scale-dependent. Therefore defining roughness parameters that can be universally applied in many surface models where roughness is a critical factor is still a current focus of research. The main problem is to parameterise the roughness of a surface with parameters which, are related to radar energy. The parameters chosen should also be directly comparable with values obtained from other work and which are relatively easy to collect and analyse. Lersch *et al.* (1988) investigated eight parameters that describe the surface roughness; two relate to elevation extremes, two relate to frequencies of extreme elevations and four give direct values of elevation variation. In a review of the literature given in the following section, the two most popular roughness parameters of the soil surface used in remote sensing studies are the RMS height (σ) and correlation length (l) introduced in Section 4.4. This chapter reviews some of the literature that has used roughness parameters in radar and other studies and describes how the roughness parameters were calculated in this research and these implication of the results for radar studies.

5.2 Literature review: Surface roughness and SAR

This section describes methods and techniques that other researchers have considered in measuring and analysing roughness parameters. The case studies presented are collated from a wide range of climatic regions, from temperate to arid zones; and from a selection of surfaces, from major catchments to individual agricultural fields. Some fundamental issues, related to the selection of the parameters that describe the surface roughness, are discussed. In addition the choice of autocorrelation function that best describes the data, the calculation of the correlation length and how this is influenced by the length of the profile, are discussed in addition to other similar issues that address the data collection procedures.

5.2.1 *Random data*

A sample record of data for a random physical phenomena may be thought of as one physical realisation of a random process (Bendat and Piersol 1986). Random processes can be categorised as being either stationary or non-stationary. Stationary data can be approximated at any time by calculating average values for a selection of sample functions that describe a random process. If such values as the mean and autocorrelation function of the samples are time-variant, then the random process is described as non-stationary. Non-stationary random processes are often simplified for analysis and measurement procedures. There are a number of ways to analyse non-stationary random data. First-level analysis might include deriving the RMS height (σ), the probability density function and the autocorrelation function ($\rho(\xi)$). The latter parameter is a measure of the distance- (or time-) related properties of the random process. Second-level of analysis would include the autospectral density function (also known as the power spectrum) which represents the rate of change of mean square value with frequency. In this study the roughness data is considered as a non-stationary process in that, at the spatial scales that roughness elements are being considered, the relationships will change if the resolution of measurements are varied. In most cases there will not be

enough sample records available to permit accurate representation of the surface. Problems associated with quantifying roughness become evident when testing different sampling methods in the field.

5.2.2 Case studies

Many roughness studies have focused on cultivated fields Wegmuller *et al.* (1994) derived height profiles using a laser profilometer and calculated the autocorrelation function. They found that the fields could be characterised in general by exponential functions as opposed to Gaussian functions. Engman and Wang (1987) studied a range of bare soils in California. They digitised field survey photographs to derive σ and l . Each of the 52 profile lengths were 1 m. They found no correlation between σ and l , low correlations between the backscatter coefficient σ° and l ($r^2 = 0.04$) and, reassuringly, some correlation between σ and σ° ($r^2 = 0.59$). They concluded that the measurements of surface roughness appeared to be a potential limitation of the data. Engman and Chauhan (1995) confirm that roughness may be equal to or greater than the effects of soil moisture on the backscatter. The effect of roughness needs to be established independently if estimates of soil moisture are required (Engman and Chauhan 1995). This is resolved by simulating the effect of roughness using the scattering model (Section 2.1.4).

Natural surfaces exhibit several spatial scales of roughness, from micro-roughness to large-scale topography. For example, Ridley *et al.* (1996) looking at desert surfaces in the Simpson Desert (Australia) argue that there are three distinct, independent scales of roughness which are important in all backscatter models. The small-scale roughness was characterised by wind ripples and uplifts of soil adjacent to plants. They used a pin profilometer, similar to the one used in this study, to measure the surface height every 0.5 cm over a length of 1 m. Two other scales of roughness were medium-scale, comprising hummocks of trapped sand and ridges on dune crests, and large-scale, comprising the dune system itself and regional slopes. Consideration was made only to the small-scale (cm) roughness variation as this was the scale that radar scattering was most dependent upon.

A two scale roughness model was used by Mo *et al.* (1988) representing a large scale correlation length, L , and a small scale correlation length, l . The autocorrelation function is given by:

$$\rho(\xi) = \exp\left[-\frac{\xi^2}{\sqrt{l^4 + L^2\xi^2}}\right] \quad (5.1)$$

which reduces to a Gaussian form when ξ approaches zero and becomes exponential when ξ becomes large. This is a useful approach for modelling as the simulated backscatter becomes very large and negative when the correlation length is large and the autocorrelation is defined as Gaussian. Similarly, two roughness scales were collected by Oh *et al.* (1992); the first using a laser profilometer at a horizontal resolution of 1 mm for a transect length of 1 m, the second roughness scale was calculated from two 3 m profiles, using chart paper and spray paint. Their study uses radar at centre frequencies of 1.50 (L-band), 4.75 (C-band) and 9.50 GHz (X-band). A profile length of 1 m was believed to be too short to accurately determine the correlation length for analysing 1.28 GHz SIR-B (Shuttle Imaging Radar) data, indicating that the optimum transect length and sampling interval may also be frequency dependent (Wang *et al.* 1986). As this study only used 5.3 GHz (C-band) radar imagery, ≈ 1 m profiles, sampled every 5 mm, were considered optimal.

On natural surfaces the surface height distributions can often be considered as being either random or displaying a theoretical distribution such as the exponential distribution. They do not normally display any periodicity (a ploughed surface might display surface height distributions that are periodic due to troughs and peaks in the surface). Periodicity was not taken into account in this study as most surfaces were considered to be in a natural or semi-natural (minor surface modification) state. Consideration of the periodic component of surface roughness and the use of longer profiles was made by Chiarantini *et al.* (1995) who used transects between 4 and 6 m, both parallel and perpendicular to the direction of tillage in ploughed fields. Their

statistical program developed to analyse the roughness data collected is shown in Figure 5.1. This diagram shows the stages of calculating surface roughness parameters.

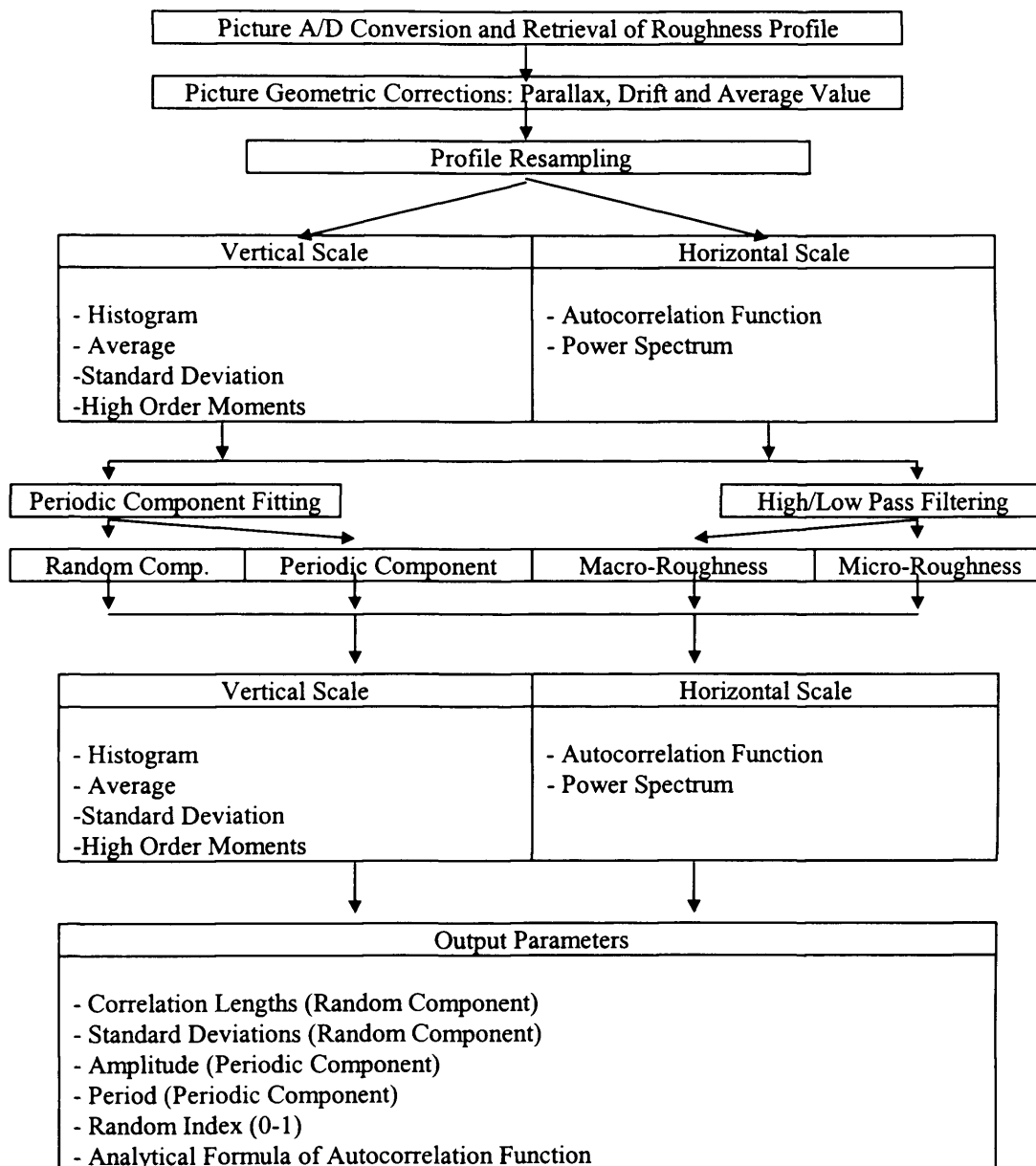


Figure 5.1. The procedure for calculating the roughness parameters outlined in a hydrological study in the Abruzzo region of Italy (Chiarantini *et al.* 1995).

In other studies only the RMS height was calculated (Ulaby *et al.* 1978) although the authors state that a complete characterisation of the surface roughness cannot be obtained solely with this measurement. Dubois *et al.* (1995) collected roughness data in an Oklahoma catchment using a 1 m laser profilometer. In their model they did not

explicitly use the correlation length parameter as it was too difficult a parameter to determine accurately. The variation in correlation length of their samples varied as much as an order of magnitude while the RMS height was accurate to within 10%. The model proposed by Oh *et al.* (1992) also does not include a correlation length parameter. The models used in this study require the correlation length parameter. Therefore it was considered necessary to estimate this value while considering the likely errors involved.

5.2.3 Higher levels of data analysis

Research into the relationships between radar backscatter parameters and other descriptors of the surface roughness have been undertaken for a range of natural surfaces. Several studies have focused on the remote sensing of lava flows and rocky terrain that would have approximately similar roughness properties to the basalt and *hammada* surfaces that are found in the eastern Badia of Jordan. A summary of the main findings are discussed in this section. An important issue that has been raised is to define a parameter whose behaviour can be understood when different scales of roughness are analysed. Power spectrum density analysis (P), an indication of the relative importance of each spatial harmonic component in constructing the measured surface (Campbell and Garvin 1993), is one approach that has been adopted. The power spectra of topography at many scales, usually exhibits the relationship $P = bk^m$, where b is the offset and m , is the slope of the spectrum (m lies between -2 and -3 when plotted in log-log space) (Sayles and Thomas 1978; Brown and Scholz 1985). In this case, the units of P , are $\text{m}^2 \text{ cycle}^{-1} \text{ m}^{-1}$ or m^3 ; and the spatial wavenumber, k , is calculated by multiplying the reciprocal of the spatial scale by 2π . The drawback is that many profiles have to be collected to average out the noise and error effects.

Farr (1992) used this type of analysis to distinguish lava flows of different ages. Profiles were collected every 1 cm over a range between 5 and 30 m. The number of profiles at each site ranged between 2 and 50. The power spectra were calculated with different curves being obtained for flows of varying age (Figure 5.2a) displayed with the values of the slope and offset derived (Figure 5.2b). The data show that between 0.016 and 0.14 Ma the offset decreases and the slope steepens, implying an overall loss of

roughness. Breaking up of the surface observed on the younger flows (similar to that observed on the Fahda Vesicular basaltic flow in this study) may also explain the greater loss of centimetre scale roughness. Between the flows of age 0.14 and 0.56 Ma the changes are more uniform. On the oldest flows surfaces become rough again, with similar values to the youngest flows. The results enable models of basalt pavement evolution to be developed and can be applied to other flows around the world to establish the stages of landscape development. Other studies established estimates of aeolian mantling and deposition (Evans *et al.* 1992) and power estimates of a flat mudpan (*qa'a*) surface (van Zyl *et al.* 1991).

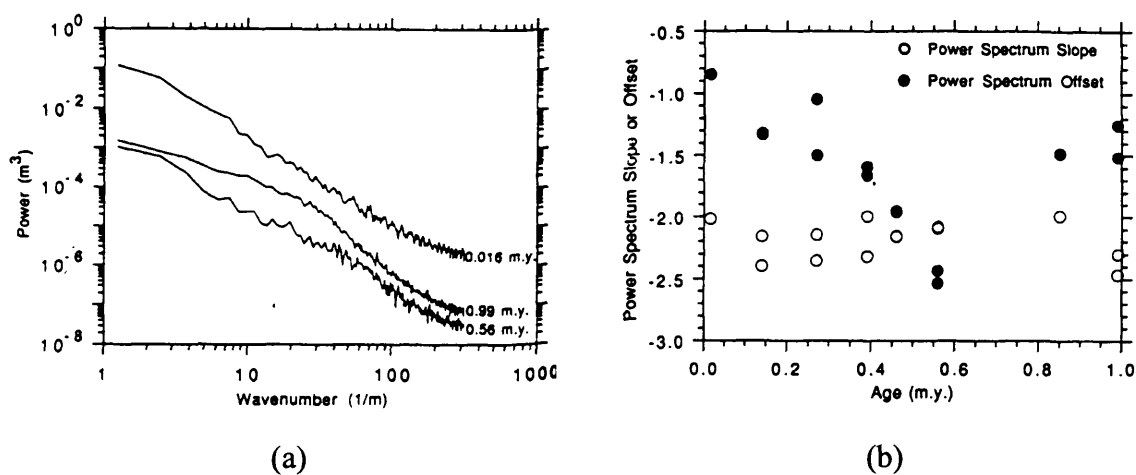


Figure 5.2. (a) Power spectra of dated basalt lava flows, showing surface roughness evolution with age, and (b) linear fits showing the slope and offset values to the power spectra (Farr, 1992).

Campbell and Garvin (1993) collected topographic profile data at 5 and 25 cm resolution from a Hawaiian lava flow. Lengths of transects varied between 5 to 8.5 m and 100 to 200 m respectively. They derived the RMS height, correlation length and the power spectra density. Their effective slope parameter, σ / l , appears to be a more useful estimator of large scale roughness for radar studies and in conclusion they stated that the correlation length is best suited when there is only one dominant scale of roughness, such as may be the case on a *qa'a* surface. One further issue is related to the profile length and the subsequent calculation of the correlation length.

The arguments presented above are supported by field data. Analysis of roughness data is given in the following section. Ultimately, the choice of field method was controlled and restricted by the equipment and time available to collect roughness and other data given the number of people in the field to act as assistants. Therefore data were collected on roughness parameters satisfying the requirements of the scattering models that are used in this study.

5.3 Data description and analysis

5.3.1 Data collection methods

Discrete data related to the surface heights of natural surfaces were collected in the field using a profilometer (Section 4.4.5). Initially, there was no standard procedure for the number of profiles taken, the profilometer in use was only 30 cm in length. During subsequent field campaigns the size of individual profiles were made up to 48 cm. During the 1997 field campaign a total of 12 profiles were taken at each site (comprising two times six profiles). The digitising and analysis phase of these data was too time consuming and it was decided that six profiles taken at each site (a total transect length of approximately 3 m) provided an appropriate balance between data volume and time available. This means that power spectrum analysis cannot be applied to these data, due to the small number of samples obtained at each site.

The selection of the transect length has a major influence on the roughness values calculated. Too short a transect length may yield an under-estimation of the correlation length. The number of discrete height measurements sampled may also be unrepresentative of a population. Too long a transect will begin to account for larger scale surface topography that is not important for radar studies using centimetre wavelengths. The literature reviewed in the previous sections indicate that there is no standard length of transect from which the roughness parameters are calculated. In addition, the reported low correlation coefficients between the correlation lengths of

surfaces and the backscatter coefficient contribute to make this a grey area, which could produce significant errors in any model validation and calibration. In an attempt to address these problems, RMS height, correlation length and autocorrelation function were calculated at each site for individual transect lengths (30 or 48 cm), ≈ 1 m transect lengths and the full transect length (up to 3 m). As the aim was to derive input parameters for the scattering models described in Section 2.6, this analysis indicated the optimal transect length that gave the best results in the model validation stages. A small number of profiles demonstrated trends attributed to a shallow slope angle present at some of the sites. Where slope effects are present, the data have been detrended by determining the average value and either subtracting or adding this to the original value. Over the small spatial scale of measurements (order of metres) considered in this study, this analysis was not necessary for the majority of sites.

5.3.2 Roughness profiles: Analysis and results

Instructions describing the field use of the profilometer were given in Section 4.4. The digitised individual heights from the profilometer were input into an Excel spreadsheet. The site used as an example of the analysis is *Marab Shubayka*, a large vegetated *marab* to the north of Safawi which has a characteristically rough surface comprising clods of silt- and clay-sized particles. The surface height profile is shown in Figure 5.3. The data (six profiles of 48 cm in length) were collected during the 1997 field campaign. A summary of the roughness data collected is given in Table 5.1a. These data equate to three sample profiles (by joining together 2 profiles each of 48 cm) of approximately 1 m in length and one long transect (by considering all six profiles in a line) of 2.88 m in length.

5.3.2.1 RMS height

The RMS height of each of the transect lengths were calculated using the Equation 4.6 (Section 4.4.2). An average value was derived for each of the six individual profiles, each of the three ≈ 1 m profiles and the full profile (Table 5.1).

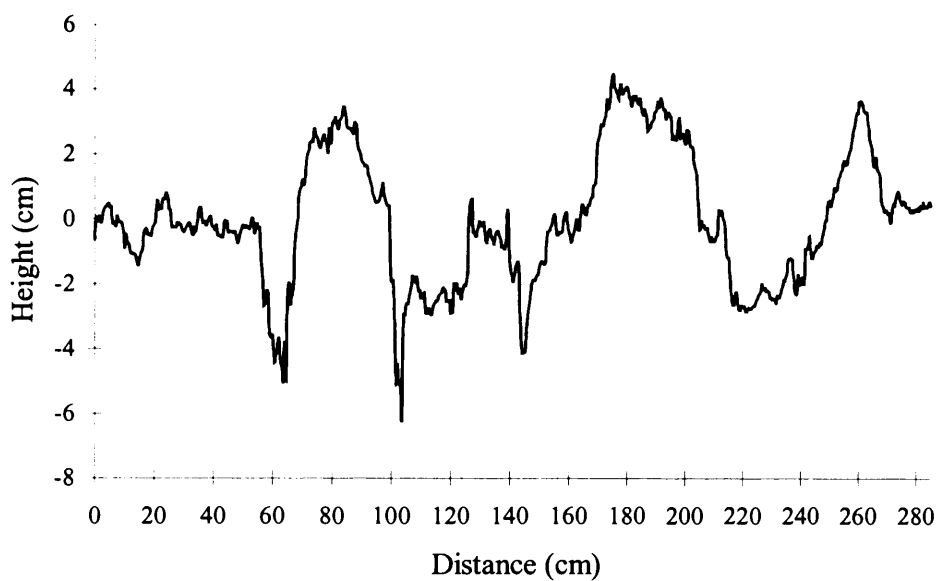


Figure 5.3. The surface height profile for Marab Shubayka derived in the spring 1997 field campaign. The peaks and troughs correspond to hummocks and cracks on the marab surface.

In this case, the values for *Marab Shubayka* do not confirm the hypothesis that the longer the transect that is used for calculating the RMS height the larger the calculated value will be; in this example the difference is not large. Data from a further site (*Marab Wutaydat*) also from 1997 show that an increase in the magnitude of the RMS height occurs with increasing profile length (Table 5.1b). The estimates of RMS height for the 48 cm, ≈ 1 m and 2.88 m profiles are 0.64, 0.96 and 1.54 cm respectively. The estimates of the correlation length also increase with increasing profile length for *Marab Wutaydat* (Table 5.1b). This observation is noted for many sites.

(a) Marab Shubayka – roughness data summary for the 1997 field campaign			
Profile length	RMS height (cm)	Correlation length (simple, Pearson) (cm)	f (autocorrelation)
Individual (48 cm)	1.72	7.8	Gaussian
≈1 m	2.02	10.5, 13.5	Gaussian
Full (2.88 m)	2.04	12, 11.9	Gaussian
(b) Marab Wutaydat – roughness data summary for the 1997 field campaign			
Individual (48 cm)	0.64	4.5	Gaussian
≈1 m	0.96	10, 14.3	Exponential
Full (2.88 m)	1.54	33, 46.3	Exponential

Table 5.1. Data summary of the roughness parameters for (a) Marab Shubayka and Marab Wutaydat. Refer to the text for an explanation of the terms listed.

5.3.2.2 Probability distribution functions of surface heights

It is an assumption of the scattering models that the probability density functions (P.D.F.) of the surface heights approximate a normal distribution (Section 2.6). The probability functions were calculated for the three ≈1 m and the full transect (2.88 m) to check this assumption. The results from the *Marab Shubayka* site are shown in figure 5.4. In this example the ≈1m distributions (b, c and d in Figure 5.4) are poor approximations to a normal distribution (distribution (b) probably being the most normal). The full transect (Figure 5.4a) displays the most normal distribution, due to the greater number of sample points. The ≈1 m profiles were much more varied in their approximation to normal distributions. At other sites distributions were observed to be sometimes bimodal or skewed. This was possibly due to some predominant land surface feature that had been detected, for example deep cracks on an otherwise smooth surface. However, there was usually at least one example of a ≈1 m transect that approximated a normal distribution.

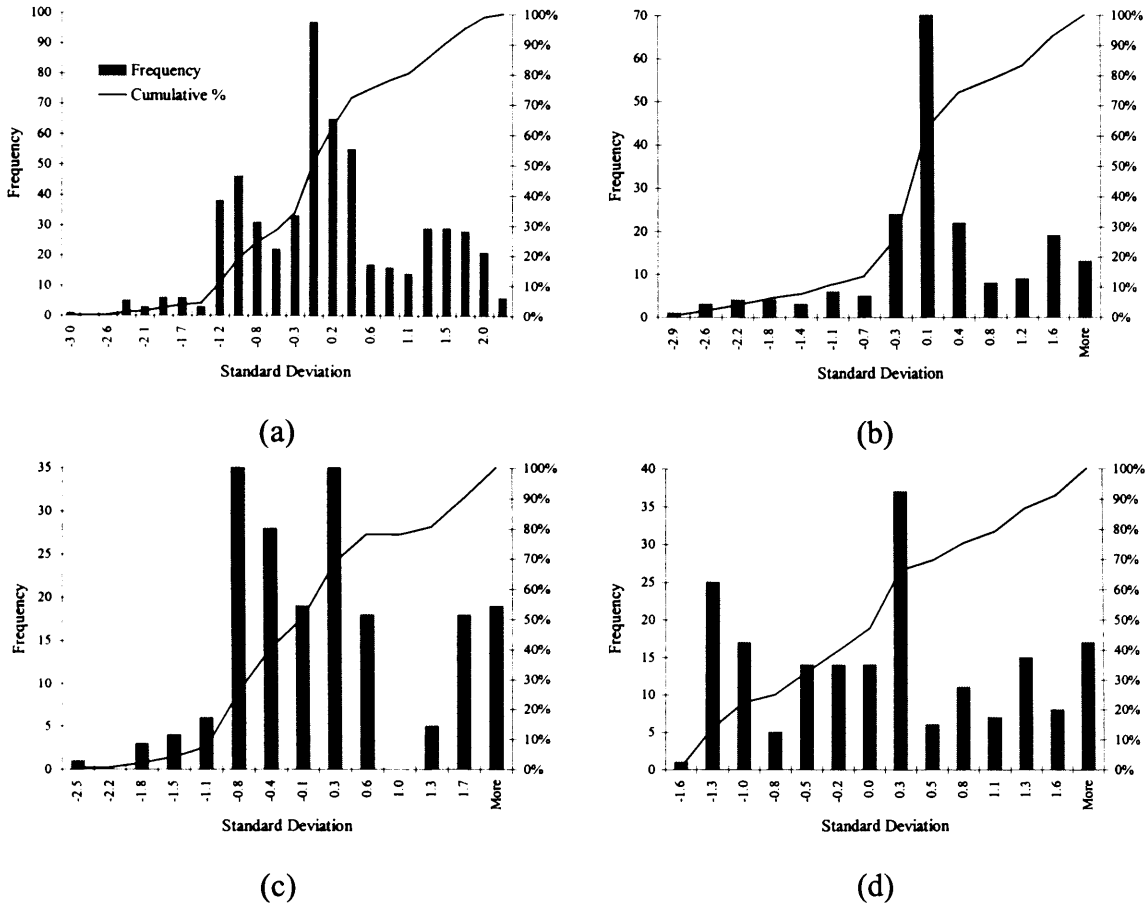


Figure 5.4. Probability density functions of surface heights for Marab Shubayka. These are displayed for the full transect of 2.88 m (a); (b), (c) and (d) show the P.D.F. of the three ≈ 1 m transects.

5.3.2.3 Correlation length

The autocorrelation of surface heights defined in Section 4.4.4, was calculated at a lag k , for the series x_i ; $i = 1, 2, \dots, n$ using the following (Equation 4.7):

$$\rho_k = \frac{\sum_{i=1}^{n-k} (x_i - \bar{x})(x_{i+k} - \bar{x})}{\sum_{i=1}^n (x_i - \bar{x})^2} \quad (5.2)$$

where,

$$\bar{x} = \frac{1}{n} \sum_{i=1}^n x_i \quad (5.3)$$

is the mean of the whole series.

Equation 5.2 is a simplification of the Pearson correlation. Cox (1983) discusses alternative methods of estimating the spatial autocorrelation in geomorphological studies and how well simplifications of the Pearson correlation represent the more complex formula. Three different simplifications are given, Equation 5.2 being the most reduced formula. This study uses correlation lengths calculated using the simple equation (5.2) and the Pearson correlation (5.4) given as:

$$\rho_k = \frac{\sum_{i=1}^{n-k} (x_i - \bar{x}') (x_{i+k} - \bar{x}'')}{\sqrt{\left[\sum_{i=1}^{n-k} (x_i - \bar{x}')^2 \sum_{i=1}^{n-k} (x_{i+k} - \bar{x}'')^2 \right]}} \quad (5.4)$$

where,

$$\bar{x}' = \frac{1}{n-k} \sum_{i=1}^{n-k} x_i \quad (5.5)$$

is the mean of the leading values, and

$$\bar{x}'' = \frac{1}{n-k} \sum_{i=1}^{n-k} x_{i+k} \quad (5.6)$$

is the mean of the lagging values.

The purpose of this exercise was to observe if the two methods produced different estimates of the correlation length. The value of the correlation length will influence which model can be used and how well it describes the observed data. Figure 5.5 shows examples of autocorrelation functions for *Marab Shubayka* for full length transects. The

results from the two methods for this particular set of profiles are very similar and therefore data from another site are shown, *Marab Wassad*. The results shown here, and those derived from other sites produce several interesting points for discussion. For *Marab Shubayka*, both methods give approximately similar results. This is by no means an isolated example. Table 5.2 lists selected estimates of the correlation length for full and ≈ 1 m transect lengths at all of the study sites. The two estimates give approximately similar results for many sites, especially on the basalt surfaces, at both the profile lengths. If, however, the calculated correlation length is greater than approximately 12 cm, then the differences between the two methods becomes greater to the extent that some correlation lengths are undefinable. Put another way, the smaller the calculated correlation length, the more likely that the two methods will produce the same value. This result is in agreement with results from Section 6.3, where the data are used to validate scattering models.

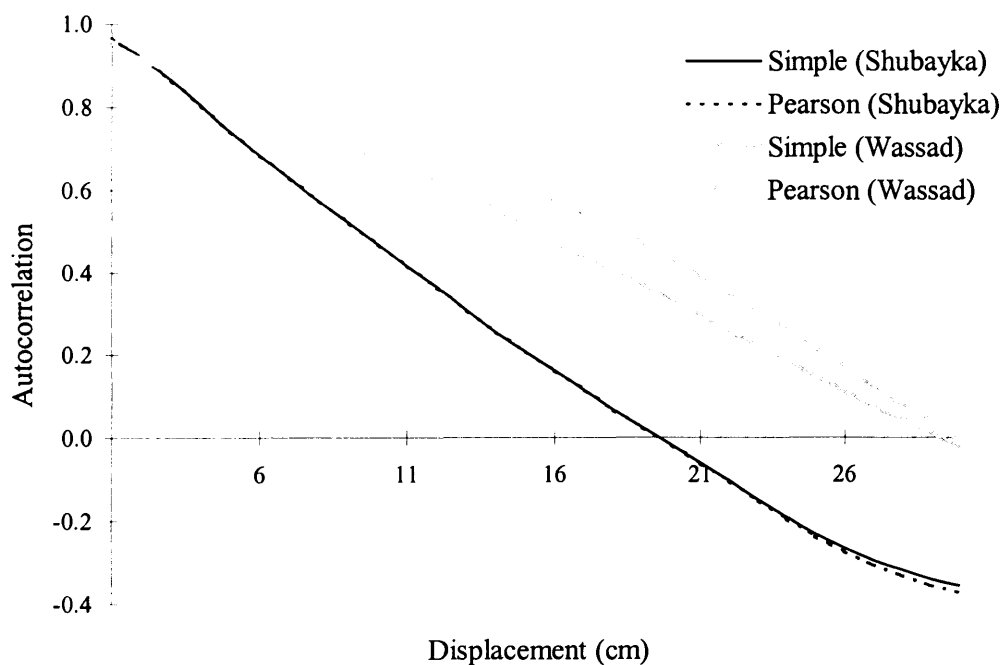


Figure 5.5. Autocorrelation relationships derived using the two estimates (simple and Pearson) of autocorrelation for two sites, Marab Shubayka and Marab Wassad. The estimates of the correlation length for the sites shown above are: Shubayka, 12 and 11.9 cm, and Wassad, 19 and 21.6 cm for the simple (Equation 5.2) and Pearson (Equation 5.4) estimates respectively.

Site name (values are in cm)	Full profile length		≈1 m profile length		Campaign year
	Simple	Pearson	Simple	Pearson	
Qa'a Qattafi	undefined	undefined	10	20.7	1997
Qa'a al Abd	undefined	48	8.5	3.7	1997
Qa'a at Ra'd	33	34.7	10.3	14.4	1997
Qa'a al Wassad	17.5	35	6.2	7.7	1997
Qa'a al Wutaydat	22	24.6	11.5	22.2	1997
Fahda Vesicular (B1)	8	8	4.8	5.2	1997
Madhala Olivine (B2)	8.5	8.9	7.3	7.5	1995
Abed Olivine (B3)	7	6.9	6.3	6.6	1996
Madhala Olivine	7.5	7.8	8	8.2	1995
Harrat edh Dhirwa	5	4.9	9.5	12	1996
Chert gravel hammada	undefined	undefined	8.2	17.7	1997
Limestone hammada	7	7.3	4.8	5	1995
Shahbat el Hazim	4	4.2	5.8	6.1	1996
Shumansaniyyat	6	6.3	6	6	1995
Sandflat	2	1.9	2	2.2	1996
Feidat ed Dihikiya	10.5	10.8	6	8.55	1995
Hashad	4	3.9	4.5	4.3	1995
Wadi el Hazim	2	2.3	2	2.1	1996
Marab Qattafi	27	39.9	10.2	11.1	1997
Marab Salma	undefined	undefined	12.7	23	1997
Marab al Wassad	19	21.6	9.3	11.5	1997
Marab al Wutaydat	33	46.3	10	14.3	1997
Qa'a al Buqayawiyya	41.5	43.2	10.2	12.4	1997
al 'Wia (cultivated)	6	6.1	5.5	5.6	1995
Shubayka	12	11.9	10.5	13.5	1997
Marab Suwaiid	undefined	47	7.8	8.9	1997

Table 5.2. Comparison of the two methods for calculating the correlation length.

Another interesting observation is that the estimate of the correlation length is often greater when calculated using the Pearson estimate. This is a disadvantage for model validation when the correlation length is large (the predicted backscatter values will be large and negative) and advantageous when the correlation length is small as the model input specification is more likely to be met. This seems to be the case for both of the profile lengths analysed. In the final analysis, both methods were considered at all sites as neither technique had major advantages or benefits over the other.

5.3.2.4 The influence of transect length on the correlation length

There are a number of sites with correlation lengths that are either large (above 25 cm) or undefinable. Correlation lengths obtained for the ≈ 1 m transects, also described in Table 5.2, give very different results. It appears that the autocorrelation of a surface is a non-stationary process that is influenced by the length of the measurements. This observation is confirmed by Sayles and Thomas (1978). They stated that the variance of the height distribution of a surface structure is related to the length of sample used. At this level of analysis, however, the relationships between the correlation length and the length of the transect are not easily definable. With further analyses, such as power spectrum analysis, relationships can be approximated to linear conditions (Sayles and Thomas 1978). However, power spectrum analysis is not considered in this study due to the limited number of transects obtained. Figure 5.6 shows the correlation functions derived using the Pearson method for the three ≈ 1 m transects compared to the full length profile. It can be seen that there is much more noise in the ≈ 1 m profiles. In this example the estimate of the average correlation length for a profile of ≈ 1 m is greater than that calculated for the full profile length. This is not the general case as a comparison between correlation length values confirms (Table 5.2). The effect of reducing the profile length to ≈ 1 m usually reduces estimates of the correlation length and also influences the autocorrelation function that the data best describes. In the example shown (Figure 5.6) the estimates of the correlation length are 11.9 cm for the full profile and 7.6, 20.9 and 12 cm for the three ≈ 1 m profiles.

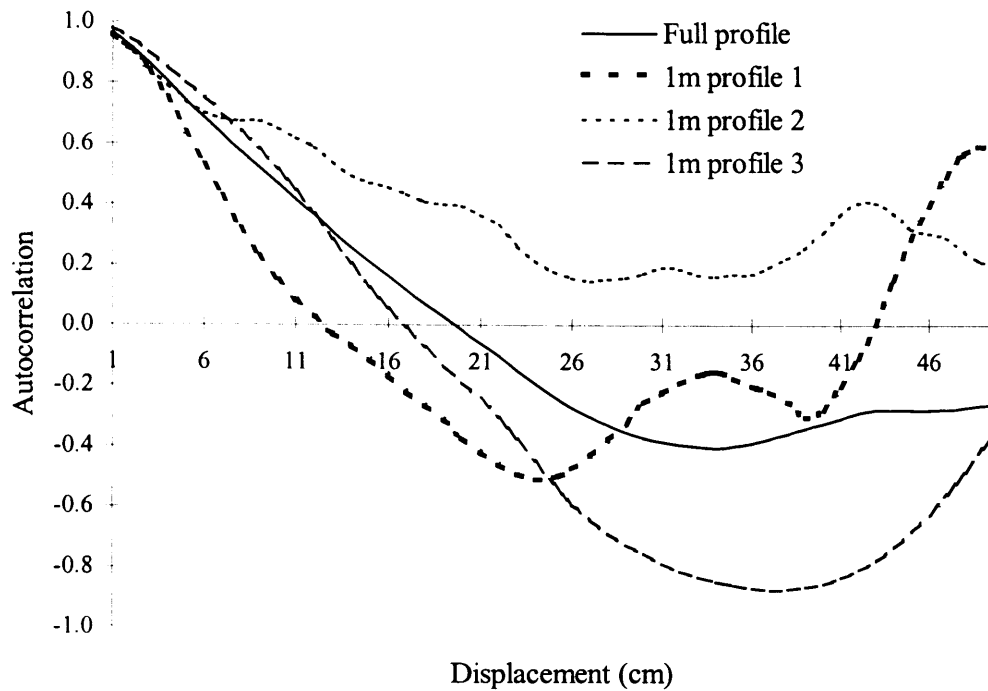


Figure 5.6. The influence of transect length on the autocorrelation coefficient is shown for the three ≈ 1 m profiles that comprise the full profile length (shown as a solid black line) for Marab Shubayka.

Therefore, there appears to be no standard profile length and the transect length affects the value of the correlation length. The majority of studies reviewed in the previous section used transects of 1 m (in this study a 96 cm profile length was used because of the profiling tool being 48 cm long). Other profile lengths have been used, Archer (1995) states that a 30 cm profile length used to calculate the correlation length was, ‘too short to accurately determine the correlation length of a playa surfaces’ (p.127) in Tunisia. This would, in most cases, produce a small estimate of the correlation length and this would be a limitation when validating the Small Perturbation Method, as Archer discovered. Leland Pierce (University of Michigan, personal communication, 1997) stated that, as a general rule of thumb, if the profile length used is less than about 50 times larger than the calculated correlation length, then the correlation length is probably wrong and you need to use a larger profile length. Overall the field data indicates that the shorter the transect length, the smaller the calculated correlation length. The outcome of this analysis was to consider all three profile lengths (individual, 1 m and long), as well as the two methods of calculating the correlation length when

deriving estimates of the roughness parameters. The usefulness of the calculated value for validating the scattering models was then tested. The results are described in Section 6.3. To prompt the discussion in Section 6.3, the ≈ 1 m profiles were the most suitable for further analysis.

5.3.2.5 The influence of slope angle on the RMS height and correlation length

The general relationships are that as slope angle increases, the RMS height and correlation lengths increase (shown in Figure 5.7 for a *hammada* site). The relationship between slope angle and correlation length is due to the slope having non-random height properties. The data distribution has a trend, be it upwards, or downwards. When analysed, profiles collected at several sites displayed significant slope characteristics. In cases where this could be easily distinguished and the slope was calculated at being over 2%, the slope effect was removed by subtracting the contribution of the slope across the profile. Roughness parameters were then re-calculated. Figure 5.7 (top) shows the surface profile for a *hammada* site located east of Azraq. The *hammada* surface is partially covered by small, angular fragments of chert and sedimentary rocks. The solid line is the non-slope corrected data, the dashed line showing the surface profile after the influences of slope angle have been averaged out. The RMS height is reduced from 1.19 to 0.75 cm. Figure 5.7 (lower) shows the autocorrelation functions for the same profiles. The estimate of correlation length is significantly reduced from 33.8 to 3.8 cm, a much more realistic value. There are potential problems in de-trending profile data. These problems are related to the length of the profile used and the scale of the slope trends that are being measured by the profilometer. It was noted that the removal of slope effects was required for longer profiles (2.88 m). Profiles of ≈ 1 m, in most cases, did not require the removal of the slope. In addition, it was important to distinguish between surface slope (linear trends) and natural surface variations that occurred over a horizontal scale of 1 m and greater. Generally though, it was important to focus on regions where the slope angle could be considered as negligible.

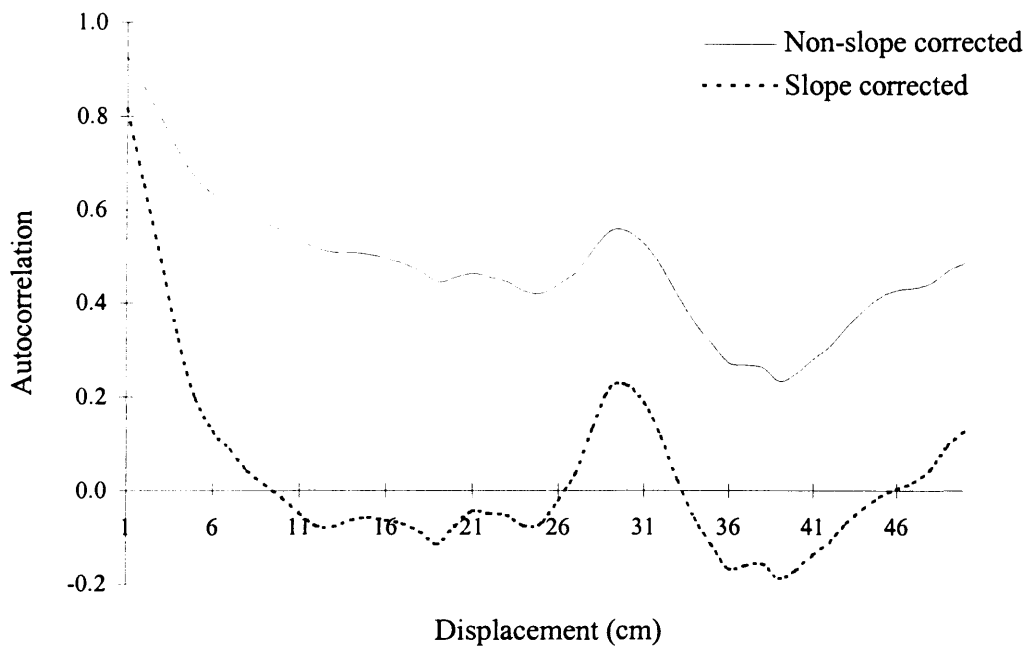
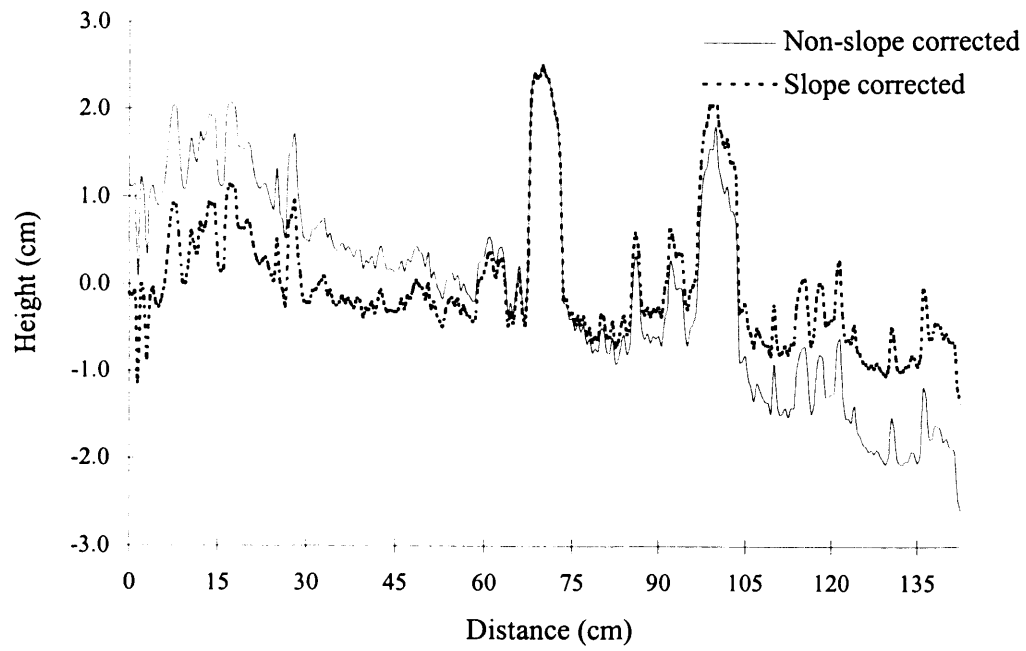


Figure 5.7. The influence of surface slope on the RMS height (top) and the correlation function (lower) for a hammada site. The values of the parameters estimated are listed in the text.

5.3.2.6 Comparison of the autocorrelation function with theoretical models

The autocorrelation function describes the relationship between the heights of two points as the distance changes between those points. For a surface to be modelled accurately it is necessary to fit the autocorrelation function to a theoretical function. In Section 2.6, the RMS slope parameter, m , was introduced as the ratio of the RMS height over the correlation length. It is necessary to calculate this parameter to satisfy the criteria for the scattering model. The autocorrelation functions were plotted (see examples in Figures 5.5 and 5.6). Based on the estimated correlation length, theoretical functions were also plotted for an exponential function, given as:

$$\rho(\xi) = \exp(-|\xi|/l) \quad (5.7)$$

or for a Gaussian function:

$$\rho(\xi) = \exp(-\xi^2/l^2) \quad (5.8)$$

where, $\rho(\xi)$ is the autocorrelation function and l is the correlation length.

The surface slope parameter, m , is calculated from

$$m = \sigma \sqrt{|\rho''(0)|} \quad (5.9)$$

where, $\rho''(0)$ is the second derivative of $\rho(\xi)$ evaluated at $\xi = 0$. This yields $m = \sigma/l$ for an exponential function and $m = \sqrt{2}\sigma/l$ for a Gaussian function.

The theoretical functions calculated for *Marab Shubayka* at the full profile length are shown in Figure 5.8. The measured autocorrelation function was closer in this instance to a Gaussian (normal) function, therefore $m = \sqrt{2}\sigma/l$ was used to calculate the RMS slope parameter.

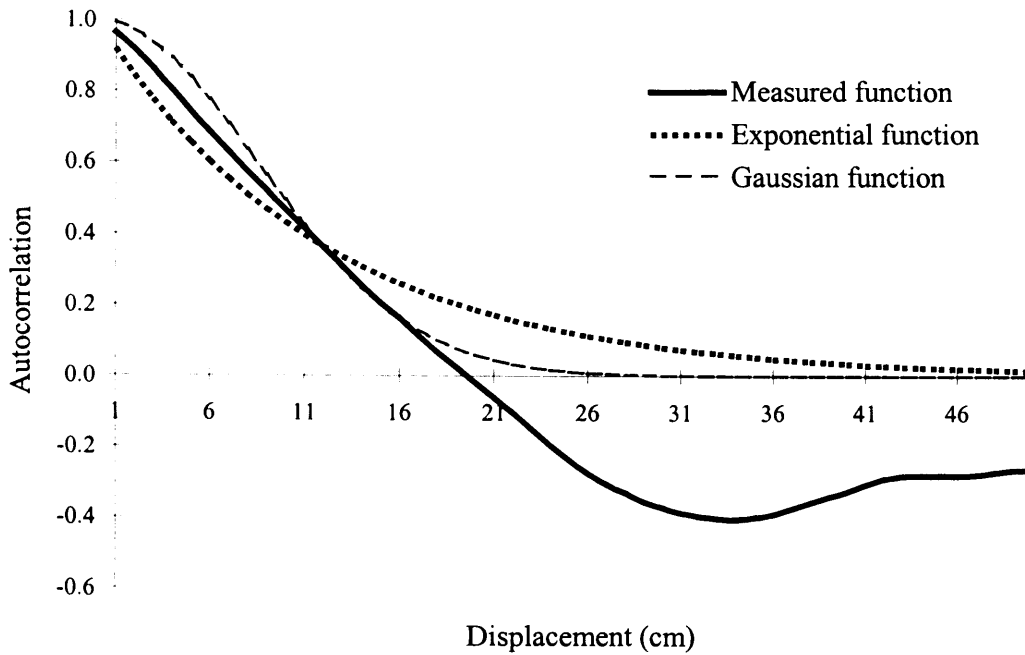


Figure 5.8. Theoretical functions plotted against the measured autocorrelation function at the full profile length, Marab Shubayka. The best fit model is Gaussian, l is 11.9 cm.

For the individual profiles, it was assumed that the surface height autocorrelation function fitted approximately to a Gaussian function (30 or 48 cm transect length). The situation was slightly different for the three ≈ 1 m profiles studied. At some sites all three profiles would yield the same approximate theoretical function, in which case this would be the one chosen for the model calculations. At other sites, two profiles fitted one distribution and the third the other distribution; e.g. *Marab Shubayka* where two profiles fitted approximately to Gaussian conditions and one profile approximately fitted an exponential function (Figure 5.9). The correlation lengths calculated in this example were 7.6, 20.9 and 12 cm respectively. In the case of *Marab Shubayka*, the Gaussian function was selected as the input criteria as it was represented twice. All of the profiles analysed were assigned to either an exponential or a Gaussian function, regardless of how different the measured data were to the theoretical data. The selection of the autocorrelation function can have a major influence on the modelled backscatter response of surfaces. This will be illustrated in Section 6.2.

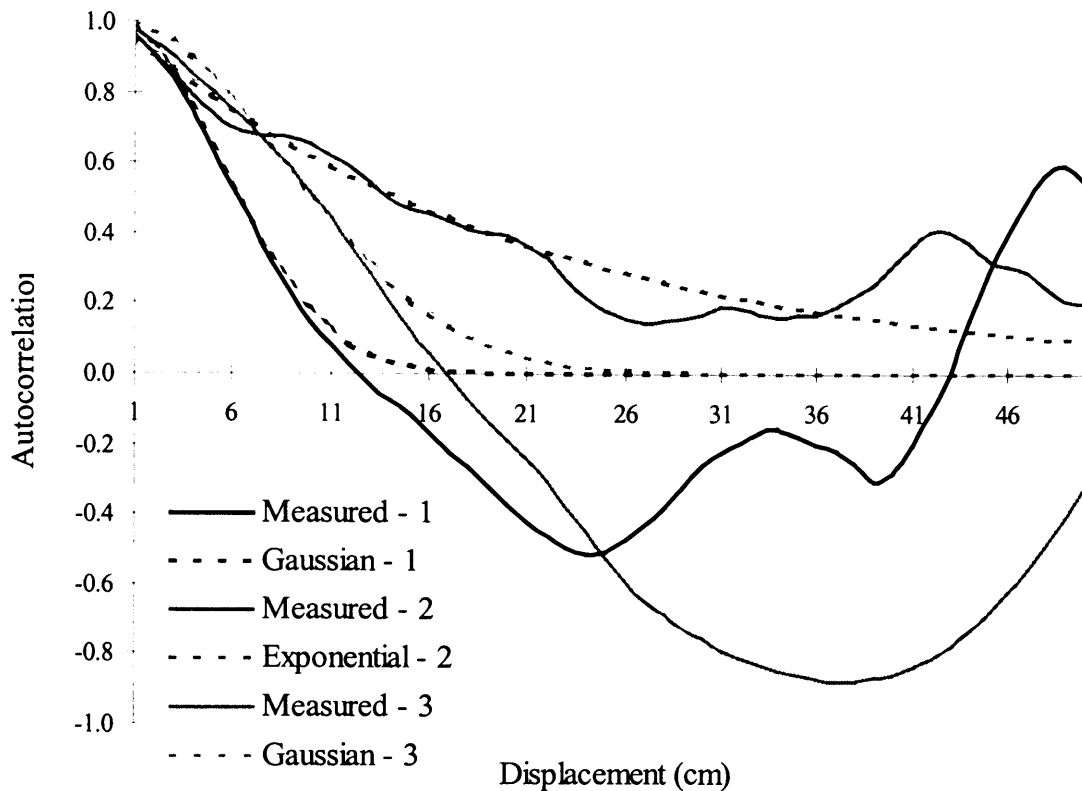


Figure 5.9. Measured ≈ 1 m correlation functions (1,2,3) shown against theoretical functions, Marab Shubayka.

5.3.3 Annual fluctuations in surface roughness properties

Any changes in the properties of surface roughness must be detected and quantified. Geomorphological processes that might induce changes in the surface roughness properties might be clay swelling, shrinking and desiccation, salt crystal growth, gravity, human modifications, animal disruption, vegetation growth and the erosion or deposition of surface sediment by wind or water action (see Section 1.3). The influence of roughness fluctuations on the backscatter returned to the satellite system can be at least as important as changes in the surface soil moisture. The sensitivity of the backscatter coefficient to changes in roughness properties was considered in Section 2.1.4. Due to the ambiguity of the correlation length outlined in the previous section, only the changes in the perceived RMS heights are considered in this section. Table 5.3 lists the RMS height measurements, for ≈ 1 m profiles, made when sites were visited.

Site name	Average RMS height (cm) for the ≈ 1 m profiles		
	Autumn 1995	Spring 1996	Spring 1997
Qa'a Qattafi	0.22	0.16	0.23
Qa'a al Abd	N/A	N/A	0.30 & 0.26
Qa'a at Ra'd	N/A	N/A	0.22 & 0.17
Qa'a al Wassad	N/A	N/A	0.17 & 0.16
Qa'a al Wutaydat	N/A	0.24	N/A
Fahda Vesicular (B1)	2.87	2.83	1.71
Madhala Olivine (B2)	2.5	3.55	N/A
Abed Olivine (B3)	3.43	4.0	N/A
Madhala Olivine	3.96	N/A	N/A
Harrat edh Dhirwa	N/A	1.12	N/A
Chert gravel hammada	N/A	0.7	0.53
Limestone hammada	0.47	0.66	N/A
Shahbat el Hazim	N/A	0.63	N/A
Shumansaniyyat	2.19	0.68	N/A
Sandflat	N/A	0.38	N/A
Feidat ed Dihikiya	0.62	N/A	N/A
Hashad	0.3	N/A	N/A
Wadi el Hazim	N/A	0.49	N/A
Marab Qattafi	0.53	N/A	0.35
Marab Salma	N/A	N/A	1.16 & 0.72
Marab al Wassad	0.32	N/A	1.16 & 0.67
Marab al Wutaydat	0.87	N/A	0.43 & 0.96
Qa'a al Buqayawiyya	0.85	0.76	0.33 & 0.83
al 'Wia (cultivated)	2.32	N/A	N/A
Shubayka	N/A	N/A	2.02 & 1.65
Marab Suwaiid	0.2	N/A	1.38

Table 5.3. Calculated RMS heights for dryland surfaces from three field visits.

Several points can be raised. Firstly, there are sites that could not be visited in the field during the field campaigns, due to problems of equipment availability and access, these are denoted as N/A. Secondly, during the 1997 campaign two sets of three 1 m profiles were collected, the two values shown in the 1997 column. For *qa'a* surfaces, the estimates of surface roughness correspond well with each other over all years. For *marab* surfaces, the two estimates do not correspond as well with each other. These values reflect the variation of surface topography of *marab* surfaces, compared to *qa'a* surfaces. Thirdly, no major changes in the RMS height, between years, were observed at any of the sites except for *Marab Suwaiid* and *Shumasaniyyat*. During the autumn of 1996, *Marab Suwaiid* was used to conduct seedling emergence, fertiliser application and irrigation experiments. The outcome of these experiments was to furrow the surface soil, perpendicular to the direction of water flow in the wadi and hence increase the surface RMS height value from 0.2 cm to 1.38 cm. This new surface profile is then accounted for in the modelling. Another *marab* which may have been influenced by human activity is *Marab Shubayka*, where no ploughing of the surface was understood to have taken place during the period of study; and a cultivated area near *Qa'a al Buqayawiyya*, which was only considered during the 1995 field campaign and has not been used since for any analysis. At *Shumasaniyyat* the surface is made up of a coarse sand soil, with randomly distributed boulders. It is likely that in 1995 the surface profile measurement included one of these boulders, the measurement in 1996 most likely did not. No major human or natural induced surface change was observed at this site. Finally, the annual changes in the RMS height for the basalt sites are quite marked. This is most likely due to the location of the profile within the basalt field, as the exact location of the profile could not be determined for repeat measurements, even though the surface was considered homogeneous. Taking the example of the Fahda Vesicular basalt site (B1) the data from 1995 and 1996 are quite similar (2.87 and 2.83 cm). Comparing these with the reduced RMS height value of 1.71 cm, the difference is quite significant. A recommendation would be to collect more 1 m profiles to obtain an average RMS height based on a large sample. However the time and equipment available made this impossible. Another approach would be to mark clearly the end of each profile so that repeat sampling can be undertaken each year. However, given the characteristics of the sites visited this was difficult.

The recommendation above applies to the whole data set. Many profiles would be required to determine the average roughness properties of a surface. During the 1997 field season, two sets of three 1 m profiles were taken at different locations within the 30 by 30 m quadrat. Pairs of estimates of the RMS height derived for *qa'a* surfaces are similar, whereas estimates for *marabs* are quite different. This emphasises that, even within a quadrat, the surface roughness is heterogeneous even if the large scale roughness can be considered homogeneous. Unfortunately the method used here cannot characterise this variability; other techniques (outlined in Section 4.4.8) may be more suitable.

5.4 Conclusions

This chapter has reviewed some of the methods for parameterising surface roughness using statistical descriptors. The physical roughness of a surface has a major influence on many geomorphological processes, and also affects the backscatter signal of an imaging radar. There are many parameters that can quantify surface roughness and many different levels of analysis to process the information. The approach taken here is model driven, therefore the models input criteria need to be satisfied. As the study is focusing on single polarised imagery at a single frequency, the measurements in the field are kept simple and are limited to calculating the RMS height, the autocorrelation function and correlation length. The profile data set was too small to consider power spectral density analysis, although this may be an option for future work. The main conclusions concerning the analysis of the roughness data can be summarised as follows.

- Two methods of deriving the correlation length were compared; no real advantages were gained by using the Pearson correlation method over the simple method.
- The correlation length appears to increase with increasing profile length and also with increasing slope angle. Therefore, care was required to maintain consistent profile lengths and to avoid surfaces with excessive slopes.

- A profile length of 1 m gave the most representative estimates of correlation length. They were also the most useful estimates when validating the surface scattering models used in this study (Section 6.2).

- The RMS height gave the most useful characterisation of the roughness of a surface.

- The autocorrelation function of a surface was described by either a Gaussian or exponential function. The major land units studied could not be characterised clearly by a particular autocorrelation function.

- There was limited flexibility when collecting roughness data for this study e.g. no major funding to purchase a laser profilometer, which would have yielded more accurate results, was available.

6. Deriving Soil Moisture Estimates with Theoretical Models

The results of the application of the theoretical models, described in Chapter 2, for understanding scattering processes in a desert environment are presented. The desert surfaces under consideration are the permanent monitoring sites (PMS) introduced in Chapter 4. This chapter is divided into several sections. Section 6.1 discusses the main results obtained by other researchers that have utilised these models in different environments or for other applications. Simulation of the sensitivity of the backscatter coefficient under varying soil moisture and surface roughness conditions are shown in Section 6.2. Furthermore, the influence of local incidence angle on the magnitude of the backscatter coefficient is also shown. Section 6.3 describes physical optics, geometric optics and small perturbation model calibration results, followed by model calibration results for the integral equation model. Section 6.4, discusses the implications for the retrieval of soil moisture information from SAR images through model inversion. The eight permanent monitoring sites are used in this analysis. Section 6.5 shows the results from the validation testing of the inversion algorithms. This testing is carried out on *Qa'a al Buqayawiyya* using soil moisture data collected during the spring 1998 field trip. Finally, Section 6.6 summarises the main findings and concludes the chapter.

6.1 Introduction

Theoretical scattering models have been used to predict the backscatter response for a range of surfaces. However, their validation has been tested mainly on agricultural fields with known surface roughness characteristics. Evaluation of the Kirchhoff and small perturbation methods, the classic solutions, was achieved for 150 agricultural fields by Engman and Wang (1987), who conclude that the small perturbation (SP) method gave the best results when fields with a definite row structure were not included in the analysis. To obtain soil moisture estimates without any ambiguity, a multi-data set approach is required. The multi-data set approach was adopted by Rao *et al.* (1993), who used a multi-frequency system to estimate soil moisture to within 2% and surface

roughness to within 10%. Mo *et al.* (1988) used C and L band data to estimate surface roughness parameters. Autret *et al.* (1989) concluded that a combination of HH and VV polarised data would minimise the sensitivity of the backscatter coefficient to surface roughness. Ridley *et al.* (1996) used both the coherent and non-coherent components of the Kirchhoff approximation to model the backscatter coefficient from altimeter data. Backscatter from altimeter data, having a nadir look angle, is independent of the polarisation of the signal. Field data collected in the Simpson Desert, Australia showed that the Kirchhoff methods gave excellent representation of the backscatter coefficient measured with TOPEX NASA radar altimeter (Ridley *et al.* 1996). Observations of the backscatter coefficient in the desert environment indicated large fluctuations in response to rainfall events. A 2 mm rainfall event produced a step increase of 5 dB with a constant decay over 48 hours afterwards. Other measurements indicate that in areas with high evaporation rates and well-drained soils, detection of rainfall induced increases in soil moisture is only possible with a repeat pass of two to three days.

Previous studies have also highlighted the limitations of using a theoretical approach for soil moisture estimation. The main restrictions of the Kirchhoff approximations are their validation regimes in relation to surface roughness parameters. Oh *et al.* (1992) derived the following conclusions from their analysis of the Kirchhoff and SP methods. First, some natural surface conditions fall outside the regions of validity for all three models, this certainly is the case for the desert surfaces considered in this study (Section 6.3). Second, none of the models provide good agreement with the measured data, particularly at incidence angles greater than 40°. Third, the physical optics (PO) model predicts that the VV polarised backscatter is less than the HH polarised backscatter. This is contrary to all observations. Therefore Oh *et al.* (1992) proposed an empirical approach while other researchers developed second-order theoretical approaches to the problem (Fung *et al.* 1992).

Backscatter measurements were compared to estimates derived from the integral equation model (IEM) and Kirchhoff methods by Chiarantini *et al.* (1995) for natural surfaces in a Mediterranean environment. They found that the agreement between measured and observed backscatter coefficients was within a mean error of 2.5 dB for the PO model, 2.7 dB for the IEM, and 3.2 dB for the geometrical optics (GO) model.

Further multi-parameter problems were introduced by local slope angle affects. The IEM has also been widely tested, focusing on simplified versions of the originally complex equation. Chen *et al.* (1995) used a simple version of the IEM to simulate the backscatter coefficient of a wide range of surfaces with known radar parameters. Favourable results are obtained when estimates from the model are compared to experimental data. However, inversion of the model to derive estimates of soil moisture requires a value of the ratio between like-polarised backscatter coefficients ($\sigma_{hh}^{\circ} / \sigma_{vv}^{\circ}$) which are not available in this study. It is important to re-iterate once again the limitations of using a fixed polarised, fixed wavelength and fixed incidence angle system to extract soil moisture or surface roughness information from the backscatter coefficient when it is possible that several surface parameters are influencing the signal. Ulaby (1998) recently stated that it is far more difficult to extract biophysical information from multi-date, single channel observations than multi-channel, single date observations.

The distribution and nature of precipitation events in semi-arid and arid regions is very important as it influences the degree of surface wetting and the amount of surface soil moisture. The study area suffers a lack of evenly distributed raingauges. They are concentrated either in the large towns (Safawi and Azraq) or in the villages located in the wetter north-west of the study area. Therefore, correlation between field sites and fixed raingauge locations is necessary. However, the errors in doing this cross-correlation can be significant. In a study located in south-west Saudi Arabia, Wheeler *et al.* (1991) collected hourly data from 100 raingauges distributed in 5 wadis. The main conclusions of this research were that rain on any day was strongly associated with elevation, most point rainfall events were of 1 to 2 hours duration and, most importantly, that the spatial distribution of the rainfall was highly localised and that even where distances between raingauges was 8 km, the probability of rainfall at both sites is less than 0.4. Where raingauges were separated by distances of approximately 20 km they found maximum probabilities of rainfall occurrence of 0.2. Even at a minimum raingauge separation of 8 km, their data was considered spatially independent. In a study under similar climatic conditions but with a more raingauge dense network, in Walnut Gulch, Arizona, showed again the localised nature of rainfall in arid regions (Osborn *et al.* 1979). The Walnut Gulch results showed that the correlation between total storm

rainfall was 0.8 where raingauges were separated by a distance of 2 km, falling to almost zero at a separation distance of 15-20 km. The implications of these studies on rainfall data acquired in the study area are that interpretations between increases in soils moisture detected, with the SAR instrument, and rainfall recorded at a raingauge site need to account for the distance between the two sites. This problem is addressed individually for each permanent monitoring site analysed in Section 6.4.

6.2 Backscatter sensitivity to soil moisture and surface roughness

Chen *et al.* (1995) stated that the first step of an inversion algorithm is to conduct a sensitivity analysis of the parameters affecting the backscatter coefficient. This is done to establish relationships and correlations between parameters. For the satellite-sensor system used in this study, this is a relatively simple process as many of the parameters are fixed (wavelength, polarisation) but for multi-sensor and parameter studies, data simulation can generate a great amount of data. In this section, the integral equation model is used because the relationships are approximately the same as the Kirchoff and SP methods and the IEM's range of validity is greater. More detailed simulations of the IEM are given by Su and Troch (1996) and Altese *et al.* (1996). In this section, the sensitivity of the backscatter coefficient to changes in soil moisture, soil type, surface roughness parameters and local incidence angle are analysed. The analysis is helped by the fact that the sensitivity of the backscatter coefficient to changes in soil moisture is independent of the roughness of the surface and that the opposite, i.e. that the sensitivity of the backscatter to surface roughness change is independent of soil moisture (offsets just occur), is also true. Section 6.2.3 displays general simulation results for the four main land cover types. All of the simulation results use the frequency of the ERS system (5.3 GHz), at VV polarisation and, unless stated, an incidence angle of 23°. In all of the figures, which display a volumetric soil moisture parameter, the units used are m³ water m⁻³ soil.

6.2.1 Sensitivity to soil moisture

The dependence of the backscatter coefficient on soil moisture is related to the dielectric properties of the soil medium. The dielectric constant of a soil medium is calculated using the empirical relationship derived by Hallikainen *et al.* (1985). Figure 6.1 shows the sensitivity of the real component of the dielectric constant to volumetric soil moisture values between 0.0 and 0.4. The results are for both a clay-size dominated (45% clay, 45% silt and 10% sand) and a sand-size dominated (60% sand, 35% silt and 5% clay) soil.

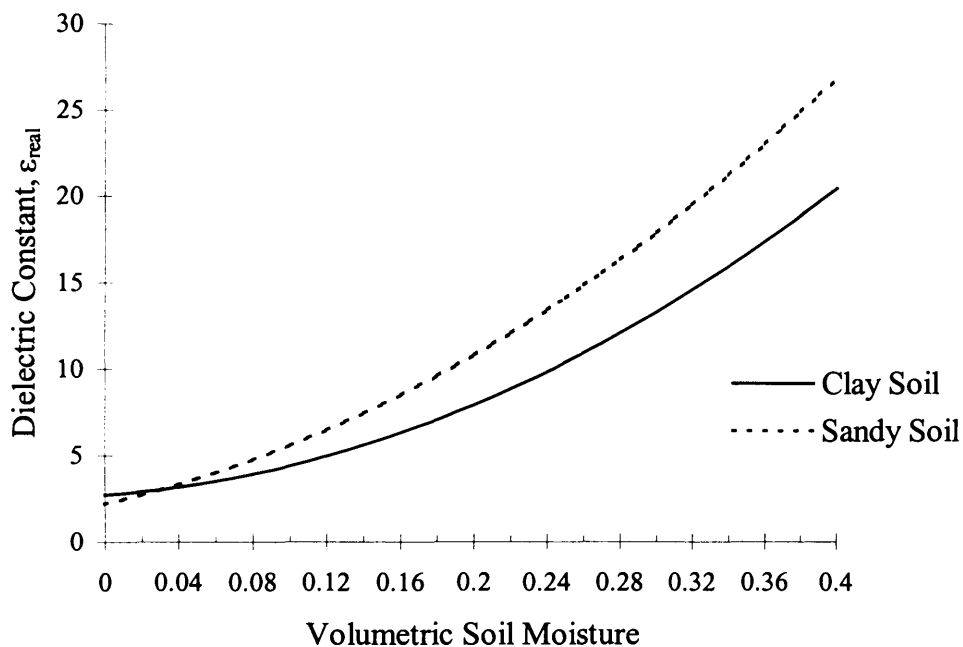


Figure 6.1. Sensitivity of the dielectric constant to soil moisture for two soil types. The clay soil comprises 45% clay and 10% sand sized particles, the sand soil comprises 60% sand and 5% clay particles in this example. For a given soil moisture above 0.03 (by volume) a sand soil has a greater dielectric constant.

The sensitivity of the backscatter coefficient to changing dielectric conditions and soil type is shown in Figure 6.2 simulated using the IEM. For each of the soils described the

silt-size particle content remains constant at 30% with the percentage of sand-size particles increasing from 10 to 60% in 10% increments. The following parameter values are used in the simulation; RMS height = 1 cm, correlation length = 8 cm, autocorrelation function = Gaussian, frequency = 5.3 GHz, polarisation = VV, incidence angle = 23° .

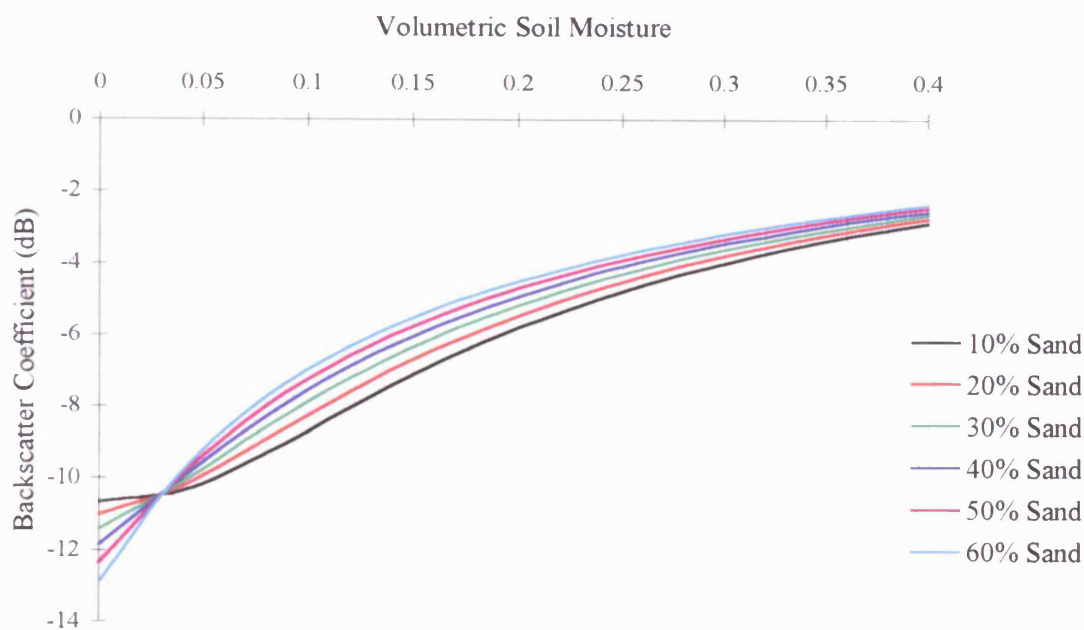


Figure 6.2. Sensitivity of the backscatter coefficient to soil moisture for a specified soil type. The IEM simulation assumes a constant silt particle size content of 30%.

Two important points can be stated from the results shown in Figure 6.2. First, that the dependence of the backscatter coefficient on soil moisture changes can be assumed to be almost independent of the soil type. The maximum difference caused by the two extremes of soil particle size is approximately 2 dB at two ranges of soil moisture values. The first occurs when soil moisture values are extremely low, less than $0.03 \text{ m}^3 \text{ water m}^{-3}$ soil, and second, when volumetric soil moisture values are in the region of 0.1. However, in this study as much information as possible about the surface was obtained so that the most accurate estimate of the backscatter properties were derived, this included information on the soil type. For an error such as 2 dB, an inversion algorithm would

yield misleading estimates of soil moisture. Second, the radiometric range of the backscatter coefficient for the values of soil moisture is large for all soil texture combinations. For a clay-size dominated soil, the model predicts a 6.5 dB increase in backscatter as volumetric soil moisture increases from 0.0 to 0.4 m³ water m⁻³ soil. For a sandy soil the same increase in soil moisture leads to a 10 dB increase in backscatter. Furthermore, sensitivity to changes in soil moisture is greater at low values of soil moisture (< 0.2 m³ water m⁻³ soil). These are values that are very likely to be found in desert regions.

The dependency of the backscatter coefficient on soil moisture may also be influenced by the location of the site in the range direction of the SAR image. This is because of the small change in incidence angle across the image from approximately 20° at near range to 26° at far range. The influence of local incidence angle effects are shown in Figure 6.3. A surface with a RMS height = 1 cm, correlation length = 8 cm, autocorrelation function = Gaussian, sand = 30%, clay = 15% is used in the simulation.

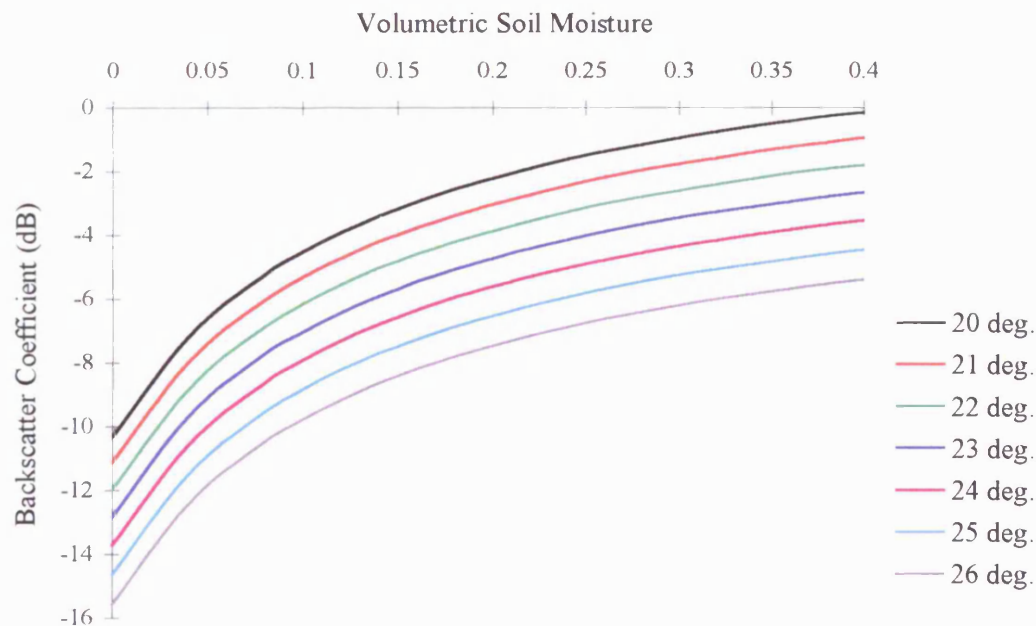


Figure 6.3. Sensitivity of the backscatter coefficient to soil moisture accounting for the variation in incidence angles across an ERS SAR image. The simulation displayed is for a 1° increment in incidence angles between 20 and 26°.

The results indicate that the sensitivity of the backscatter coefficient is independent of the incidence angle between 20 and 26°. However, the relative position of the study site in the range direction affects the intensity of the backscatter coefficient. As most of the information extracted from the images was from successive 35-day repeat overpass the range location for each site was approximately the same. The precise value of local incidence angle (between 20 and 26°) was accounted for in both the observed backscatter coefficient, calculated from the SAR data, and the predicted backscatter coefficient, calculated from the models.

6.2.2 Sensitivity to surface roughness

For model calibration, information is required on the RMS height, correlation length and autocorrelation function of the surface. Therefore, the influence of each of these parameters on the backscatter coefficient needs to be established. Figures 6.4 and 6.5 show the dependency of the backscatter signal on the RMS height for a given correlation length and autocorrelation function. For both simulations presented, volumetric soil moisture = 0.1 m³ water m⁻³ soil, sand = 30%, clay = 15%, incidence angle = 23°, frequency = 5.3 GHz and polarisation = VV. Figure 6.4 displays the simulation results as RMS height increases from 0.2 to 2.6 cm, at 5 correlation lengths (4, 6, 8, 10 and 12 cm) for a surface described by a Gaussian autocorrelation function. Figure 6.5 shows the simulation results under similar conditions (note the y-axis scale change) as Figure 6.4, but for a surface described by a exponential autocorrelation function. The following points need to be raised:

- Focusing on Figure 6.4 (a Gaussian surface), the backscatter coefficient is very sensitive to fluctuations in RMS height for surfaces with a RMS height < 1 cm. This sensitivity is reduced as the correlation length of the surface is reduced. For large correlation lengths (> 10 cm), the dependency of the backscatter coefficient on the RMS height is still significant up to a value of approximately 1.5 cm (RMS height).

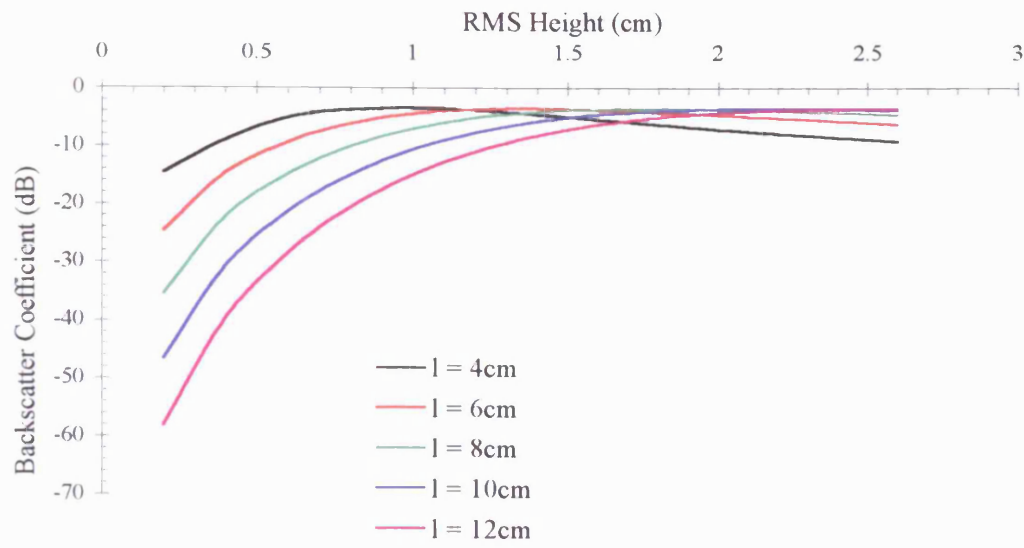


Figure 6.4. Sensitivity of the backscatter coefficient to RMS height for a specified correlation length (l). The autocorrelation function used in this simulation is Gaussian.

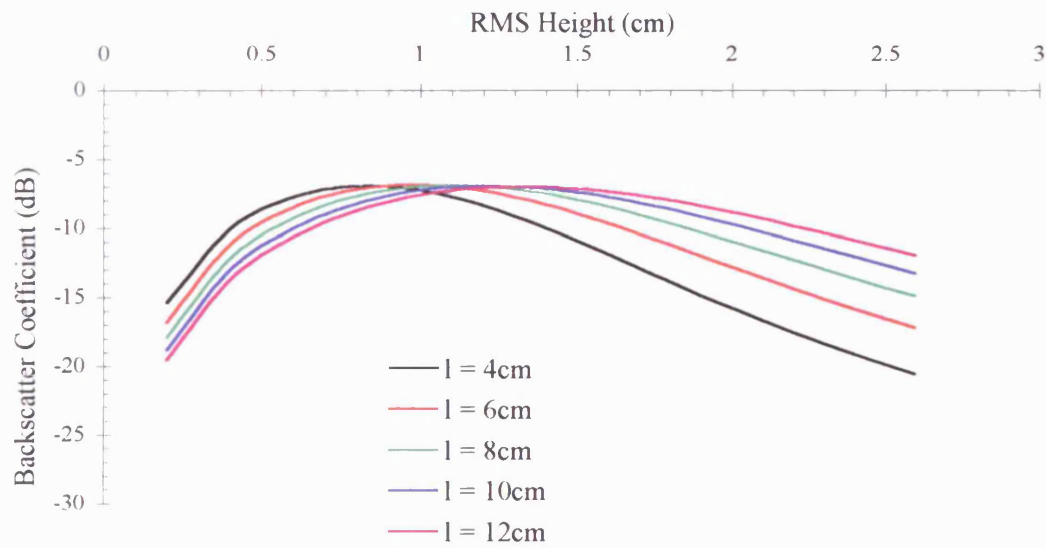


Figure 6.5. Sensitivity of the backscatter coefficient to RMS height for a specified correlation length (l). The autocorrelation function used in this simulation is exponential.

- At a RMS height greater than 1.2 cm, the backscatter coefficient is almost independent of surface roughness, unless the calculated correlation length is large, i.e. greater than 10 cm, or small, i.e. less than 4 cm (Figure 6.4).

- For surfaces with a large RMS height and small correlation length, the backscatter coefficient decreases for an increase in roughness (Figure 6.4). The field measurements indicated that surfaces with low roughness usually exhibited low values of correlation length and surfaces with high roughness do not usually yield very low estimates of the correlation length.

- For surfaces with a small to moderate RMS height, characterised by a large correlation length and a Gaussian autocorrelation function, the resultant estimate of backscatter coefficient would be very large and negative. Therefore it was important to account for any local slope effects that would increase the correlation length (Section 5.3.2.5), to reduce the chance of this result being obtained. The lowest estimates of the backscatter coefficient found on the SAR imagery was approximately -25 dB over very flat, specular surfaces. Hence predicted backscatter coefficients less than -25 dB were ignored.

- For a surface best described by an exponential distribution function (Figure 6.5), the backscatter coefficient is also very sensitive to surface roughness, at all the correlation lengths tested, when the RMS is less than 0.5 cm. The magnitude of this dependence is much reduced compared to a Gaussian surface but is still sufficiently large not to be considered independent.

- Figure 6.5 indicates that the backscatter coefficient is approximately independent of surface roughness if the RMS height of a surface is between approximately 0.8 and 1.5 cm and the correlation length is greater than 5 cm. After 1.5 cm the backscatter coefficient is once again significantly influenced by an increase in surface roughness resulting in a decrease in the estimated backscatter coefficient.

The sensitivity of the backscatter coefficient to RMS height for a specified incidence angle is shown in Figure 6.6. In the simulation the following variables are specified. Volumetric soil moisture = $0.1 \text{ m}^3 \text{ water m}^{-3} \text{ soil}$, sand = 30%, clay = 15%, correlation length = 8 cm, autocorrelation function = exponential, frequency = 5.3 GHz, polarisation = VV.

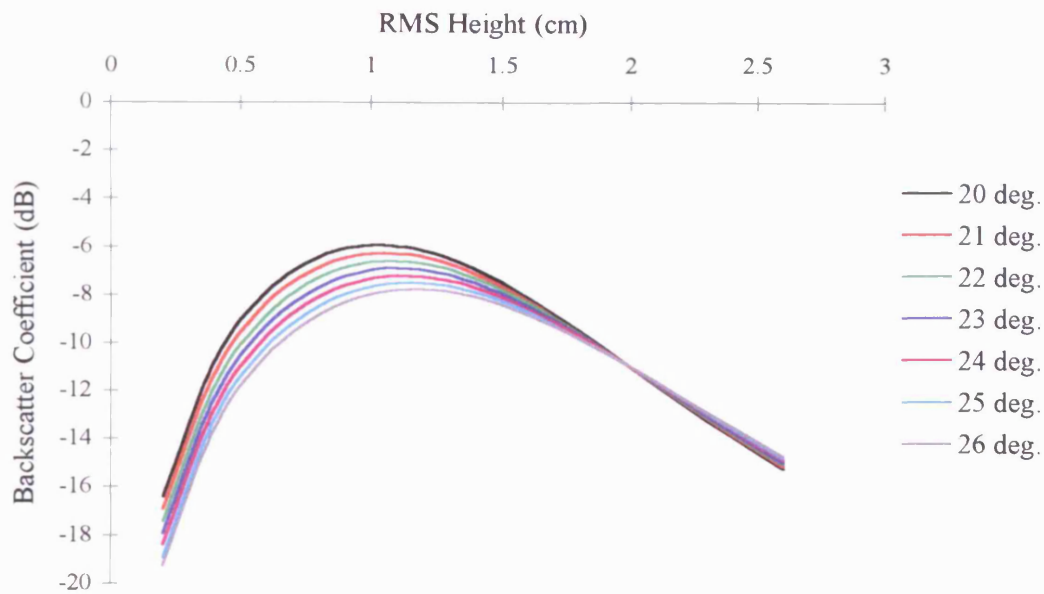


Figure 6.6. Sensitivity of the backscatter coefficient to RMS height accounting for the variation in incidence angle across an ERS SAR image. The simulation displayed is for 1° increments for incidence angles between 20° and 26° . This variation is accounted for in the image pre-processing stages of the analysis.

The model indicates that the position of the target in the range direction has a direct influence on the intensity of the signal received, the intensity of a scatterer at near range (20°) having a backscatter coefficient 2 dB greater than the same scatterer registering at the far range (26°) of an image. This result is consistent with surfaces having RMS height values less than 1.2 cm. The backscatter coefficient of a surface with a RMS height greater than 1.2 cm is almost independent of the change in incidence angle across

a SAR scene. Therefore, it is important to account for any significant change in range location of a study site in an image and then re-calculate the local incidence angle.

It can be seen from the simulation experiments that the relationships between the surface roughness parameters, required as data input, and the backscatter coefficient are complex. It is necessary, therefore, to obtain the most accurate information about the study sites as possible to yield the most accurate model predictions. Chapter 5 discussed the problems surrounding the measurement and application of the correlation length parameter in radar studies as an example. Even so, it is still important to test the application of theoretical models in a semi-arid or desert environment for soil moisture studies.

6.2.3 Sensitivity analysis: Main land cover types

Given the simulation results, the sensitivity of the backscatter coefficient to soil moisture variations and small changes in surface roughness can be calculated for the main land cover types: basalt, *marab*, *qa'a* and *hammada*. The simulation uses input data that characterise the general properties of these desert surfaces. For example, the basalt surfaces generally have a higher RMS height than the *hammadas*. *Marab* surfaces, cannot be characterised by a general relationship as the roughness of the *marab* varies from site to site. Figure 6.7 displays the sensitivity of the backscatter coefficient to soil moisture for selected general land cover types. The simulation shows that the backscatter coefficient is almost independent of surface roughness properties, the roughness of a surface influencing only the offset of the curve and the gradient of the *marab* surface (caused by the autocorrelation function). Small variations in curve shape are caused by differences in the particle size distribution of the surface soil. All of the surfaces show a significant dynamic range of C-band backscatter over the range of soil moisture simulated, on average 10 dB for an increase of soil moisture from 0.0 to 0.4 m³ water m⁻³ soil.

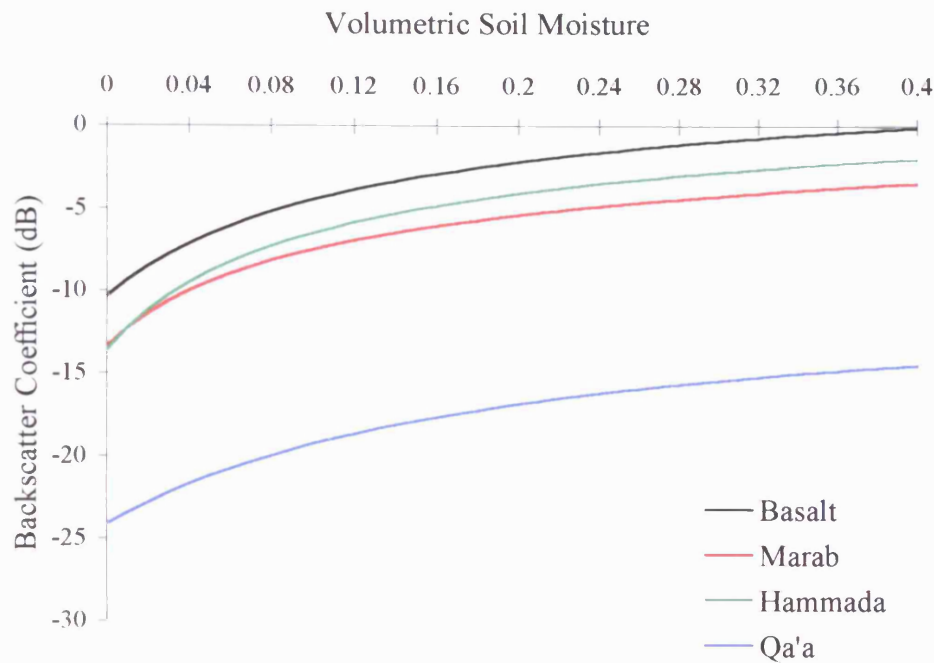


Figure 6.7. Sensitivity of the backscatter coefficient to soil moisture for the four main land cover types.

The sensitivity of the backscatter coefficient to small fluctuations in the RMS height of the main land cover types, is illustrated in Figure 6.8. The simulation shows that the backscatter is highly dependent on the RMS height when the surface is relatively flat, e.g. for a *qa'a* surface. The greater the RMS height the less influence small changes in RMS height has on the backscatter coefficient. For rough surfaces displaying Gaussian autocorrelation functions, changes in RMS height have negligible influences on the backscatter, as do exponential surfaces when the RMS height approximates to 1 cm.

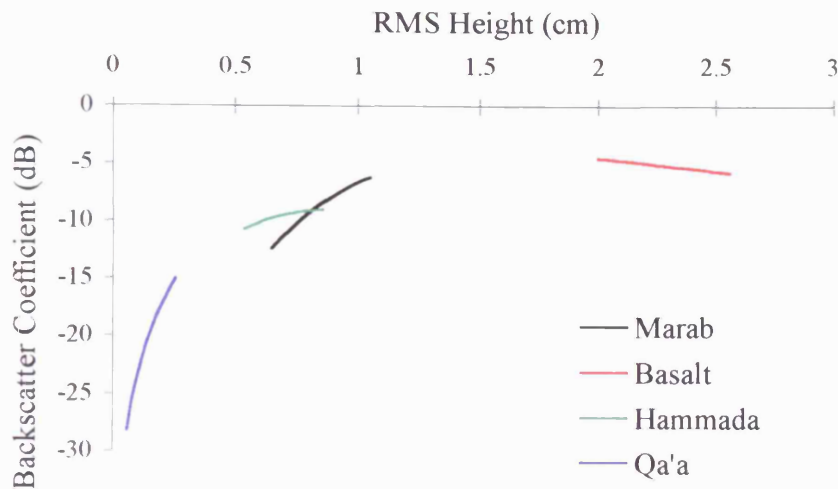


Figure 6.8. Sensitivity of the backscatter coefficient to RMS height for the four main land cover types.

6.3 Model calibration

To test the usefulness of the models in predicting the backscatter coefficient from the ERS SAR system, observed values of backscatter were compared with predicted values. This section is divided into four sub-sections. The first describes the calibration results obtained using the small perturbation (SP), physical optics (PO) and geometrical optics (GO) models. The second sub-section describes the calibration results obtained from the integral equation model (IEM). The third sub-section describes what are perceived to be the optimal results obtained using the IEM with selective estimates of the observed backscatter coefficient. The fourth sub-section presents concluding remarks. Four controls and assumptions apply. Please note, for clarity in this section, where simple estimates of the correlation length are referred to, the word will be followed by the roughness in brackets, i.e. ...simple (roughness) estimates of the correlation coefficient. Where simple estimates of the backscatter coefficient are referred to, simple will be followed by σ° in brackets, i.e. ...simple (σ°) estimates of the backscatter coefficient.

(i) The results are shown for several scenarios. These are using the three different profile lengths, short (30 or 48 cm), ≈ 1 m and full (2.88 m). They are also given for two separate estimates of the correlation length, the simple (roughness) and Pearson methods (Chapter 5). [Note that only the Pearson estimate of correlation length was calculated from the short profile lengths].

(ii) Results are given for two estimates of the observed backscatter coefficient calculated from the satellite data, the simple (σ°) and comprehensive estimates. In addition there is a third estimate using comprehensive estimates from ERS-1 data and simple (σ°) estimates from ERS-2 data described in Section 3.3.

(iii) The model calibration procedure has only been undertaken for field data that conforms to the validation criteria of the models. These data are from all sites visited in 1995, 1996 and 1997.

(iv) In some cases, field data have yielded values what I have assumed to be unrepresentative, that have resulted in erroneous estimates of the backscatter coefficient. These data came from large value estimates of the correlation length that resulted in unrealistic estimates of the backscatter coefficient. These data have been ignored in the final analysis.

Therefore, for each model grouping, 10 different analyses are displayed. Point (iii), concerning the validation criteria, is very important as it stipulates the number of sample points that can be used to calibrate the model of interest. As an example, the validation conditions for the SP, PO, GO and IEM, discussed in Section 2.6 are illustrated in Figure 6.9. Calculated roughness parameters collected during the first three field seasons are plotted within the validation domains. The data are calculated from ≈ 1 m profile lengths, using the simple (roughness) method of calculating the correlation length. Basalt sites have not been included in this example. These results indicate the limitations of using the classical models of surface scattering for predicting the backscatter of natural desert surfaces. A number of sites have roughness properties characterised by a moderate RMS height and short correlation length or a small RMS height and moderate correlation length, regions that the classical models do not account

for. In the example shown (Figure 6.9) there are potentially 11 points that could be used to calibrate the classical models whereas there are 28 points that could be used to calibrate the IEM. This observation is consistent for all of the scenarios tested.

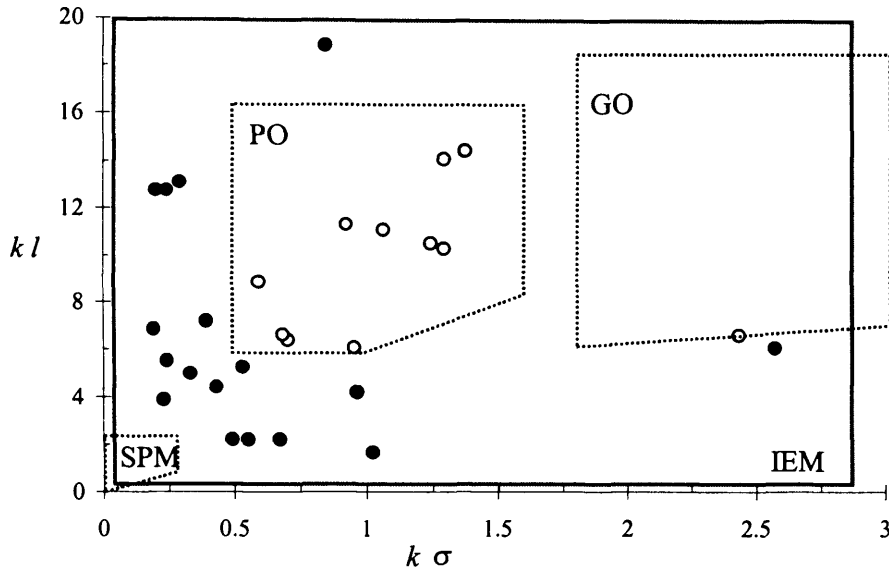


Figure 6.9. Illustration of the validation criteria of the SP, PO, GO models and IEM used in this study. Field data, excluding basalt sites, are plotted in a roughness feature space comprising correlation length (l) against RMS height (σ), k is the wavenumber and ≈ 1.11 at 5.3 GHz. In this example, ≈ 1 m profiles have been used to calculate the roughness parameters and the simple method adopted for calculating the correlation length. Those sites that lie within the validation domains of the SP, PO and GO models (dashed polygons) are displayed as hollow circles, those that fit the criteria of only the IEM (solid polygon) are displayed as solid circles.

6.3.1 SP, PO and GO model calibration

It is evident that a basic limitation in using these classical solutions are the lack of data that can be used to fully test the models in a desert environment. Table 6.1 summarises the results obtained. Listed are the methods of calculating the roughness parameters, the

number of sites that can be used to validate the models, and the correlation coefficient calculated when the predicted model backscatter coefficients are compared with observed backscatter coefficients.

Summary of the Calibration Results of the SP, PO and GO Classical Models				
Length of transect	Correlation function (simple (roughness) or Pearson)	Observed backscatter coefficient (simple (σ°) or comprehensive)	No. of sites for calibration	Correlation coefficient
Short	Pearson	Comprehensive	9	0.89
≈ 1 m	Pearson	Comprehensive	10	0.8
	Simple (roughness)		16	0.65
Full	Pearson	Comprehensive	11	0.78
	Simple (roughness)		9	0.77
Short	Pearson	Simple (σ°)	10	0.8
≈ 1 m	Pearson	Simple (σ°)	10	0.8
	Simple (roughness)		16	0.63
Full	Pearson	Simple (σ°)	11	0.8
	Simple (roughness)		9	0.8

Table 6.1. Summary of the results of the calibration of the SP, PO and GO models using field data acquired during three field seasons. The models have been tested using 10 scenarios of different estimates of the correlation length, profile length and the calculation of the observed backscatter coefficient.

The results show the small number of sites that were used to calibrate the models. Using a ≈ 1 m profile length and the simple method of deriving the correlation length, up to 16 sites can be used, although this yields a poor correlation (0.65). In contrast, the results using a short profile, the Pearson method and a comprehensive estimate of the observed

backscatter coefficient yields a correlation coefficient of 0.89. However this is based on observations made at only 9 sites. There seems to be no clear advantage in using the comprehensive estimate of the backscatter coefficient or using the Pearson method of calculating the correlation length when long profile lengths (>1 m) are used. The results, however, do seem to be dependent on these criteria if the other profile lengths are used.

The calibration results are illustrated in Figure 6.10 for the scenarios listed in Table 6.1. To compare the results obtained when using the two different methods of calculating the backscatter coefficient (simple and comprehensive) from ERS SAR imagery at a given profile length the graphs adjacent to each other need to be interpreted. The two different methods of calculating the correlation length (simple and Pearson) can be compared using the graphs above each other within each box.

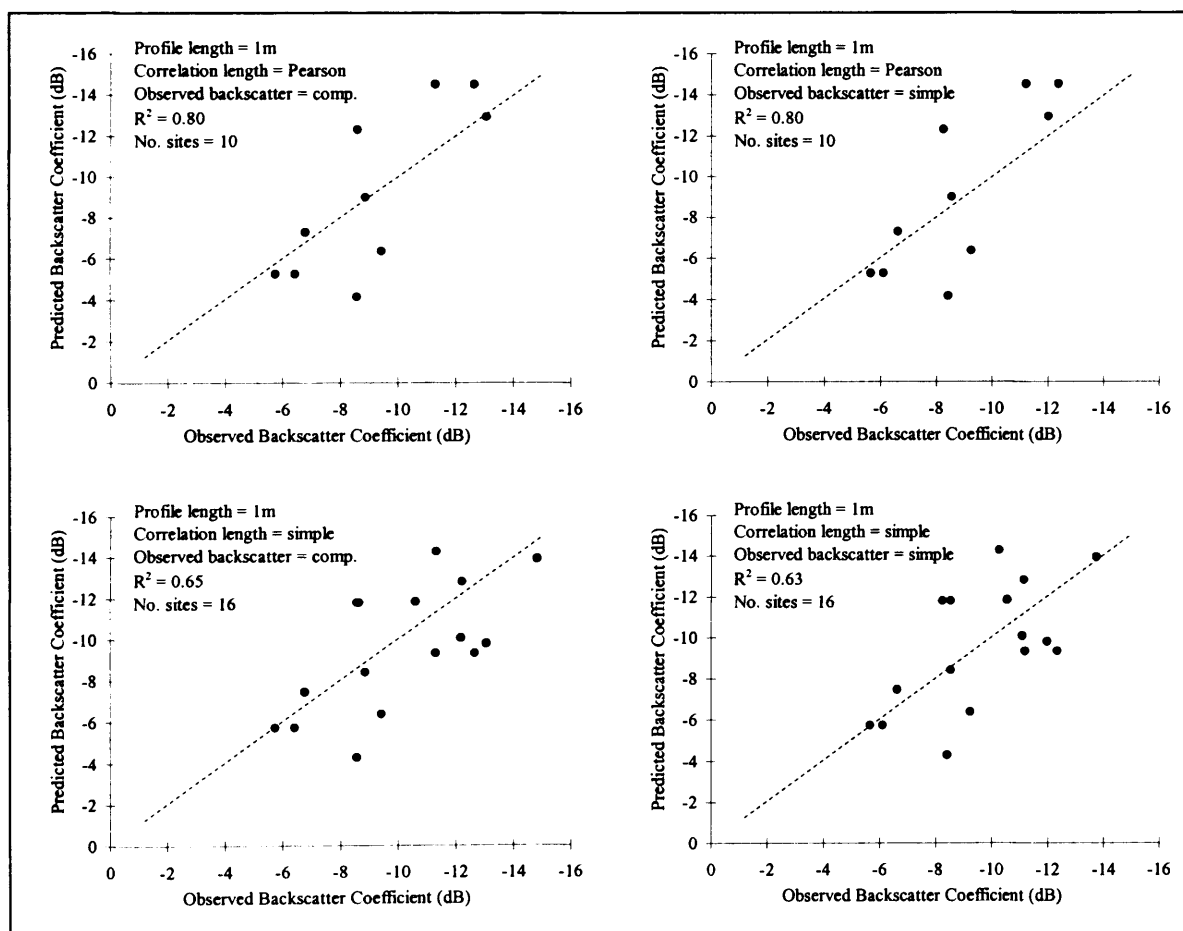


Figure 6.10. (continued on the following page).

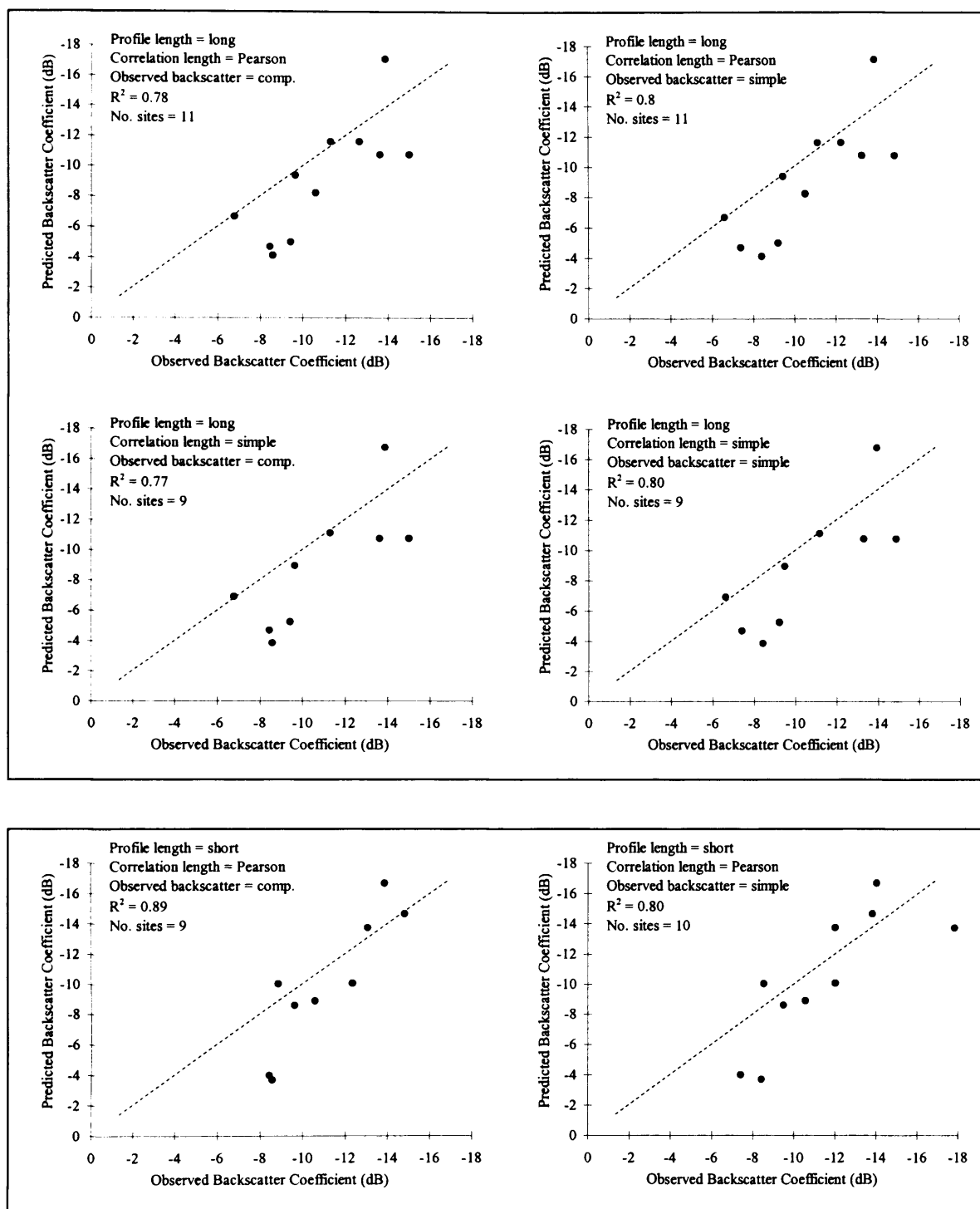


Figure 6.10. Kirchhoff and small perturbation model calibration results for the ten scenarios listed in Table 6.1. Observed backscatter coefficients are derived from ERS SAR PRI data. Predicted backscatter coefficients have been calculated from the SP, PO and GO models using field data that have satisfied all of the validation criteria. The calibration coefficients between observed and predicted measurements are shown.

6.3.2 IEM calibration

The IEM has more potential than the classical models for the current application, due to a larger validation domain that encompasses most the roughness parameters that were measured in the field. Table 6.2 shows the calibration results obtained using the IEM, displayed in a form similar to that shown in Table 6.1.

Summary of the Calibration Results of the Integral Equation Model (IEM)				
Length of transect	Correlation function (simple or Pearson)	Observed backscatter coefficient (simple or comprehensive)	No. of sites for calibration	Correlation coefficient
Short	Pearson	Comprehensive	35	0.79
≈1 m	Pearson	Comprehensive	34	0.86
	Simple (roughness)		36	0.84
Long	Pearson	Comprehensive	28	0.87
	Simple (roughness)		30	0.86
Short	Pearson	Simple (σ°)	36	0.78
≈1 m	Pearson	Simple (σ°)	32	0.88
	Simple (roughness)		36	0.84
Long	Pearson	Simple (σ°)	28	0.87
	Simple (roughness)		30	0.85

Table 6.2. Summary of the results of the calibration of the IEM using field data acquired during three field seasons. The models have been tested using 10 scenarios of different estimates of the correlation length, profile length and the calculation of the observed backscatter coefficient.

In all cases the IEM is calibrated with a greater number of sites. Better correlation coefficients were obtained between observed and predicted backscatter coefficients for all of the scenarios tested. Although the results are very similar to each other, the most

accurate method appears to be with the use of ≈ 1 m profiles using the Pearson method of calculating the correlation length, and comparing the values to either the simple (σ°) or the comprehensive estimates of the backscatter coefficient. It is interesting to note that the accuracy is not significantly increased using the comprehensive equation to derive the backscatter coefficient from the SAR data. The same is almost true of the selection of the method to derive the correlation length, neither method having significant advantages over the other. The recommendation that a 1 m (or as near to 1 m) profile should be used in future studies is enforced here as the use of too short a profile leads to a decrease in the prediction accuracy of the model, and too long a profile, apart from introducing potential slope influences, reduces the potential number of calibration data points that can be used. The results from IEM calibration are displayed in Figure 6.11.

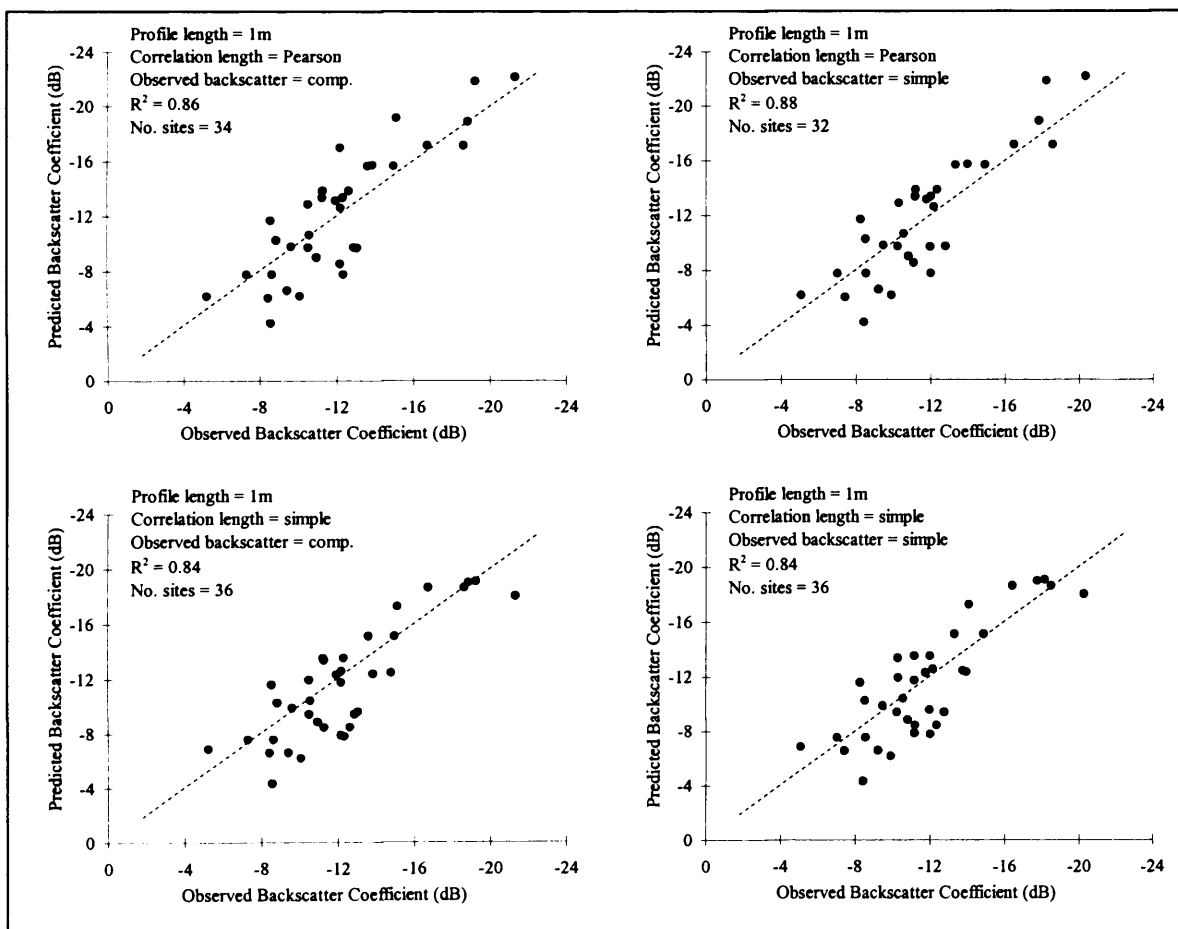


Figure 6.11. (continued on the following page).

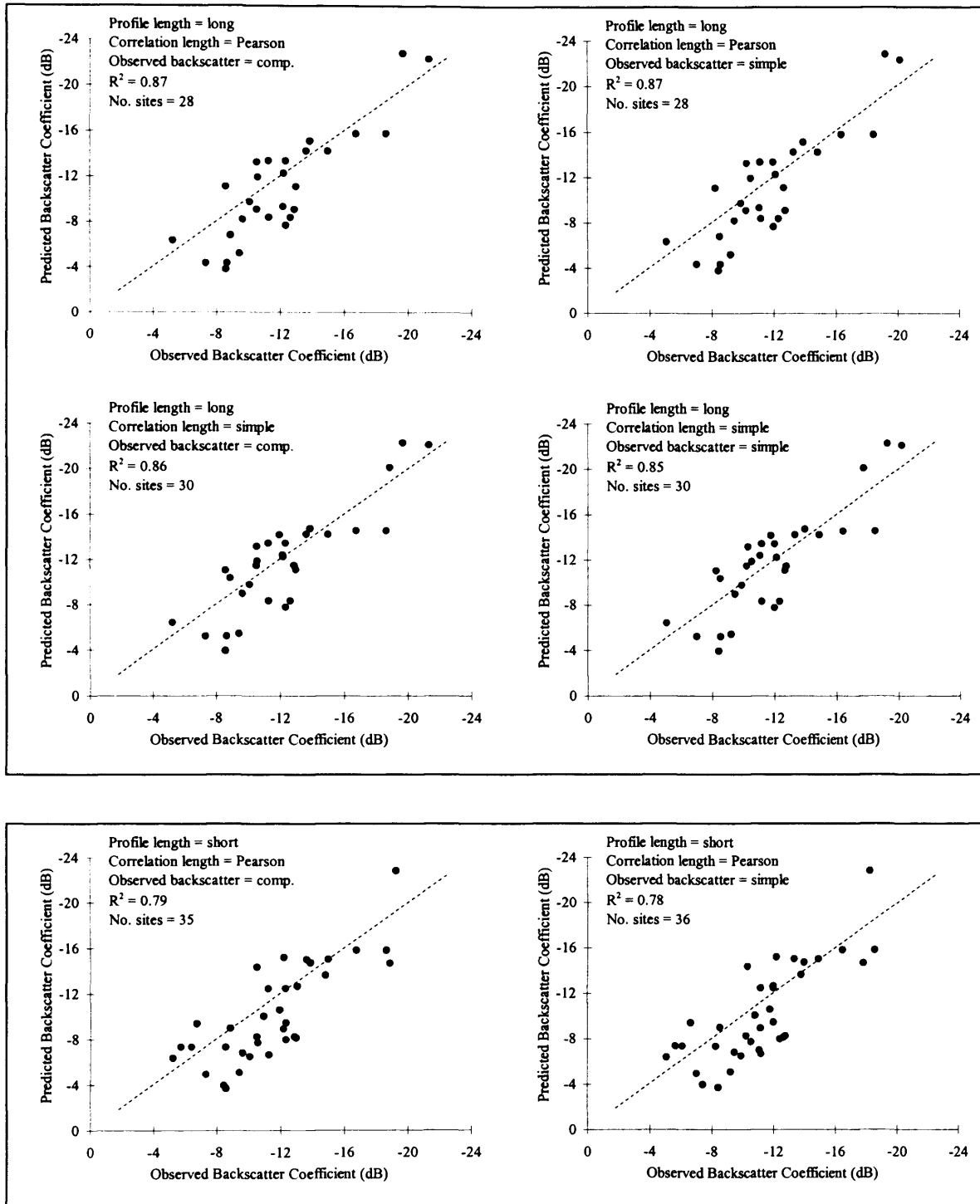


Figure 6.11. IEM calibration results for the ten scenarios listed in Table 6.2. Observed backscatter coefficients are derived from ERS SAR PRI data. Predicted backscatter coefficients have been calculated from the IEM using field data that have satisfied the validation criteria. The correlation coefficients between observed and predicted values are shown.

6.3.3 *Optimal calibration results*

In addressing the problems created by possible calibration errors observed in the derivation of the backscatter coefficient from ERS SAR PRI data (Section 3.3) by using different methods of deriving surface roughness parameters, an optimal methodology can be suggested for the most accurate model calibration results. This methodology is based on the results shown in Figures 6.10 and 6.11 and for both ERS-1 and ERS-2 data.

- The model most appropriate for this study is the IEM. This recommendation is based on the number of samples that can be used for calibration and the increased confidence gained by having a larger dataset.

- A 1 m (or ≈ 1 m) profile length is selected because it is relatively easy to determine in the field, has been utilised in other studies (Chapter 5) and appears to give accurate results.

- The final recommendation is for the use of the comprehensive estimate of the backscatter coefficient when considering ERS-1 SAR data, and the simple (σ°) estimate to be used when considering ERS-2 SAR data. This result is shown in Figure 6.12, for both simple (roughness) and Pearson estimates of the correlation length.

It is still unclear which method of deriving the correlation length gives the best results, in terms of a larger correlation coefficient as opposed to a larger sample dataset. The results indicate that no significant improvement in the models' predictive ability can be gained by changing the data related to the observed backscatter coefficient. However, due to the large differences between the two estimates of the backscatter coefficient observed in ERS-2 data acquired in 1997 and 1998, this approach is going to be adopted for the model inversion and calibration stages. The recommendation is actually being enforced by ESA, who have removed the correction for the product replica power variations from the calibration of ERS-2 SAR PRI products (see Section 3.3)

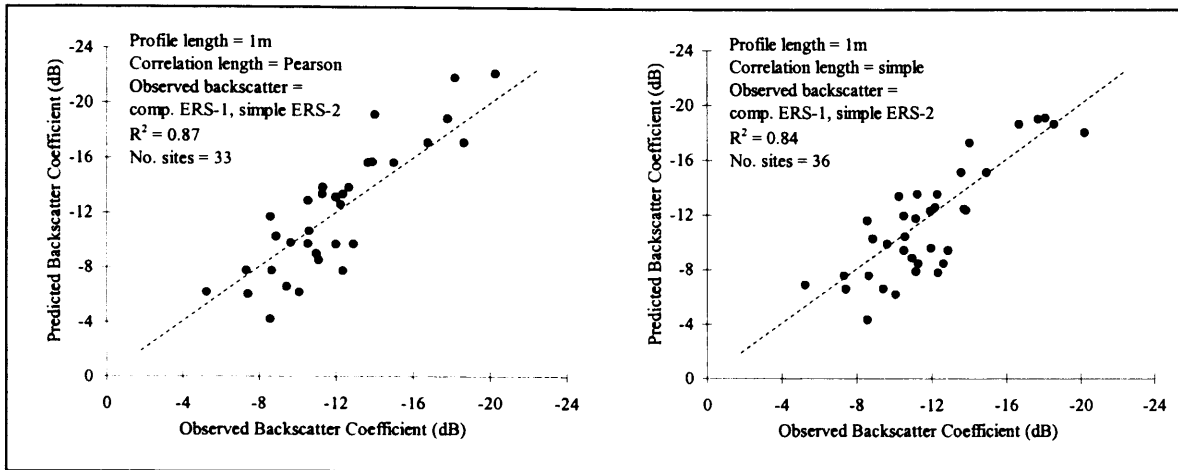


Figure 6.12. IEM calibration results for the selected optimal parameterisation with two correlation length methods.

6.3.4 Model calibration: Conclusions

The procedure of model calibration assesses the application of the model in predicting the outcome of the process under study. The results indicate potential shortfalls and errors, but also give confidence in the model's general flexibility and accuracy. The Kirchhoff and small perturbation solutions have been shown to be inappropriate to the desert surfaces discussed in this study. The nature of many of the surfaces visited have properties that fall into regions of surface roughness that the classical solutions cannot adapt to. The geometrical optics (GO) solution, however, does account for the backscatter of the basalt surfaces well, where the approximation of the IEM cannot derive a solution. However, the basalt surface permanent monitoring site (Fahda Vesicular basalt) has a measured RMS height that can be validated with the IEM ($k\sigma < 3$). The IEM has been shown to predict, with good agreement, the backscatter coefficient for a range of desert surfaces, under different seasonal conditions. The results are encouraging for all of the different measurement criteria, although the best results are obtained using a ≈ 1 m profile length. Small improvements in accuracy are gained using the Pearson method of calculating the correlation length and by varying the method of calculating the backscatter coefficient discussed in Laur *et al.* (1996). The good agreement between predicted and observed backscatter coefficients, provides a degree

of confidence in the model's ability to predict the scattering characteristics of these desert surfaces. This enables simple inversion algorithms to be developed for specific sites and the potential to extract soil moisture information from ERS SAR images to be fully exploited.

6.4 Model inversion: Results and limitations

The possibility of model inversion to predict the soil moisture of desert surfaces using ERS SAR data depends on one major assumption. This assumption states that surface roughness is not a variable parameter over the series of observations made. Field data indicate that this may be the case in some of the sites studied, however the limited roughness data acquired, and the method of measurement, mean that the assumption cannot be fully verified in this study. Nevertheless, this assumption has to be accepted, unless strong evidence suggests that surface roughness changes occurred during this study. In certain circumstances, the backscatter has been shown to be almost independent of surface roughness. There are some desert surfaces for which this assumption cannot be applied. These are mainly *qa'a* surfaces, which are so flat that millimetre-scale variations in roughness can significantly influence the backscatter coefficient. Moreover these variations cannot be detected with the present method of measuring roughness. For each of the permanent monitoring sites (PMS) an inversion algorithm has been generated. Detailed monitoring of soil moisture distribution at *Qa'a al Buqayawiyya* is presented. The inversion algorithm is based on the following criteria.

- There are no general inversion methods that cover the main land cover types. For example, no general soil moisture - backscatter relationship can be derived for all *marab* surfaces because of the differences in surface roughness between *marabs*.

- Assumptions are made concerning the calculation of the correlation length before a simulation of soil moisture estimation is made for each of the PMS. The correlation length parameter is chosen partly because of concerns expressed over the validity of the parameter previously in this study, the methods of deriving the correlation length and the potentially significant errors encountered. Correlation lengths were

therefore optimised using the model to extract the value that would best describe the observed backscatter coefficient.

- Actual estimates of the RMS height, autocorrelation function and soil parameters were used in generating the inversion algorithms for each of the PMS comprising a third order polynomial equation with a best fit correlation coefficient greater than 0.99. The roughness parameters were derived from ≈ 1 m profile lengths.

- The model used was the IEM. Predictions are made for the 1995/96 winter because of the greater availability of temporal SAR data. Units of volumetric soil moisture presented in the thesis are $\text{m}^3 \text{ water m}^{-3} \text{ soil}$.

6.4.1 Soil moisture retrieval: *Qa'a Qattafi*

The specific soil moisture - backscatter coefficient relationship, derived in accordance with the assumptions listed above, for *Qa'a Qattafi* is displayed in Figure 6.13. Due to the inconsistency between ERS-1 and ERS-2 backscatter coefficients recorded at this site, two calibration curves have been developed and calibrated with data from consecutive field seasons. The requirement for a second relationship, for use with ERS-2 SAR imagery, is backed up with predictions from the ERS-1 curve of very high soil moisture levels on the *qa'a* during March 1997. The values were not confirmed with field measurements made at this time. From this simulation curve, an inverse algorithm has been developed that mathematically characterises the relationship. For the ERS-1 data the equation for an estimate of the volumetric soil moisture (m_v) given the backscatter coefficient (σ°) can be expressed as a third order polynomial:

$$m_v = 0.000557\sigma^\circ{}^3 + 0.0366\sigma^\circ{}^2 + 0.8186\sigma^\circ + 6.2694 \quad (6.1)$$

and for the ERS-2 data,

$$m_v = 0.00056\sigma^\circ{}^3 + 0.0308\sigma^\circ{}^2 + 0.5847\sigma^\circ + 3.8498 \quad (6.2)$$

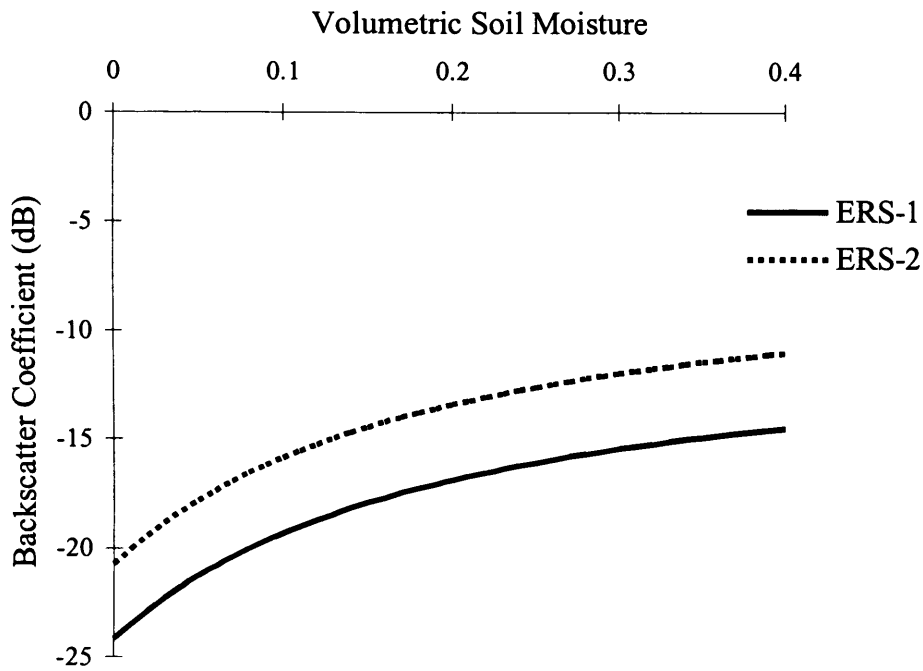


Figure 6.13. Soil moisture - backscatter coefficient curves generated for *Qa'a Qattafi* using the calibrated IEM. The input parameters are; ERS-1 data, RMS height = 0.16 cm, correlation length = 4.5 cm, autocorrelation function = Gaussian, incidence angle = 23° ; ERS-2 data, RMS height = 0.23 cm, correlation length = 4.5 cm, autocorrelation function = Gaussian, incidence angle = 23° .

From Equation 6.1 it is possible to generate estimates of the volumetric soil moisture for all of the ERS-1 scenes acquired for *Qa'a Qattafi*. The result for ERS-2 data is validated separately by predicting the soil moisture from the imagery acquired in the 1998 field season (Section 6.5). The predicted soil moisture curve through the winter of 1995 and spring of 1996 is displayed in Figure 6.14. The data are compared with precipitation data from the station at Safawi, even though this station is over 30 km away. It is acknowledged that correlating rainfall between regions 30 km away is very erroneous in

semi-arid environments and therefore these values only illustrate the relationships between surface soil moisture and rainfall (see Section 6.1). No rainfall data are available in the central parts of the study area.

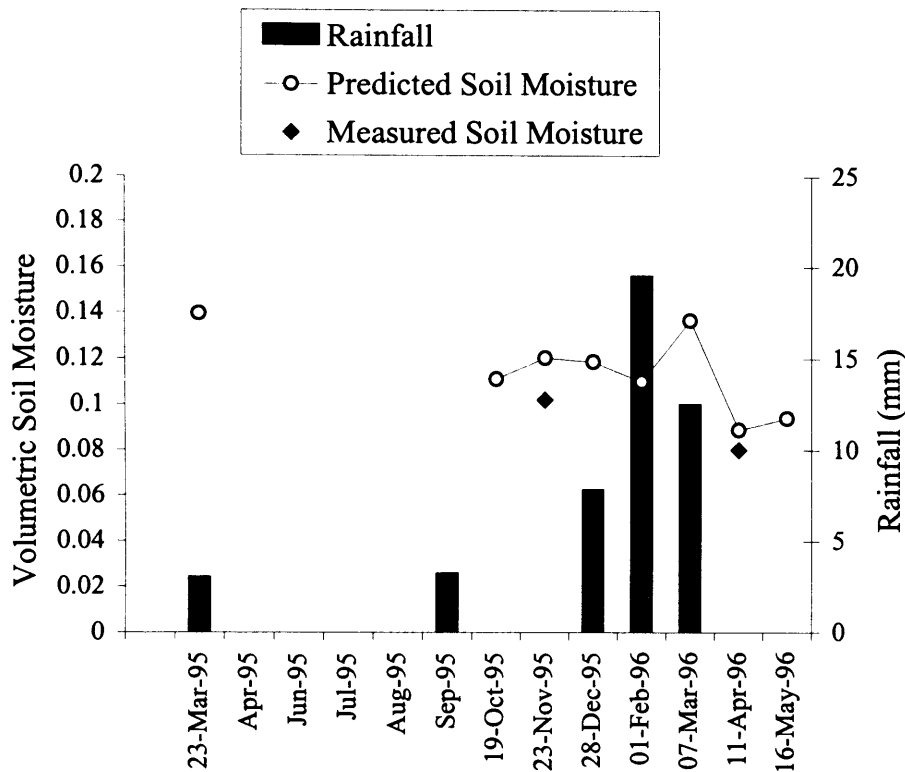


Figure 6.14. Estimated soil moisture values for Qa'a Qattafi, over the winter of 1995, calculated from backscatter coefficients derived from ERS-1 SAR data. Actual estimates of soil moisture from in-situ measurements (taken at the same time as the satellite acquisition) are shown for comparison. Rainfall data from the Safawi station are also presented.

The results of the model inversion algorithm shown in Figure 6.14 indicate that levels of soil moisture at this site reach approximately $0.14 \text{ m}^3 \text{ water m}^{-3} \text{ soil}$. These are at times when precipitation events are occurring or have just occurred (7 March 1996) or when antecedent soil moisture values are high, after a prolonged season of higher than average rainfall totals (23 March 1995). Compared to actual values of soil moisture taken in the field there is a slight over prediction, however estimates are reasonably accurate. The

result shown assumes that significant variation in surface roughness did not occur over this period. For such a flat surface any change can be interpreted as being significant and also difficult to detect. Therefore, the result described may be erroneous and without a multi-parameter dataset the true result is difficult to establish. These surfaces are sinks for water and sediment and field observations show that soil moisture in the dominantly clay soils may never reach very low values.

6.4.2 Soil moisture retrieval: *Qa'a al Wassad*

The soil moisture - backscatter coefficient relationship simulated with the IEM for *Qaa al Wassad* is shown in Figure 6.15.

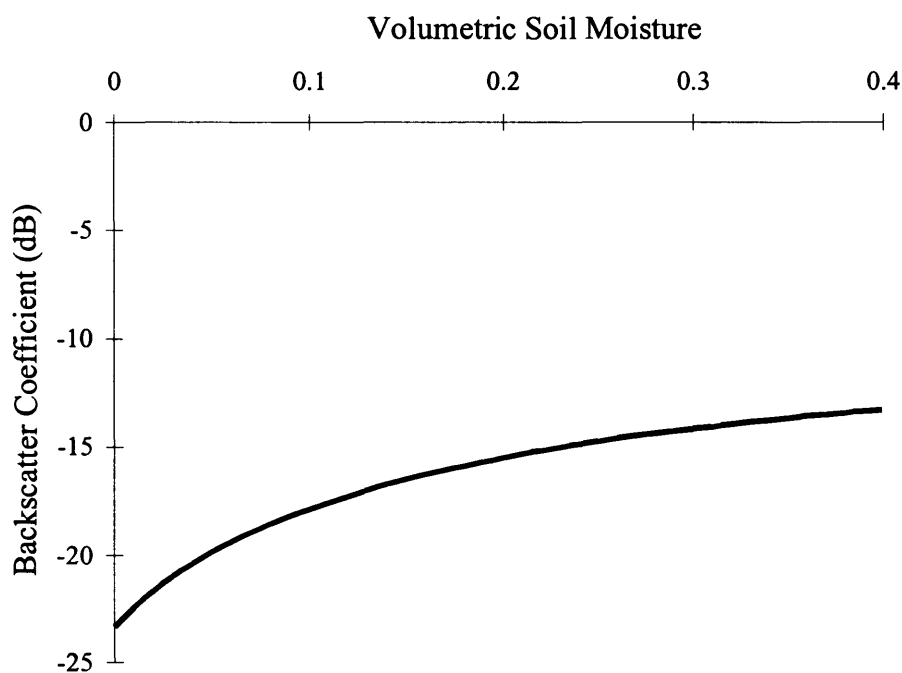


Figure 6.15. Soil moisture - backscatter coefficient relationship curves generated for *Qa'a al Wassad* using the calibrated IEM. The input parameters are; ERS-2 data, RMS height = 0.17 cm, correlation length = 5.9 cm, autocorrelation function = exponential, incidence angle = 22°.

The surface is characteristically very smooth with no major variations in surface roughness observed during each of the four field seasons. *Qa'a al Wassad* is also located in the far south-eastern part of the study area, and is beyond the limit of the image track that covers the majority of the study area (track 257). Therefore, the temporal coverage of this site is not as good as the other PMS and no predictions of the soil moisture over the 1995/96 winter can be calculated. No distinction is made between comprehensive backscatter observations made by ERS-1 and simple estimates made by ERS-2, therefore only one general relationship is simulated. Even so, given the data acquired in the field, comparison with SAR imagery resulted in a mathematical relationship expressed as a third order function. The volumetric soil moisture (m_v) of *Qa'a al Wassad* can be calculated from the backscatter coefficient (σ°) by the following:

$$m_v = 0.000583\sigma^{\circ 3} + 0.0365\sigma^{\circ 2} + 0.7757\sigma^\circ + 5.6282 \quad (6.3)$$

The relationship has been developed using field data acquired in 1997 and the correlation length optimised for maximum soil moisture prediction. The pattern of soil moisture values over the winter of 1995 cannot be shown for *Qa'a al Wassad* as the temporal coverage by the ERS satellites was not as consistent or concise as for the sites located within the central sub-satellite track. Equation 6.3 is validated by predicting the soil moisture value for *Qa'a al Wassad* from satellite data collected during the 1998 field season.

6.4.3 Soil moisture retrieval: *Qa'a al Buqayawiyya*

The soil moisture - backscatter coefficient relationship for *Qa'a al Buqayawiyya* is illustrated in Figure 6.16. *Qa'a al Buqayawiyya* shows a fluctuating temporal backscatter signature (see Figure 3.13) thought to be caused by changing soil moisture contents over the winter. The vegetated surface is rough (of the order of 0.5 to 1 cm), reducing the sensitivity of the backscatter coefficient to variations in the surface height and maximising the sensitivity to soil moisture changes. The relationship has been derived using the IEM, with an optimised value of the correlation length. If simple

estimates of the ERS-2 backscatter coefficient are used, these are comparable with ERS-1 estimates. Therefore only one curve is required.

The third order polynomial equation that best represents the relationship given in Figure 6.16 can be expressed as:

$$m_v = 0.00061\sigma^{\circ 3} + 0.0265\sigma^{\circ 2} + 0.3866\sigma^{\circ} + 1.9622 \quad (6.4)$$

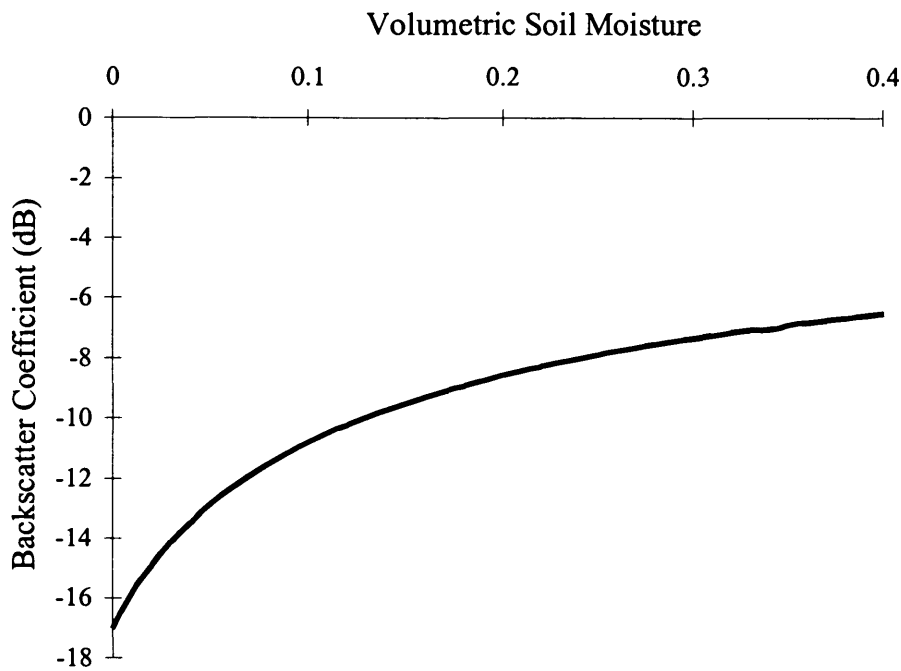


Figure 6.16. Soil moisture - backscatter coefficient curve generated for Qa'a al Buqayawiyya. The input parameters are; ERS-1 data, RMS height = 0.76 cm, correlation length = 25 cm, autocorrelation function = exponential, incidence angle = 21.2°.

Figure 6.17 shows the predicted volumetric soil moisture values at Qa'a al Buqayawiyya over the winter 1995 period. The predicted relationships have been established by assuming an exponential autocorrelation function. Figure 6.5 shows that exponential surfaces with a RMS height in the region of 1 cm do not have any significant influence on the backscatter coefficient. Therefore if the roughness

parameters calculated are accurate, then any fluctuation in the backscatter coefficient may be assumed to be caused by changing soil moisture conditions. The data in Figure 6.17 indicate a significant increase in values at times of the images acquired in November 1995 and March 1996. During March 1995, the region was partially flooded. The values recorded are sufficiently high for vegetation to be able to establish itself on the *marab* as was witnessed during the spring of 1995. Observations at the exact time of overpass at *Qa'a al Abd* (north of Safawi) on the 23 November 95 recorded that rainfall was falling. Rainfall data for the Safawi weather station are presented in Figure 6.18.

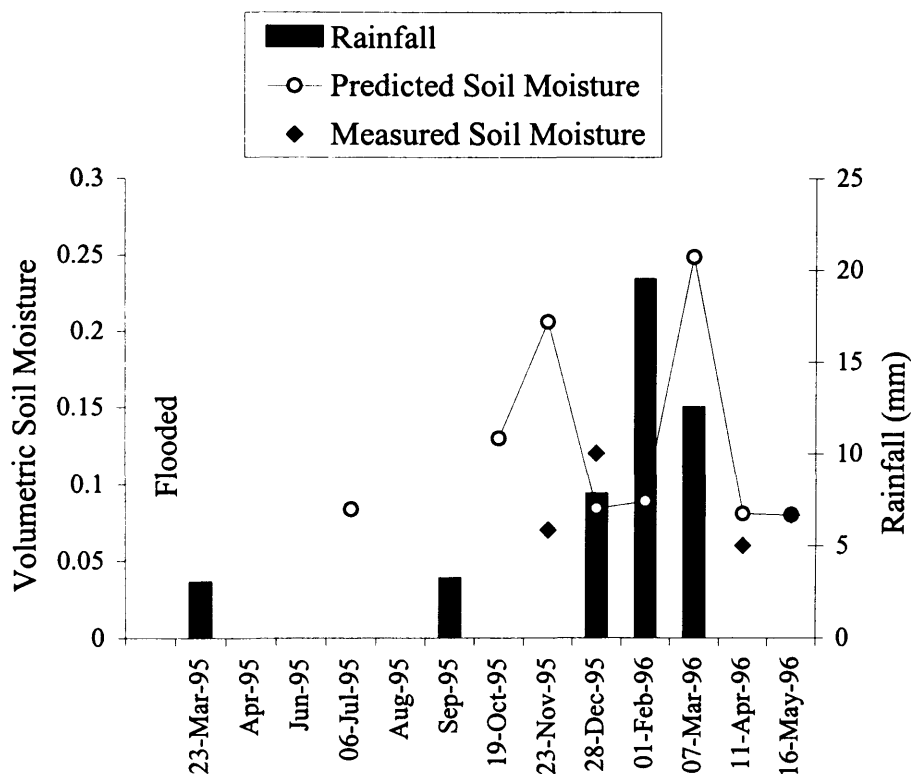


Figure 6.17. Estimated soil moisture values for *Qa'a al Buqayawiyya*, over the winter of 1995, calculated from backscatter coefficients derived from ERS-1 SAR data. Actual estimates of soil moisture from in-situ measurements (taken at the same time as the satellite acquisition) are shown for comparison. Rainfall data from the Safawi station are also presented. The last estimation on May 16th 1996 shows good agreement with the measured value of soil moisture.

Comparison with *in-situ* measurements of volumetric soil moisture shows that *in-situ* measurements do not characterise the variability of surface moisture contents indicated by the SAR data. The most obvious mis-representation is the measurement that corresponds to the 23 November 1995 image. The model predicts a soil moisture content of approximately $0.2 \text{ m}^3 \text{ water m}^{-3} \text{ soil}$, *in-situ*, a value of $0.07 \text{ m}^3 \text{ water m}^{-3} \text{ soil}$ was recorded. However, the difference can be explained because of a delay in collecting *in-situ* soil moisture data at this site of 36 hours. The precipitation event observed in the north of the study area (that wasn't actually recorded at the Safawi weather station) may have deposited a covering of moisture on to the surface of *Qa'a al Buqayawiyya*. Once again though this result demonstrates the highly spatial nature of semi-arid precipitation and the need for increasing numbers of rainfall gauges to be sited in the project area. The SAR is very sensitive to small increases of soil moisture when surface conditions are originally dry. Another theory might suggest that moisture deposited on the night of the 23 November may have evaporated when *in-situ* measurements were taken on the 25 November. Again, this is difficult to prove, therefore assumptions have to be made concerning the occurrence of rainfall at these sites. The model will be validated in Section 6.5 on field data and imagery acquired during the 1998 field season.

6.4.4 Soil moisture retrieval: *Marab Suwaiid*

The soil moisture - backscatter coefficient relationships simulated with the IEM for both ERS-1 and ERS-2 missions are displayed in Figure 6.18. *Marab Suwaiid* is distinguished from other PMS and *marab* sites, because of modifications to the surface roughness that occurred in the autumn of 1996. The modifications involved some ploughing and direct drilling to conduct seed emergence experiments. Therefore, a relationship can be generated for ERS-1 SAR data, but another relationship that accounts for the increase in surface roughness is required for ERS-2 data. The increase in surface RMS height, measured from 0.2 to 1.38 cm between 1996 and 1997, increases the overall magnitude of the backscatter coefficient but does not influence the sensitivity of the signal to variations in soil moisture.

For data acquired from the ERS-1 system (i.e. before autumn 1996), the equation for an estimate of the volumetric soil moisture (m_v) given the backscatter coefficient (σ°) can be expressed as a third order polynomial:

$$m_v = 0.00052\sigma^\circ{}^3 + 0.0291\sigma^\circ{}^2 + 0.5212\sigma^\circ + 3.3407 \quad (6.5)$$

and for the ERS-2 data (i.e. after autumn 1996),

$$m_v = 0.00063\sigma^\circ{}^3 + 0.0288\sigma^\circ{}^2 + 0.4536\sigma^\circ + 2.4926 \quad (6.6)$$

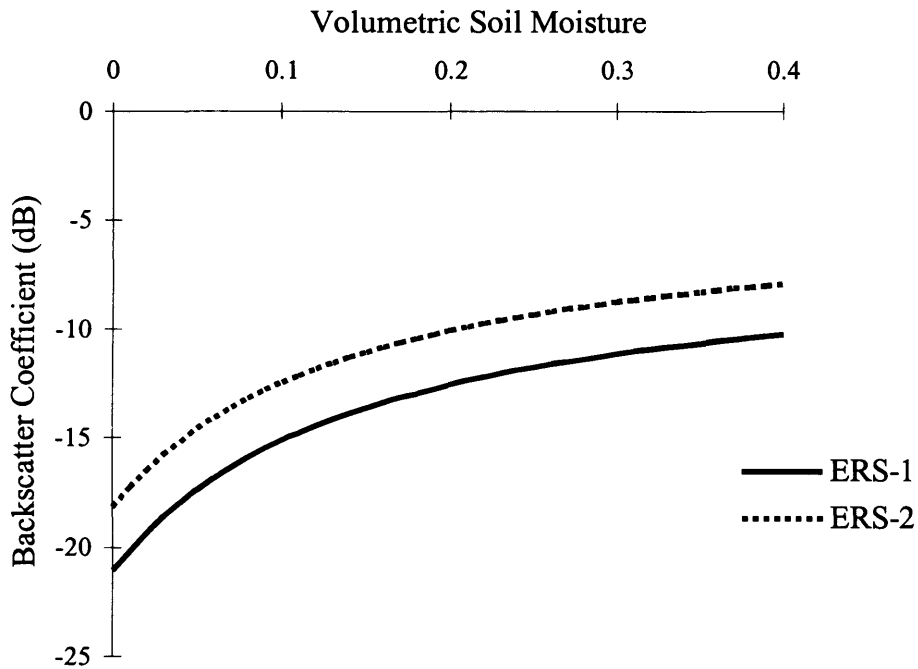


Figure 6.18. Soil moisture - backscatter coefficient curves generated for Marab Suwaiid. The input parameters are; ERS-1 data, RMS height = 0.2 cm, correlation length = 3.2 cm, autocorrelation function = exponential, incidence angle = 23.7°. ERS-2 data, RMS height = 1.38 cm, correlation length = 13.9 cm, autocorrelation function = Gaussian, incidence angle = 23.7°.

Equation 6.5 yields a prediction of the pattern of volumetric soil moisture change through the 1995 winter (Figure 6.19). Also, shown in Figure 6.19 are *in-situ* estimates of soil moisture and precipitation data recorded at Safawi (the nearest weather station, Safawi, is 40 km from *Marab Suwaiid*). Equation 6.6 is needed if future estimations of soil moisture are to be made that account for the new roughness of *Marab Suwaiid*.

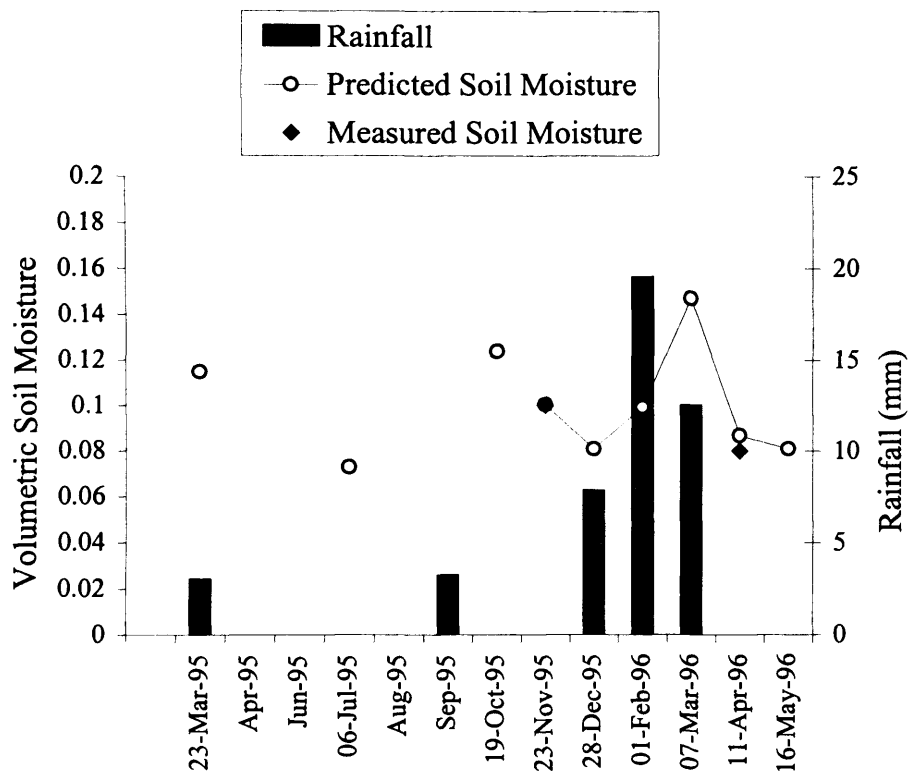


Figure 6.19. Estimated soil moisture values for *Marab Suwaiid*, over the winter of 1995, calculated from backscatter coefficients derived from ERS-1 SAR data. Actual estimates of soil moisture from *in-situ* measurements (taken at the same time as the satellite acquisition) are shown for comparison. Rainfall data from the Safawi station are also presented.

The temporal fluctuation of soil moisture on this *marab* is significant, reaching values of around $0.15 \text{ m}^3 \text{ water m}^{-3} \text{ soil}$ during October 1995 and March 1996. Measurements made in the field during the 1997 field season were calculated to be 0.18 (by volume) indicating that this particular *marab* is active, in terms of soil moisture fluctuations.

Comparison with *in-situ* measurements show that the model predicts the moisture content reasonably well, although measurements were not taken at times of significant levels of soil moisture (7 March 1996) as estimated from the SAR data. It is difficult to relate precipitation data collected in Safawi, some distance away, with increases of soil moisture measured with the satellite SAR. *Marab Suwaiid* has been ear-marked for detailed studies on the effects of soil crusting, tillage and the incorporation of organic matter on seed emergence and crop growth. Accurate estimates of rainfall are required for these studies and investment into a raingauge network in this region is required.

6.4.5 Soil moisture retrieval: *Marab Wutaydat*

The soil moisture - backscatter coefficient relationship simulated with the IEM, using field parameters collected during the 1995 field season, is displayed in Figure 6.20.

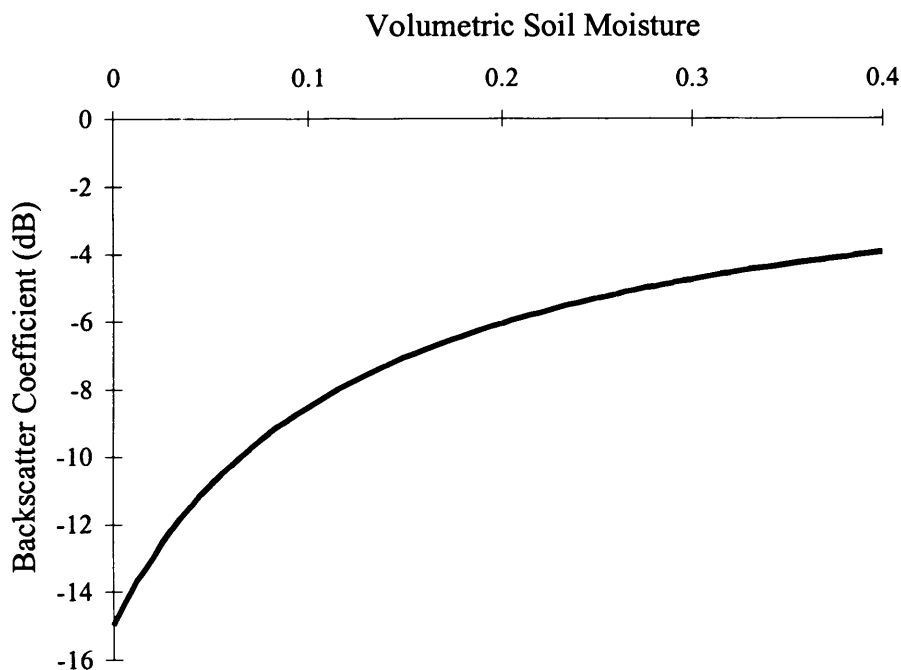


Figure 6.20. Soil moisture - backscatter coefficient curves generated for *Marab Wutaydat*. The input parameters are; ERS-1 data, RMS height = 0.87 cm, correlation length = 7 cm, autocorrelation function = Gaussian, incidence angle = 25°.

Marab Wutaydat is located in the far south-eastern part of the study area. The surface is characteristically very sandy, vegetation is present but does not fluctuate in amount during the wet season (Section 4.8) and it has a moderate roughness (slightly below 1 cm, RMS height) caused by aeolian depositional forms (e.g. ripples) and stones. The *marab* does not display a backscatter profile which fluctuates by much over time. This observation is understandable considering that the site is located in one of the most arid regions of the study area and the 1995/96 winter was very dry. Expressing the relationship shown in Figure 6.20 as a third order polynomial function of the backscatter coefficient the model can be used to predict the volumetric soil moisture (m_v) of *Marab Wutaydat* from ERS SAR imagery.

$$m_v = 0.00058\sigma^\circ{}^3 + 0.0204\sigma^\circ{}^2 + 0.2486\sigma^\circ + 1.09 \quad (6.7)$$

The predictions from the IEM are shown in Figure 6.21 for the 1995-1996 winter. Comparison is made with *in-situ* measurements of soil moisture, limited to a single measurement during 1995/96. It does not make sense to compare the pattern of soil moisture with precipitation data because of the huge distance to the nearest station, \approx 100 km (see Section 6.1). The results show the very stable nature of this particular *marab*, therefore no realistic soil moisture predictions can be made for *marab* regions. The small increase, of no real significance, in soil moisture predicted by the model occurring on the 19 October 1995 cannot be explained fully as no weather station information is available in the south-east of the region. This particular *marab* is vegetated by shrubs. The vegetation must therefore tap into moisture located in sub-surface layers. The chances of greater soil moisture levels at depth are increased due to the soil properties. The soil surface is protected by a layer of sand that varies in thickness. This layer would reduce the amount of evaporation in the upper surface layers during the spring months, thus enabling plants to tap into this potential water source situated in the finer substrate beneath.

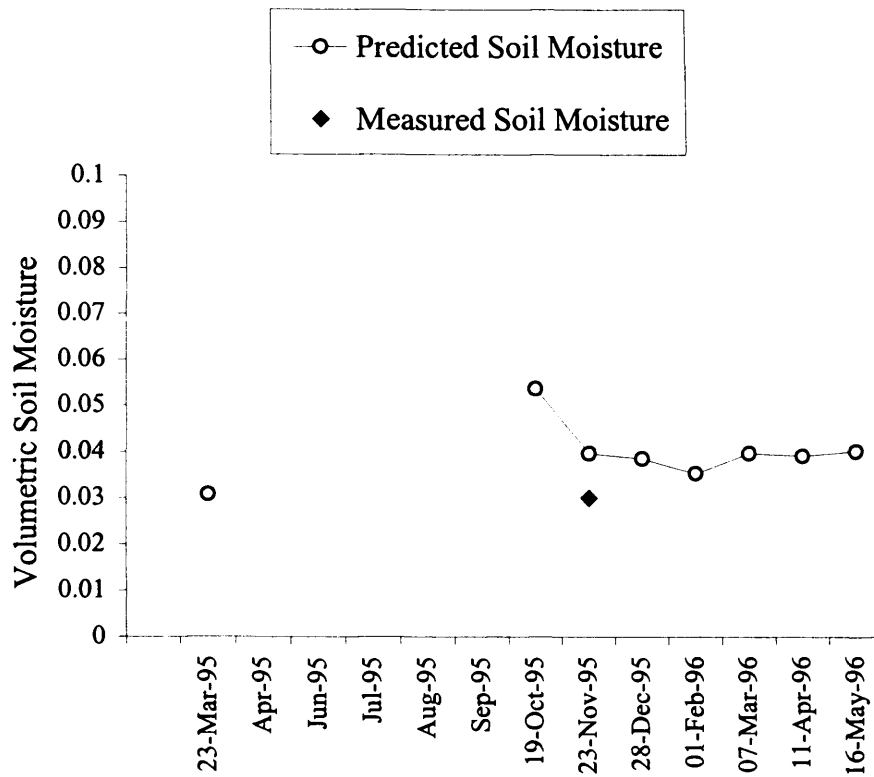


Figure 6.21. Estimated soil moisture values for Marab Wutaydat, over the winter of 1995, calculated from backscatter coefficients derived from ERS-1 SAR data. Actual estimates of soil moisture from in-situ measurements taken at the same time as the satellite acquisition are shown for comparison.

6.4.6 Soil moisture retrieval: Chert hammada

The specific soil moisture - backscatter coefficient relationship of the chert *hammada* is shown in Figure 6.22. Only one curve is shown, as the ERS-2 simple (with respect to the method of deriving the observed backscatter coefficient) backscatter coefficients can be related to the ERS-1 comprehensive coefficients in this example. The equation for an estimate of the volumetric soil moisture (m_v) given the backscatter coefficient (σ°) can be expressed as a third order polynomial:

$$m_v = 0.00052\sigma^\circ{}^3 + 0.0159\sigma^\circ{}^2 + 0.17\sigma^\circ + 0.6712 \quad (6.8)$$

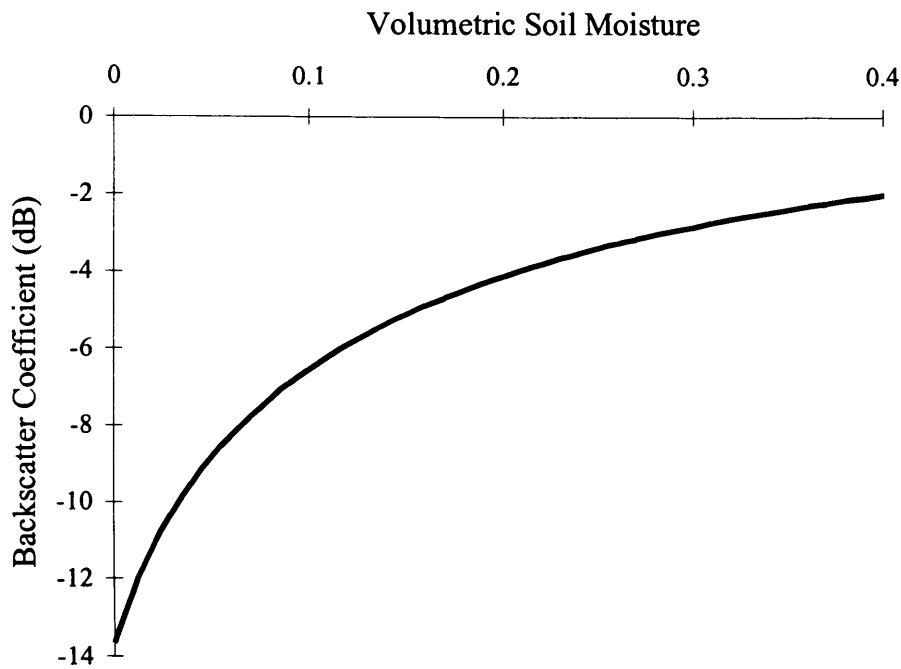


Figure 6.22. Soil moisture - backscatter coefficient curve generated for the chert hammada. The input parameters are; ERS-1 data, RMS height = 0.7 cm, correlation length = 5.5 cm, autocorrelation function = exponential, incidence angle = 21° .

Based on the relationship represented in Equation 6.8, the seasonal soil moisture characteristics of the hammada surface can be determined. Figure 6.23 displays the predicted trend in soil moisture values over the winter of 1995, actual estimates of soil moisture from *in-situ* measurements and precipitation data from Safawi, (the nearest weather station). The model indicates that soil moisture levels do not vary by any large amount even during periods of wet weather, and do not reach any significantly high value. This prediction is confirmed by low values of soil moisture measured *in-situ* in 1996 and 1997 at this site and similar *hammada* surfaces located further south towards Azraq. The reason that fluctuations in soil moisture are detected on these surfaces (Chapter 3) may be due to the strong sensitivity of the backscatter coefficient to increases in soil moisture when low antecedent values exist (discussed previously in this chapter). Therefore, the detection of soil moisture changes on *hammada* surfaces are dependent on the occurrence of rainfall events immediately prior to the satellite overpass. Furthermore, fluctuations of surface soil moisture may be more severe on

hammada surfaces because of their exposure to climatic parameters (strong winds and more insolation) resulting in an increased chance for water evaporation.

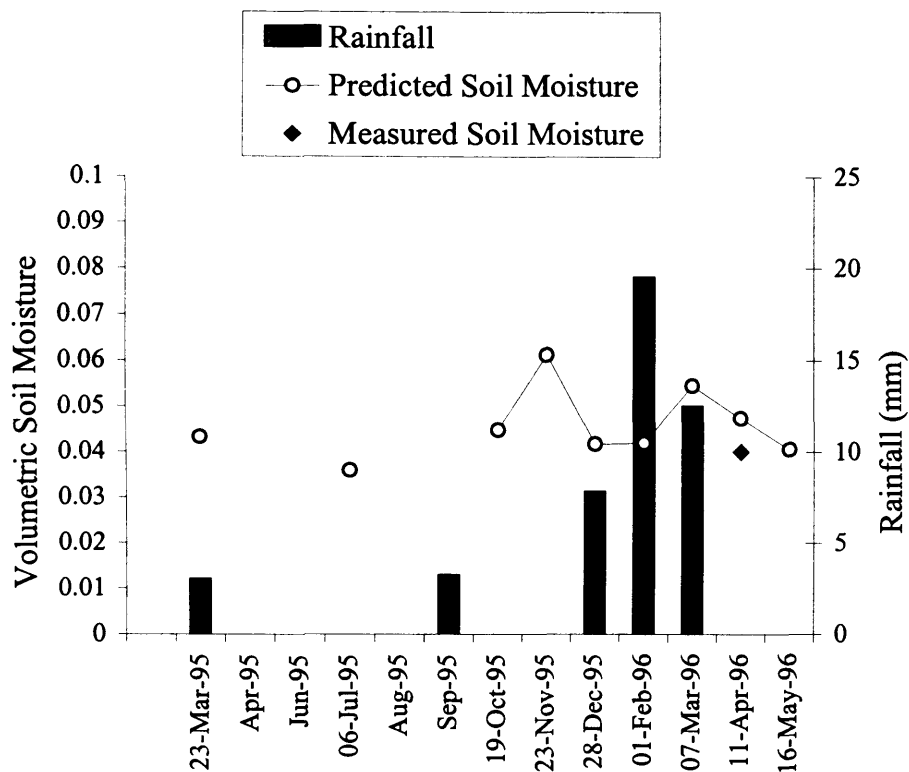


Figure 6.23. Estimated soil moisture values for the chert hammada surface, over the winter of 1995, calculated from backscatter coefficients derived from ERS-1 SAR data. Actual estimates of soil moisture from in-situ measurements (taken at the same time as the satellite acquisition) are shown for comparison. Rainfall data from the Safawi station are also presented.

6.4.7 Soil moisture retrieval: Limestone hammada

The soil moisture - backscatter coefficient relationship predicted using the IEM is illustrated in Figure 6.24. The limestone *hammada* sites situated near to the town of Azraq lies towards the south within one of the most arid parts of the study region. Precipitation in this region is infrequent. The lack of rainfall is reflected in the very low

estimates of soil moisture measured in the field. The surface has approximately the same roughness characteristics as the chert *hammada* region situated further north, but does not exhibit the same seasonal fluctuation in the backscatter signature.

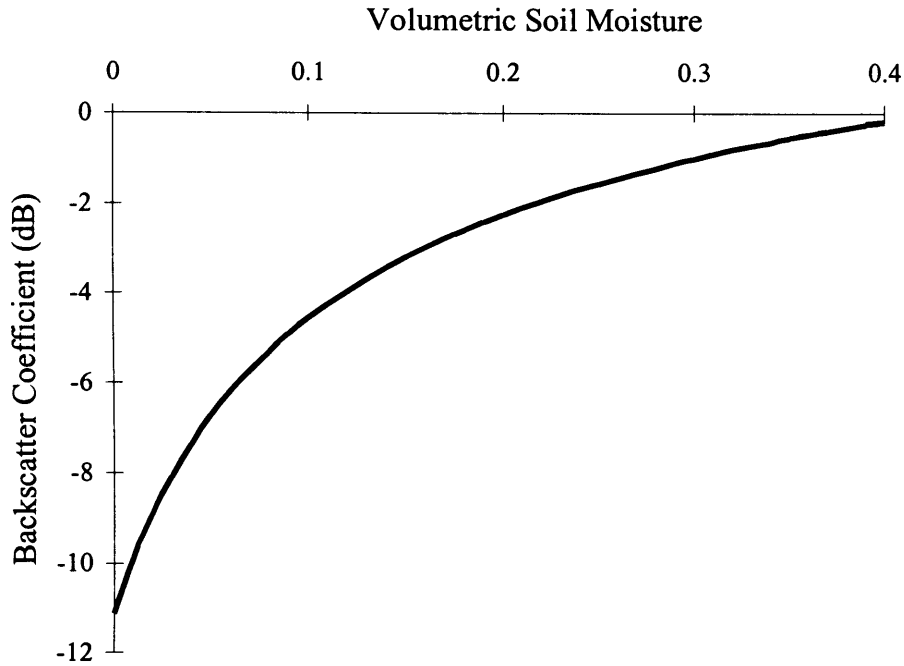


Figure 6.24. Soil moisture - backscatter coefficient curve generated for the limestone *hammada*. The input parameters are; ERS-1 data, RMS height = 0.66 cm, correlation length = 5.5 cm, autocorrelation function = Gaussian, incidence angle = 19.8° .

The limestone *hammada* was found to exhibit mainly Gaussian surface autocorrelation characteristics. The equation for an estimate of the volumetric soil moisture (m_v) given the backscatter coefficient (σ°) can be expressed as:

$$m_v = 0.00058\sigma^\circ{}^3 + 0.0139\sigma^\circ{}^2 + 0.1213\sigma^\circ + 0.4123 \quad (6.9)$$

Using the retrieval formula given in Equation 6.9, volumetric soil moisture values were calculated for the limestone *hammada* surface over the winter of 1995/96 (Figure 6.25).

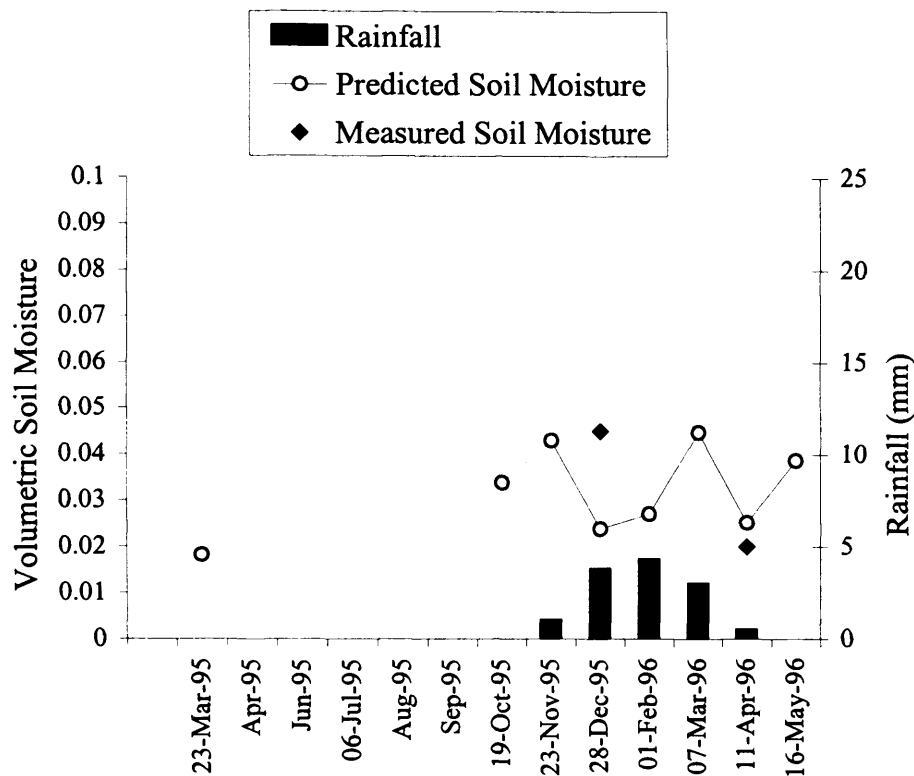


Figure 6.25. Estimated soil moisture values for limestone hammada, over the winter of 1995, calculated from backscatter coefficients derived from ERS-1 SAR data. Actual estimates of soil moisture from in-situ measurements (taken at the same time as the satellite acquisition) are shown for comparison. Rainfall data from the Azraq station are also presented.

The values predicted are low, soil moisture never attaining $0.05 \text{ m}^3 \text{ water m}^{-3} \text{ soil}$. Small peaks are observed on the November 1995 and March 1996 acquisitions at times of recorded precipitation in the north of the study region (*Marab Salma* station). Comparison with *in-situ* measurements cannot confirm the ability of SAR to detect changes in soil moisture because of the small range of soil moisture values observed. *In-situ* measurements again never reached above $0.05 \text{ m}^3 \text{ water m}^{-3} \text{ soil}$, this is not surprising given the exposure of these surfaces to climate and soil conditions that increase potential evaporation and that large areas of *hammada* do not support the growth of vegetation.

Precipitation data from the Azraq weather station are also shown in Figure 6.25. The winter of 1995/96 was, on record, significantly dryer than average winter totals and this is reflected in the amounts of precipitation recorded at Azraq. The data indicate that a small amount of rainfall may have fallen over the limestone *hammada* site at this time. However, the fluctuations in the temporal backscatter signal may also be caused by SAR system noise as the fluctuations are generally less than 2 dB. Therefore, the potential for SAR to extract soil moisture information from this surface may be limited. However, it cannot be fully verified whether this site (and other similar sites) can be monitored during periods with higher amounts of rainfall.

6.4.8 Soil moisture retrieval: *Fahda Vesicular basalt*

The Fahda Vesicular basalt site is difficult to characterise in terms of its roughness properties. However, for the purpose of moisture retrieval from the spaces between the stones where the soil is exposed, the surface has a high RMS height ($\sigma \geq 2.3$ cm from 1997 roughness data) and measurements indicate a Gaussian surface autocorrelation function. These parameters ensure that the backscatter coefficient is independent of changes in surface roughness. The temporal signature of the basalt surfaces calculated from ERS-1 SAR data is very stable for reasons discussed in Section 3.2.1. Very small fluctuations are observed and, if these fluctuations are to be interpreted as changes in volumetric soil moisture, the soil moisture - backscatter coefficient relationship needs to be established (Figure 6.26).

Inversion of this relationship leads to an equation for the estimate of volumetric soil moisture (m_v) given the backscatter coefficient (σ°), expressed as:

$$m_v = 0.00061\sigma^\circ{}^3 + 0.0145\sigma^\circ{}^2 + 0.1214\sigma^\circ + 0.4056 \quad (6.10)$$

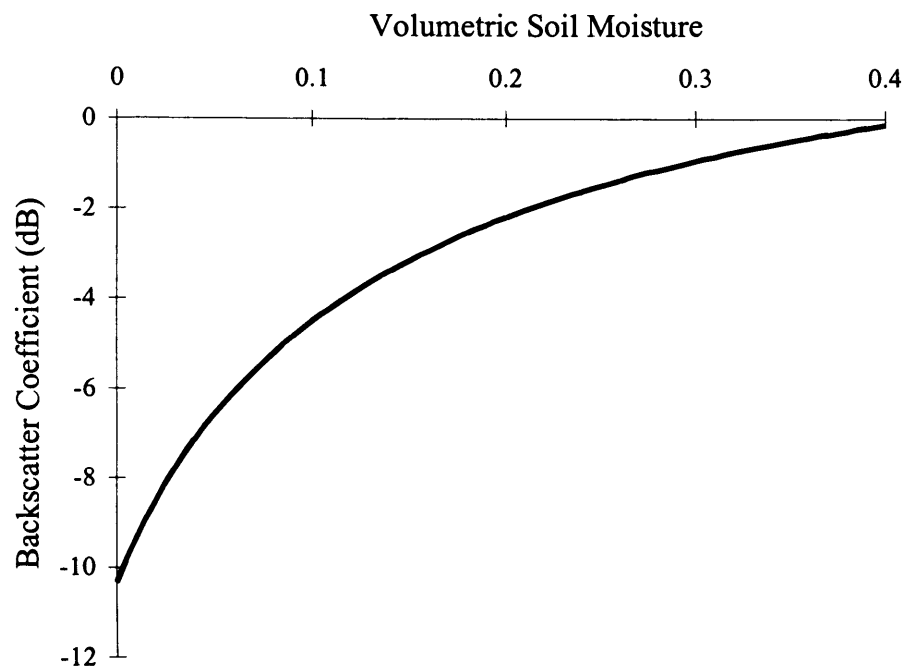


Figure 6.26. Soil moisture - backscatter coefficient curve generated for the Fahda Vesicular basalt. The input parameters are; ERS-1 data, RMS height = 2.3 cm, correlation length = 7.2 cm, autocorrelation function = Gaussian, incidence angle = 21.9°.

Calculated volumetric soil moisture values over the winter of 1995 are shown in Figure 6.27. The values indicate that the soil moisture of the basalt site is very constant. A slight increase is estimated for the 23 November 1995 overpass where rainfall was observed falling close by to the Fahda Vesicular basalt. An increase in backscatter is not registered for the 7 March 1996 acquisition, for which a precipitation event occurred just prior to this date. One possible interpretation of this phenomenon is that if the basalt boulders and surrounding soil are covered with water (the case on the 23 November 1995) then the SAR will detect this. If the rainfall event occurred prior to the image acquisition (the case on the 7 March 1996) then it would most likely have evaporated from, or drained off, the boulder surface which have most influence on the intensity of the signal, due to the roughness of the surface. Comparison with *in-situ* estimates of soil moisture taken at the Fahda Vesicular basalt site are limited because measurements at this site were not taken during the spring 1996 field trip. This was because fieldwork time (alongside colleagues) had to be concentrated on other basalt sites. The cross-

comparison with ERS-2 data acquired in 1997 yielded some problems discussed in the following paragraph. The potential for soil moisture retrieval over basalt surfaces is again limited by the very small changes in backscatter coefficient that are detected and the possibility that these can be attributable to system noise and processing errors.

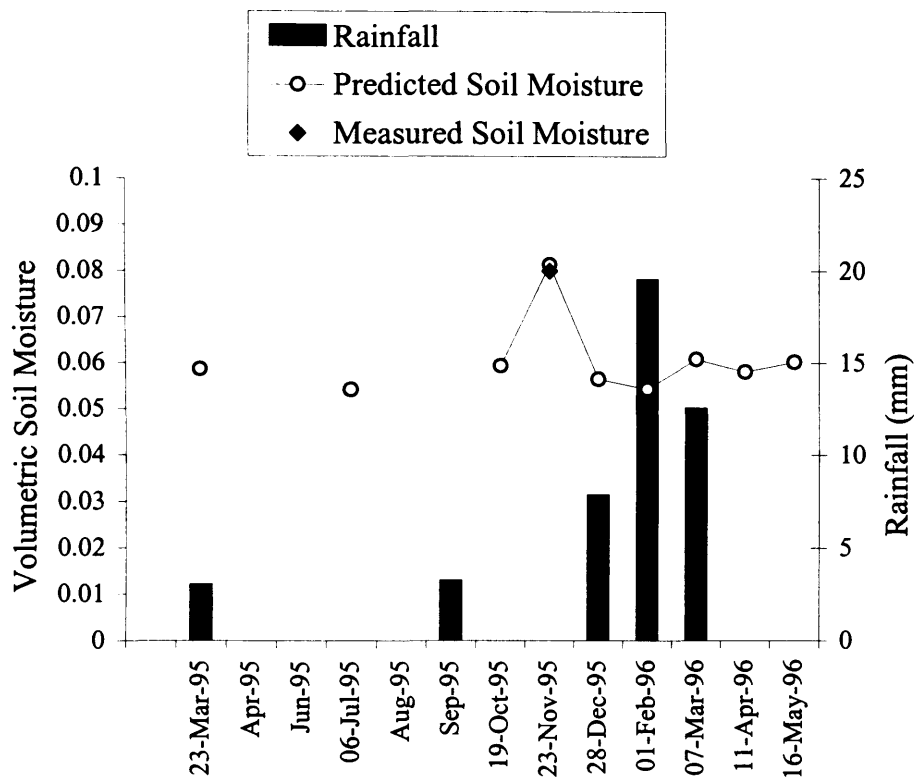


Figure 6.27. Estimated soil moisture values for Fahda Vesicular basalt, over the winter of 1995, calculated from backscatter coefficients derived from ERS-1 SAR data. Actual estimates of soil moisture from in-situ measurements (taken at the same time as the satellite acquisition) are shown for comparison. Rainfall data from the Safawi station are also presented.

Simple estimates of the backscatter coefficient calculated from ERS-2 SAR data used to calculate volumetric soil moisture values using Equation 6.10 indicate a reduction in soil moisture to around 0.05 (by volume) for the images acquired in the spring of 1997 and of 1998. Both images were acquired during wet periods. It is evidence such as this that indicates possible inter-calibration problems between the ERS-1 and ERS-2 SAR

systems. However, the possibility of a reduction in soil moisture occurring during these overpass acquisitions cannot be ruled out, due to the limited field data available.

6.5 Model Validation

The IEM results were validated by comparing satellite-derived estimates of the soil moisture content with in-situ measurements taken in a different part of the site (but still within the 500 by 500 m homogeneous area, see Section 4.2). Unfortunately, the model validation results were hampered by the failure of the ERS-2 SAR instrument (too many missing lines) to acquire data on the 17 April 1998 for the two central image scenes (track 257). The majority of the model validation testing was undertaken in relation to this overpass. The acquisition on the 29 March 1998, covering the eastern section of the study region was successful, although only two of the permanent monitoring sites were covered by this overpass (*Marab Wutaydat* and *Qa'a al Wassad*). It was decided to apply the model results to the data acquired on the 6 February 1998, and to use the soil moisture values collected during the March and April of that month to try and establish the soil moisture conditions at that time. It is fully acknowledged that the inversion algorithms cannot be fully tested as the observed values of soil moisture do not relate in time to when the predictions are made. However, as 1998 was a particularly wet year on average, with conditions similar in February to that observed in March and April, cold and cloudy with regular precipitation events, at least some validation of the model's abilities could be obtained. The eight permanent monitoring sites were visited during the 1998 field visit. Soil moisture, roughness and field descriptions were recorded. Detailed analysis was conducted at the *Qa'a al Buqayawiyya* as this site was in the vicinity of all major land cover types and was easily accessible. The observed volumetric soil moisture ($m_{v\ obs.}$), backscatter coefficient (σ°) calculated from either the 6 February or 29 March 1998 image, and predicted volumetric ($m_{v\ pred.}$) soil moisture using the algorithms stated in Section 6.4 are presented in Table 6.3. The predictive ability of the model can be viewed more clearly in Figure 6.28.

PMS	σ° (image date)	$M_{v\ pred.}$	$m_{v\ obs.}$
Limestone hammada	-10.79 (6-Feb-98)	0.00	0.01
Qa'a Qattafi	-16.15 (6-Feb-98)	0.08	0.10
Chert gravel	-10.81 (6-Feb-98)	0.04	0.08
Fahda Vesicular basalt	-8.27 (6-Feb-98)	0.05	0.11
Marab Suwaiid	-13.61 (6-Feb-98)	0.07	0.09
Marab Wutaydat	-10.96 (29-Mar-98)	0.05	0.08
Qa'a al Wassad	-13.64 (29-Mar-98)	0.36	0.12
Qa'a al Buqayawiyya 1	-10.88 (6-Feb-98)	0.11	0.13
Qa'a al Buqayawiyya 2	-11.95 (6-Feb-98)	0.09	0.11
Qa'a al Buqayawiyya 3	-12.82 (6-Feb-98)	0.08	0.12
Qa'a al Buqayawiyya 4	-11.02 (6-Feb-98)	0.10	0.09

Table 6.3. Model validation results, developed for the retrieval of volumetric soil moisture information from 1998 ERS-2 SAR imagery.

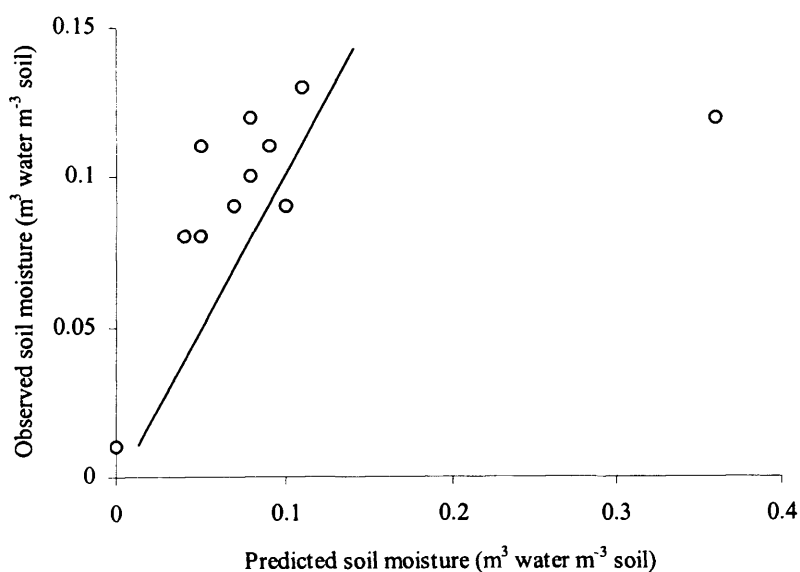


Figure 6.28. Estimates of soil moisture from ERS-2 SAR data compared against soil moisture estimates derived in-situ in 1998. Apart from the outlying over prediction of soil moisture at Qa'a al Wassad, the inversion model slightly under estimates the value of soil moisture estimated in the field. The line $x = y$ is shown.

In the example described here, the null hypothesis states that there is no regression line slope (β), i.e. the mean of the observed soil moisture does not change at all when the predicted soil moisture changes. The alternative hypothesis suggests that there is a relationship between the two parameters. In this example, a one-sided test is adopted, stating that there is a positive association between the predicted and observed soil moisture estimates (Moore, 1995). The hypothesis statements are summarised below followed by the statistical results.

$H_0: \beta = 0$ (null hypothesis)

$H_1: \beta > 0$ (alternative hypothesis), where β is the slope of the relationship.

- Considering all 11 sample points the regression analysis (degrees of freedom = 9 {=11-2}) yielded a t value of 1.78 and a two-sided P value of 0.108. Dividing the P value by two (for a one-sided test) gives a new P value of 0.054. This indicates that there is strong evidence (the null hypothesis can be rejected at a 10% level of significance for a one-sided test) that a relationship exists between the predicted and observed soil moisture values. This means that the confidence level in using the model to predict soil moisture is approximately 80%.

- By incorporating a knowledge of the physical interaction of SAR waves (with the ground surface) and having a brief description of the surface properties the confidence level of the model can be improved. This is done, for one example, by removing surfaces that are extremely flat, for reasons discussed previously. In this case, the outlying sample point (for *Qa'a al Wassad*) is removed from the analysis. The new t value calculated is 4.276 and the associated two-sided P value is 0.0027 (degrees of freedom = 8). Dividing P by two a value of 0.00013 (for a one-sided test) shows that the null hypothesis can be rejected with a 99% level of significance. This indicates that there is a very strong positive relationship between the two parameters and that the model predicts the observed values with a confidence level in excess of 98%. However, the amount of confidence that should be placed on estimates derived from SAR imagery should be considered carefully using as much information on surface properties as possible.

The results indicate that the model predictions are, in most cases, lower than the values of soil moisture measured in the field. The exceptional case of *Qa'a al Wassad* can be explained by the fact that heavy and sustained rainfall occurred for two days prior to the data acquisition on the 29 March 1997. Due to the surface sediment characteristics of *qa'a*, penetration of the moisture into the lower strata, may not have occurred. The soil moisture ThetaProbe (Section 4.3) derives an estimate from the upper 6 cm of the soil and not the very surface layers. In this particular example, all of the radar interactions and scattering of the signal may have occurred in the upper few cm of the surface and not at lower depths. Another explanation for the increase in backscatter might be caused by small increases in surface roughness that were not measurable in the field. The inversion algorithms have been shown to yield realistic estimates of the volumetric soil moisture for a range of desert surfaces given the backscatter coefficient from ERS-2, now it is operating alone.

The inversion algorithms can be exploited further by transforming an ERS SAR image, which has been initially converted to an estimate of the backscatter coefficient, to a thematic map of surface volumetric soil moisture. This is carried out at *Qa'a al Buqayawiyya*, one of the permanent monitoring sites, shown in red in Figure 6.29. The spatial and temporal pattern of surface soil moisture distribution in *Qa'a al Buqayawiyya* (described in Section 3.2.3) is illustrated in Figure 6.30. The key to the classification map and a location diagram (Figure 6.30a) are shown on the following page. *Qa'a al Buqayawiyya* is surrounded to the north by basalt boulders and to the south by a chert *hammada*. In the north-west of the marab, small agricultural fields have been developed by ploughing of the soil. These areas of temporal cultivation (dependent on the amount of rainfall) are clearly distinguished on the images that follow. In Figure 6.30, ERS SAR PRI data have been converted to a backscatter coefficient (ERS-1 SAR to a comprehensive backscatter estimate, ERS-2 SAR to a simple backscatter estimate) using the equation given by Laur *et al.* (1996), assuming that the change in incidence angle across the image sub-scene has a negligible effect on the backscatter coefficient. The estimates of backscatter coefficient have been transformed into a volumetric soil moisture value using Equation 6.4 and have been divided into soil moisture classes.

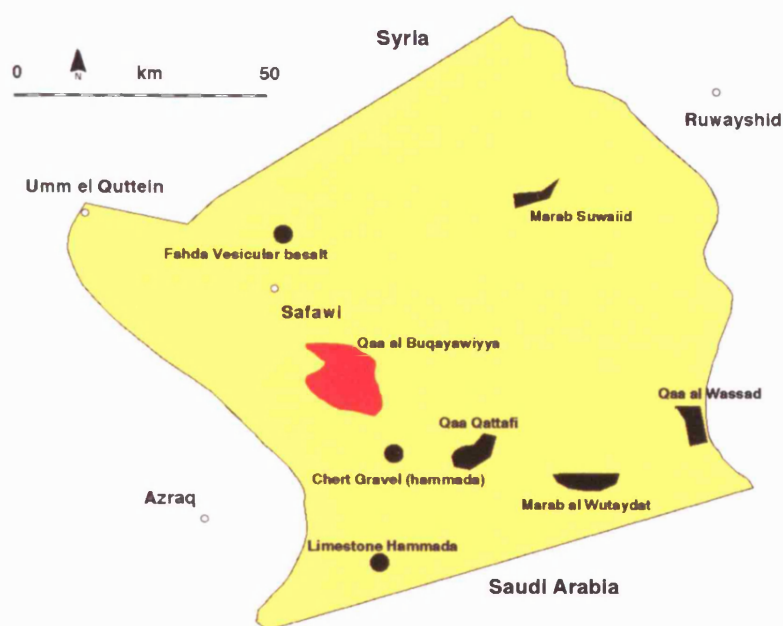
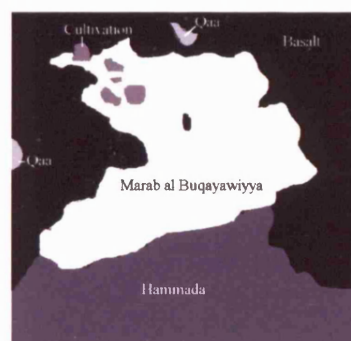
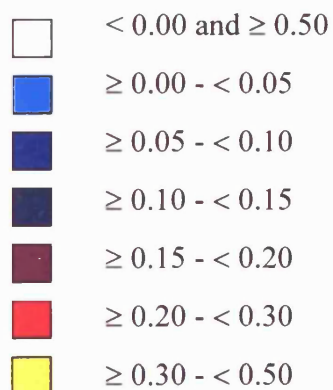


Figure 6.29. Location of Qa'a al Buqayawiyya (shown in red) in the north-eastern Jordan Badia.

Key to Figures 6.30 b – m
(following page).

Units are

Volumetric soil moisture
($\text{m}^3 \text{ water m}^{-3} \text{ soil}$)



(a) reference diagram

Figure 6.30. (Continued on the following page).

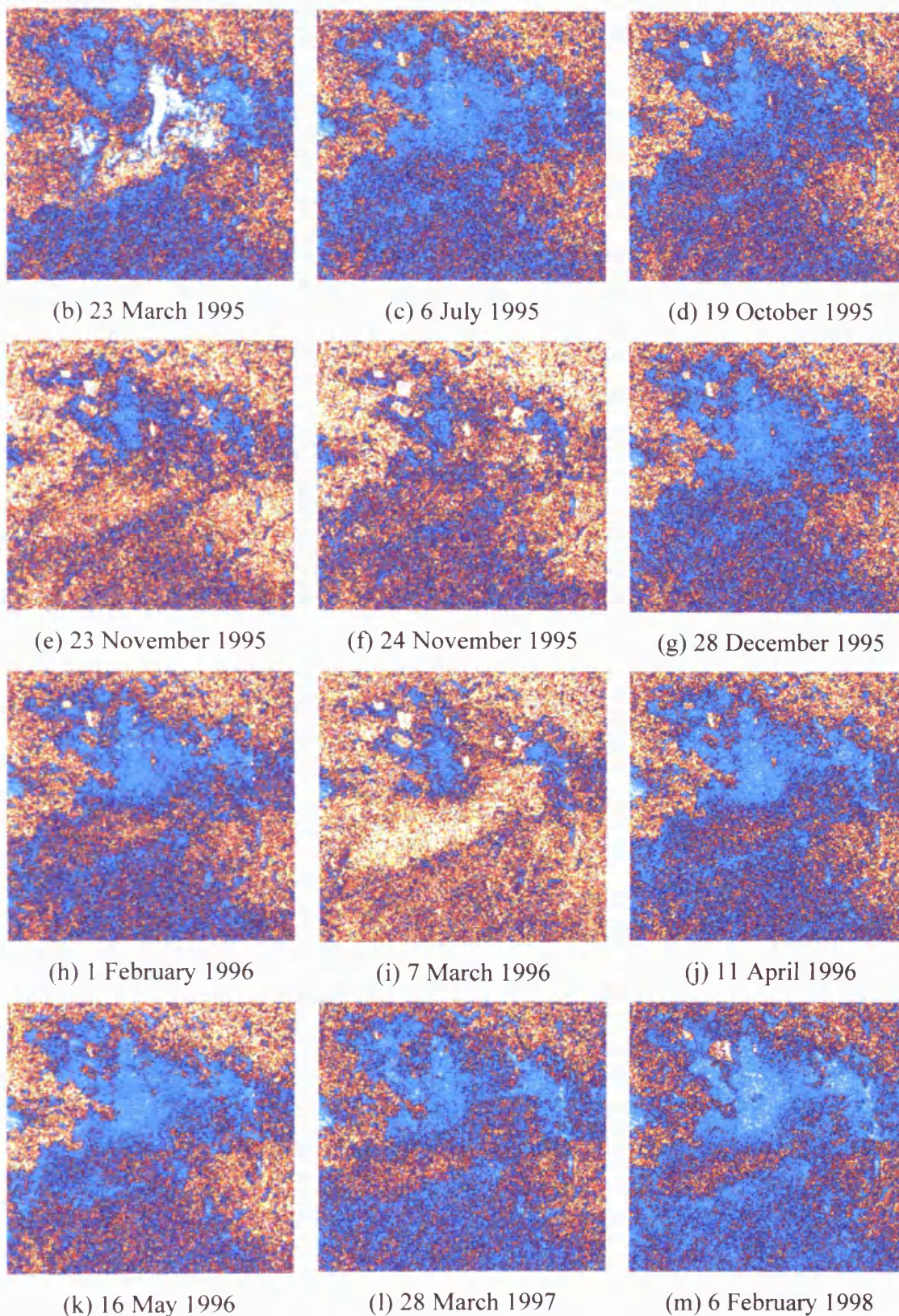


Figure 6.30. Soil moisture distribution maps of Qa'a al Buqayawiyya, derived from ERS-1 and ERS-2 SAR imagery. The images covers 9 by 8 km, north is to the top.

The sequence shows the ability of SAR to make quantitative estimates of the volumetric soil moisture both over a winter period (1995 - 1996) and between consecutive seasons (spring 1995, 96, 97 and 98). The maps have been classified to indicate regions of low soil moisture (light blue) to regions of moderate soil moisture (blue to dark blue) to areas of high soil moisture (purple, red and yellow). It should be stated that the conversion algorithm for soil moisture estimation is only meaningful on the *marab* region and not applicable to the surrounding basalt or desert pavement surfaces (Figure 6.30a). The soil moisture map on the 23 March 1995 (Figure 6.30b) distinguishes clearly the extent of flooding, shown in white due to the low backscatter properties of calm water. Surrounding the standing water and also an area stretching towards the south are regions of high soil moisture, which is likely to be almost saturated (displayed as zones of yellow and red). However, immediately surrounding areas of standing water, there are regions indicated by light blue colours signifying low soil moisture. It is difficult to fully explain this observation; one possible reason is that a reduction in the backscatter coefficient may be caused by volume scattering within vegetation, that is flourishing in the high soil moisture conditions. Volume scattering processes, are not considered in this research, although the author acknowledges that volume scattering may be an important factor at times when vegetation cover becomes greater than 30%. The southern reaches of the *marab* appear to have low soil moisture values, indicating that the ephemeral water body had not extended to this region prior to the image being acquired.

The next acquisition, on the 6 July 1995 (Figure 6.30c), displays the *marab* in mainly blue hues indicating that average soil moisture levels across the region are low. The cultivated region in the north-west section of the map is easily distinguished as is the surrounding basalt. The estimates indicate that the volumetric moisture of the surface soil is between 0.05 and 0.1 m³ water m⁻³ soil. In dry conditions, volume scattering from sub-surface layers may be contributing to the overall backscatter signal; this scattering factor is not accounted for in this study. During October (Figure 6.30d), conditions are much the same, as temperatures are still high, rainfall is almost totally absent (and had been since May) and surface soil moisture levels are minimal (see Section 4.7 for climate data). The two following image acquisitions, are from ERS-1

and ERS-2 operating in tandem mode (Figure 6.30e and f). A precipitation event occurring on the day the image was collected (as discussed in Section 6.4.3) is reflected by an observed increase in soil moisture values for large parts of the central and southern sections of the *marab*. Twenty-four hours later, the soil moisture map suggests that these areas are already starting to dry up, these areas are indicated by increasingly blue hues. A large area, located in the upper central part of the *marab* appears to be almost unaffected by the precipitation event as the low soil moisture values remain relatively constant. The tandem images highlight the potential of SAR to detect rainfall events that increase soil moisture levels in the surface soil, but also illustrate the variable nature of soil moisture in desert regions and the limitations of depending on images acquired every 35 days.

During December and January of the 1995/96 winter, small increases in soil moisture are observed in localised regions of the *marab*, particularly for January (Figure 6.30h). The large increase in soil moisture that is estimated over almost all of *Qa'a al Buqayawiyya* is due to a large precipitation event (Section 4.7) that occurred prior to and during the image acquisition on the 7 March 1995 (Figure 6.30i). Increases in soil moisture are detected in the southern parts of the *marab*. Even though the image indicates high levels of soil moisture across the *marab*, the winter of 1995/96 was not particularly wet and no vigorous ephemeral grass growth occurred. Conditions in April and May of that year (Figures 6.30j and k) show diminishing estimates of the soil moisture content in response to the cessation of rainfall.

The remaining two images, acquired during March 1997 (Figure 6.30l) and February 1998 (Figure 6.30m), display relatively low soil moisture levels across large parts of the *marab*. In both of these years, average rainfall values were higher than normal, although this is not reflected in the upper soil moisture estimates that the C-band SAR system is most sensitive to. It is evident here that the temporal coverage of the ERS SAR system (35 days) is too coarse to give any realistic indication of the likelihood of vegetation growth in desert regions. It is acknowledged, however, that one main image every 35 days in the wet season is the best that we can hope to obtain. The exploitable aspect of SAR in this example has been to demonstrate the ability to detect changes in soil moisture in response to precipitation events and general seasonal conditions. Similar

multitemporal soil moisture maps can be produced for all PMS. It is not important here to display similar results for the other PMS.

It is impossible, in this example, to state the accuracy of the inversion algorithm. Further testing is required. However, in the example cited above for *Qa'a al Buqayawiyya*, realistic estimates of surface soil moisture have been derived for most of the designated site area. The estimation has been made, in accordance with the over-riding assumption that surface roughness variation in the *marab* is negligible or at least minimal, based on the measured roughness properties and the model simulation results. Any significant fluctuations across the *marab* will not influence the sensitivity of the backscatter coefficient to changes in soil moisture, but will affect the absolute value of the backscatter coefficient. For example, if a region of *marab* has a significantly greater surface roughness than the validation sites, then it will be assigned a soil moisture value of 0.2 m³ water m⁻³ soil during the summer months. This is clearly an error, but assumptions like the one stated above have to be made if the potential of using single band data is to be fully exploited in such an application.

6.6 Conclusions

Studies cited previously in this chapter have established that information about the surface soil moisture of a surface can be derived most easily from a multi-parameter system. This approach is required because of other surface parameters, mainly surface roughness, that influence the scattering of the radar wave. Any attempt to extract soil moisture from a fixed SAR system is inherently difficult (Ulaby, 1998). To get around this, an assumption is made that surface roughness does not significantly change on an inter-annual and intra-annual time scale. For surfaces that are radiometrically rough, the dependence of the backscatter coefficient on changes in surface roughness is negligible. For surfaces that are radiometrically smooth, any change in surface roughness needs to be quantified. The following conclusions are stated.

- Simulation of variations in the model parameter values show that the backscatter coefficient is sensitive to changes in surface roughness when the RMS

height is less than 0.5 cm, regardless of the amount of soil moisture. The dependence of the backscatter coefficient to changes in the dielectric properties of the soil medium is large and therefore encouraging.

- The backscatter coefficient is particularly sensitive to soil moisture increases from 0.0 to 0.2 m³ water m⁻³ soil, and is independent of the roughness of the surface. The soil texture has a small impact on the sensitivity, a dominantly sand-size soil having a larger dynamic range for a change in soil moisture from 0.0 to 0.4 m³ water m⁻³ soil, than a dominantly clay-size soil.

- The type of autocorrelation function that best describes the surface under study has an important influence on the sensitivity of the backscatter coefficient. Whether a natural surface is described best by a Gaussian or an exponential autocorrelation function has implications on whether or not the backscatter coefficient is dependent on variations in the RMS height.

- In this chapter the classical scattering models (Kirchoff and Small Perturbation methods) have been validated for their use in interpreting the scattering relationships for desert surfaces located within the eastern Badia of Jordan. Field data acquired during field visits to a number of regions yielded only a small number of potentially useful sites that could be used for model calibration. This is because the roughness characteristics of some of the Badia surfaces did not fit the validation criteria.

- The IEM, which has a larger validation domain, is shown to give good agreement between observed and predicted backscatter coefficients. Correlation coefficients calculated are in excess of 0.8. The number of samples that can be used to calibrate the model and the accuracy of the predictions depends on the length of profile used, the method of calculating the correlation length, and the observed backscatter estimate to which the predicted value is compared. Two methods are available to determine this latter parameter.

- The best results were obtained using a profile approximately 1 m in length. Different statistical methods of calculating the correlation length were investigated though no one method was obviously superior. Furthermore, an experiment was conducted to test different estimates of calculating the backscatter coefficient from ERS SAR imagery (based on differences between the product replica power of ERS-1 and ERS-2 imagery). Only slight improvements in model accuracy were obtained and these recommendations were discussed. An optimal method for model calibration is presented to yield the most accurate results.

A relationship was derived between the soil moisture and the backscatter coefficient for each of the eight permanent monitoring sites (PMS). This relationship was mathematically described by a third-order polynomial equation and inverted to give a site-specific equation that yielded an estimate of the volumetric moisture content given the average backscatter coefficient value calculated from either ERS-1 or ERS-2 SAR data. The following conclusions are stated.

- For each of the eight sites the predicted soil moisture levels over the 1995 winter were reasonable and realistic given the geographical locations of the sites, their surface characteristics and relating these factors to climatic data.

- Validation of the inverse model was achieved by comparing soil moisture estimates calculated from the model with measurements made in the field during the spring 1998 field visit. Due to an unforeseen problem with the satellite data, field data were compared with a ERS-2 SAR image collected on the 6 February 1998. For selected surfaces that fit certain site criteria of roughness and stability the results showed that model predictions have confidence levels greater than 80%. There was a general under-prediction of the soil moisture content. To improve the accuracy of the model, detailed information on surface characteristics (e.g. surface roughness parameters) are essential.

The results, however, illustrate the difficulties in making predictions of soil moisture content of surfaces that do not match certain criteria of surface roughness (e.g. *qa'a*, smooth *marab* and rough basalt surfaces). The inversion algorithms can be applied on a larger spatial scale by assuming that the larger area is approximately homogeneous and

similar to the smaller study site. This assumption only holds if verification of the homogeneity of the general site and specifically surface roughness conditions are made. This introduces problems of up scaling the method to larger areas. The spatial distribution of roughness conditions needs to be quantified before extraction of soil moisture values is possible. This yields a map of surface soil moisture distribution for the region of interest. Illustrated in the previous section is an example of *Qa'a al Buqayawiyya* which is a seasonally vegetated *marab* that is of great importance in supplying natural sources of vegetation. The maps show the spatial and temporal variations in the surface soil moisture in response to precipitation events, the evaporation of surface moisture and inundation by water causing a flooding event. The ERS SAR system shows that that the *marab* is very dynamic in terms of fluctuations in soil moisture and data can be used to provide reasonable quantitative estimates of volumetric soil moisture distribution. This sort of thematic map can be used as input to a spatial vegetation model to predict, for example, the on-set of ephemeral grass growth in the region.

7. Conclusions

7.1 Objectives

The active microwave instruments on board the European Space Agency ERS-1 and ERS-2 satellites provide the scientific community with high quality, global microwave imagery of the Earth's surface. The scattering of microwave radiation is dependent upon the dielectric properties of the surface medium. For a soil, an increase in soil moisture leads to a corresponding increase in the dielectric constant of the surface. The ERS SAR instruments operating at a fixed wavelength ($\lambda = 5.3$ cm), a fixed incidence angle (23° at mid-range), and a fixed polarisation (VV), have been utilised to address the following objectives:

- (1) To assess and exploit the ability of the ERS SAR instrument to monitor geomorphological and hydrological changes in the environment of the north-eastern Badia (desert) of Jordan.**
- (2) To calibrate theoretical microwave scattering models using field reference data (including soil moisture, surface roughness, soil type and vegetation) and assess their application to desert environments.**
- (3) To simulate the dependence of the backscatter coefficient on soil moisture fluctuations and surface roughness changes with the aim of improving the understanding of microwave interactions with desert surfaces.**
- (4) To investigate the potential for extraction of quantitative soil moisture estimates from ERS SAR data.**

These four research objectives were investigated in north-east Jordan as part of the Jordan Badia Research and Development Programme (BRDP). Multitemporal images were acquired, from the spring of 1995 through to the spring of 1998. Field data (including soil moisture, surface roughness estimates and climate data) were obtained from four separate visits (winter 1995, spring 1996, 1997 and 1998) to aid interpretation of the microwave data. The BRDP area, located in the western half of the 'pan-handle' of north-eastern Jordan, has the following characteristics:

- A total land cover area of approximately 11,200 km². A semi-arid to arid moisture regime and a large annual temperature range.
- Desert surfaces comprising over 50% basalt plateau. This plateau mainly covers the north and east of the study area. Further south, desert pavements (*hammada*) of cherts and limestone dominate the landscape. Superimposed within these major geomorphic units is the drainage system comprising *qa'a* (flat, unvegetated mud-pans), wadis and *marab* (vegetated, outwash zones from the ephemeral wadi network).
- A region of increasing population, imposing further restrictions on the limited natural resources. Increasing use of irrigation water places further demand on groundwater and surface water supplies.

7.2 Multitemporal image analysis

In Chapter 3 multitemporal ERS SAR data were converted to an estimate of the backscatter coefficient so that geophysical modelling could be undertaken. The time series of backscatter coefficients was analysed for the four main surface cover types located in the eastern Badia region; namely basalt regolith, *hammada*, *qa'a* and *marab*. The analysis shows that the ERS SAR instrument is able to detect temporal fluctuations in the backscatter coefficient for selected land cover types (*marab* and *qa'a*). The instrument has also shown an ability to detect relative stability's in the backscatter coefficient for other surface types (basalt regolith and *hammada*), which are less than the estimated noise fluctuation of the ERS SAR instrument. The results show that the

radiometric calibration, particularly of the ERS-1 SAR, is consistent and reliable. The fluctuation in backscatter coefficient observed on *marab* and *qa'a* surfaces is greater than the estimated fluctuation due to noise. The observed fluctuations can be attributed to two main processes:

- Changes in soil moisture content. The dependence of the backscatter coefficient on soil moisture is independent of the surface roughness properties of a surface. This implies that for a given input of surface soil moisture, a *hammada* (moderately rough) and a *qa'a* surface (relatively flat), should respond, radiometrically, by a similar amount. This study has shown that different desert surfaces respond to changes in surface moisture in different ways. This is caused by the way in which soil moisture is stored or drained from the surface layers and also due to the dominant scattering processes (surface, double-bounce and volume scattering). Natural *marab* surfaces have low vegetation coverage and a surface of mainly coarse sediments that help to stabilise the surface, reducing erosion. If surface roughness remains approximately constant, then any fluctuations in the backscatter coefficient will be caused by changes in the dielectric properties of the soil surface.

- Changes in surface roughness. The backscatter coefficient is very sensitive to changes in surface roughness, at low values of RMS height (< 0.5 cm) with respect to wavelength. *Qa'a* surfaces are characteristically very flat and therefore have a low RMS height. Any small changes in surface roughness are difficult to measure using a pin profilometer, the only method available in this research to determine this parameter. Hence, the contribution of surface roughness change to the fluctuation in backscatter observed is inherently difficult to determine. As *marab* surfaces are relatively rough, having larger RMS height estimates, the sensitivity of the backscatter coefficient to variations in RMS height is reduced.

These qualitative observations were numerically analysed using theoretical scattering models. Field data of soil moisture, surface roughness and soil particle size were used as inputs to the models. Additional information on the vegetation characteristics and climate were also collected.

Objective (1), concerning the ability of the ERS SAR to monitor geomorphological and hydrological processes in dryland regions, has been fulfilled by the observations made above.

7.3 Parameterisation of roughness

In Chapter 5 the usefulness of the parameters that describe the roughness of natural surfaces and that are specified as input data to the scattering models were investigated. Three parameters of roughness are required as input data; RMS height, correlation length and autocorrelation function. There are a number of methods available to estimate surface roughness. A number of factors influence the estimates derived, for example, the length of the transect and the surface slope. Data were acquired from four field seasons using a pin profilometer, the instrument itself having several disadvantages over a laser profiling method. These profiles were digitised and roughness estimates calculated. The following conclusions were reached:

- The RMS height parameter describes the roughness of a surface better than the correlation length.

- The estimate of correlation length was dependent on the length of transect used. Correlation length increased as the transect length increased. No method of estimating the optimal transect length is specified in the research literature available.

- Roughness parameters were estimated for three profile lengths; short (30 or 48 cm), ≈ 1 m and long (up to 3 m). The best and most reliable results were obtained for ≈ 1 m transect lengths. A short transect length yielded too small a correlation length for model calibration to be achieved, while too long a transect length incorporated slope and larger scale roughness effects.

- The influence of surface slopes on the estimate of roughness parameters not only altered the RMS height, but also increased the correlation length. Ideally therefore a level surface is required to determine the roughness parameters.

- Two methods of deriving the correlation length were compared, the Pearson method and a simplification of this method. In this research no real advantages were gained in using the Pearson method.

- The autocorrelation function, describing the horizontal relationship between surface heights, for the natural surfaces studied can be described mathematically as approximating a Gaussian or an exponential function. Analysis of field data, for basalt, *hammada*, *qa'a* and *marab* sites show that there is no preference for either function for any of these major land units. The function that best describes the data varied spatially (collected at a different position within the site) and temporally (collected during different seasons and years) in some cases.

- A laser profilometer would reduce the time-consuming process of obtaining pin profilometer measurements, and would increase the sample data-set and accuracy. Errors introduced in the collection (photography), digitising and processing stages are difficult to quantify. Higher levels of data analysis, e.g. power spectrum, could also be used with this amount of data.

7.4 Theoretical modelling

The small perturbation (SP), Kirchoff (comprising the geometrical optics (GO) and physical optics (PO)) methods and the integral equation model (IEM) were tested for their application in a dryland environment. Prior to calibration, it was necessary to simulate the sensitivity of the backscatter coefficient to changing surface roughness and soil moisture conditions. The main findings of the simulation experiment results, illustrated in Chapter 6, are:

- A large sensitivity of the backscatter coefficient to surface roughness, when the RMS height was <0.5 cm. This relationship is independent of the amount of moisture in the soil.

- The soil type, parameterised by the particle size distribution, has a relatively small (maximum 2 dB difference between a clay-rich soil and a sand-rich soil) influence on the backscatter coefficient.

- The selection of the autocorrelation function parameter, described by either a Gaussian or an exponential relationship, has a significant influence on the sensitivity of the backscatter coefficient to changes in surface roughness.

Having acquired an understanding of how surface parameters influence the backscatter coefficient, the models were calibrated to test their accuracy in predicting the backscatter response of desert surfaces. Field data were input into the model to generate predicted backscatter coefficients. These values were compared to estimates calculated from ERS SAR PRI data, acquired synchronously. The model calibration process was divided into two stages. Stage 1 was concerned with calibration of the first-order scattering models; SP, GO and PO methods. Stage 2 was concerned with the calibration of an approximation of the second-order IEM. Field data were acquired in the November 1995, spring 1996 and 1997 seasons. The main conclusions of the stage 1 calibrations are:

- Significant limitations in the use of the SP, GO and PO methods. The roughness characteristics of the desert surfaces studied often did not fall within the validation criteria specified by these approaches.

- The number of sample points that could be used to calibrate the SP, GO and PO methods were a limiting factor in obtaining confidence in the future use of these models. For ten different scenarios tested, i.e. using different estimates of the correlation length as previously stated, the number of sample points ranged between 9 and 16. Correlation coefficients between predicted and observed estimates, varied between 0.63 and 0.89.

Stage 2 calibration of the IEM yielded better results. The main conclusions are:

- A greater range of the model's application, restricted only in the prediction of the backscatter coefficient from very rough surfaces (RMS height > 2.7 cm).
- For ten different scenarios tested, the number of sample points that were used, ranged between 28 and 36. Correlation coefficients calculated between predicted and observed estimates of the backscatter coefficient ranged between 0.78 and 0.88.
- The best results were obtained using a transect length of ≈ 1 m to calculate the roughness parameters, a result previously confirmed in analysis of roughness parameters (Section 7.3).
- Due to calibration discrepancies observed between ERS-1 and ERS-2 backscatter coefficients, results could be slightly improved using two different methods to calculate the backscatter coefficient. For ERS-1 SAR data, a comprehensive equation was used to calculate the backscatter coefficient. For ERS-2 SAR data, a simple equation was used.

Objectives (2) and (3) have been fulfilled in this section of the research. The results show the restricted application of the classical scattering models in a dryland environment. However, encouraging results were obtained with the IEM in predicting the backscatter response of the desert surfaces that characterise the eastern Badia of Jordan. Although this approximation of the IEM is not applicable to very rough basalt surfaces, understanding of the scattering processes has been improved through model simulation and calibration.

Consequently, from the encouraging results obtained with the IEM, the potential of model inversion for the extraction of soil moisture values from ERS SAR imagery was investigated, fulfilling Objective (4) of this thesis. Two major assumption were specified in undertaking model inversion. The first assumption stated that the roughness of the natural desert surfaces was constant or any changes did not have a major influence on the backscatter coefficient i.e. when the RMS height is > 1 cm. This

assumption is almost definitely not true for *qa'a* surfaces in the eastern Badia but is assumed for the other main surface types. The second assumption was related to the correlation length. This parameter has been shown to be unrelated to the backscatter coefficient and was difficult to determine accurately from field measurements. Therefore, an optimal value of the correlation length was assigned to each permanent monitoring site studied. This enabled a realistic simulation of changing soil moisture conditions to be achieved.

Soil moisture simulation and inversion procedures were undertaken for eight permanent monitoring sites located in basalt, desert pavement (*hammada*), *qa'a* and *marab* land units. Using input data that parameterised field conditions at each site, a third-order polynomial equation was calculated that best described the relationship between the backscatter coefficient and the volumetric soil moisture content. The main conclusions derived from this procedure were:

- For imagery acquired over the winter of 1995, the soil moisture levels are shown to increase in response to rainfall events recorded prior to the image being collected. This is consistent for the majority of the permanent monitoring sites. Under the assumption that surface roughness change is not responsible for any of the variations observed in the backscatter coefficient, realistic estimates of volumetric soil moisture are derived for all of the sites.

- The soil moisture characteristics of the basalt surfaces are relatively constant throughout the year with only small reductions in predicted soil moisture occurring in the summer months. The greatest seasonal variation in soil moisture occurs in *marab* regions. The assumption that roughness is not changing in these regions, is validated through field observation and measurement.

- Conversion of the backscatter coefficient image to a volumetric soil moisture image show the spatial distribution of surface soil moisture. These show areas of temporary moisture accumulation, areas of prolonged moisture retention and areas of seasonal inundation. Regions that show relatively large estimates of soil moisture

accumulating over consecutive images highlight zones of possible ephemeral vegetation growth.

The inversion procedure, a simple best-fit line approach, was tested by predicting the volumetric soil moisture for the permanent monitoring sites in the spring of 1998. Unfortunately the inverse algorithms could not be fully validated due to the failure of an image scheduled for acquisition in April 1998, caused by too many missing lines. To avoid wasting the large amount of field data that were collected for this purpose, the observed moisture levels were compared to predicted moisture levels from an image acquired in February 1998. Although no direct comparison can be made, conditions, it seems, were not that different, in terms of rainfall levels, during these months. The results showed that there was a general under-prediction of the soil moisture content from ERS SAR imagery. Regression analysis on the predictive ability of the model indicated confidence levels were in excess of 80%. Improvement of the model's predictive ability can be achieved by incorporating some local knowledge about surface characteristics and then making informed judgements about the suitability of the surface for extracting soil moisture estimates.

Objective (4), therefore, can only be partially fulfilled. Complete testing of the ability to extract quantitative soil moisture estimates of desert surfaces using ERS SAR has not been achieved here, due to an instrument malfunction. No future opportunity to acquire satellite data and field data is possible in this research. Even so, the potential for the ERS SAR instrument to be used to extract soil moisture information has been shown. By overcoming the problems of a fixed wavelength, incidence angle and polarisation system, in assuming that surface roughness and soil type are fixed parameters, realistic quantification of the soil moisture and seasonal change in soil moisture levels can be determined for natural desert surfaces in the eastern Badia of Jordan.

7.5 Application of results: Jordan Badia Research and Development Programme

The results contained within this thesis show the potential for soil moisture measurement using microwave remote sensing techniques in a dryland environment. Having basic information about surface conditions, and a series of multitemporal radar images, soil moisture monitoring and mapping can be achieved through the method described here. Spatial maps of soil moisture can be used as input to distributed hydrological models or vegetation growth models, or more simply used to locate zones of soil moisture change, accumulation and drainage that may also indicate regions of vegetation growth. The data presented here are of importance to both the Bedouin people of the Badia landscape and research scientists. As well as providing information related to surface water resource, the SAR data have also proved to be sensitive to surface roughness variations of desert surfaces, complementing existing archives on the geology and geomorphology of the region. Furthermore, SAR provides a tool for the accurate mapping of the distribution and size of flooding events. The satellite data and soil moisture maps will become important information layers in the Jordan BRDP GIS, a regional tool to aid decision making for all aspects of development in the area.

The real potential for the estimation of surface soil moisture levels will only be achieved if near-real time imagery is collected and delivered to the user. Implementation of the algorithms described here can produce real-time estimates of the spatial distribution of soil moisture levels and, furthermore, yield a quantification of these levels. This can only be achieved with an investment into the acquisition of frequent and real-time imagery.

On a wider scale, the results show that the extraction of representative soil moisture values is possible using a fixed wavelength, incidence angle and polarisation system. This is achieved by assuming that roughness conditions of specific desert surfaces do not fluctuate by an amount that affects the backscatter coefficient. For some desert surfaces found within the eastern Badia of Jordan and in other desert environments, this assumption cannot be accepted. Literature cited in this thesis indicates that playa (*qa'a*)

surfaces are very active, their surface responding to changes in surface moisture by forming cracks, caused by swelling and shrinking of the salt and smectite clay-rich surfaces. Other desert surfaces studied in this thesis, basalt regolith, *hammada* and *marab*, are considered to have stable roughness properties over the time scale considered in this study (three years). In some cases, human modifications to natural desert surfaces through cultivation practices, modify the roughness. These roughness changes need to be quantified to model the corresponding change in the microwave backscatter coefficient.

To accurately determine the individual contribution of changes in soil moisture and surface roughness, a multi-parameter (e.g. polarisation, wavelength) approach is desired. Models that require multi-parameter field data for their calibration are widely available for soil moisture applications (Chapter 2). Unfortunately multi-parameter data, either from the L-band JERS-1 system or the RADARSAT multi-incidence angle system, could not be utilised in this project even though limited coverage from these satellites are available.

7.6 Recommendations for future research and ENVISAT

Further areas of research that would build on the results of this project are:

- Calibration of a sub-surface soil moisture model that can utilise spatial surface soil moisture data, obtained from this research, to predict the penetration of moisture into the critical rooting zones of perennial shrubs and ephemeral grasses.
- Investigate interferometric SAR products (e.g. coherence) for dryland studies.
- In the analysis of the parameters that describe surface roughness, estimates of the correlation length parameter, were found to be inconsistent and were dependent upon the length of profile and surface slope. Future research should investigate other methods of determining the horizontal roughness of a natural surface. A sampling method that enables a large number of transects to be acquired would increase the

confidence level of roughness measurements and reduce the noise variations introduced by a limited sample number.

- The space-borne SAR instrument used in this study, has a temporal resolution of 35 days. On desert surfaces, soil moisture fluctuations can be rapid, for example, a rainfall event between image acquisitions could go totally undetected by the satellite. In this thesis, the ERS SAR instrument has been able to detect fluctuations in the backscatter coefficient of vegetated desert surfaces in response to precipitation events occurring prior or during the acquisition. Future research might involve the use of an airborne SAR that acquires images on consecutive days after a precipitation event. This would yield useful information on the spatial distribution of surface soil moisture and fluctuations occurring after the surface has been wetted. As rainfall in desert regions is often unpredictable and inconsistent, it is only good fortune that the overpass occurs at the same time as a rainfall event. Ideally, the temporal resolution needs to be as large as possible for accurate monitoring of dryland soil moisture.

- To determine the magnitude of changes in surface roughness on the backscatter coefficient and to enable empirical and semi-empirical modelling of scattering, multi-parameter data are required. The following section discusses the advantages of using a multi-parameter system, namely, the next generation ESA satellite, ENVISAT, carrying the advanced synthetic aperture radar (ASAR) instrument. Case studies of fluctuating soil moisture and surface roughness are presented, using field data from the eastern Badia. The extra information that ENVISAT can potentially offer is discussed.

7.6.1 ENVISAT

ENVISAT will be launched in 1999 and will have on board a very sophisticated radar system having a number of modes of operation; image, wide swath, wave, alternative polarisation and global monitoring. The orbit will be similar to that of ERS-2 giving a repeat cycle of 35 days. ENVISAT will be able to operate at different imaging resolutions, from the image mode similar to that of ERS-2 (approx. 30 m spatial resolution) to global monitoring (approx. 1 km spatial resolution). The latter mode

covers a swath width of over 400 km. The main advantage for the application presented in this thesis is the alternating polarisation mode that enables scenes to be imaged simultaneously in vertical (VV) and horizontal (HH) polarisation (ESA 1997). Exploitation of the various modes have already been established for general remote sensing science, earth science (land), marine and ice science applications (DRA 1997). To illustrate the potential benefits of alternating polarisation data, for soil moisture studies, examples of model simulations are presented. The model used is the integral equation model, calibrated with data used in this study. For both VV and HH polarisations, the dependence of the backscatter coefficient on changes in volumetric soil moisture ($\text{m}^3 \text{ water m}^{-3} \text{ soil}$) and surface roughness are modelled. The main findings of the experiments are:

- The smaller the estimate of RMS height, the larger the difference between the two polarisations becomes, especially at low levels of soil moisture. Figure 7.1 shows the dependence of the backscatter coefficient to changes in volumetric soil moisture ($\text{m}^3 \text{ water m}^{-3} \text{ soil}$), for a *hammada* surface and a *qa'a* surface. An increase in soil moisture should be detectable by monitoring the size of the difference between polarisations of multitemporal images.
- The integral equation model (IEM) indicates, at these surface and satellite system configurations, that the HH polarised backscatter coefficient is always less than the VV polarised backscatter coefficient.
- For rough surfaces (RMS height $>2 \text{ cm}$), the difference between HH and VV backscatter coefficients is negligible, for all values of soil moisture. The difference is also independent of other roughness parameters. The value of RMS height at which the differences between HH and VV polarisations become negligible may give an indication of the absolute roughness of a surface. Two estimates of the RMS height were calculated, from an average of three $\approx 1 \text{ m}$ profiles, for *Marab Salma* during 1997. The two estimates of RMS height measured were 0.72 and 1.16 cm. Both profiles were assigned a Gaussian autocorrelation function and calculated correlation lengths were 8 and 12 cm respectively. The sensitivity of the backscatter coefficient to changes in soil moisture at these two roughness estimates is shown in Figure 7.2.

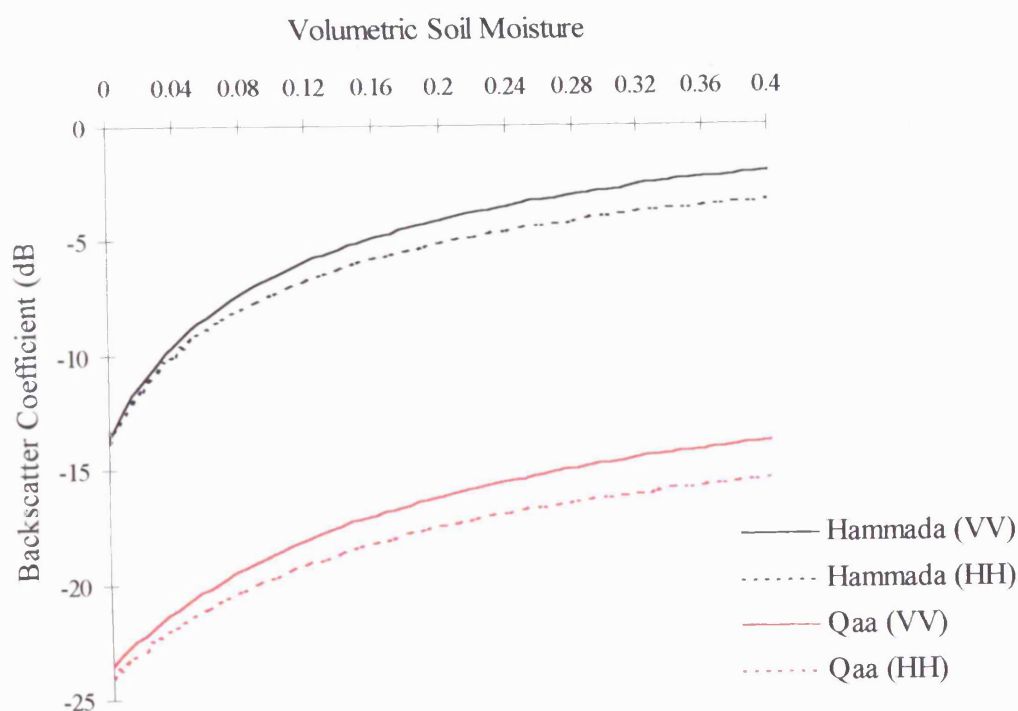


Figure 7.1. Dependence of the backscatter coefficient to changes in soil moisture (m^3 water m^{-3} soil) expressed as a function of polarisation and roughness. The RMS height of the hammada surface is 0.7 cm, and the qa'a, 0.22 cm.

The simulation results illustrated in this section present a case for further research into the monitoring and modelling of dryland soil moisture, using the eastern Badia of Jordan as a test site. With ENVISAT ASAR data it is possible to obtain surface RMS height estimates if soil moisture levels are known, these are easily obtained using the single polarised method discussed in this thesis or from in-situ measurements.

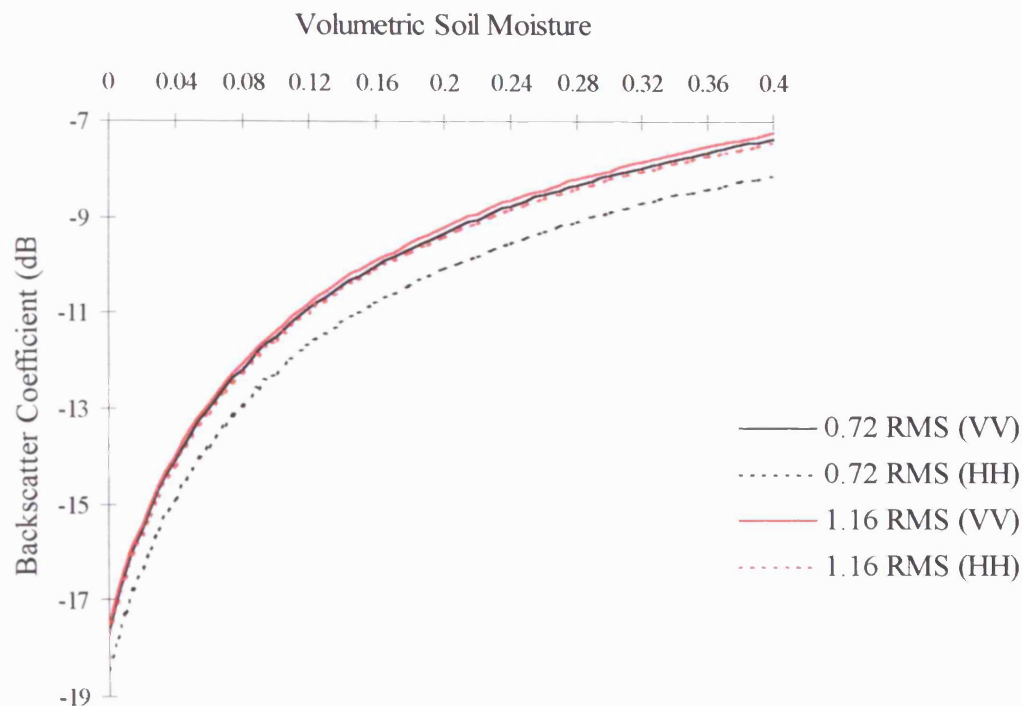


Figure 7.2. Dependence of the backscatter coefficient to changes in soil moisture (m^3 water m^{-3} soil). The simulation indicates that a surface (e.g. Marab Salma) with a RMS height of 1.16 cm does not display different scattering intensities at VV and HH. At a lower RMS height (0.72 cm), the differences in backscatter are greater, a measurable indication of the absolute roughness of the surface.

The results achieved in this study highlight the encouraging potential for dryland resource monitoring applications. The European Space Agency's 'Strategy for Earth Observation', is for a series of complementary polar-orbiting and geostationary satellites to study the Earth's environment and resources, to continue to improve meteorological observations (ESA 1997). Microwave remote sensing has become a growing component of this overall strategy. For the future, SAR, will be a useful tool in mapping and monitoring natural resources in dryland regions.

8. Bibliography

Agnew, C.T. and Anderson, E., 1988, Dewfall and atmospheric conditions, *Journal of Oman Studies*, Vol. 3, pp. 213-216.

Al-Homoud, A.S., Allison, R.J., Sunna, B.F. and White, K., 1996, A study on geology, geomorphology, hydrology, groundwater, and physical resources of the desertified Badia environment in Jordan towards sustainable development, *Environmental Geology*, Vol. 27, pp. 198-209.

Allison, R.J., Higgett, D.L., Kirk, A.J., Warburton, J., Al-Homoud, A.S., Sunna, B.F. and White, K., 1998, Geology, geomorphology, hydrology, groundwater, and physical resources, in *Arid Land Resources and Their Management: Jordan's Desert Margin*, Dutton, R.W., Clarke, J.I. and Battikhi, A.M. (Ed.), Kegan Paul International, London, pp. 21-47.

Altese, E., Bolognani, O., Mancini, M. and Troch, P.A., 1996, Retrieving soil moisture over bare soil from ERS-1 synthetic aperture radar data: Sensitivity analysis based on a theoretical surface scattering model and field data, *Water Resources Research*, Vol. 32, 3, pp. 653-661.

Anderson, M.B. and Burt T.P., 1977, Automatic monitoring of soil moisture conditions in a hillslope spur and hollow, *Journal of Hydrology*, Vol. 33, pp. 27-36.

Archer, D.J., 1995, *Monitoring Geological Processes on the Chott el Djerid Playa using the ERS-1 SAR*, Ph.D. thesis, University of Reading, UK, p. 188.

Attema, E.P.W. and Ulaby, F.T., 1978, Vegetation modelled as a water cloud, *Radio Science*, Vol. 13, pp. 357-364.

Autret, M., Bernad, R. and Vidal Madjar, D., 1989, Theoretical study of the sensitivity of the microwave backscattering coefficient to the soil surface parameters, *International Journal of Remote Sensing*, Vol. 10, 1, pp. 171-179.

Bally, P. and Fellah, K., 1995, *Evaluation of the Accuracy of the Backscattering Coefficient Measurement in SAR Data Products*, ESA/ESTEC/Earth Sciences Division Technical Note, p. 15.

Beckmann, P. and Spizzichino, A., 1963, *The Scattering of Electromagnetic Waves from Rough Surfaces*, Pergamon Press, Oxford, p. 503.

Bendat, J.S. and Piersol, A.G., 1986, *Random data: Analysis and measurement procedures*, 2nd edition, Wiley, New York, p. 566.

Bender, F., 1968, *Geologie von Jordanien*, Beitr. Regionale Geologie erde, Vol. 7, Gebruder Borntrager, Berlin, p. 230.

Bender, F., 1974, *Geology of Jordan*, Gebruder Borntrager, Germany, p. 196.

Black, C.A., 1965, *Methods of Soil Analyses: Part 1, Physical and Mineralogical Properties, Including Statistics of Measurement and Sampling*, American Society of Agronomy, Madison, Wisconsin, p. 770.

Blake, G.S., 1928, *Geology and Water Resources of Palestine*, Jerusalem.

Blake, G.S., 1930, *The Mineral Resources of Palestine and Transjordan*, Publication No. 2, the Geological Advisor in Palestine.

Blom, R.G., 1988, Effects of variation of look angle and wavelength in radar images of volcanic terrain and aeolian terrains, or Now you see it, now you don't, *International Journal of Remote Sensing*, Vol. 9, pp. 945-965.

Borgeaud, M., Noll, J. and Bellini, A., 1994, Use of ERS-1 SAR data for land applications, *Proceedings of the Second ERS-1 Symposium, Hamburg, Germany, 1993*, ESA SP-361, pp. 845-847.

Bowler, J.M., 1986, Spatial variability and hydrological evolution of Australian lake basins: analogue for Pleistocene hydrological change and evaporite formation, *Palaeogeography, Palaeoclimatology, Palaeoecology*, Vol. 54, pp. 21-41.

Brakenseik, D.L., Osborn, H.B. and Rawls, W.J., 1979, Field manual for research in agricultural hydrology, *Handbook 224*, U.S. Dept. of Agriculture, Washington D.C.

Breed, C.S., McCauley, J.F. and Whitney, M.I., 1992, Wind erosion forms, in *Arid Zone Geomorphology*, Thomas, D.S.G. (Ed.), Belhaven, London, pp. 284-310.

Bresler, E. and Kemper, W.D., 1970, Soil water evaporation as affected by wetting methods and crust formation, *Soil Science Society of America Proceedings*, Vol. 34, pp. 3-8.

Briant, P., 1982, *État et Pasteurs au Moyen Orient ancien.*, Paris: Editions de la Maison des sciences de l'Homme, and Cambridge: Cambridge University Press, p. 267.

Brown, S.R. and Scholz, C.H., 1985, Broad bandwidth study of the topography of natural rock surfaces, *Journal of Geophysical Research*, Vol. 90, B14, pp. 12575-12582.

Bryant, R.B., 1993, *The sedimentology and geochemistry of non-marine evaporites on the Chott el Djerid, using both ground and remotely sensed data*, PhD. Thesis, University of Reading, UK, p. 267.

Burdon, D.J., 1959, *Handbook of the Geology of Jordan*, Government of the Hashemite Kingdom of Jordan, Amman, p. 82.

Campbell, B.A. and Garvin, J.B., 1993, Lava flow topographic measurements for radar data interpretation, *Geophysical Research Letters*, Vol. 20, 9, pp. 831-834.

Campbell, D. and Roe, A., 1998, Results of a preliminary survey of livestock owners, in *Arid Land Resources and Their Management: Jordan's Desert Margin*, Dutton, R.W., Clarke, J.I. and Battikhi, A.M. (Ed.), Kegan Paul International, London, pp. 189-196.

Champion, I, 1996, Simple modelling of radar backscattering coefficient over a bare soil: Variation with incidence angle, frequency and polarisation, *International Journal of Remote Sensing*, Vol. 17, pp. 783-800.

Chen, K.S., Yen, S.K. and Huang, W.P., 1995, A simple model for retrieving bare soil moisture from radar scattering coefficients, *Remote Sensing of Environment*, Vol. 54, pp. 121-126.

Chiarantini, L., Coppo, P., Gagliani, S., Luzi, G. and Benvenuti, M., 1995, ERS-1 SAR image analysis for hydrological studies in the Abruzzo Region (Italy): Experimental activities for soil moisture and roughness estimations, in Mougin, E., Ranson, K.J. and Smith, J.A. (Ed.), *Multispectral and Microwave Sensing of Forestry, Hydrology and Natural Resources*, SPIE Vol. 2314, pp. 494-501.

Chuah, H.T. and Kung, W.L., 1994, A microwave propagation model for estimation of effective attenuation coefficients in a vegetation canopy, *Remote Sensing of Environment*, Vol. 50, pp. 212-220.

Cihlar, J., Pultz, T.J. and Gray, A.L., 1992, Change detection with synthetic aperture radar, *International Journal of Remote Sensing*, Vol. 13, 3, pp. 401-414.

Clapp, R.E., 1946, A Theoretical and Experimental Study of Radar Ground Return, *MIT Radiation Laboratory, Report 6024*.

Cooke, R.U. and Warren, A., 1973, *Geomorphology in Deserts*, Batsford, London, p. 374.

Cooke, R.U., 1970, Stone pavements in deserts, *Association of American Geographers, Annals*, Vol. 60, pp. 560-577.

Cope, T.A. and El-Eisawi, D., 1998, Checklist of the flora, in *Arid Land Resources and Their Management: Jordan's Desert Margin*, Dutton, R.W., Clarke, J.I. and Battikhi, A.M. (Ed.), Kegan Paul International, London, pp. 183-188.

Cox, N.J., 1983, On the estimation of spatial autocorrelation in geomorphology, *Earth Surface Processes and Landforms*, Vol. 8, pp. 89-93.

Derooin, J.P., Company, A. and Simonin, A., 1997, An empirical model for interpreting the relationship between backscattering and arid land surface roughness as seen with the SAR, *IEEE Transactions on Geoscience and Remote Sensing*, Vol. 35, 1, pp. 86-92.

Dixon, J.C., 1994, Aridic soils, patterned ground and desert pavements, *Geomorphology of Desert Environments*, Abrahams, A.D. and Parsons, A.J. (Ed.), Chapman and Hall, London, pp. 64-81.

Dobson, M.C. and Ulaby, F.T., 1981, Microwave backscatter dependence on surface roughness, soil moisture and soil texture: Part III - soil tension, *IEEE Transactions on Geoscience and Remote Sensing*, Vol. 19, 1, pp. 51-62.

Dobson, M.C. and Ulaby, F.T., 1986, Preliminary evaluation of the SIR-B response to soil moisture, surface roughness and crop canopy cover, *IEEE Transactions on Geoscience and Remote Sensing*, Vol. GE-24, pp. 517-526.

Dobson, M.C., Pierce, L., Srabandi, K., Ulaby F.T. and Sharik, T., 1992, Preliminary analysis of ERS-1 SAR for forest ecosystem studies, *IEEE Transactions on Geoscience and Remote Sensing*, Vol. 30, pp. 203-211.

Dobson, M.C., Ulaby, F.T., Hallikainen, M.T. and El-Rayes, M.A., 1985, Microwave dielectric behaviour of wet soil - part II: Dielectric mixing models, *IEEE Transactions on Geoscience and Remote Sensing*, Vol. 23, 1, pp. 35-46.

Dotteridge, J., 1998, Water resources quality, sustainability and development, in *Arid Land Resources and Their Management: Jordan's Desert Margin*, Dutton, R.W., Clarke, J.I. and Battikhi, A.M. (Ed.), Kegan Paul International, London, pp. 67-80.

DRA, 1997, *ASAR Workshop Report*, Defence Research Agency (DRA) report, DRA/CIS(CIS2)/CR/96/076, p. 30.

Drury, D., 1998, Baseline hydrochemical study of the Azraq basin, in *Arid Land Resources and Their Management: Jordan's Desert Margin*, Dutton, R.W., Clarke, J.I. and Battikhi, A.M. (Ed.), Kegan Paul International, London, pp. 81-86.

Dubois, P.C., van Zyl, J. and Engman, E.T., 1995, Measuring soil moisture with imaging radars, *IEEE Transactions on Geoscience and Remote Sensing*, Vol. 33, 4, pp. 915-926.

Dutton, R.W., 1998, Population, environment and development, in *Arid Land Resources and Their Management: Jordan's Desert Margin*, Dutton, R.W., Clarke, J.I. and Battikhi, A.M. (Ed.), Kegan Paul International, London, pp. 1-20.

Edwards, M.C., 1999, *Remote sensing of arid land vegetation using ATSR-2*, Ph.D. thesis, University of Leicester, UK, p. 270.

Engman, E.T. and Chauhan, N., 1995, Status of microwave soil moisture measurements with remote sensing, *Remote Sensing of Environment*, Vol. 51, pp. 189-198.

Engman, E.T. and Wang, J.R., 1987, Evaluating roughness models of radar backscatter, *IEEE Transactions on Geoscience and Remote Sensing*, Vol. 25, 6, pp. 709-713.

ESA, 1992, *ERS-1 Product Specification*, ESA SP-1149, p. 19.

ESA, 1993, *ERS User Handbook*, ESA SP-1148, p. 129.

ESA, 1997, *ENVISAT-1: Mission & system summary*, European Space Agency Publication, c/o ESTEC, The Netherlands, p. 84.

Evans, D.L., Farr, T.G. and van Zyl, J.J., 1992, Estimates of surface roughness derived from Synthetic Aperture Radar (SAR) data, *IEEE Transactions on Geoscience and Remote Sensing*, Vol. 30, 2, pp. 382-389.

Farr, T.G., 1992, Microtopographic evolution of lava flows at Cima volcanic field, Mojave Desert, California, *Journal of Geophysical Research*, Vol. 97, B11, pp. 15171-15179.

Findlay, A.M. and Maani, M., 1998, Population fertility trends, in *Arid Land Resources and Their Management: Jordan's Desert Margin*, Dutton, R.W., Clarke, J.I. and Battikhi, A.M. (Ed.), Kegan Paul International, London, pp. 197-214.

Ford, J.P., Bloom, R.G., Bryan, M.L., Daily, M.I., Dixon, T.H., Elachi, C. and Xenos, E.C., 1980, Seasat views of North America, the Caribbean, and Western Europe with imaging radar, *JPL Publication No. 80-67*, NASA-JPL.

Frost, V.S., Stiles, J.A., Shanmugan, K.S., Holtzman, J.C. and Smith, S.A., 1981, An adaptive filter for smoothing noisy radar images, *Proceedings of the IEEE*, Vol. 69, pp. 133-135.

Fung, A.K., 1994, *Microwave Scattering and Emission Models and Their Applications*, Artech House, Norwood, Massachusetts, p. 573.

Fung, A.K., Li, Z. and Chen, K.S., 1992, Backscattering from a randomly rough dielectric surface, *IEEE Transactions on Geoscience and Remote Sensing*, Vol. 30, 2, pp. 356-369.

Gaskin, G.J. and Miller, J.D., 1996, Measurement of soil water content using a simplified impedance measuring technique, *Journal of Agricultural Engineering Research*, Vol. 63, pp. 153-160.

Goudie, A.S., 1992, Weathering processes, in *Arid Zone Geomorphology*, Thomas, D.S.G. (Ed.), Belhaven, London, pp. 11-24.

Haaland, A., 1998, Hydrogeology and hydrochemistry of the Sirhan and Hammad basins, in *Arid Land Resources and Their Management: Jordan's Desert Margin*, Dutton, R.W., Clarke, J.I. and Battikhi, A.M. (Ed.), Kegan Paul International, London, pp. 95-102.

Hallikainen, M.T., Ulaby, F.T., Dobson, M.C., El-Rayes, M.A. and Wu, L.K., 1985, Microwave dielectric behaviour of wet soil - part I: Empirical models and experimental observations, *IEEE Transactions on Geoscience and Remote Sensing*, Vol. 23, 1, pp. 25-34.

Heathcote, R.L., 1983, *The Arid Lands: Their Use and Abuse*, Longman, London, p. 323.

Herbel, C.H. and Gile, L.H., 1973, Field moisture regimes and morphology of some arid-land soils in New Mexico, *Field Soil Water Regimes*, Soil Science Society of America, Madison, Wisconsin, pp. 119-152.

Higgitt, D.L. and Allison, R.J., 1998, Characteristics of the basalt boulder surfaces, in *Arid Land Resources and Their Management: Jordan's Desert Margin*, Dutton, R.W., Clarke, J.I. and Battikhi, A.M. (Ed.), Kegan Paul International, London, pp. 171-182.

Hillel, D., 1977, *Computer Simulation of Soil-Water Dynamics: a compendium of recent work*, International Development Research Centre, Ottawa, Canada, p. 214.

Huang, C. and Bradford, J.M., 1990, Portable laser scanner for measuring soil surface roughness, *Soil Science Society of America Journal*, Vol. 54, pp. 1402-1406.

Ibrahim, K., 1993, *The Geologic Framework for the Harrat Ash-Shaam Basaltic Super-Group and its Volcanotectonic Evolution*, Natural Resources Authority, Amman, p. 26.

Idso, S.B., Jackson, R.D. and Reginato, R.J., 1975a, Detection of soil moisture by remote surveillance, *American Scientist*, Vol. 63, pp. 549-557.

Idso, S.B., Schmugge, T.J., Jackson, R.D. and Reginato, R.J., 1975b, The utility of surface temperature measurements for the remote sensing of soil water status, *Journal of Geophysical Research*, Vol. 80, pp. 3044-3049.

Jaber, J.O., Probert, S.D. and Badr, O., 1997, Energy and environmental issues for Jordan, *Applied Energy*, Vol. 57, 1, pp. 45-101.

Jackson, T.J. and Le Vine, D.E., 1996, Mapping surface soil moisture using an aircraft-based passive microwave instrument: algorithm and example, *Journal of Hydrology*, Vol. 184, pp. 85-99.

John, B., 1992, Soil moisture detection with airborne passive and active microwave sensors, *International Journal of Remote Sensing*, Vol. 13, pp. 481-491.

Kingsley, S.P. and Quegan, S., 1992, *Understanding Radar Systems*, McGraw-Hill Book Company, London, p. 272.

Kirk, A.J., 1997, *Relationships between Sediment, Moisture and Soil Crust Characteristics in Arid Environments*, Ph.D. thesis, University of Durham, UK, pp. 351.

Kirk, A.J., 1998, A synthesis of climatic data with specific interest in the precipitation record, in *Arid Land Resources and Their Management: Jordan's Desert Margin*, Dutton, R.W., Clarke, J.I. and Battikhi, A.M. (Ed.), Kegan Paul International, London, pp. 47-66.

Knight, M.J., 1980, Structural analysis and mechanical origins of gilgai, at Boorook, Victoria, Australia, *Geoderma*, Vol. 23, pp. 245-283.

Köppen, W., 1931, *Die Klimate der Erde*, Berlin.

Kuan, D.T., Sawchuk, A.A., Strand, T.C. and Chavel, P., 1985, Adaptive noise smoothing filter for images with signal dependent noise, *IEEE Transactions on Pattern Analysis and Machine Intelligence*, Vol. 7, pp. 165-177.

Lancaster, W. and Lancaster, F., 1991, Limitations on Sheep and Goat Herding in the Bâdia of Jordan: an Ethno-archaeological Enquiry, *Levant* 23, London: British Academy, pp. 125-138.

Lancaster, W. and Lancaster, F., 1997, Indigenous resource management systems in the Bâdia of the Bilâd ash-Shâm, *Journal of Arid Environments*, Vol. 35, pp. 367-378.

Lancaster, N. and Nickling, W.G., 1994, Aeolian sediment transport, in *Geomorphology of Desert Environments*, Abrahams, A.D. and Parsons, A.J. (Ed.), Chapman and Hall, London, pp. 447-473.

Laur, H., Bally, P., Meadows, P., Sanchez, J., Schaettler, B. and Lopinto, E., 1996, *Derivation of the backscattering coefficient σ^0 in ESA ERS SAR PRI products*, ESA ES-TN-RS-PM-HL09, Issue 2, Rev. 2, p. 41.

Laur, H., Bally, P., Meadows, P., Sanchez, J., Schaettler, B. and Lopinto, E., Esteban, D., 1998, *Derivation of the backscattering coefficient σ^0 in ESA ERS SAR PRI products*, ESA ES-TN-RS-PM-HL09, Issue 2, Rev. 5b, p. 47.

Laur, H., Meadows, P., Sanchez, J.I. and Dwyer, E., 1993, ERS-1 SAR radiometric calibration, *Proceedings of the CEOS SAR Calibration Workshop*, (ESA WPP-048), pp. 257-281.

Le Toan, T., 1982, Active microwave signatures of soil and crops: Significant results of three years of experiments, *1982 IEEE International Geoscience and Remote Sensing Symposium (IGARSS'82) Digest*, Vol. I, Munich, Germany, 662-665.

Le Toan, T., Smacchia, P., Souyris, J.C., Beaudoin, A., Merdas, M., Wooding, M. and Lichteneger J., 1994, On the retrieval of soil moisture from ERS-1 SAR data, *Proceedings Second ERS-1 Symposium*, Hamburg, Germany, 11-14 October, 1993, pp. 883-888.

Lee, J-S., 1980, Digital image enhancement and noise filtering by use of local statistics, *IEEE Transactions on Pattern Analysis and Machine Intelligence*, Vol. 2, pp. 165-177.

Lehrsch, G.A., Whisler, F.D. and Romkens, M.J.M., 1988, Spatial variation of parameters describing soil surface roughness, *Soil Science Society of America Journal*, Vol. 52, pp. 311-319.

Maani, M., Hunaiti, H. and Findlay, A.M., 1998, Demographic change and population projections, 1976-2013, in *Arid Land Resources and Their Management: Jordan's Desert Margin*, Dutton, R.W., Clarke, J.I. and Battikhi, A.M. (Ed.), Kegan Paul International, London, pp. 215-246.

de Martonne, E. and Aufrère, L., 1927, Map of interior basin drainage, *Geographical Review*, Vol. 17, p. 414.

Massonet, D., Rossi, M., Carmona, C., Adragna, Pelzer, G., Feigl, K. and Rabaute, T., 1993, The displacement field of the Landers earthquake mapped by radar interferometry, *Nature*, Vol. 364, pp. 138-142.

McCarroll, D., 1992, A new instrument and techniques for the field measurement of rock surface roughness, *Zeitschrift Fur Geomorphologie*, Vol. 36, 1, pp. 69-79.

McCarroll, D. and Nesje, A., 1996, Rock surface roughness as an indicator of degree of rock surface weathering, *Earth Surface Processes and Landforms*, Vol. 21, 10, pp. 963-977.

McDonald, K.C. and Ulaby, F.T., 1993, Radiative transfer modelling of discontinuous tree canopies at microwave frequencies, *International Journal of Remote Sensing*, Vol. 14, 11, pp. 2097-2128.

McFadden, L.D., Wells, S.G., Dohrenwend, J.C. and Turrin, B.D., 1984, Cumulic soils formed in eolian parent materials on flows of the Cima Volcanic Field, Mohave Desert, *Geological Society of America Guidebook*, Annual Meeting, Reno, NV, Vol. 14, pp. 134-149.

McFadden, L.D., Wells, S.G. and Jerconovich, M.J., 1987, Influences of eolian and pedogenic processes on the origin and evolution of desert pavements, *Geology*, Vol. 15, pp. 504-508.

Meigs, P., 1953, World distribution of arid and semi-arid homoclimates, *Arid Zone Hydrology, UNESCO Arid Zone Research Series*, Vol. 1, pp. 203-209.

Millington, A.C., White, K., Drake, N.A., Wadge, G. and Archer, D.J., 1995, Remote sensing of geomorphological processes and surficial material geochemistry in drylands, in *Advances in Environmental Remote Sensing*, Danson, F.M. and Plummer, S.E., Ed., John Wiley and Sons Ltd, pp. 105-122.

Mo, T., Schmugge, T.J. and Jackson, T.J., 1984, Calculations of radar backscattering coefficient of vegetation-covered soils, *Remote Sensing of Environment*, Vol. 15, pp. 119-133.

Mo, T., Wang, J.R. and Schmugge, T.J., 1988, Estimation of surface roughness parameters from dual-frequency measurements of radar backscattering coefficients, *IEEE Transactions on Geoscience and Remote Sensing*, Vol. 26, 5, pp. 574-579.

Moore, D.S., 1995, *The Basic Practice of Statistics*, W.H. Freeman and Company, New York, p. 680.

Nadler, A. and Lapid, Y., 1996, An improved capacitance sensor for in-situ monitoring of soil moisture, *Australian Journal of Soil Research*, Vol. 34, pp. 361-368.

Njoku, E.G. and Entekhabi, D., 1996, Passive microwave remote sensing of soil moisture, *Journal of Hydrology*, Vol. 184, pp. 101-129.

Noble, P., 1998, Quantification of the recharge to the Azraq basin, in *Arid Land Resources and Their Management: Jordan's Desert Margin*, Dutton, R.W., Clarke, J.I. and Battikhi, A.M. (Ed.), Kegan Paul International, London, pp. 103-110.

Oberlander, T.M., 1994, Global deserts: a geomorphic comparison, in *Geomorphology of Desert Environments*, Abrahams, A.D. and Parsons, A.J. (Ed.), Chapman and Hall, London, pp. 13-36.

Oh, Y., Sarabandi, K. and Ulaby, F.T., 1992, An empirical model and an inversion techniques for radar scattering from bare soil surfaces, *IEEE Transactions on Geoscience and Remote Sensing*, Vol. 30, 2, pp. 370-381.

Oh, Y., Sarabandi, K. and Ulaby, F.T., 1994, An inversion algorithm for retrieving soil moisture and surface roughness from polarimetric radar observations, *Proceedings of IGARSS'94*, IEEE, Pasadena, CA, pp. 1582-1584.

Osborn, H.B., Renard, K.G. and Simanton, J.R., 1979, Dense networks to measure convective rainfalls in the Southwestern United States, *Water Resources Research*, Vol. 15, pp. 1701-1711.

Owe, M., van de Griend, A.A. and Chang, A.T.C., 1992, Surface moisture and satellite microwave observations in semi-arid southern Africa, *Water Resources Research*, Vol. 28, pp. 829-839.

Pampaloni, P. and Paloscia, S., 1986, Microwave emission and plant water content: a comparison between field measurements and theory, *IEEE Transactions on Geoscience and Remote Sensing*, Vol. 24, pp. 900-905.

Parker, D.H., 1971, *The Hydrogeology of the Mesozoic-Cainozoic aquifers of the Western Highlands and Plateau of East Jordan*, PhD. thesis, University of Nottingham, UK, 2 volumes.

Peel, R.A., 1960, Some aspects of desert geomorphology, *Geography*, Vol. 45, pp. 241-262.

Penck, A., 1894, *Morphologie der Erdoberfläche*, Stuttgart, p. 363.

Penman, H. 1948, Natural evaporation from open water, bare soils and grass, *Philosophical Transactions of the Royal Society of London*, A 193, pp. 120-145.

Phene, C., Hoffman, G.J. and Rawlins, S.L., 1971, Measuring soil matric potential in-situ by sensing heat dissipation within a porous body, I: Theory and sensor construction, *Soil Science Society of America Proceedings*, Vol. 35, pp. 27-33.

Phene, C., Hoffman, G.J. and Austin, R.S., 1973, Controlling automated irrigation with soil matric potential sensor, *Transactions ASAE*, Vol. 16, pp. 773-776.

Posner, F.L., 1993, Texture and speckle in high resolution synthetic aperture radar clutter, *IEEE Transactions on Geoscience and Remote Sensing*, Vol. 31, 1, pp. 192-203.

Quegan, S., 1995, Recent advances in understanding SAR imagery, in *Advances in Environmental Remote Sensing*, Danson, F.M. and Plummer, S.E. (ed.), John Wiley and Sons Ltd, pp. 89-104.

Rao, K.S., Raju, S. and Wang, J.R., 1993, Estimation of soil moisture and surface roughness parameters from backscattering coefficient, *IEEE Transactions on Geoscience and Remote Sensing*, Vol. 31, 5, pp. 1094-1099.

Rawls, W.J. and Asmussen, L.E., 1973, Neutron probe field calibration for soils in the Georgia coastal plain, *Soil Science*, Vol. 110, pp. 262-265.

Reid, I. and Frostick, L.E., 1992, Channel form, flows and sediments in deserts, in *Arid Zone Geomorphology*, Thomas, D.S.G. (Ed.), Belhaven, London, pp. 117-135.

Richards, L.A., 1949, Methods of measuring soil moisture tension, *Soil Science*, Vol. 68, pp. 95-112.

Richards, J.A., Sun, G-Q. and Simonet, D.S., 1987, L-band radar backscatter modelling of forest stands, *IEEE Transactions on Geoscience and Remote Sensing*, Vol. 25, pp. 487-498.

Ridley, J., Strawbridge, F., Card, R. and Phillips, H., 1996, Radar backscatter characteristics of a desert surface, *Remote Sensing of Environment*, Vol. 57, pp. 63-78.

Rignot, E.J.M. and van Zyl, J.J., 1993, Change detection techniques for ERS-1 SAR data, *IEEE Transactions on Geoscience and Remote Sensing*, Vol. 31, 4, pp. 896-906.

Rowell, D.L., 1994, *Soil science: Methods and Applications*, Longman Scientific and Technical, p. 350.

Sarabandi, K., Oh, Y. and Ulaby, F.T., 1996, A numerical simulation of scattering from one-dimensional inhomogeneous dielectric random surfaces, *IEEE Transactions on Geoscience and Remote Sensing*, Vol. 34, 2, pp. 425-432.

Saxton, K.E., Johnson, H.P. and Shaw, R.H., 1974, Modelling evapotranspiration and soil moisture, *Transactions ASAE*, Vol. 17, pp. 673-677.

Sayles, R.S. and Thomas, T.R., 1978, Surface topography as a nonstationary random process, *Nature*, Vol. 271, pp. 431-434.

Schmugge, T.J., 1980, Effect of texture on microwave emission from soils, *IEEE Transactions on Geoscience and Remote Sensing*, Vol. 18, 4, pp. 353-361.

Schmugge, T.J., 1983, Remote sensing of soil moisture: recent advances, *IEEE Transactions on Geoscience and Remote Sensing*, Vol. 21, pp. 336-344.

Schmugge, T.J., 1990, Measurements of surface soil moisture and temperature, in *Remote Sensing of Biosphere Functioning*, Hobbs, R.J. and Mooney, H.A. (Ed.), Springer Verlag, New York, pp. 41-61.

Schmugge, T.J., Jackson, T.J. and McKim, H.L., 1980, Survey of methods for soil moisture determination, *Water Resources Research*, Vol. 16, 6, pp. 961-979.

Shantz, H.L., 1956, History and problems of arid lands development, in *The Future of Arid Lands*, White, G.F. (Ed.), American Association for the Advancement of Science, Washington, DC, pp. 3-25.

Shaw, P.A. and Thomas, D.S.G., 1992, Playas, pans and salt lakes, in *Arid Zone Geomorphology*, Thomas, D.S.G. (Ed.), Belhaven, London, pp. 184-208.

Smith, A.M., Wilson, C. and Meadows, P.J., 1994, The EODC SAR processor, *International Journal of Remote Sensing*, Vol. 15, pp. 785-801.

Smoot, J.P. and Lowenstein, T.K., 1991, Depositional environments of non-marine evaporites, in *Developments in Sedimentology, 50: Evaporites, Petroleum and Mineral Resources*, Melvin, J.L., Ed., Elsevier, Amsterdam, pp. 189-347.

Sreenivas, K., Venkataratnam, L. and Narasimha-Rao, P.V., 1995, Dielectric properties of salt-affected soils, *International Journal of Remote Sensing*, Vol. 16, pp. 641-649.

Su, Z., and Troch, P.A., 1996, Soil surface parameters and radar backscattering, *Paper presented at the 21st General Assembly of the European Geophysical Society*, The Hague, 6-10 May, 1996.

Tansey, K.J., 1994, *An Evaluation of the Performance of Recording Rain Gauges*, National Rivers Authority - North West Region, unpublished report, p. 60.

Tansey, K., White, K. H., Battikhi, A. and Millington, A. C., 1996, Relationships between surface roughness and ERS-1 SAR backscatter on desert surfaces in eastern Jordan: preliminary results, *Proceedings of the 22nd Annual Conference of the Remote Sensing Society*, Durham, pp. 45-52.

Tansey, K.J. and Millington, A.C., (in press), Investigating the potential for soil moisture monitoring in the Jordanian desert using ERS-1 and ERS-2 SAR data, *International Journal of Remote Sensing*, in press.

The Soils of Jordan, 1993, *National Soil Map and Land Use Project: Level I Reconnaissance Soil Survey*, Ministry of Agriculture, the Hashemite Kingdom of Jordan, 3 volumes.

The Soils of Jordan, 1994, *National Soil Map and Land Use Project: Level II Semi-detailed Studies*, Ministry of Agriculture, the Hashemite Kingdom of Jordan, 3 volumes.

Thomas, D.A. and Squires, V.R., 1991, Available soil moisture as a basis for land capability assessment in semi-arid regions, *Vegetatio*, Vol. 91, pp. 183-189.

Thomas, D.S.G., 1988, Arid and semi-arid areas, in *Biogeomorphology*, Viles, H.A. (Ed.), Blackwell, Oxford, pp. 191-221.

Thomas, D.S.G., 1992, The nature of arid environments, in *Arid Zone Geomorphology*, Thomas, D.S.G. (Ed.), Belhaven, London, pp. 1-10.

Torgersen, T., De Dekker, P., Chivas, A.R. and Bowler, J.M., 1986, Salt lakes: a discussion of processes influencing palaeoenvironmental interpretation and recommendations for future study, *Palaeogeography, Palaeoclimatology, Palaeoecology*, Vol. 54, pp. 7-19.

Trevett, J.W., 1986, *Imaging Radar for Resource Surveys*, Chapman and Hall, Cambridge, p. 313.

Ulaby, F.T. and Elachi, C., 1990, *Radar Polarimetry for Geoscience Applications*, Dedham, Massachusetts: Artech House, p. 350.

Ulaby, F.T., Batlivala, P.P. and Dobson, M.C., 1978, Microwave backscatter dependence on surface roughness, soil moisture and soil texture: Part I - bare soil, *IEEE Transactions on Geoscience Electronics*, Vol. 16, pp. 286-295.

Ulaby, F.T., Bengal, T.H., Dobson, M.C., East, J.R., Garvin, J.B. and Evans, D.L., 1990a, Microwave dielectric properties of dry rocks, *IEEE Transactions on Geoscience and Remote Sensing*, Vol. 28, 3, pp. 325-336.

Ulaby, F.T., Bradley, G.A. and Dobson, M.C., 1979, Microwave backscatter dependence on surface roughness, soil moisture and soil texture: Part II - vegetation covered soil, *IEEE Transactions on Geoscience Electronics*, Vol. 17, pp. 33-40.

Ulaby, F.T., Moore, R.K. and Fung, A.K., 1981, *Microwave Remote Sensing: Active and Passive, Vol. I: Microwave Remote Sensing Fundamentals and Radiometry*, Addison-Wesley, Reading, Massachusetts, p. 456.

Ulaby, F.T., Moore, R.K. and Fung, A.K., 1982, *Microwave Remote Sensing: Active and passive, Vol. II: Radar Remote Sensing and Surface Scattering and Emission Theory*, Addison-Wesley, Reading, Massachusetts, p. 608.

Ulaby, F.T., Moore, R.K. and Fung, A.K., 1986, *Microwave Remote Sensing: Active and Passive, Vol. III: From Theory to Applications*, Artech House, Boston, London, p. 1098.

Ulaby, F.T., Sarabandi, K., McDonald, K., Whitt, M. and Dobson, M.C., 1990, Michigan microwave canopy scattering model, *International Journal of Remote Sensing*, Vol. 11, 7, pp. 1223-1253.

Ulaby, F.T., 1998, SAR biophysical retrievals: Lessons learned and challenges to overcome, *Retrieval of bio- and geo-physical parameters from SAR data for land applications workshop*, ESA-ESTEC, 21-23 October 1998.

Visvalingham, M. and Tandy, J.D., 1972, The neutron method for measuring soil moisture content - a review, *Journal of Soil Science*, Vol. 243, pp. 499-511.

Waddingham, J., 1998, Water demand, in *Arid Land Resources and Their Management: Jordan's Desert Margin*, Dutton, R.W., Clarke, J.I. and Battikhi, A.M. (Ed.), Kegan Paul International, London, pp. 119-126.

Wadge, G., Archer, D.J. and Millington, A.C., 1994, Monitoring playa sedimentation using sequential radar images, *Terra Nova*, 6, pp. 391-396.

Wang, J., Schmugge, T.J. and Williams, D., 1978, Dielectric constants of soils at microwave frequencies, II, *Technical Note 1238, National Oceanic and Atmospheric Administration*, Greenbelt, MD.

Wang, J.R. and Schmugge, T.J., 1980, An empirical model for the complex dielectric permittivity of soils as a function of water content, *IEEE Transactions on Geoscience and Remote Sensing*, Vol. 18, 4, pp. 288-296.

Wang, J.R., Engman, E.T., Shiue, J.C., Rusek, M. and Steinmeier, C., 1986, The SIR-B observations of microwave backscatter dependence on soil moisture, surface roughness and vegetation covers, *IEEE Transactions on Geoscience and Remote Sensing*, Vol. 24, pp. 510-516.

Water Authority of Jordan, 1998, data from the 'Monthly summary of weather observations', *Water Authority of Jordan*, Amman.

Watson, A., 1992, Desert crusts and varnishes, in *Arid Zone Geomorphology*, Thomas, D.S.G. (Ed.), Belhaven, London, pp. 25-55.

Wegmuller, U. and Werner, C., 1997, Retrieval of vegetation parameters with SAR interferometry, *IEEE Transactions on Geoscience and Remote Sensing*, Vol. 35, 1, 18-24.

Wegmuller, U., Matzler, C., Huppi, R. and Schanda, E. 1994, Active and passive microwave signature catalogue on bare soil (2-12 GHz), *IEEE Transactions on Geoscience and Remote Sensing*, Vol. 32, 3, pp. 698-702.

Wegmuller, U., Strozzi, T., Farr, T. and Werner, C., 1998, Arid land surface characterisation with repeat-pass SAR interferometry, *Retrieval of bio- and geo-physical parameters from SAR data for land applications workshop*, ESA-ESTEC, 21-23 October 1998.

Wells, S.G., Dohrenwend, J.C., McFadden, L.D., Turrin, B.D. and Mahrer, K.D., 1985, Late Cenozoic landscape evolution of lava flow surfaces of the Cima Volcanic Field, Mojave Desert, California, *Geological Society of America, Bulletin*, Vol. 96, pp. 1518-1529.

Wesemael, B., Poesen, J., Figueiredo, T. and Govers, G., 1996, Surface roughness evolution of soils containing rock fragments, *Earth Surface Processes and Landforms*, Vol. 21, pp. 399-411.

Whalley, W.R., 1993, Considerations on the use of time-domain reflectometry (TDR) for measuring soil water content, *Journal of Soil Science*, Vol. 44, pp. 1-9.

Wheater, H.S., Butler, A.P., Stewart, E.J., and Hamilton, G.S., 1991, A multivariate spatial-temporal model of rainfall in southwest Saudi Arabia. I. Spatial rainfall characteristics and model formulation, *Journal of Hydrology*, Vol. 125, pp. 175-199.

Wu, S.T. and Fung, A.K., 1972, A non-coherent model for microwave emissions and backscattering from the sea surface, *Journal of Geophysical Research*, Vol. 77, pp. 5917-5929.

Zebker, H.A. and Goldstein, R.M., 1986, Topographic mapping from interferometric synthetic aperture radar observations, *Journal of Geophysical Research - Solid Earth and Planets*, Vol. 91, NB5, pp. 4993-4999.

Zegelin, S.J., White, I. and Jenkins, D.R., 1989, Improved field probes for soil water content and electrical conductivity measurement using time domain reflectometry, *Water Resources Research*, Vol. 25, pp. 2367-2376.

van Zyl, J.J., Burnette, C.F. and Farr, T.G., 1991, Inference of surface power spectra from inversion of multifrequency polarimetric radar data, *Geophysical Research Letters*, Vol. 18, 9, pp. 1787-1790.